Modeling Crystal Growth of Organic Materials

Nucleation, Steps and Morphology

Menno Deij

Modeling Crystal Growth of Organic Materials

Nucleation, Steps and Morphology

een wetenschappelijke proeve op het gebied van de
Natuurwetenschappen, Wiskunde en Informatica

Proefschrift

ter verkrijging van de graad van doctor
aan de Radboud Universiteit Nijmegen,
op gezag van de rector magnificus prof. mr. S.C.J.J. Kortmann,
volgens besluit van het College van Decanen
in het openbaar te verdedigen op
woensdag 9 januari 2008, om 15.30 uur

door

Menno Alexander Deij

geboren op 20 april 1975
te Utrecht

Promotor: pof. dr. E. Vlieg

Copromotor: dr. H. Meekes

Manuscriptcommissie: prof. dr. A. P. M. Kentgens

prof. dr. J. P. van der Eerden
Universiteit Utrecht

dr. F. J. J. Leusen
University of Bradford,
Verenigd Koninkrijk

Deij, Menno

PhD Thesis, University of Nijmegen, The Netherlands
With summary in Dutch
ISBN-13: 978-90-9022336-0
printed by: PrintPartners Ipskamp

In memoriam dr. L. J. L. Deij

10 april 1907 – 29 juli 2006

Dankwoord

Het resultaat van vier jaar onderzoek, zoals samengevat in dit proefschrift, had niet kunnen ontstaan zonder de medewerking van een aantal mensen die ik in dit dankwoord graag voor hun bijdrage wil bedanken.

Allereerst wil ik graag mijn promotor en co-promotor Elias Vlieg en Hugo Meekes bedanken. Elias, zonder het in mij gestelde vertrouwen aan het begin van de rit zou het nooit zover zijn gekomen. Gedurende de vier jaar heb ik me altijd thuis gevoeld bij Vaste Stof en ik heb je aanwezigheid en begeleiding altijd als leerzaam en prettig ervaren. Hugo “in verband met allerlei redenen” Meekes was mijn dagelijkse begeleider. Je *laissez faire* begeleiding vond ik een zeer prettige en werkzame aanpak: je liet me vrij om allerlei richtingen in het onderzoek te verkennen en zolang ik regelmatig goed nieuws had hoefde je me niet bij te sturen. De schrijfsels die van mijn hand op jouw bureau terecht kwamen, zijn door jouw kritisch lezen en het samen bespreken een set mooie artikelen geworden.

Piet Bennema was mijn leermeester op het gebied van de klassieke kristallografie, PBC-theorie en *attachment energy* berekeningen. Je prachtige verhalen over de (met de hand) PBC-analyse van granaat hebben diepe indruk gemaakt. Ook voor Venlafaxine heb je voor vorm **I** de PBC analyse met de hand gedaan. Als adviseur bij Synthon fungeerde je als brug tussen bedrijf en universiteit, en hebt daarmee het project in goede banen geleid.

Op het gebied van de *computational chemistry* wil ik graag Paul Verwer bedanken, die mij de achterliggende theorie en praktische ervaring in *molecular modelling* heeft bijgebracht. Ik vond het jammer dat je na verloop van tijd de universiteit hebt moeten verlaten, ik had nog veel van je kunnen leren.

Zjak, ik wil je graag bedanken voor een goede samenwerking in het “Synthon project”. Halverwege de rit werd je ernstig ziek, en na een levensreddende operatie en herstelperiode ben ook jij nu bezig met het afronden van je proefschrift. Ik bewonder je voor je doorzettingsvermogen en positieve instelling, waarmee je mede vormgegeven hebt aan het project. De vele ochtenden met een bak veel te sterke koffie bij Jan van Kessel staan me nog helder voor de geest: na aan flinke bak drukinkt konden we er weer tegen aan voor die dag!

Het project werd vanuit Synthon begeleid door Bertus, Rolf en Raymond. Ik wil Synthon in het algemeen, en jullie in het bijzonder, bedanken voor de begeleiding, de vrijheid die aan het onderzoek werd gegeven en het gemak waarmee wij met de 'kroonjuwelen' van Synthon aan de slag konden, en de resultaten konden presenteren en publiceren.

Verder ben ik dank verschuldigd aan René de Gelder, Jan Smits en Carmen Guguta. Niet alleen voor de eenkristal structuurbepalingen, maar ook de klimaatkamerstudie voor Ondansetron en verdere discussie over kristallografie, groei en morfologie.

Elias, Hugo, Willem, Herma, Jan Los en ik vormden een flinke tijd de stepclub. Regelmatig kwamen we bijeen om de fijnere theoretische nuances in de rol van stappen op groeiende kristal oppervlakken te bespreken, in de eerste instantie naar aanleiding van het werk van Herma, en na verloop van tijd ook voor de ontwikkelingen rond STEPLIFT. Jullie hebben me enorm geholpen zodat theoretische achtergrond van STEPLIFT goed in elkaar zit, wat leidde tot een mooie publicatie.

De eerste publicatie, over het groei gedrag van een gele kleurstof uit de fotografische industrie, had niet tot stand kunnen komen zonder het experimentele werk van Edwin. Ik kreeg een volledig experimenteel uitgezocht systeem in mijn schoot geworpen met de vraag 'of ik er niet eens wat met MONTY aan zou willen doen'. Mede dankzij de waardevolle experimentele data was het groeigedrag van theoretische zijde snel uitgezocht en dat resulteerde in een mooi verhaal in Langmuir. Voor het tot stand komen van dit werk ben ik verder dank verschuldigd aan Geert Deroover van Agfa, Luc van Meervelt van de Katholieke Universiteit Leuven en Steef Boerrigter.

Tijdens het schrijven en debuggen van MONTY2 heb ik als test een keer klein cluster van deeltjes uit laten groeien. Nadat het een paar duizend deeltjes groot was geworden leek het qua vorm al aardig op de bekende morfologie van het kristal en was het idee voor MONTY-3D in concept uitgewerkt. De theorie van uitgroeiende clusters en de daaraan gekoppelde waarschijnlijkheid tot uitgroeien kwam uit Delft, van Joop ter Horst. Voor onze goede samenwerking, waarvan de resultaten in hoofdstuk 4 en 5 staan, wil ik hem graag bedanken.

In de vier jaar als promovendus ben ik ook in de bevoorrechte positie geweest om een aantal studenten te begeleiden. Hanny was bezig met een experimentele stage bij Zjak, en wilde graag ook wat aan het modelleren doen. Hoewel de experimentele kant je meer lag, ben je toch enthousiast aan de slag gegaan met de soms ondoorgrondelijke MONTY input bestanden en heb je het groeigedrag van de verbinding waar je aan werkte zowel van experimentele als theoretische kant bestudeerd. Bas en Dennis kwamen voor een snuffelstage ook aan het modelleerwerk ruiken. 8 weken lang zetten jullie je in om de simulaties tot een goed einde te brengen. Bas, later heb je ook een experimentele stage gedaan bij Zjak en Ernst en je werk aan Ondansetron met vaste stof NMR heeft bijgedragen aan de laatste twee hoofdstukken van dit proefschrift. Mede dankzij jouw resultaten hebben we een overtuigende zaak kunnen maken van de wanorde in de structuur van Ondansetron.

De laatste student die ik heb begeleid was natuurlijk Teun. Teun, je bent ruim een jaar onder mijn hoede geweest en je enigszins onorthodoxe aanpak en aanstekelijk goede humeur zullen me uit deze tijd bijblijven. Nog lang na je vertrek heb ik jouw stopwoord “APPARAAT!!” gebruikt als er weer eens iets niet deed wat het moest doen. Ook je onvergetelijke uitspraak “Het leven is geen lolletje, paraplu, paraplu, parasolletje!” wil ik bij deze vereeuwigd zien in dit dankwoord. Je hebt een prachtig stuk werk afgeleverd, waarvan je de resultaten in hoofdstuk 6 terugziet. Je hebt heel zelfstandig gewerkt, zeker in de tijd dat ik in Australië was. Je zocht hulp bij Willem en Jan Los dat leidde tot de ontwikkeling van de *growth site theory*.

I spent a busy five weeks at Curtin University in Perth, Australia working with Julian Gale, Stefano Piana and Sean Fleming, on integration of MONTY and GDIS, implementing a forcefield in GULP and studying diffusion with MONTY. I would like to thank you and the members of the Nanochemistry Research Institute for a warm reception and a very enjoyable time.

Verder wil ik alle mensen van de Vaste Stof Chemie groep die in de jaren zijn gekomen en gegaan, of er altijd al waren, of nooit meer zijn weggegaan, graag bedanken voor de gemoedelijke sfeer (Sinterklaas en het jaarlijkse labuitje gevolgd door barbecue waren de jaarlijks terugkerende hoogtepunten!). Cristina, Daniel, Elias, Elizabeth, Herma, Hugo, Ismail, Jan van Kessel, Jan Los, Jelena, Maurits, Natalia, Neda, Paul Poodt, Paul Verwer, Sander, Willem, Wim en Wisiek: dank jullie wel! (ik hoop dat ik niemand ben vergeten...)

Mijn ouders Kees en Ingrid wil ik bedanken voor hun onvoorwaardelijke steun en de vrijheid die ze me gegeven hebben mijn eigen koers te varen in het leven.

Als laatste wil ik graag Roland bedanken. Je hebt me in de vier jaar promotietijd altijd ondersteund en in evenwicht gehouden en we zijn nu samen aan ons volgende hoofdstuk begonnen. Vorig weekend vierden we ons tienjarig samenzijn, en ik hoop dat er nog veel jubilea zullen volgen!

6 Augustus 2007

Menno

Inhoudsopgave

Chapter 1

Steps on surfaces in modeling crystal growth

1.1 Polymorphism and morphology prediction

The study of polymorphism of organic materials is important in the development of new products in, e.g., the pharmaceutical, photographic and food industry. For pharmaceutical compounds, the study of polymorphism is an important part in the development of a new drug.[1] As each polymorph has different metabolical characteristics, often only one polymorph can be used in a drug formulation.[2] Knowledge of the polymorphs and their relative stabilities is therefore indispensable for the development of drugs that are administered in crystalline form. Apart from formulation issues, each new polymorph can be patented, so also for protection of intellectual property adequate knowledge of polymorphism is needed.

Polymorphs can have different crystal morphologies, because morphology is largely determined by the crystal packing at the molecular level and the crystallization process. It is desirable to be able to exert control over the morphology, because it determines among other things the bioavailability and the processability of the compound. The bioavailability depends on the dissolution rate of the crystals, which is in turn partly determined by the crystal morphology. Concerning processability, it can generally be said that block-like crystals habits are desired over plate-like crystals and needles because the latter forms tend to block filters, are more difficult to dry and give problems during tabletting.

Crystal morphology can be predicted computationally using various methods of different complexity and demand for computing power. Well-known approaches are the method developed by Bravais, Friedel, Donnay and Harker (BFDH) based on the interplanar distances of crystallographic orientations[3, 4] and the method developed by Hartman and Perdok[5, 6, 7], and later by Hartman and Bennema[8], which uses the concept of the crystal graph to determine the slice and attachment energies of crystallographic orientations, and relates these energies to the growth rate of the orientations.

The development of detailed crystal growth simulations, for instance using Monte Carlo techniques, has been facilitated by the ongoing development and availability of ever faster computers. A recent development is a program called Monty with which growth simulations can be performed for arbitrary crystal structures in any crystallographic orientation as a function of the driving force for crystallization.[9]

1.2 Morphology prediction methods

Generally speaking, growth morphologies can be constructed using a kinetic Wulff construction.[10] In this construction the distance $\mathbf{r}_{hkl}$ of a face (hkl) from the origin of the crystal is taken to be linearly related to the growth rate R_{hkl} of that face.

$$\mathbf{r}_{hkl} \propto R_{hkl} \tag{1.1}$$

By constructing a three-dimensional set of faces perpendicular to the crystallographic orientations (hkl) the growth morphology can be constructed if the growth rates of the faces are known. Different theories have been developed to derive or compute expressions for the growth rate R_{hkl}. Three of these will be discussed below.

1.2.1 BFDH method

Although being an approach for predicting equilibrium morphology, the BFDH method is commonly used to relate the growth rate of a crystallographic orientation to the inverse of the interplanar distance d_{hkl}. The relevant indices (hkl) are those allowed by the spacegroup selection rules. The distance from the center of the crystal to a surface (hkl) is then given by

$$|\mathbf{r}_{hkl}| = \frac{1}{d_{hkl}}. \tag{1.2}$$

In retrospect, the rationale behind the method is that the larger d_{hkl} is, the larger the energy content of the growth layer will be, and therefore the smaller the growth rate of the corresponding orientation will be. This limits the predictive power of the BFDH method in the case of anisotropic crystal structures. The determination of the values for d_{hkl}, however, is trivial once the space group and lattice parameters are known, making the BFDH a very fast method. Given its limited applicability, the use of the BFDH model is now largely superseded by the use of the attachment energy model or other models.[11, 12, 13, 14, 15, 16, 17, 18]

1.2.2 Hartman Perdok theory and the determination of the crystal graph

In the extension of the Hartman-Perdok theory by Hartman and Bennema, the concept of the crystal graph is introduced.[8] The crystal graph is a mathematical representation of the crystal structure as an infinite three dimensional graph, in which the graph vertices represent the growth units and the graph edges represent the interactions between the growth units.

The crystal graph is used to determine Periodic Bond Chains (PBCs). PBCs are uninterrupted chains of bonds between symmetry-related growth units with an overall periodicity $[uvw] = u\mathbf{a} + v\mathbf{b} + w\mathbf{c}$, $(u,\ v,\ w\ \in \mathbb{Z})$ of the primitive lattice, which contains no other lattice translation. PBCs are stoichiometric with respect to the contents of the crystal unit cell. Combinations of two or more intersecting PBCs in non-parallel directions in a growth layer define so-called connected nets.

Crystallographic orientations that have connected nets are likely to determine the growth morphology of the crystal.[19] In the Hartman-Perdok theory, the attachment energies of the connected nets in all crystallographic orientations determine the growth morphology. The bonds that are present in a crystal slice together make up the crystal's slice energy; the other bonds define the slice attachment energy. Together, they are equal to the crystallization energy:

$$
\begin{aligned}
E_{hkl}^{att} &= \sum_i \phi_{hkl}^{i,att} \\
E_{hkl}^{slice} &= \sum_i \phi_{hkl}^{i,slice} \\
E^{cryst} &= E_{hkl}^{att} + E_{hkl}^{slice}
\end{aligned}
\tag{1.3}
$$

Once the attachment energies for all orientations that have one or more connected nets have been computed, the attachment energies are related to growth rates R_{hkl} as

$$R_{hkl} \propto E_{hkl}^{att} = E^{cryst} - E_{hkl}^{slice}, \tag{1.4}$$

allowing for the prediction of the attachment energy morphology. The attachment energy method can thus be considered as a refinement of the BFDH method using the slice energy as the parameter determining the growth. The BFDH method uses the interplanar distance, which is merely a geometrical parameter.

1.2.3 Monte Carlo growth simulations

The methods described above give a reasonable approximation of the growth morphology in several cases. It is well-known, however, that the growth morphology depends on the driving force (i.e. the solution supersaturation) and growth mechanism during growth of the crystal.[20] This is not taken into account when a morphology is calculated using the BFDH approach nor when based on the Hartman-Perdok theory. Recently the program MONTY was developed by Boerrigter et al. that is able to perform growth simulations on any crystal structure in any crystallographic orientation.[9]

In these simulations a box with lateral periodic boundary conditions is prepared in a certain crystallographic orientation (hkl) on which particles may attach and detach with the following probabilities:

$$\begin{aligned} \mathcal{P}^{+}_{ij} &= \exp\left(-\beta\lambda(\Delta U - \Delta U_{ij}) - \beta(\lambda-1)(\Delta\mu)\right) \\ \mathcal{P}^{-}_{ij} &= \exp\left(-\beta(\lambda-1)(\Delta U - \Delta U_{ij}) - \beta\lambda(\Delta\mu)\right) \end{aligned} \tag{1.5}$$

where ij denotes a particle i having a bonding configuration j with surface bonding energy U_{ij} and $\beta = (k_B T)^{-1}$. These probabilities ensure microscopic reversability at all times. The probabilities allow for a choice of the parameter $0 \leq \lambda \leq 1$, which controls the contribution of $\Delta\mu$ vs. the surface bonding ΔU_{ij} to the probabilities. When $\lambda = 0$, the attachment probability, $\mathcal{P}^{+}_{ij}$ is completely determined by the driving force $\Delta\mu$ and the detachment probability $\mathcal{P}^{-}_{ij}$ is completely determined by the surface bonding energy ΔU_{ij}. This probability scheme is called ‘random rain’ and has been shown to give good results for the simulation of crystal growth from solution.[21] Growth rates can be computed directly from the Monte Carlo results, allowing for a kinetic Wulff construction of the growth morphology.

Examples of the use of Monte Carlo simulations in understanding the crystal growth are found in the study of model systems[22, 23, 24, 25, 26, 27] and ‘real world’ crystals, like fats[9], urea[28, 29], aspartame[30, 31] and polycenes[32].

1.3 The importance of steps in the crystal growth process

Recently shortcomings of the Hartman-Perdok theory were found when studying the growth morphology of aspartame.[30, 31] In this study it was shown that the orientations on the needle-tips of aspartame crystals were growing rough, i.e. fast, already at the lowest driving forces, despite the presence of connected nets which are built up of relatively strong bonds. This, together with the needle side faces which showed slow growth, could explain the extreme needle-shaped morphology. The Hartman-Perdok theory failed to predict the needle morphology of aspartame as growth mechanisms are not incorporated in this theory.

More or less at the same time that the Hartman-Perdok theory was developed, it became clear that crystal F-faces cannot maintain their flat appearance under all circumstances. Any facet (hkl) will become rough, i.e. rounded off, above a critical temperature, the roughening temperature, T^R_{hkl}, or beyond a threshold driving force for crystallization $\Delta\mu^c_{hkl}$ (kinetic roughening). The roughening temperature is closely related to the Ising order-disorder transition temperature of 2D lattice of spin states.[33] Once rough, an orientation generally grows fast.

As an integration of the Hartman-Perdok theory and the theory of the roughening transition, connected nets can be used to estimate a lower bound on roughening temperatures by computing the Ising order-disorder transition temperatures of connected nets. Simple connected nets can be mapped directly onto a two-dimensional Ising spin model and Rijpkema et al. showed that for any connected net that contains no crossing bonds an Ising temperature can be computed.[34] The Ising temperature is a measure for the tendency of a certain orientation to become rough and can thus be used as a classification of morphological importance. This was, for example, shown for the morphology of fat crystals.[35] This interpretation of connected nets also implies a non-zero roughening temperature for any connected net, i.e. connected net orientations are F-faces, while orientations (hkl) without a connected net are always rough and have T^R_{hkl}=0.

In the remainder of this chapter we will discuss the progress made in the recent past along the line of connected net theory. These recent developments were necessary because of the failure of the attachment energy method for the aspartame morphology and other cases, as will be illustrated using three model systems. First, however, we make a small detour by drawing analogies between the ideas of the attachment energy method and concepts used in the field of crystal engineering. Next, for each of the model systems used we study some orientations with one or more connected nets that nevertheless have no nucleation barrier and show S- or K-face character. The zero roughening temperature of S- and K-faces is reflected in a zero step free energy for certain step directions on these faces. This indicates the need to look at steps on surfaces to better understand the growth behavior of these orientations. This is possible both by using the program STEPLIFT, which is introduced in Chapter 3, and by performing Monte Carlo simulations[9]. These complimentary methods give good insight in the growth behavior of these anomalous faces. Finally, we draw conclusions from the examples and peculiarities presented, and give an outlook that addresses the need to look in a detailed way at steps and simulated growth behavior of crystals to better understand the experimentally observed crystal habits. Furthermore, detailed knowledge of surface structures, especially as a function of driving force and temperature, can be used to tailor the physicochemical properties of these interfaces.

1.4 Network solids and their relation to crystal graphs

To start with, we look at networks in crystals to try and bridge the two fields of crystal engineering and crystal growth by identifying common patterns and their usage. The PBC and connected net terminology has been used exclusively in the description of crystal growth, but the idea of networks in crystalline structures is of course far more widespread: in the field of crystal engineering, there have been numerous studies on synthesis, properties and functionality of network solids and molecular tectonics, i.e. the phenomenon that carefully chosen molecular synthons are able to form 'zero-dimensional' polyhedra, one-dimensional chains, two-dimensional sheets or three-dimensional networks.[36, 37, 38, 39] These networks are commonly built up using metal coordination chemistry or hydrogen bonding, two supramolecular interactions that have directionality. Using these types of interactions, intriguing structures of different dimensionality have been created in the past decades.[40] Three-dimensional networks based on coordination chemistry are either close-packed solids or microporous materials, in which case they are often referred to as metal-organic frameworks.[41] This kind of porous structure typically finds application as gas-sorption materials or separation membranes.

To draw analogies between the field of (designed) network solids and our use of crystal graphs, it can be argued that the crystal graph is conceptually similar to the 3D network, the connected nets to the 2D sheets and the PBCs to the 1D chains. As said, often the networks are based on hydrogen bonding and/or metal coordination chemistry. For crystal graphs, however, all supramolecular interactions between two separate molecules – hydrogen bonds, electrostatics and van der Waals interactions – are lumped together in a single line with corresponding energy. The nodes represent the separate molecules. All lines and nodes together from the network, or crystal graph.

Molecular crystals have been recognized[42] as 'supramolecule[s] *par excellence*', given the periodic arrangement of supramolecular interactions holding the molecules in the crystal structure. As the interactions between the molecules of a crystal are a subtle interplay of various supramolecular interactions, the combination of all contributions to a bond between molecules is a logical choice for a description of the growth behavior. Nevertheless, a refinement in this description of interactions between molecules would be to study the relative contribution of the various types of supramolecular interactions to a single bond, to be able to quantify specific solvent and growth unit interactions at the growing surface.

In crystal engineering one is mainly interested in the interactions in the bulk of the crystal. In crystal growth studies, however, the crystal surface plays the key role. In the crystal graph theory the bulk crystal structure is used to also model the structure of the surface, thereby neglecting surface relaxations and surface reconstructions. Thus, connected nets are specific bulk terminations

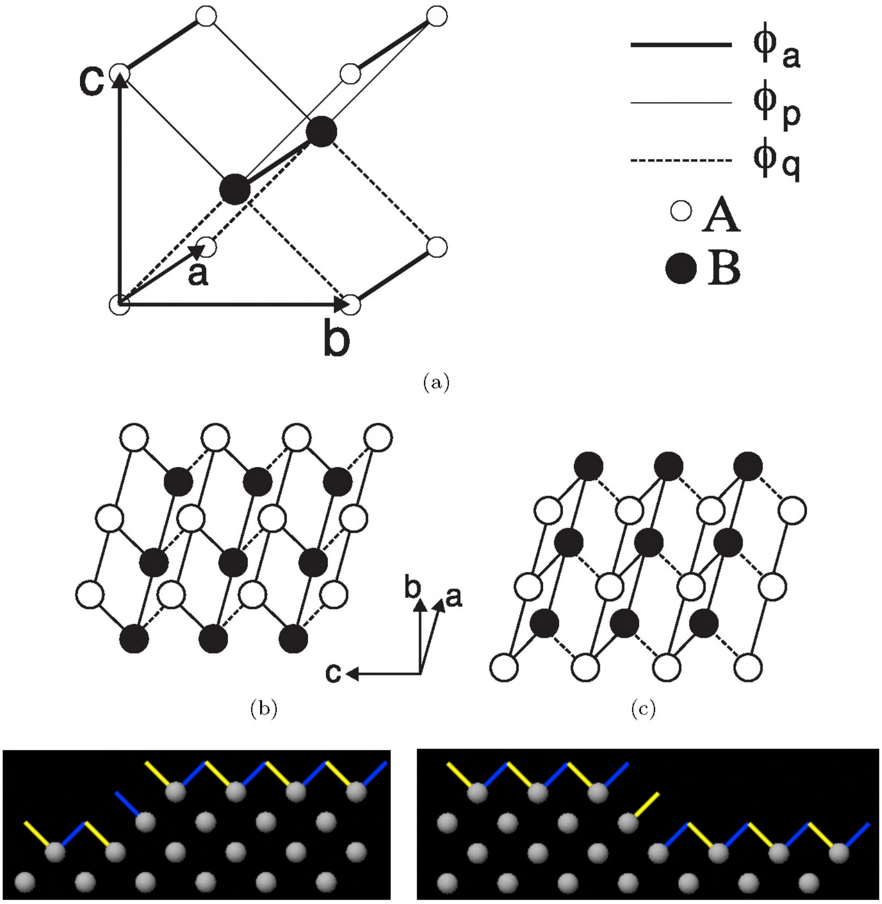

(a)

(b) (c)

(d) (e)

Figure 1.1: Symmetry roughening for the {010} orientations of an anisotropic Kossel model graph, shown in 1.1(a). A and B represent two growth units (molecules) in the unit cell. The two possible connected nets for {010} are shown in 1.1(b) and 1.1(c). The steps along [100] shown in 1.1(d) and 1.1(e) are two opposite step edges that can be formed on this orientation, which both have zero step energy, as the same number of yellow and blue bonds is broken in the step edges as on the terraces. In the last two pictures the yellow and blue lines represent the broken bonds at the surface, ϕ_p and ϕ_q respectively.

of the crystalline material. Specific interactions between growth units at the surface and solvent molecules are usually also not taken into account, and these may also be an excellent opportunity for refinement in the study of crystal growth using crystal graph theory. In fact, specific interactions between crystal surfaces and solvents are already a field of investigation, mainly using molecular dynamics.[28, 43, 44, 45, 46, 47]

1.5 Connected nets without a nucleation barrier

In the following sections we will use the connected nets of a number of model systems to highlight the shortcomings of the attachment energy theory by showing that these connected nets have no nucleation barrier, and have, consequently, a zero roughening temperature.

1.5.1 Symmetry roughening: symmetric S-type graph

Recently, we have found crystal graphs in which certain connected net orientations have multiple connected nets, but no 2D-nucleation barrier.[48] For a number of these graphs, this behavior could be understood in terms of the spacegroup symmetry, and the phenomenon was called ‘symmetry roughening’, as the orientations show rough growth behavior due to the absence of a 2D nucleation barrier, i.e. T^R=0. An example of this is shown in Figure 1.1, where a crystal graph is shown for an anisotropic Kossel model. This model has symmetry roughened orientations for the $\{010\}$ form. These orientations have two connected nets, related by mirror symmetry, as shown in Figures 1.1(b) and 1.1(c). It is, however, possible to create steps on this connected net that have zero step energy in the [001] and $[00\bar{1}]$ directions, as shown in Figure 1.1(d) and 1.1(e). These opposite steps can be combined to form two sides of an island. This means that, in terms of the Hartman-Perdok classification, the face is not an F-face, but an S-face, despite the presence of connected nets.

1.5.2 Symmetric K-type graph

A second example in which symmetry roughening plays a role is displayed in Figure 1.2. The graph shown in Figure 1.2(a) is derived from the CsCl crystal structure, by introduction of two different bonds, ϕ_p and ϕ_q. The orientations where symmetry roughening plays a role is (100) and its symmetry-related counterparts $(\bar{1}00)$, (010) and $(0\bar{1}0)$ (the spacegroup of this graph is P4mm; the fourfold axis is parallel to **c**). Although the attachment energy for these orientations is equal to $4(\phi_p+\phi_q)$ for both connected nets present, steps with step front orientations (i.e. having the orientation perpendicular to the step front) $[0\bar{1}0]$, [010], [001] and $[00\bar{1}]$ have zero step energy (see Figures 1.2(b) - 1.2(e)). These four opposite steps can be combined to form a zero energy island, giving this orientation a K-face character. Again, this is a case of symmetry roughening due to the action of the mirror symmetry elements.

1.5.3 Asymmetric S-type graph

Next, in a detailed investigation of the growth behavior of aspartame and later followed by other experimental crystal structures, we have discovered that there are also connected net orientations that have a zero 2D nucleation barrier, but that this could not be based on any symmetry argument.[30, 49, 50] Thus, the absence of a 2D nucleation barrier for connected nets seems to be more common than the few cases of symmetry-related connected nets. Two examples are shown in Figures 1.3 and 1.4. Figure 1.3 shows the model crystal graph derived from the (111) face of aspartame phase II-A. The two steps in Figures 1.3(b) and 1.3(c) have a step energy of -ϕ_q and ϕ_q respectively, which, when combined, result in an island with the sum of the opposite step energies equal to zero. This means that this face will have an S-face character.

To illustrate the presence and complexity of steps of zero step energy in 'real' crystals, in Figure 1.4 two steps on the $(0\bar{1}\bar{1})$ surface of aspartame II-A are displayed. In each unit cell, the number and strength (different bonds have different colors) of the broken bonds are the same, leading to both steps having zero step energy. Also in this case, there is no symmetry roughening involved. Again, due to both steps having zero step energy, this face will have an S-face character, with T^R=0. In fact, almost all the faces in the $\{00l\}$ zone have a zero roughening temperature, due to zero or even negative step energies. The remaining few faces in that zone all have very low step energies, which makes growth in the **c**-axis direction very fast, resulting in the needle-shaped morphology. This needle-shaped morphology is indeed found both from Monte Carlo simulations[30] and from a comprehensive step energy analysis, using the STEPLIFT procedure[49].

1.5.4 Formation of steps with zero step energy

In all cases described above, it has been possible to create step configurations that have zero step energy, or, when combining two opposite steps, gave zero island energy. In all cases, we note that the creation of an island with zero step energy is realized by using a non-stoichiometric number of growth units, i.e. it is not possible to use an integer number of unit cells to create such step structures. After the creation of an initial non-stoichiometric island, however, it is of course possible to add complete unit cells without additional step energy cost, because of translational symmetry. Describing crystal growth solely on the basis of whole unit cells[51] is therefore not advisable, as these special zero step energy cases can be overlooked in that case.

Another interesting point is that the creation of zero energy step configurations often relies on saturating an A-B bond, while at the same time creating a

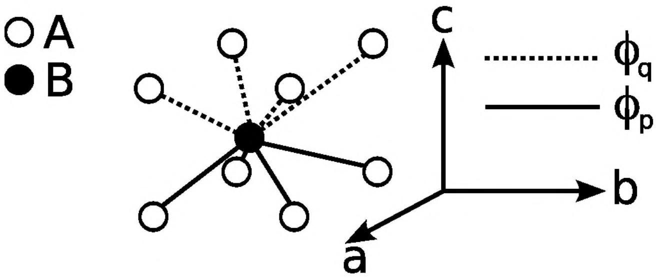

(a)

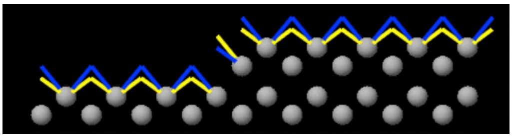

(b) View of (100) along [001]

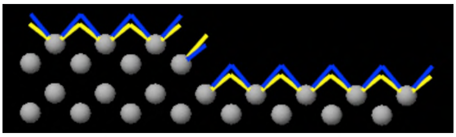

(c) View of (100) along [001]

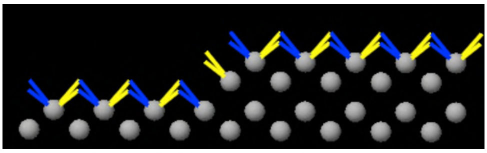

(d) View of (100) along [010]

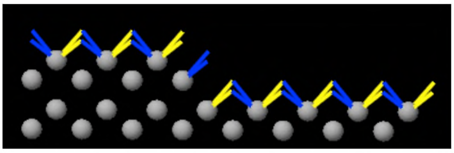

(e) View of (100) along [010]

Figure 1.2: Symmetry roughening for the $\{100\}$ orientations of a graph derived from the CsCl crystal structure. The steps with step front orientations $[0\bar{1}0]$, $[010]$, $[001]$ and $[00\bar{1}]$ (1.2(b) - 1.2(e)) all have zero step energy. The yellow and blue lines represent the broken bonds at the surface, ϕ_q and ϕ_p, respectively.

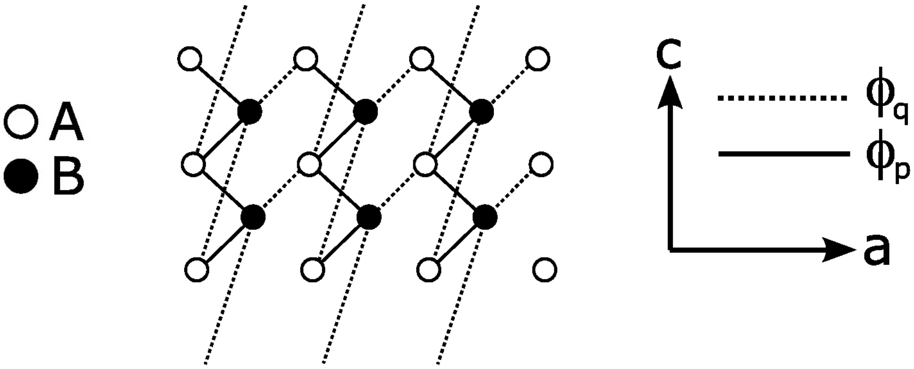

(a)

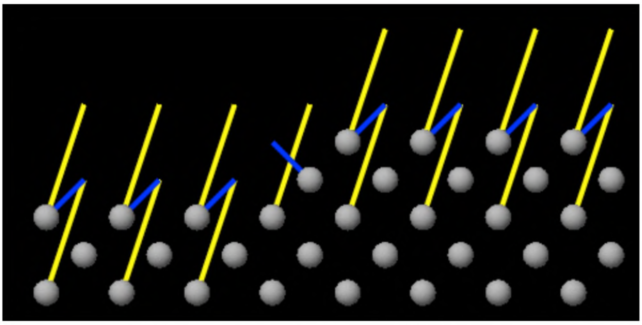

(b) View of (001) in the [010] direction

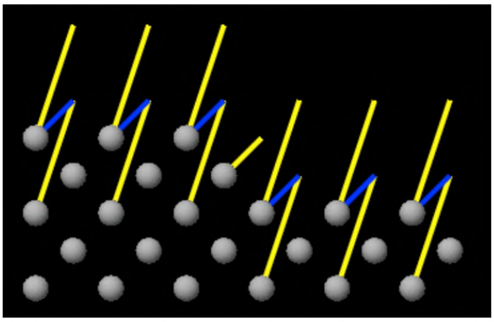

(c) View of (001) in the [010] direction

Figure 1.3: The model crystal graph derived from the (111) face of aspartame II-A, viewed along the **b**-axis, is displayed in Figure 1.3(a). The two steps shown in 1.3(b) and 1.3(c) have step energies of -ϕ_q and ϕ_q respectively, giving an island with two opposite steps that have the sum of their step energies equal to zero. In the last two pictures the blue and yellow lines represent the broken bonds at the surface, ϕ_p and ϕ_q respectively.

Table 1.1: The bond strengths used in the simulations of the three model systems.

Bond Strengths [kJ·mol^{-1}]	Symmetric S-type graph (Figure 1.1)	Asymmetric S-type graph (Figure 1.2)	K-type graph (Figure 1.3)
ϕ_a	5.0	5.0	-
ϕ_p	4.0	4.0	3.0
ϕ_q	6.0	6.0	4.5

broken B-A bond. As the energy of a broken bond between A and B is equal regardless of particle identity, this occurs without additional energy cost. The interaction of A and B with the solvent can be different however, and may lead to additional energetic terms. This phenomenon of 'bond polarity' was indeed found in naphthalene, on the (011) face.[13]

1.6 Monte Carlo simulations

Monte Carlo simulations have been a very useful tool to simulate crystal growth in order to study fundamental problems as outlined in Section 1.5[48] and the growth behavior of complex organic crystals.[9, 30, 31, 50, 52, 53] The study of the latter was greatly facilitated by the development of the MONTY simulation package, which allows for the simulation of crystal growth on any crystallographic orientation of any crystal structure by means of its crystal graph.[9] The three model systems, a symmetric S-type graph (Figure 1.1), a symmetric K-type graph (Figure 1.2) and an asymmetric S-type graph (Figure 1.3), which were used earlier to illustrate connected nets that have S-face and K-face character are here studied using Monte Carlo growth simulations.

The symmetric and asymmetric S-type graphs have three different bonds ϕ_a, ϕ_p and ϕ_q; the symmetric K-type graph has two different bonds, ϕ_p and ϕ_q, all listed in Table 1.1. The choice of these bond strengths ensures that each graph has the same total crystallization energy of 30 kJ·mol^{-1}.

For the simulations a random-rain probability scheme was used, which means that the incoming flux of particles depends solely on the driving force $\Delta\mu/kT$, while the probability of growth unit removal from the growing surface is governed by the strength with which the particle is bound to the surface.

One of the results that can be obtained from the simulations is the sticking fraction S, which is defined as

$$S = \frac{N_{gr} - N_{et}}{N_{gr}} \tag{1.6}$$

where N_{gr} is the number of particles grown and N_{et} is the number of particles etched. The sum of the two is equal to the number of Monte Carlo events: one move is either a growth event or an etch event. The sticking fraction indicates the fraction of growth events that resulted in actual growth taking place.

The sticking fractions are displayed in Figure 1.6 as a function of driving force for the anomalous orientations of the crystal graphs of Figures 1.1, 1.2 and 1.3, simulated at 300K. As can be seen from this Figure, the crystal surfaces that have no 2D nucleation barrier grow already at very low driving force. To compare, (100) of the symmetric S-type graph, an F-face that does have a nucleation barrier, is also shown. Even at $\Delta\mu/kT$=0, the surfaces without nucleation barrier tend to roughen due to statistical fluctuations. Pictures of the resulting surface configurations at a very low driving force of $\Delta\mu/kT$=0.02 for all graphs are shown in Figure 1.5. It can be clearly seen that the graphs with S-face character (Figures 1.5(a) and 1.5(c)) have elongated surface structures, as the islands that form on these surfaces have two opposite step orientations with zero step energy. The K-face surface (Fig. 1.5(b)) shows an even more rough surface, as this has no step edges with a non-zero step energy. The quantitative numbers of the sticking fraction are also partly determined by the finite size of the simulation box. Enlarging the simulation box in the direction of the elongated surface structures gives higher values for the sticking fraction. A finite size effect, however, is not the cause for the slight downward curvature of the sticking fraction of the K-type graph (100) face simulations: enlarging the simulation grid by a factor of 25 does not significantly change the values of the sticking fraction. The initial non-linear curvature of the K-type graph is probably due to the fact that during growth, not all particles that can attach to the surface may do so without cost in energy. Only when four surrounding A growth units are present can a B growth unit attach without an energetic cost, and vice versa. Therefore, only a selected number of specific sequences of growth unit attachments lead to growth without an energetic barrier.

When the temperature is lowered, the S- and K-face character becomes even more pronounced in the resulting surface configurations, as thermal fluctuations become less probable. The same simulations were run at 150 K and $\Delta\mu/kT$=0.1 and the resulting surface configurations are shown in Figure 1.7. The K-face graph (Fig. 1.7(b)) still shows a rough surface; islands on the surfaces of the two S-type graphs become very elongated.

1.7 Step energy determination

Although Monte Carlo simulations give a good insight in the overall surface structure and growth rate of various crystal faces they do not offer an explanation for the growth behavior simulated. As was shown in the Figures 1.1, 1.2 and 1.3 the determination of step structures on surfaces does offer insight in this behavior. In an effort to determine step structures for any crystal structure and any crystallographic orientation, the program STEPLIFT was developed.[49, 54] This program enables us to calculate all the step configurations along PBC-

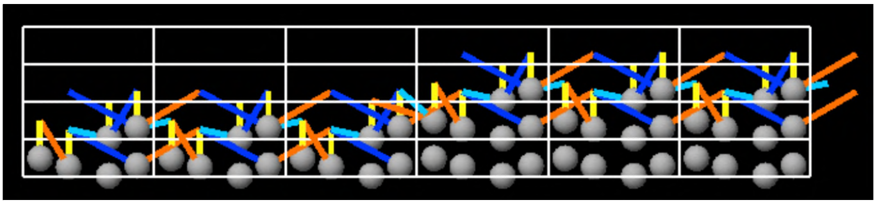

(a) View of $(0\bar{1}\bar{1})$ in the $[0\bar{1}1]$ direction

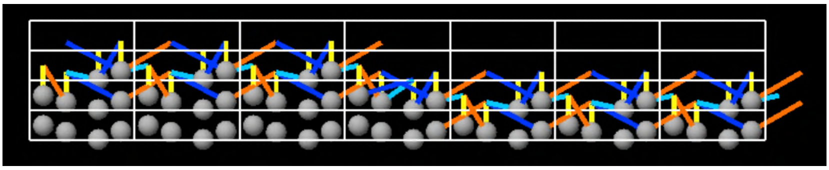

(b) View of $(0\bar{1}\bar{1})$ in the $[0\bar{1}1]$ direction

Figure 1.4: Two steps on the $(0\bar{1}\bar{1})$ surface of aspartame II-A. The white outlines represent the unit cells, the grey particles the aspartame molecules and the colored lines the broken bonds of different strength between molecules. Both steps have zero step energy. This can most easily be visualized as follows: for the step in Figure 1.4(a) the step front is in the fourth column of cells, and for each column of cells, the number of broken bonds is the same: three red, two light blue, three dark blue and four yellow bonds are broken in each column. For the opposite step in Figure 1.4(b) the same applies; the step front is also in the fourth column of cells.

directions on all connected net orientations of a crystal graph. The advantages of the STEPLIFT method are twofold. First of all, although it ignores entropic contributions of kinks, it allows for a fast calculation of step energies, compared to the MONTY simulations. Secondly, the graphical user interface of the program gives a detailed three-dimensional overview of the steps. All the pictures of steps shown in Figures 1.1 - 1.4 are actually screenshots of the STEPLIFT program. This can give a better understanding of the growth in terms of the step structures that are possible on the crystallographic orientations of interest.

Another application of the step energies calculated with STEPLIFT is the use of the average step energy on a certain crystallographic orientation in expressions for the growth rate as a function of the driving force, which allows for the prediction of the growth morphology as a function of the driving force. This method is applied to the morphology prediction of a number of complex organic crystals: aspartame II-A, Venlafaxine and two polymorphs of a yellow isoxazolone dye.[49] In this application it is shown that the morphology based on the average step energies is closer to the experimentally observed morphology than the morphology obtained using the attachment energy method. This, and the fact that the method is fast, makes STEPLIFT a promising morphology prediction tool.

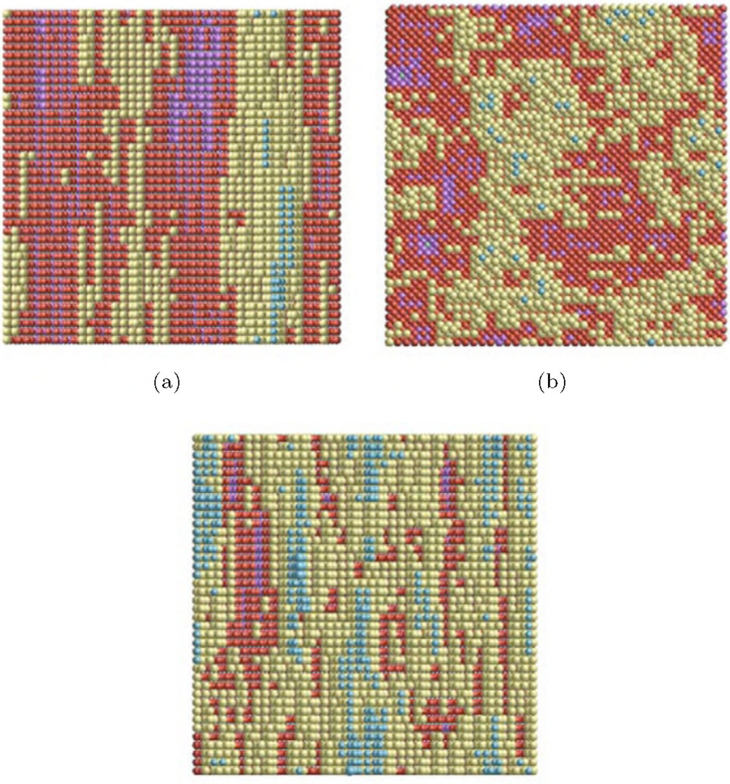

(a)

(b)

(c)

Figure 1.5: Surface configurations of the symmetric S-type graph (010) orientation (a), the K-type graph (001) orientation (b) and the non-symmetric S-type graph (001) orientation (c). All surface configurations are the result of a Monte Carlo growth simulation at very low driving force, $\Delta\mu/kT$=0.02 and temperature 300K.

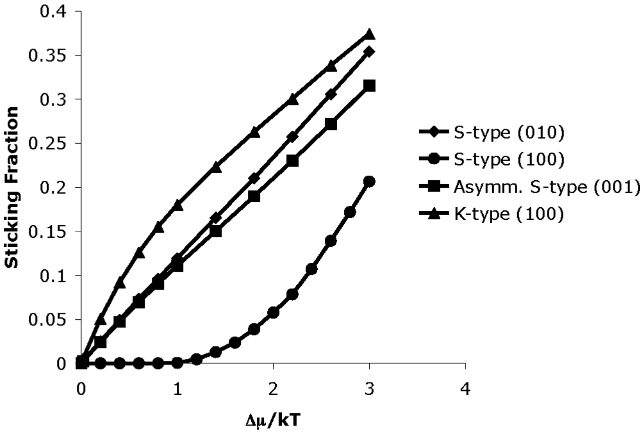

Figure 1.6: The sticking fraction of the three graphs determined at 300 K with Monte Carlo simulations. The symmetric S-type graph (010) face shows S-face character, the (100) face is an F-face. Note that this F-face only starts to grow at a $\Delta\mu/kT=1.0$, and that the initial curvature is not linear. The S- and K-face character of the other faces can be seen in the fact that there is no nucleation barrier: at very low $\Delta\mu/kT$ the crystal already has a non-zero sticking fraction. Also, the dependence on $\Delta\mu/kT$ is more or less linear, when compared to the sticking fraction of the F-face, indicating a rough growth behavior.

1.8 Conclusions and outlook

In recent years the need to look in a detailed way at steps on growing surfaces has become apparent, both due to the symmetry roughening phenomenon, as well as the discovery of zero roughening temperatures of certain connected nets that could not be explained on the basis of symmetry. We have pursued two ways to address this problem, Monte Carlo simulations and the determination of step configurations. In the former approach this resulted in the development of MONTY, the Monte Carlo simulation package for simulation of crystal growth for any crystal structure in any crystallographic orientation. Next, we have made considerable progress in tackling the general task of being able to determine arbitrary step configurations for any crystal structure and any crystallographic orientation. The development of STEPLIFT has allowed to do this in a fast and automated way.

We found that zero roughening temperatures for certain connected nets could be explained by looking at the step structures. These step structures have two important characteristics: first, they are based on a non-stoichiometric number of particles, compared to the number of particles in the unit cell. This means that methods that only use the complete unit cell will miss these special step configurations. Secondly, the special step structures are based on bond polarity: when for instance an A-B bond is saturated, a B-A bond becomes unsaturated.

In our approach, the bond energies involved are identical, but in practice these may be different, for instance due to different interactions with the solvent.

The result of the presence of orientations that have a zero roughening temperature, despite having a connected net, is that the attachment energy method will give erroneous results for these orientations. This may have a small effect, when other orientations are close in attachment energy, but it may also lead to a dramatic failure of the attachment energy method. This was found for Aspartame phase II-A and also for phase II of a yellow isoxazolone dye, and can be explained both by performing MC simulations and by looking at steps.[30, 49, 50]

In STEPLIFT and MONTY, a number of assumptions have been made. Both being based on the graph representation of the crystal structure, the procedures can not take surface relaxation or surface reconstruction into account. Also specific interactions with solvents are currently not taken into account. A first approach to take on this specific problem is to look at the various contributions that make up a bond between two growth units in the crystal graph, and correlating this with interactions between growth units and solvent molecules. This can for instance be done using techniques similar to COSMO[55], used for the quantitative computation of solvent-solute interactions.

Another approach to overcome the shortcomings of the methods outlined in this chapter is to use more sophisticated techniques like molecular dynamics, which have up to now been computationally prohibitively expensive. With the advent of ever faster computers and the adoption of GRID-based computing, these kind of simulations are becoming feasible, and these refinements should definitely be pursued. Recently, initial steps in that direction have been taken for relatively simple molecular solids, like urea.[28, 29, 43]

With respect to the calculation of step energies from first principles, STEPLIFT is at the moment a technique that works at 0K, thereby ignoring the contribution of kinks to the step free energy. To be able to include kinks and to study thermal and kinetic roughening, a rigorous theoretical framework for kinks in arbitrary lattices is needed, as well as an expansion of the automatic method for finding step configurations that includes the calculation of kink configurations.

This all leads to a better understanding of the surface structure as a function of driving force, opening the way for numerous applications, like rational design of tailor-made additives and nucleation inhibitors, epitaxial growth and templating, surface reactivity and catalysis, and the creation of chemically and physically nanostructured interfaces.

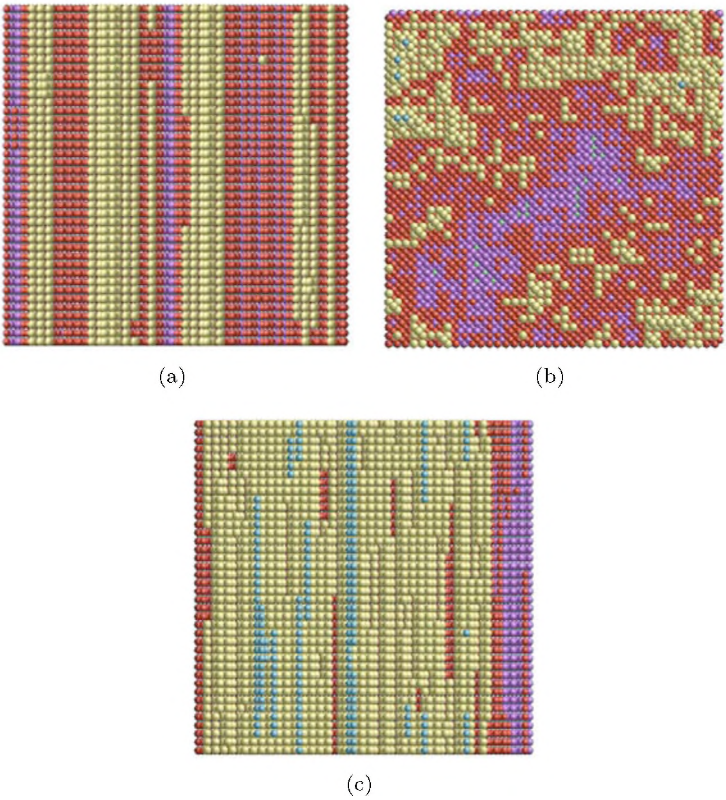
(a) (b)

(c)

Figure 1.7: Low temperature surface configurations of the symmetric S-type graph (010) orientation (Fig. 1.7(a)), the K-type graph (001) orientation (Fig. 1.7(b)) and the asymmetric S-type graph (001) orientation (Fig. 1.7(c)). All surface configurations are the result of a Monte Carlo growth simulation at low driving force, $\Delta\mu/kT$=0.1 and temperature 150K.

Chapter 2

On the determination of step energies. Theoretical considerations and application to an anisotropic Kossel model

2.1 Introduction

Models for crystal morphology prediction date back to the 19$^{\text{th}}$ century, in which Bravais and Friedel, followed by Donnay and Harker, developed the theory nowadays known as the BFDH theory.[3, 4] This theory states that, when taking into account certain symmetry arguments, the morphological importance of a crystallographic face (hkl) is proportional to the interplanar distance d_{hkl}. Although only the lattice parameters are considered, this theory works quite well for crystal structures with isotropic interactions.

In the 1950s the attachment energy theory was introduced by Hartman and Perdok, which was later refined by Bennema and Hartman.[5, 6, 7, 8] In this theory the crystal structure and bonds are taken into account. It relates the attachment energy of crystal slices of orientation (hkl) to the morphological importance of that orientation. Generally, if the attachment energy released upon growing a slice with thickness d_{hkl} is high, the growth rate in that direction will be high as well.

The Hartman-Perdok theory considers the energy of flat faces, but it is well known that in the actual crystal growth process, steps are more important than the flat terraces. Indeed, for several crystals with a needle morphology, it has been shown that the Hartman-Perdok approach fails and that the step structure is essential for understanding the morphology.[30, 31, 50] Therefore, in this chapter we no longer look at the attachment energy between faces, but at the energies of steps *on* these faces.

Steps on surfaces play a fundamental role in crystal growth. Apart from rough growth for surfaces that have the step free energy $\gamma_{st}(\mathbf{u}) + \gamma_{st}(-\mathbf{u}) \leq 0$ for one or more step front orientations $\mathbf{u}$[56], the three main growth mechanisms all involve steps. Firstly, on a misoriented surface, step flow determines the growth. Secondly, when growth is taking place on a perfectly flat surface, 2D-nucleation and layer-by-layer growth is observed. Lastly, when a screw dislocation is present in the surface, the resulting spiral growth pattern emerges from a continuous step source. For all these mechanisms, the free energy of the steps plays a central role in the description of crystal growth.[20, 57]

Most of the crystal growth mechanisms have been studied using one of the simplest crystal models, the Kossel model.[58] Other models have been applied successfully to the understanding of equilibrium surface phase diagrams, like the Body Centered Solid on Solid (BCSOS) model for crystals containing two growth units in the unit cell.[59, 60, 61]

Real crystals, however, usually have more complex structures, often with more than one growth unit in the unit cell and with different bonds, resulting in various step configurations. The Kossel model and derived theories have limited applicability to these crystal structures. The growth involves multiple growth unit incorporation barriers, different for each incorporation site configuration. Also, the order in which the different growth units incorporate affects the overall energetics profile, and multiple pathways to the same structure can have very different energetics associated with them. This is reflected in a large set of possible step structures. The first approach in dealing with this complexity would be to calculate the step energies of straight single steps, which would be the step free energy at zero Kelvin.

Although we are currently capable of simulating crystal growth for any crystal structure in any crystallographic orientation[9], these simulations give no fundamental insight into the processes taking place. The aim of the research presented in this and the next chapter is therefore to develop methodology to calculate single step energies for any crystal structure in any crystallographic orientation and to use the information obtained to come to a fundamental understanding of the crystal growth process in terms of step energies and 2D nucleation barriers. First, however, in this chapter, it will be shown that a direct and unique determination of *single* step energies is impossible in many cases. This is shown for a low-symmetry orientation in an anisotropic Kossel model. The inability to assign step energies in this model was already reported by Akutsu *et al.*, when studying an Ising antiferromagnet in an external field.[62] As a solution we propose a method which uses the geometry of a step on a given surface and given crystal structure. This method enables us to calculate the energy of a single step. For the determination of step energies for lattice models of any crystal structure, we have developed a computer program called STEPLIFT which will be introduced in the next chapter.

2.2 Determination of step energies

In this chapter, the determination of step energies is done within the framework of lattice models. These models use a number of implicit assumptions. First of all, the lattice nature of the model implies that the surface has a bulk termination, that is, relaxation and reconstruction are not taken into account. Secondly, when bonds are broken between particles in a lattice model, the broken bond energy is divided equally between the two particles. When a surface is created by cleaving a crystal, both interfaces will have the same interfacial energy. The convention used in this chapter is to denote ϕ as the energy of a broken bond *per particle*. This means that if one bond between two particles is broken, both particles gain ϕ in energy. A last assumption made in this chapter is that all step configurations are calculated at zero Kelvin, implying zero kink density. In other words, entropy is ignored. As the step free energy has both positive energetic contribution ϵ_{st}, and a negative entropic contribution s_{st}, a positive step free energy at non-zero temperatures depends on the existence of a positive ϵ_{st}. Therefore, we look at step energy alone as an approximation for the step free energy. This approximation is expected to be better for conditions for which the kink density is small, that is, at relatively low temperature and supersaturation.

2.2.1 Calculation of single step energies

As was already briefly mentioned, a surface will have a non-zero roughening transition temperature if the sum of the energies of two opposing steps is greater than zero:

$$\gamma_{st}(\mathbf{u}) + \gamma_{st}(-\mathbf{u}) > 0 \;\forall \mathbf{u},\; \mathbf{u} \cdot \mathbf{k} = 0 \tag{2.1}$$

with $\mathbf{k}$ the surface normal. However, to determine the optimal shape of a 2D island with minimal step energy, the step energy of opposite steps has to be calculated individually.

This can be seen in Figure 2.1. Here two situations are shown, in which the sum of the step energies ϵ_1 and ϵ_2 is equal in both cases. In Figure 2.1a $\epsilon_1 = \epsilon_2$, whereas in Figure 2.1b $\epsilon_1 < \epsilon_2$. The result is that the shape of the 2D island changes due to the difference in single step energies ϵ_1 and ϵ_2. Therefore a method for the determination of energies of single steps is needed.

For simple systems, like the Kossel crystal, single step energies can be calculated directly. This is illustrated in Figure 2.2 and is the 'traditional' method to determine step energies.[19] When the stepped and unstepped surfaces have broken bonds of the same strength at the same lateral position, the step energies can be calculated by subtracting the number of broken bonds of the unstepped surface from the number of broken bonds of the stepped surface. As the same type of bonds are broken on the unstepped surface and on the lower and upper terrace of the stepped surface, the only extra broken bond is located at the step

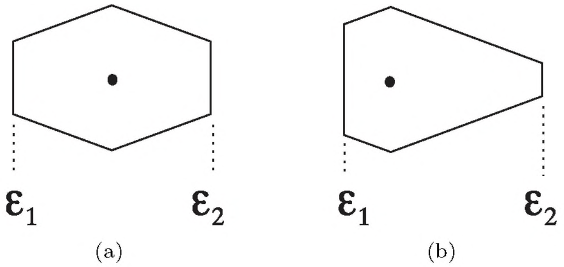

Figure 2.1: Two situations in which the sum of the step energies $\epsilon_1 + \epsilon_2$ is equal, but their individual contributions are different. Figure (a) shows the situation where $\epsilon_1 = \epsilon_2$ and in Figure (b) $\epsilon_1 < \epsilon_2$. The black dot indicates the origin of the Wulff shape.

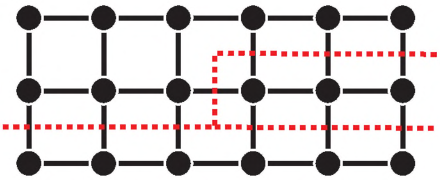

Figure 2.2: Direct determination of step energies in a Kossel crystal, viewed in a projection along the **a**-axis. The determination of the energy of this single step is done by subtracting the number of broken bonds of the flat contour from the number of broken bonds of the stepped contour, giving the step energy as $\epsilon_{st} = \phi$.

front, giving the step energy of one broken bond, ϕ, per unit cell. In the next section, an example will be given where the bonds broken on the stepped surface are not located at the same lateral position as the bonds broken on the unstepped surface, leading to the inability to calculate single step energies directly, i.e. by just counting broken bonds.

2.2.2 Low symmetry surface: $(0\bar{1}1)$ of an anisotropic Kossel Model

We will use an anisotropic Kossel model which is just complex enough to illustrate the problem of the determination of single step energies directly. The crystal graph of this anisotropic Kossel model is displayed in Figure 2.3. A crystal graph is a mathematical graph representation of the crystal structure: growth units are represented by graph vertices; pair-wise interactions between growth units by weighted undirected graph edges, as known from mathematical graph theory. There are three types of bonds in the model, a, b and c with associated bond strengths ϕ_a, ϕ_b and ϕ_c having $\phi_a = \frac{1}{2}(\phi_b + \phi_c)$. The anisotropy parameter δ is defined through $\phi_b = \delta\phi_c$ and is chosen in such a way that the $\delta = 1$ situation describes the classical Kossel model.

The steps with step front directions [011] and $[0\bar{1}\bar{1}]$ on the $(0\bar{1}1)$ surface will be discussed next to illustrate the inability of the direct determination of single step energies. Due to the symmetry of the system, this also holds for the [011] and $[0\bar{1}\bar{1}]$ steps on the $(01\bar{1})$ surface and the $[0\bar{1}1]$ and $[01\bar{1}]$ steps on the (011) and the $(0\bar{1}\bar{1})$ surfaces.

First note that the formation energy of an infinitely elongated island, involving two opposing steps ('up' and 'down'), can always be calculated directly, using the 'traditional' method of subtracting the broken bond energy of a flat surface from that of the surface with the two opposing steps. However, as was already pointed out before, to determine the optimal shape of a 2D island, single step energies are needed. The problem with determining these single step energies directly is illustrated in Figure 2.4. The figure displays an island viewed along the **a**-axis, infinitely elongated in that direction. The formation energy of the island (i.e. the sum of the 'up' and the 'down' step) per unit length of the **a**-axis is calculated by subtracting all broken bonds of a flat surface (in the top figure $6(\phi_b + \phi_c)$) from the broken bonds of the doubly stepped surface ($8\phi_b$+$6\phi_c$), giving an island formation energy of $2\phi_b$.

Next in Figure 2.4, the island is cut at either a horizontal ϕ_c bond (Figure 2.4b) or at a horizontal ϕ_b bond (Figure 2.4c). One of the newly formed islands is shifted one unit cell to the right and the total energy is calculated for the two islands formed. In Figure 2.4b, this results in two islands, one having a net energy of $2\phi_c$ and the other of $2\phi_b$. The increase in total net energy with respect to the original island (a) is $2\phi_c$. The same procedure can be followed for breaking extra ϕ_b bonds (Figure 2.4c), and in this case the extra energy is $2\phi_b$. In both situations two new steps are created, and the simplest choice is to distribute the extra energy equally between both steps. This choice results in the following step energies for the four steps in Figure 2.4d: $\epsilon_{st,d1} = \epsilon_{st,d4} = \phi_c$ and $\epsilon_{st,d2} = \epsilon_{st,d3} = \phi_b$. That this is not correct can be seen from the fact that the original island in Figure 2.4a is built up from two steps, (d1) and (d3), which would lead to a total island energy of $\phi_b + \phi_c$, a result that is in disagreement with the value $2\phi_b$ derived directly by counting the difference in broken bond energy.

The solution to this problem is shown in Figure 2.5. In this Figure a situation is shown in which first the step energies of two steps of double height are calculated directly (Figure 2.5a). The energy of these individual double height steps can be calculated by virtue of the fact that there is a perpendicular lattice vector between the upper terrace and the lower terrace, which means that all bonds that stick out from the upper terrace are also sticking out from the lower terrace at the same lateral position (i.e. the condition for calculating step energies directly). The step energy is then simply equal to the bonds that are broken at the side of the step, i.e. $\phi_b + \phi_c$. Next, in Figures 2.5b-e, the single steps are calculated by creating two steps of single height leading again to a situation in which a perpendicular lattice vector exists between the lower terrace and the uppermost terrace, which allows for the cancellation of broken

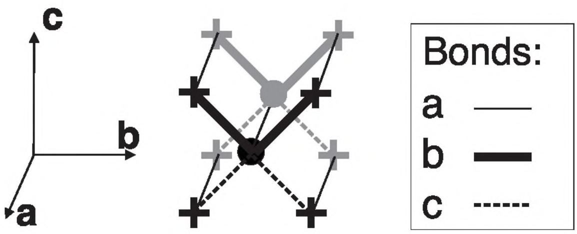

Figure 2.3: The anisotropic Kossel model crystal graph.

bonds at the lower and uppermost terrace. This is done for the two single ‘up’ steps (type d1 in Figure 2.5b and type d2 in 2.5c) and two single ‘down’ steps (type d3 in Figure 2.5d and type d4 in 2.5e). Since the two single steps are identical, the energy of a single step is simply half the total energy. This brings us to the correct solution of $\epsilon_{st,d1} = \epsilon_{st,d2} = \frac{1}{2}(\phi_b + \phi_c)$ for the ‘up’ steps and $\epsilon_{st,d3} = \frac{3}{2}\phi_b - \frac{1}{2}\phi_c$ and $\epsilon_{st,d4} = \frac{3}{2}\phi_c - \frac{1}{2}\phi_b$ for the two ‘down’ steps in Figure 2.4d.

2.3 Step geometry

In the previous section the ambiguity for determining step energies directly was illustrated using an example of the [011] and $[0\bar{1}\bar{1}]$ steps on the $(0\bar{1}1)$ orientation of an anisotropic Kossel model. A solution was found by looking at steps of double height, so that the upper and lower terraces are the same, i.e. there is a perpendicular lattice vector between the upper and lower terrace. In the general case, it may take several individual steps before the upper and lower terrace are the same, but once this is achieved, the energy of an individual step can be determined.

In this section, a general method will be introduced to determine step energies of single height steps, by taking the step terrace geometry into account. First the conditions for determining single step energies directly are treated.

2.3.1 Conditions for determining single step energies directly

Single step energies on a (hkl) surface with a step height equal to the interplanar distance d_{hkl} can be calculated directly when there is a direct lattice vector $\mathbf{n}$ of length d_{hkl}, perpendicular to the surface (hkl).

The indices (hkl) refer to the reciprocal lattice vector $\mathbf{k}_{hkl}$, normal to the (hkl) surface, which is defined as

$$\mathbf{k}_{hkl} = h\mathbf{a}^* + k\mathbf{b}^* + l\mathbf{c}* , \tag{2.2}$$

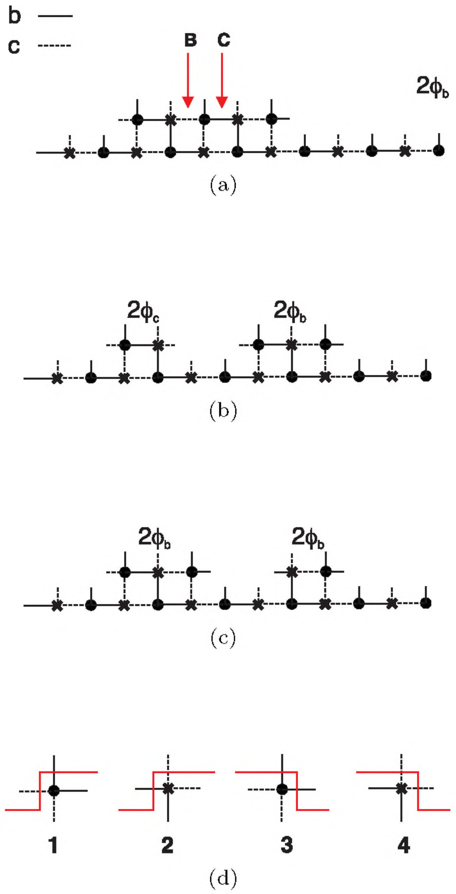

Figure 2.4: Ambiguity in the assignment of step energies to the $[011]$ and $[0\bar{1}\bar{1}]$ steps on the $(0\bar{1}1)$ orientation of the anisotropic Kossel model. Two extra steps are created by cutting an existing island (a) either at location ‘B’ or ‘C’. The new islands, displayed in (b) and (c) respectively, give an extra energy of $2\phi_c$ and $2\phi_b$. When this extra energy is divided evenly over the steps created, the four steps displayed in (d1) to (d4) get either ϕ_c or ϕ_b. However, this distribution of step energy is not correct! This can be seen in the island (a), which has two steps, (d1) and (d3). When the island energy of (a) is calculated as the sum of these two step energies, the island energy would become $\phi_b + \phi_c$, and it clearly is $2\phi_b$. Therefore the equal distribution of the broken bond energy over the steps created is not correct.

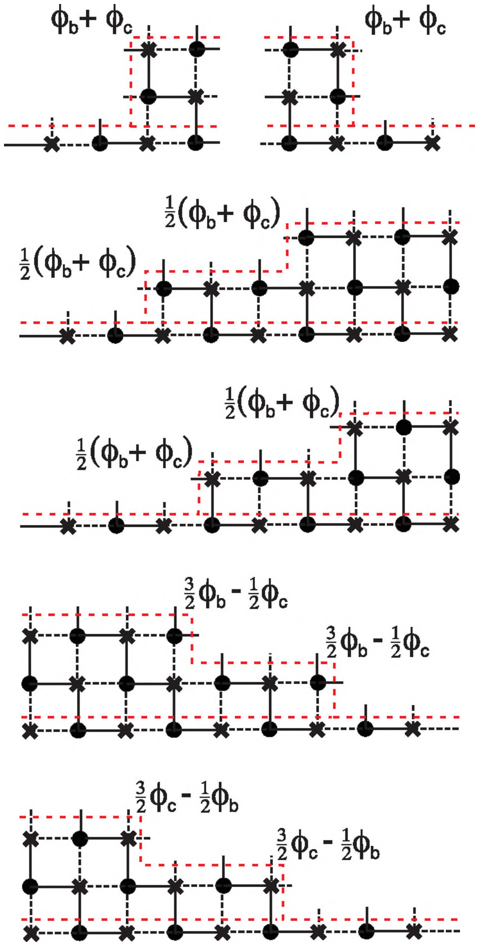

Figure 2.5: The step energy of steps of double height can be calculated directly due to the presence of a perpendicular lattice vector between the top and bottom terrace. The step energy of all steps of double height is equal to $\phi_b + \phi_c$ for both double-height steps. Next, in the lower four figures, two steps of single height are created to get the same bonds at the same lateral position on the lower terrace and the uppermost terrace. The energy of each single step can be determined to be $\frac{1}{2}(\phi_b + \phi_c)$ for the first two single steps, and $\frac{3}{2}\phi_b - \frac{1}{2}\phi_c$ and $\frac{3}{2}\phi_c - \frac{1}{2}\phi_b$ for the third and fourth single step, respectively.

with $\mathbf{a}^*$, $\mathbf{b}^*$ and $\mathbf{c}^*$ the reciprocal lattice vectors. The length of the vector $\mathbf{k}_{hkl}$ then is $1/d_{hkl}$, where d_{hkl} is the interplanar distance of the (hkl) surface. The set Λ of direct lattice vectors $\mathbf{m}$ is given by:

$$\mathbf{m} = u\mathbf{a} + v\mathbf{b} + w\mathbf{c} \qquad u, v, w \in \mathbb{Z}. \tag{2.3}$$

with $\mathbf{a}$, $\mathbf{b}$ and $\mathbf{c}$ the direct lattice vectors. Therefore, step energies can be calculated directly if there is a $\mathbf{n} \in \Lambda$ satisfying:

$$\Lambda \ni \mathbf{n} = d_{hkl}^2 \mathbf{k}_{hkl} \tag{2.4}$$

Conversely, when there is no perpendicular lattice vector of length d_{hkl}, single step energies can not be calculated directly, unless two opposing steps are identical due to symmetry.

2.3.2 Determining step energies through symmetry

Step energies can also be calculated directly when there exists a mirror plane or a two-fold axis perpendicular to the surface. In these cases, two opposite steps can be created that have a similar configuration by virtue of the symmetry in the system, and hence, both steps will contribute equally to the island energy. A mirror plane can be present in systems without a translational vector perpendicular to the surface, for instance in the spacegroup Cm at the (200) surface. An example of that situation is displayed in Figure 2.6, which has two steps whose energy can be determined to be $\frac{3}{2}\phi$ and $\frac{1}{2}\phi$. In spacegroups of higher symmetry, both perpendicular translational symmetry and a mirror plane or two-fold axis can be present at the same time. While the use of symmetry can thus allow for a direct derivation of the energy of an individual step for such special cases, the same result is obtained by using the general approach described next.

2.3.3 A general approach

The general approach to calculate single step energies uses the given crystal's geometry in addition to the bonding topology. Without losing generality, this approach uses a unit cell with the $\mathbf{a}$- and $\mathbf{b}$-axes defining the surface plane of interest, i.e. (001). Any surface (hkl) can be transformed into (001) by a proper choice of axis transformations. The resulting unit cell is called a slice cell, and its axes will be labeled $\mathbf{a}_s$, $\mathbf{b}_s$ and $\mathbf{c}_s$.[9] The slice cell transformation is chosen in such a way that the $\mathbf{a}_s$ vector lies parallel to the step front. As $\mathbf{a}_s$ and $\mathbf{b}_s$ lie in the plane of interest, $\mathbf{c}_s$ has the only perpendicular component with respect to the surface.

As was already shown in Figure 2.5, for a single step a perpendicular lattice vector of length d_{hkl} allows for a direct calculation of its step energy. If there is no such perpendicular lattice vector for a step of single height, we can proceed by constructing a perpendicular lattice vector for a multiple height step, satisfying:

$$(w\mathbf{c}_s)_\perp = w d_{hkl}^2 \mathbf{k}_{hkl} \approx \mathbf{n} \in \Lambda \tag{2.5}$$

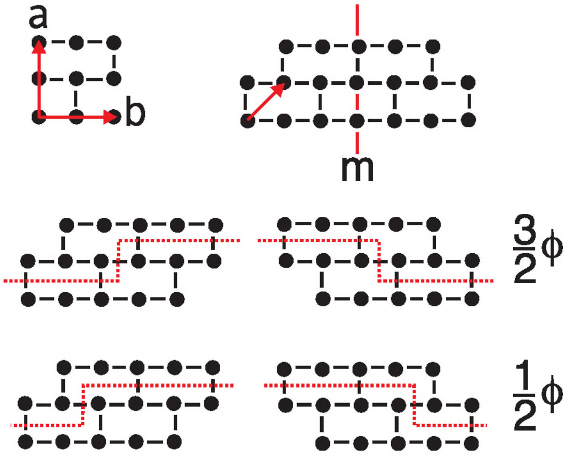

Figure 2.6: The top left figure displays a unit cell of a structure with the spacegroup Cm. This is a case where there is no perpendicular translational symmetry between (200) surfaces (a (200) translational symmetry vector, $\frac{1}{2}(\mathbf{a}+\mathbf{b})$, is indicated by the vector in the top right figure). There is a mirror plane perpendicular to $\mathbf{b}$ and parallel to $\mathbf{c}$, and due to this mirror symmetry the steps (left and right) in the middle and bottom figure are equivalent, and their energy can be calculated to be $\frac{3}{2}\phi$ (middle) and $\frac{1}{2}\phi$ (bottom)

for some integer number w. Clearly, for some crystals, $(w\mathbf{c})_\perp$ may not be exactly equal to a lattice vector for any w, but it can be chosen arbitrarily close to a lattice vector $\mathbf{n}$. Now, for a step of height w, all bonds that were broken at the lower terrace are also broken at the same lateral position on the upper terrace w layers higher, which means that their energies cancel exactly, allowing for the calculation of the total step formation energy.

To create a construction with w similar single steps as shown in Figure 2.7, the $\mathbf{b}_s$-axis is used v times. Any convenient value for v is allowed. The total translation is then given by the lattice vector $(v\mathbf{b}_s + w\mathbf{c}_s)$. The length of the vector product of parallel component of this lattice vector with the vector a_s defines the total projected area under the full step structure A_{total} (see also Figure 2.7):

$$\begin{aligned}
A_{\text{total}} &= |\mathbf{a}_s \times (v\mathbf{b}_s + w\mathbf{c}_s)_{\|}| \\
&= |\mathbf{a}_s \times (v\mathbf{b}_s + w[\mathbf{c}_s - \mathbf{c}_{s,\perp}])| \\
&= \left|\mathbf{a}_s \times \left(v\mathbf{b}_s + w[\mathbf{c}_s - \frac{\mathbf{c}_s \cdot (\mathbf{a}_s \times \mathbf{b}_s)}{|\mathbf{a}_s \times \mathbf{b}_s|^2}(\mathbf{a}_s \times \mathbf{b}_s)]\right)\right| \\
&= w\left|\mathbf{a}_s \times \left(\frac{v}{w}\mathbf{b}_s + \mathbf{c}_s - \frac{\mathbf{c}_s \cdot (\mathbf{a}_s \times \mathbf{b}_s)}{|\mathbf{a}_s \times \mathbf{b}_s|^2}(\mathbf{a}_s \times \mathbf{b}_s)\right)\right|
\end{aligned} \tag{2.6}$$

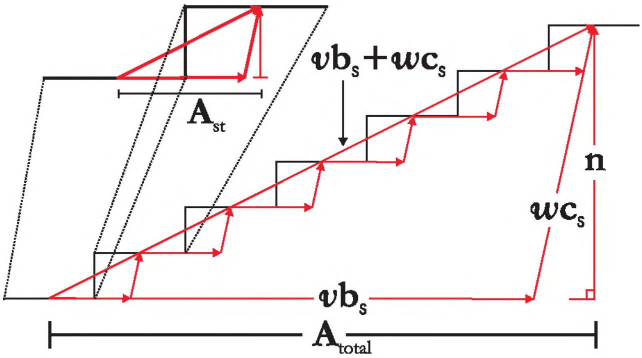

Figure 2.7: The construction of w steps (for $w = 6$) to let the perpendicular component of $w\mathbf{c}_s$ coincide with a lattice vector $\mathbf{n} \in \Lambda$ perpendicular to the surface. This choice, together with $\mathbf{a}_s$, defines the total area under the full step structure, A_{total}. In the left upper part a single step structures is enlarged to show the area under a single step structure A_{st}.

Now, to calculate the formation energy of w identical steps in this construction, we use the following equation:

$$wE_{\text{step}} = E_w - A_{\text{total}}\mathcal{E}_{\text{surf}} \tag{2.7}$$

where E_w is the total broken bond energy of the surface with the w steps. This energy is well-defined because the upper and lower terrace are identical. The specific surface energy $\mathcal{E}_{\text{surf}}$ is given by

$$\mathcal{E}_{\text{surf}} = \frac{E_s}{|\mathbf{a}_s \times \mathbf{b}_s|} \tag{2.8}$$

where E_s is the surface energy per slice cell for a step-free surface.

The structure shown in Figure 2.7 can also be understood in terms of a vicinal surface along the translational vector $(v\mathbf{b}_s + w\mathbf{c}_s)$, so that the E_w term in Eq. 2.7 is equal to the vicinal surface energy. The vicinal surface energy must, however, be taken with respect to the underlying flat surface area, A_{total}, not the area of the vicinal surface, which would be equal to $|\mathbf{a}_s \times (v\mathbf{b}_s + w\mathbf{c}_s)|$.

Since the total step energy given in Eq. 2.7 consists of w indentical individual steps, the energy of a single step is given by

$$E_{\text{step}} = \frac{E_w}{w} - \frac{A_{\text{total}}}{w}\mathcal{E}_{\text{surf}} \tag{2.9}$$

Per step, the projected area A_{st}, is equal to

$$A_{\text{st}} = \frac{A_{\text{total}}}{w} = \left|\mathbf{a}_s \times \left(\frac{v}{w}\mathbf{b}_s + \mathbf{c}_s - \frac{\mathbf{c}_s \cdot (\mathbf{a}_s \times \mathbf{b}_s)}{|\mathbf{a}_s \times \mathbf{b}_s|^2}(\mathbf{a}_s \times \mathbf{b}_s)\right)\right| \tag{2.10}$$

As E_w is built up from w contributions, E_w is written as

$$E_w = wE_1 \tag{2.11}$$

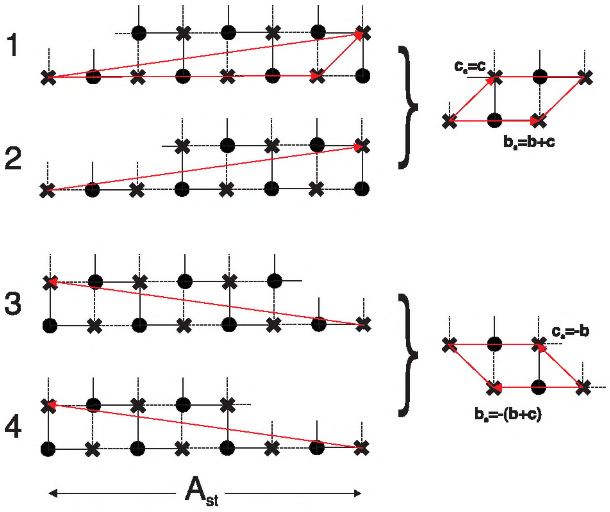

Figure 2.8: The four single steps in the [011] and $[0\bar{1}\bar{1}]$ directions on the $(0\bar{1}1)$ surface. The numbers correspond to the ones in Figure 2.4d. The slice cell used is displayed on the right and the arrows on the left define the vector $(\frac{v}{w}\mathbf{b}_s + \mathbf{c}_s)$ which, projected on the lower terrace, gives A_{st}. A_{st} is in all cases equal to $\frac{7}{2}|\mathbf{a} \times (\mathbf{b} + \mathbf{c})|$. The vectors $\mathbf{c}_s$ and $\mathbf{b}_s$ of the slice cells on the right are expressed in terms of the axes of the original unit cell in Figure 2.3.

and using these expressions, the single step formation energy becomes

$$E_{\text{step}} = E_1 - A_{\text{st}}\mathcal{E}_{\text{surf}} \tag{2.12}$$

Thus we find that the energy of a single step can be determined by first calculating the total energy of a surface with a single step and by subtracting from this the energy of the corresponding flat surface. The latter is the surface with the same projected area and with the specific surface energy $\mathcal{E}_{\text{surf}}$.

2.3.4 Application to the anisotropic Kossel model

The four steps discussed earlier are displayed in Figure 2.8. For the two steps labeled '1' and '2' the slice cell basis vectors as defined in section 2.3.3 are given by $\mathbf{a}_s = \mathbf{a}$; $\mathbf{b}_s = \mathbf{b} + \mathbf{c}$ and $\mathbf{c}_s = \mathbf{c}$. For the other two steps, '3' and '4', they are $\mathbf{a}_s = \mathbf{a}$; $\mathbf{b}_s = -(\mathbf{b} + \mathbf{c})$ and $\mathbf{c}_s = -\mathbf{b}$. In all figures displaying steps for this model, the step front lies along the $\mathbf{a}_s$ axis.

The arrows in Figure 2.8 (left) indicate the lattice vector $(\frac{v}{w}\mathbf{b}_s + \mathbf{c}_s)$, which is used for the definition of new periodic boundary conditions corresponding to a vicinal orientation, which includes the step of interest. The lattice vector $(\frac{v}{w}\mathbf{b}_s + \mathbf{c}_s)$ is in all four cases $3\mathbf{b}_s + \mathbf{c}_s$, with $v = 6$ and $w = 2$ (see Eq. 2.5). This results in A_{st} being equal to $\frac{7}{2}|\mathbf{a}_s \times \mathbf{b}_s|$, which expressed in the original lattice vectors equals $\frac{7}{2}|\mathbf{a} \times (\mathbf{b} + \mathbf{c})|$ for all the steps.

Table 2.1: Step energies and individual contributions according to Eqn. 2.12, calculated for the step configurations in Figure 2.8.

$[uvw]$	E_w	A_{st}	$\mathcal{E}_{\text{surf}}$	E_{step}
1 $[0\bar{1}\bar{1}]$	$4(\phi_b+\phi_c)$	$\frac{7}{2}\lvert\mathbf{a}\times(\mathbf{b}+\mathbf{c})\rvert$	$\frac{(\phi_b+\phi_c)}{\lvert\mathbf{a}\times(\mathbf{b}+\mathbf{c})\rvert}$	$\frac{1}{2}(\phi_b+\phi_c)$
2 $[0\bar{1}\bar{1}]$	$4(\phi_b+\phi_c)$	$\frac{7}{2}\lvert\mathbf{a}\times(\mathbf{b}+\mathbf{c})\rvert$	$\frac{(\phi_b+\phi_c)}{\lvert\mathbf{a}\times(\mathbf{b}+\mathbf{c})\rvert}$	$\frac{1}{2}(\phi_b+\phi_c)$
3 $[011]$	$5\phi_b+3\phi_c$	$\frac{7}{2}\lvert\mathbf{a}\times(\mathbf{b}+\mathbf{c})\rvert$	$\frac{(\phi_b+\phi_c)}{\lvert\mathbf{a}\times(\mathbf{b}+\mathbf{c})\rvert}$	$\frac{3}{2}\phi_b-\frac{1}{2}\phi_c$
4 $[011]$	$3\phi_b+5\phi_c$	$\frac{7}{2}\lvert\mathbf{a}\times(\mathbf{b}+\mathbf{c})\rvert$	$\frac{(\phi_b+\phi_c)}{\lvert\mathbf{a}\times(\mathbf{b}+\mathbf{c})\rvert}$	$\frac{3}{2}\phi_c-\frac{1}{2}\phi_b$

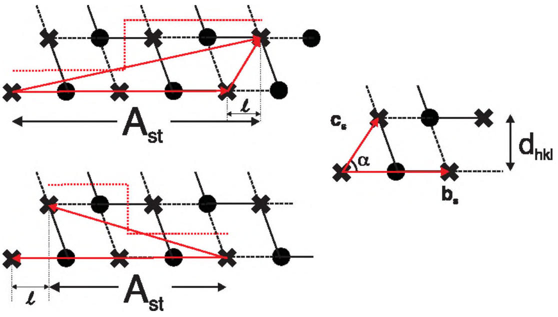

Figure 2.9: Dependence of step energy on the angle α.

The surface energy of the surface with the single step has to be calculated along the vicinal orientation, using periodic boundary conditions for the vicinal surface. The resulting energies are listed in Table 2.1. Using Eq. 2.12, the two $[0\bar{1}\bar{1}]$ steps both have a step energy of $\frac{1}{2}(\phi_b+\phi_c)$ and the two $[011]$ steps have step energies of $\frac{3}{2}\phi_b-\frac{1}{2}\phi_c$ and $\frac{3}{2}\phi_c-\frac{1}{2}\phi_b$ respectively. This is, as expected, consistent with the results found for the earlier approach using steps of double height (see Figure 2.5). For the island formation energy, combining an up and a down step, we find either $2\phi_b$ or $2\phi_c$, depending on the choice of the $[011]$ step position, which is also consistent with the direct calculations on islands shown in Figure 2.4. When the anisotropy factor δ equals 1, so that $\phi_b=\phi_c=\phi$, giving the classical isotropic Kossel model, the step energy becomes $E_{\text{step}}=\phi$ for all steps in Table 2.1. Hence, this method for determining single step energies is also in accordance with the underlying Kossel model for $\delta=1$.

2.3.5 Application to a variable-angle anisotropic Kossel model

It is well known that crystallographic angles may vary, depending on for instance temperature or pressure. To investigate the effect of a varying angle on the step energy, we now apply the method introduced previously to the model shown in

Figure 2.9. In this case we allow the slice cell angle α to be variable. It will be shown that the energy of single steps becomes angle-dependent, but that in any combination of two opposing steps the dependence on the angle vanishes.

Again, the specific surface energy $\mathcal{E}_{\text{surf}}$ is given by

$$\mathcal{E}_{\text{surf}} = \frac{(\phi_b + \phi_c)}{|\mathbf{a_s} \times \mathbf{b_s}|}$$

The angle α can be expressed as

$$\tan\alpha = \frac{d_{hkl}}{l}$$

where l is the length of the $\mathbf{c}_s$-axis projected on the $\mathbf{b_s}$-axis. This means that for the steps, shown in Figure 2.9, the projected areas are given by: $A_{\text{st}} = (2 + \frac{l}{|\mathbf{b_s}|})|\mathbf{a}_s \times \mathbf{b}_s|$ for the step up and $A_{\text{st}} = (2 - \frac{l}{|\mathbf{b_s}|})|\mathbf{a}_s \times \mathbf{b}_s|$ for the step down.

The step energies of the steps become:

$$E_{\text{step, up}} = 3(\phi_b + \phi_c) - (\phi_b + \phi_c)\left(2 + \frac{d_{hkl}}{|\mathbf{b}_s|\tan\alpha}\right)$$

$$E_{\text{step, down}} = 3\phi_b + \phi_c - (\phi_b + \phi_c)\left(2 - \frac{d_{hkl}}{|\mathbf{b}_s|\tan\alpha}\right)$$

Combining the up and down step gives an energy of $2\phi_b$, without a dependence on the angle.

2.4 Discussion

We have shown that the energy of a single step can be calculated directly and unambiguously only when a certain symmetry is present. This symmetry can be either a perpendicular lattice vector, mirror plane or twofold axis. In fact, such symmetry, present in many simple models, has facilitated the calculation of single step energies in the past. Thus, in these cases, the geometry of the system was implicitly used in the calculation of step energies.

The method presented here is based on a perpendicular lattice vector, the presence of which makes the upper and lower terraces identical. This also means that our method is not applicable to steps that have different upper and lower terraces. Although crystals are usually terminated by similar surfaces below the roughening temperature, examples are known that do not have the same surface for the upper and lower terrace, for instance crystals with an A-B layered structure.[63] Also crystals with interlaced step patterns [64] will need special attention.

In the framework of statistical physics, step energies are calculated based on bonding topology alone.[62] When a crystal lattice parameter is altered, for instance a change in the angle α, as shown in Section 2.3.5, translational symmetry will be altered, and as a result the step energies change in our approach. This raises the question, whether the step energy should be allowed to change when the crystal lattice is altered without any change in bonding topology. On the basis of the topology alone, this question should be answered negatively. However, when the crystal lattice is altered, the bond strengths may change as they are all a function of distance between interacting growth units. Thus, bonding topology and geometry are not independent in practice, and upon modification of the crystal lattice the step energy will therefore change both because of a change in geometry as well as a change in all the bond strengths.

The formation of kinks on steps is analogous to the formation of steps on surfaces, but one dimension lower: a straight step is analogous to a flat surface, a kink is analogous to a step on a surface. Our method can in principle be used to calculate kink energies. The roughening behaviour of steps is different, however: steps are always rough, as opposed to surfaces. The prerequisite that kinks should have the same lower and upper step front can therefore not always be fulfilled and, although kink energies can be calculated using the method, this can become very complicated in the general case.

One of the applications of the step energies, when calculated using our method, is to find the 2D-island with minimal step energy. As the single step energies can always be determined using the geometric method, the shape of the island only depends on the magnitude of the step energies and the step front orientations. The total island energy can be used as a measure for the nucleation barrier on a surface. When nucleation is the rate limiting step for crystal growth, this result for the nucleation barrier can be used as a parameter to estimate the growth rate.

2.5 Conclusion

It has been shown that the step energy of steps lacking a perpendicular lattice vector of length d_{hkl} or any alternative appropriate symmetry can not be determined directly. Using the geometry of the crystal in addition to the bonding topology, this problem was solved. For the anisotropic Kossel model it was shown that this method is both consistent with the energy of an island, i.e. two opposing steps, and with the limiting case of the Kossel model.

A result of our approach is that the step energies change when the geometry is distorted. From a statistical mechanical point of view, this is a remarkable result. We argue, however, that in reality bonding topology and geometry for crystals are closely connected. The geometry is determined by the bonding properties and, conversely, the bond strength will depend on the geometry.

The method put forward in this chapter will be applied to a number of crystal structures studied experimentally the next chapter, in which an automated method for the determination of step energies is presented and applied to predict crystal morphology.

Chapter 3

The step energy as a habit controlling factor. Application to the morphology prediction of aspartame, venlafaxine and a yellow isoxazolone dye.

3.1 Introduction

Morphology prediction started to mature in the 19th century with the theory developed by Bravais and Friedel, which was later expanded by Donnay and Harker, to what we now know as the BFDH theory.[3, 4] This theory takes a crystal structure and its symmetry and computes the morphology based on the interplanar distance d_{hkl}, taking into account selection rules which are the same as the systematic reflection conditions in X-ray diffraction theory. The BFDH theory works well for relatively simple, isotropic crystalline materials, such as metals.

In the 1950s, the attachment energy model was developed by Hartman and Perdok using periodic bond chains (PBCs) and connected nets. Attachment energies were related to growth rates by Hartman and Bennema.[5, 7, 6, 8] The attachment energy method predicts the growth morphology according to $R_{hkl} \propto E_{hkl}^{\mathrm{att}}$, where the attachment energy E_{hkl}^{att} is defined as the bond energy per growth unit gained when a new growth layer is attached to a growing crystal in the direction of a crystal face orientation (hkl). A kinetic Wulff construction, which relates the growth rate R_{hkl} to the morphological importance of an orientation (hkl), then gives the morphology.

In models for crystal growth, however, the step free energy γ_{st} plays a key role during birth and spread growth, as well as for spiral growth. In the former mechanism, the 2D nucleation rate and the kinetics of layer growth by incorporation of growth units into the island step edge determine the growth rate. In the case of spiral growth, a screw dislocation provides an inexhaustible step source. Then the kinetics of the growth unit incorporation, as well as interactions between growth spirals determine the growth rate. All these processes depend on the configuration of the step edges, and the corresponding step free energies. As the step free energy becomes lower, the creation of steps on a surface becomes easier and, for all growth mechanisms considered before, the result is that the face will grow faster.[20] In recent years, numerous examples of crystals with orientations that have unexpectedly low step energies have been found.[30, 48] The corresponding growth rates are considerably higher than expected on the basis of the attachment energy.

The goal of the research reported on in thischapteris to unite the obvious importance of steps in crystal growth with morphology modelling, in order to come to a morphology prediction tool that leads to a qualitatively better result than the attachment energy method and still is fast enough for practical use, when used for complex crystal structures. To this end an automated procedure called STEPLIFT was developed for finding the 'molecular' configurations that make up a step. The step energies ϵ_{st} found can then be related to growth rates of the corresponding faces calculated using existing growth rate equations. Given the complexity of crystal structures and the often large number of ways steps can be made on a crystal surface, the procedure will be limited to infinitely long and straight steps without kinks, so-called f-steps. These steps represent minima in the 2D polar plot of the step energy. Any kinks that may form on the steps are not taken into account, as they would only increase the step energy, ϵ_{st}. Although we realize that the step *free* energy, γ_{st}, may be lowered by the introduction of kinks at non-zero temperatures as a result of the entropic contribution, we expect the step energy ϵ_{st} to be the most important, especially at not too high driving forces for crystallization and not too high temperatures.

In earlier work, an automated routine called FACELIFT[65] was developed for finding all faces having connected nets[19] for any crystal structure from its crystal graph. The crystal graph is the representation of the crystal structure used in our recently developed morphology prediction tools FACELIFT, MONTY and now STEPLIFT. An overview of these methods is given in Figure 3.1. Referring to this Figure, the FACELIFT routine can find all PBCs for a given crystal graph, and combine them to find connected nets. The programs MONTY and STEPLIFT both produce growth rates for crystal faces (hkl), which, when used in a kinetic Wulff construction, give the predicted morphology, in which the orientations with the lowest growth rates will have the highest morphological importance. The program MONTY determines growth rates by performing Monty Carlo simulations for any crystal orientation.[9] This method, though allowing for entropic contributions, is rather time-consuming.

In the presentchapterall possible combinations of two F-faces having a common periodic bond chain (PBC) are used to create steps. From the step energies in all PBC-directions, the Wulff shape of the 2D nucleus is constructed and the

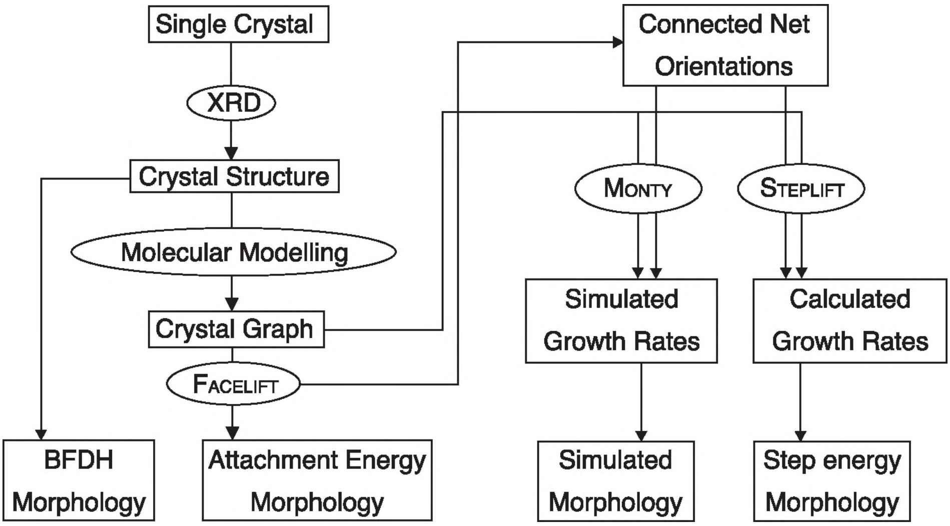

Figure 3.1: Sequence of morphology modelling using various techniques. Once a crystal structure is known from e.g. X-ray diffraction, a crystal graph can be calculated using molecular modelling techniques. This graph is the basis for the FACELIFT routine, the MONTY simulation program and also for STEPLIFT. Four different morphologies can be predicted: the simplest being the BFDH morphology, based on the crystal lattice alone. The attachment energy morphology can be calculated using the FACELIFT routine, whereas both MONTY and STEPLIFT produce more reliable growth rates. Using a kinetic Wulff construction growth rates give the simulated and step energy morphologies respectively.

total energy defined by the Wulff shape is used to give an estimate of the growth rate of the particular face. For that the analysis is presently limited to a 2D nucleation growth mechanism as for this mechanism growth rate equations are well elaborated, including multiple nuclei and anisotropy in step energies. For a spiral growth mechanism, on the other hand, essential parameters like the dislocation density are difficult to predict at present. By combining the results of the 2D-nucleation mechanism for all faces of the crystal, the corresponding morphology is found. During 2D nucleation, the 2D nucleus is in (unstable) equilibrium with the supersaturated parent phase, as the attachment and detachment frequencies are equal. This means that the shape of the 2D nucleus will correspond to the equilibrium shape, i.e. the Wulff shape.

The method of calculating the 2D nucleus for all face orientations, and subsequently using the energy of formation of this nucleus for the prediction of the growth rates is applied to aspartame, Venlafaxine and two polymorphs of a yellow isoxazolone dye. As the growth mechanism of all these examples is a 2D-growth mechanism, as has been established in earlier reports, these are considered to be good candidates for testing the limits and potentials of the method in its present form.

3.2 Finding step configurations

3.2.1 Connected nets, steps and roughening

The calculation of step energies in thischapteris done using lattice models, with the crystal graph representation of the crystal structure. Consequently, the surface termination has the structure of the bulk crystal, i.e. there is no surface relaxation or reconstruction. Also, when breaking a bond between growth units, the broken bond energy will be distributed equally between the two growth units.

All orientations having a connected net can be determined by the FACELIFT routine. Briefly, using this routine all periodic bond chains (PBCs) in a crystal graph can be found. These PBCs are subsequently combined to create connected nets. A valid connected net can be formed when two non-parallel PBCs with periodicities described by the vectors $\mathbf{u}_1$ and $\mathbf{u}_2$ (defined on the direct lattice, as $\mathbf{u}_i = u_i\mathbf{a} + v_i\mathbf{b} + w_i\mathbf{c}$) can be combined to a reciprocal lattice vector $\mathbf{k}$ that determines the interplanar distance d_{hkl} as $d_{hkl} = |\mathbf{k}|^{-1}$; $\mathbf{k}$ is given by the vector product: $\mathbf{k} = \mathbf{u}_1 \times \mathbf{u}_2$. Crystallographic orientations that have one or more connected nets can be F-faces, but that depends on the roughening temperature of the connected net orientation. The roughening behaviour of a connected net orientation is governed by the formation of steps on the surface (hkl) which has the connected net configuration.[19]

Orientations with a connected net are flat faces, when any step orientation $\mathbf{u}$ fulfills the condition given by van Beijeren et al.[56]:

$$\gamma_{st}(\mathbf{u}) + \gamma_{st}(-\mathbf{u}) > 0 \quad \forall \mathbf{u}, \mathbf{u} \cdot \mathbf{k} = 0, \tag{3.1}$$

where $(\mathbf{u})$ is a vector both perpendicular to the step front and perpendicular to the surface normal. Note that for a 2D island this means that it can have steps in certain directions $\mathbf{u}$ with zero or negative step energy, as long as this is 'compensated' by steps in the opposite direction. An example of this is sketched in Figure 3.2, where a number of possible combinations of steps in mutually orthogonal directions is sketched. If two opposite orientations both have a negative step energy, the criterion of van Beijeren et al. will not be met (Eq. 3.1). This means that this orientation will grow rough, due to the absence of a 2D nucleation barrier. All the situations in Figure 3.2 are covered by the criterion of van Beijeren et al.

There are situations, however, that are not accounted for by the van Beijeren condition. Figure 3.3 shows two shapes of the step free energy as a function of orientation on a triangular lattice, where both shapes would lead to a flat face according to Eq. 3.1, as all sums of the step free energies in the $\pm\mathbf{u}_i$ (i=1..3) directions are positive. While in Figure 3.3(a) this indeed leads to a flat face, we argue, however, that for the shape drawn in Fig. 3.3(b) the three negative step energies in the directions $-\mathbf{u}_i$ will cause the system to show rough growth. Therefore we introduce a generalisation of Eq. 3.1:

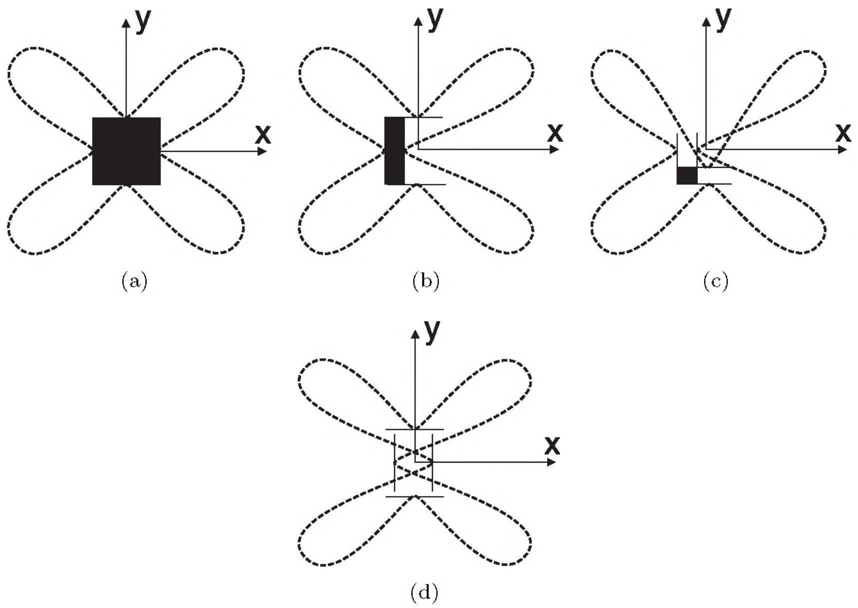

Figure 3.2: Four illustrations of different $\gamma_{st}(\mathbf{u})$ (the dotted lines). The morphology of a 2D island (black rectangles) is determined by the shape of the $\gamma_{st}(\mathbf{u})$ curves. The curve in Fig. 3.2(a) has positive step energies in the $\pm x$ and $\pm y$ directions, leading to a square 2D island morphology. Fig. 3.2(b) has a negative step energy in the $+x$ direction, giving the rectangular morphology. Fig. 3.2(c) has negative step energies in both the $+x$ and $+y$ directions giving the smaller square morphology. The last example, Fig. 3.2(d) has negative step energies in $\pm x$ directions, which leads to a non-defined 2D island shape. This leads to a zero nucleation barrier, and the corresponding orientation will grow rough.

$$\oint \mathrm{d}\mathbf{u}\gamma_{st}(\mathbf{u}) > 0 \;\; \forall \mathbf{u}, \mathbf{u}\cdot\mathbf{k} = 0 \text{ for any island .} \tag{3.2}$$

This condition indicates that a face will be flat when the sum of all step energies of any island is larger than zero. Criterion 3.2 indicates a roughened surface for Figure 3.3b as the sum of all the inner step energies, i.e. $\sum_i \gamma_{st}(-\mathbf{u}_i)$, is negative.

In order to use Eq. 3.2 the energy of a *single* step has to be determined. This led to the development of a method for determining these single step energies, which was introduced in an earlier paper.[54] In that paper it was shown that when there is no perpendicular lattice vector between the upper and lower terrace of a step, the calculation of the step energy based on bonding topology alone is generally not possible. By combining the step geometry and bonding topology, this problem was solved, allowing for the facile calculation of step energies for any crystal structure, and for any crystallographic orientation.

Recently, differences in opposing step energies were experimentally observed, measured and explained on a (1×2) reconstructed Au(110) surface.[66] The influence of step energy anisotropy on 2D island dynamics was highlighted in a recent review by Kodambaka et. al.[67]

3.2.2 Connected nets as terrace and step front configurations

The $\gamma(\mathbf{u})$ function of a 2D nucleus on the surface of a crystal will have minima at f-steps, which are the steps of lowest energy.[68] The automated STEPLIFT procedure for finding f-steps (see also Figure 3.4) takes two 'copies' of one connected net separated by d_{hkl}, and designates them to be the lower and upper terrace. The distance between the two is bridged by a second connected net that has a PBC in common with the first net. The step front will then be oriented along this PBC and have the configuration of the second connected net (see Figure 3.5). A combination of two non-parallel connected nets therefore gives two steps with opposite step front orientation, thus limiting the number of possible steps on a surface to 2 times the number of other F-faces at maximum. The step front orientations $\mathbf{u}$ and $-\mathbf{u}$ are given by Eq. 3.3 where $\mathbf{k}_1$ is the normal of the terrace connected net that defines the crystal surface and $\mathbf{k}_2$ the normal of the bridging connected net.

$$\begin{aligned} \mathbf{u}\cdot[\mathbf{k}_1 \times \mathbf{k}_2] = 0 \;\; \wedge \\ \mathbf{u}\cdot\mathbf{k}_1 = 0 \end{aligned} \tag{3.3}$$

This implies that the step front orientation $\mathbf{u}$ is both perpendicular to the step front and perpendicular to the surface normal. The present approach in terms of connected nets implies that the steps are straight without any entropic contributions and can therefore be considered as step attachment energies of growth units, expressed as energy per unit of length.

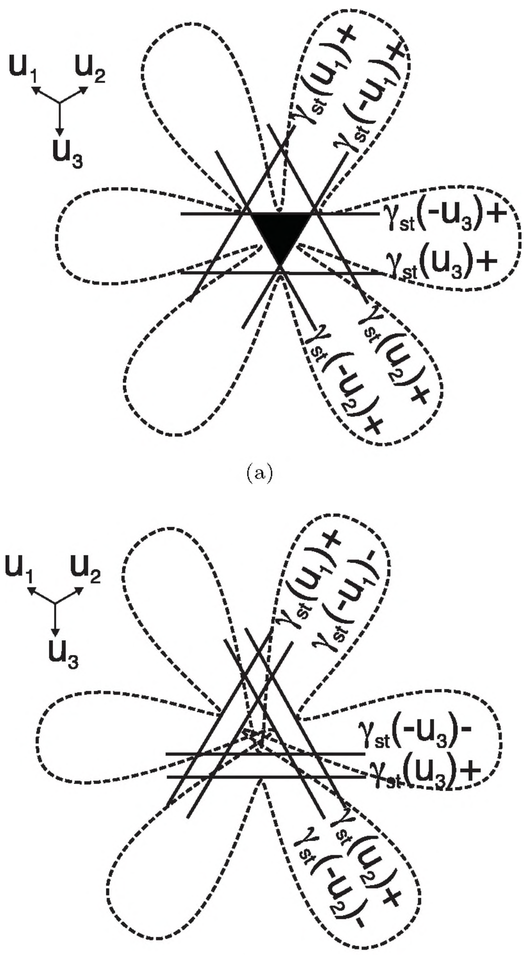

(a)

(b)

Figure 3.3: An example where $\gamma_{st}(\mathbf{u}) + \gamma_{st}(-\mathbf{u}) > 0$ for $\mathbf{u} = \pm\mathbf{u}_1, \pm\mathbf{u}_2$ and $\pm\,\mathbf{u}_3$ for both figures. Plus and minus signs behind the $\gamma_{st}(\pm\mathbf{u}_i)$ symbols indicate whether the step free energy is positive or negative. The dotted lines indicate $\gamma_{st}(\mathbf{u})$. In (a), all the step energies are positive, resulting in a defined Wulff shape, indicated by the black triangle. In (b), the step energies in the $-\mathbf{u}_i$ directions are negative, but $|\gamma_{st}(\mathbf{u}_i)| > |\gamma_{st}(-\mathbf{u}_i)|$ for $i = 1..3$, so that $\gamma_{st}(\mathbf{u}) + \gamma_{st}(-\mathbf{u}) > 0$ still holds. The black triangle is no longer defined, indicating an undefined Wulff shape. This means that the orientation will grow rough, a situation which is also covered by Eq. 3.2.

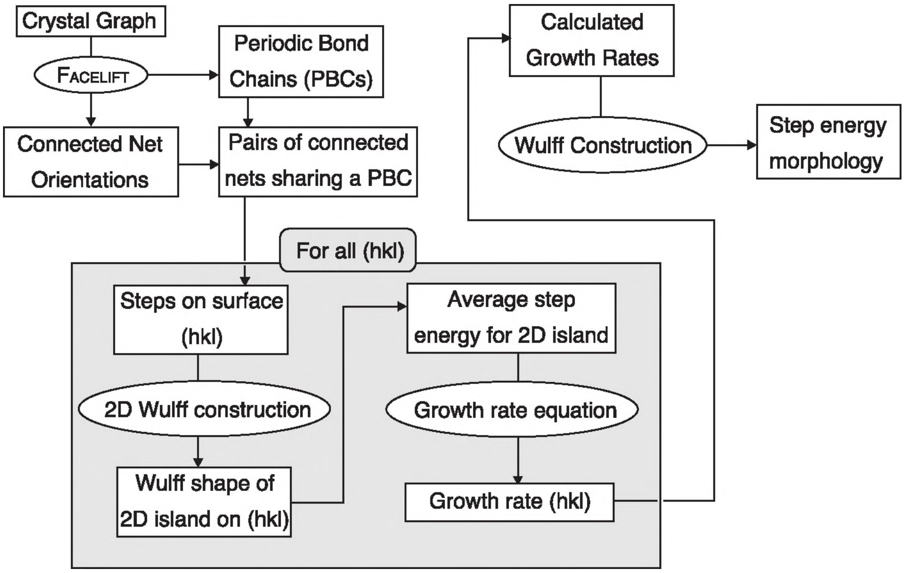

Figure 3.4: The STEPLIFT routine takes information of FACELIFT about connected nets and periodic bond chains and creates steps for all connected net orientations (hkl). Steps on (hkl) are used to create a Wulff shape of the 2D island with minimal step energy, and the average 2D island energy is calculated. From these energies growth rates are calculated, in dependence of the driving force for crystallization, $\Delta\mu/kT$ using a theoretical growth rate equation. 2D nucleus energies and related growth rates of all connected orientations (hkl) allow for a 3D Wulff construction to give the morphology, in dependence of $\Delta\mu/kT$.

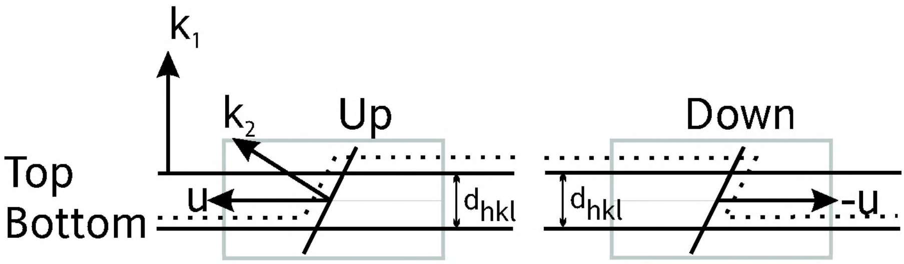

Figure 3.5: A view along a step which is constructed from two connected nets. The direction of the shared PBC is perpendicular to the drawing. The bottom and top nets are identical and separated by d_{hkl}. The second connected net bridges the two to form a step. The step contour is given by the dotted line. In (a) a step with step front orientation $\mathbf{u}$ is formed, in (b) a step with orientation $-\mathbf{u}$ is formed. In grey, two unit cells of the crystal are displayed.

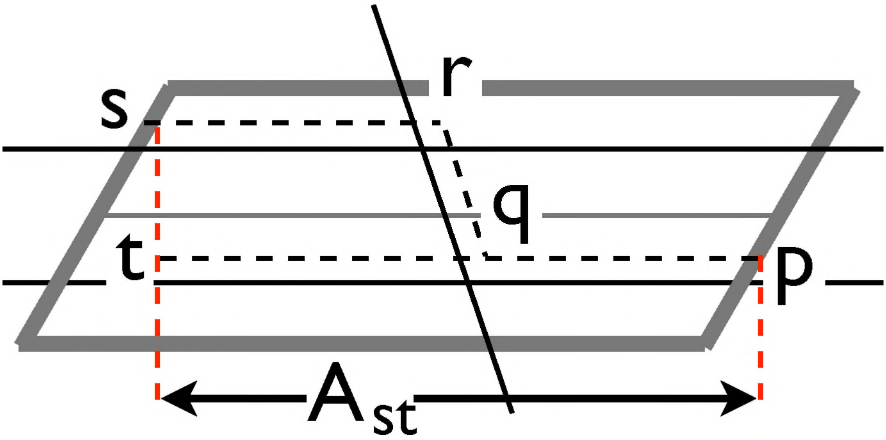

Figure 3.6: A step 'down' to illustrate the terms used in Eq. 3.4. The total step energy E_1 is the broken broken bond energy along the contour $pqrs$. The flat surface energy is the broken bond energy energy $A_{\rm st}\mathcal{E}_{\rm surf}$, calculated along the contour pqt.

3.2.3 Determining step energies

In earlier work, it was shown that *single* step energies can not be determined directly in many cases.[54] This was attributed to the absence of symmetry in the system: a perpendicular translational vector of length d_{hkl}, a mirror plane perpendicular to the surface and parallel to the step front or a two-fold axis perpendicular to the surface allows for a direct calculation of single step energies. When such symmetry elements are not present, the method introduced in [54] can be used to calculate single step energies. For the STEPLIFT routine this method is also used when the symmetry is present. In short, for a step of height d_{hkl}, the projected area under the step is represented by $A_{\rm st}$ (see also Figure 3.6) and the expression for the net formation energy of a single step becomes:

$$E_{st} = E_1 - A_{\rm st}\mathcal{E}_{\rm surf} \tag{3.4}$$

where E_1 is the total broken bond energy of a single step, i.e. the lower and upper terrace combined with the step edge, and $\mathcal{E}_{\rm surf}$ the specific broken bond energy of the flat surface.

The specific step energy, i.e. the step energy per unit step length, is then found by determining E_{st} over a direct lattice vector with length l_{st} along the step to give

$$\epsilon_{st} = \frac{E_{st}}{l_{st}}. \tag{3.5}$$

This approach is applied to calculate the step energies of all steps on a surface (hkl).

3.2.4 2D island shapes

Using the step energies obtained, a 2D Wulff construction can be made, giving the shape of the 2D nucleus with the lowest edge energy. This result subsequently leads to the average step energy, $\bar{\epsilon}_{st}$, of 2D nuclei:

$$\bar{\epsilon}_{st} = \frac{\sum_{\mathbf{u}} \epsilon_{st}(\mathbf{u}) l(\mathbf{u})}{\sum_{\mathbf{u}} l(\mathbf{u})} \tag{3.6}$$

In this equation the product $\epsilon_{st}(\mathbf{u})l(\mathbf{u})$ is the product of the step energy in the direction $\mathbf{u}$ and the length of that step in the 2D nucleus. The total is normalized by the total length of all steps involved.

3.2.5 Step interlacing and steps on sublayers

Step interlacing is a phenomenon where sublayers, often related by screw axis or glide plane symmetry, have different step propagation velocities in the same direction. This happens when a unit height of d_{hkl} contains multiple connected nets. Although these connected nets are related by screw axis or glide plane symmetry, the prerequisite of steps having the same upper and lower terrace configuration [54] is not fulfilled in a crystallographic sense, i.e. there is no translational symmetry between the connected nets.[64] In the STEPLIFT procedure, this situation is handled by not computing the energies of single steps for connected nets of sublayers, but by dividing the sum of the step energy of two opposing steps evenly between those steps. This is clearly not the correct procedure, as in criterion 3.2 it was shown that single step energies must be used. The impact of the approximation will be discussed for two of the examples presented here.

3.3 From step energies to morphology

The step energies obtained from the STEPLIFT procedure were used in the previous section to calculate the averate step energy of a 2D island on a surface (hkl). To predict morphologies, one could use the step energy as an indication for the morphological importance of a face, i.e. $R_{hkl}^{-1} \propto \bar{\epsilon}_{st,hkl}$, much like the attachment energy morphology. With the aid of crystal growth theory however, we can do better, and predict the growth rate R_{hkl} in dependence of the driving force, $\Delta\mu/kT$. Therefore, in this section we will use the average step energies to come to growth rates using a 2D nucleation growth mechanism. Of course, other mechanisms, like spiral growth, can also be considered as the step energy is an essential parameter in the corresponding growth rate expressions. For the latter mechanism, however, another essential parameter, namely the dislocation density is difficult to predict. Moreover, in the case of spiral growth a large anisotropy in step energies leads to a very complicated growth behaviour of successive rotations of the spiral and an adequate expression for the corresponding growth rate is not available. In thischapterwe, therefore, limit the analysis to the 2D-nucleation mechanism.

3.3.1 Calculation of 2D nucleation growth rates

For 2D-nucleation, the growth rate R_{hkl}, in dependence of the driving force $\Delta\mu/kT$ is given by[20]

$$R_{hkl} \propto \beta_{st}^{hkl} \left[\frac{\Delta\mu}{kT}\right]^{\frac{5}{6}} \exp\left(-\frac{\Delta G^{*}_{hkl}}{3kT}\right) \tag{3.7}$$

in which β_{st}^{hkl} is the step kinetic coefficient and ΔG^{*}_{hkl} the excess free energy of the 2D nucleus,

$$\Delta G^{*}_{hkl} = \frac{\Omega}{d_{hkl}} \frac{\bar{\gamma}^{2}_{E,hkl}}{\Delta\mu} \tag{3.8}$$

where Ω is the growth unit volume, d_{hkl} the step height and $\bar{\gamma}_{E,hkl}$ the average step free energy for the orientation (hkl). The exponential prefactor in Eq. 3.7, $(\Delta\mu/kT)^{\frac{5}{6}}$, is resulting from a *birth and spread* model in which nuclei can form on growing nuclei. This factor has a relatively small impact on the overall dependence of the growth rate on $\Delta\mu/kT$.

In our approach, we substitute the average step energy found by the construction of the Wulff shape for the average step *free* energy. Eq. 3.7 then becomes:

$$R_{hkl} \propto \beta_{st}^{hkl} \left[\frac{\Delta\mu}{kT}\right]^{\frac{5}{6}} \exp\left(-\frac{\Omega\bar{\epsilon}^{2}_{st,hkl}}{3kT\, d_{hkl}\Delta\mu}\right) \tag{3.9}$$

Using Eq. 3.9, the growth rate can be calculated as a function of $\Delta\mu/kT$. Assuming that the kinetic step coefficient is constant and independent of the step front orientation and face orientation, a kinetic Wulff construction leads to the morphology as a function of $\Delta\mu/kT$. For all calculations in thischapterwe use a temperature of 300 K, i.e. room temperature, which is close to the practical temperatures for crystals growing from solution.

In the following sections, we will apply this procedure to three examples, Venlafaxine, Aspartame and two polymorphs of a yellow isoxazolone dye.

Table 3.1: The bonds in the crystal graph of Venlafaxine after scaling to the enthalpy of dissolution in heptane. Symmetry-related bonds are not listed. For example, the second entry in the table can be read as follows: the bond goes from growth unit ‘1’ to growth unit ‘3’ in the unit cell next to it in the positive *b* direction. Its energy is -2.45 kcal·mol^{-1}.

Bond	Energy [kcal·mol^{-1}]
$1^{[000]}$ - $2^{[000]}$	-3.20
$1^{[000]}$ - $3^{[010]}$	-2.45
$1^{[000]}$ - $2^{[100]}$	-1.90
$1^{[000]}$ - $3^{[000]}$	-1.63
$1^{[000]}$ - $1^{[100]}$	-1.47
$1^{[000]}$ - $1^{[010]}$	-1.06
$1^{[000]}$ - $3^{[\bar{1}00]}$	-0.68

3.4 Application to Venlafaxine

Venlafaxine is a bicyclic phenylethylamine-based anti-depressant, which is believed to work by simultaneously blocking the reuptake of neuronal norepinephrine and serotonin.[69] Polymorph I of the free base is the stable polymorph at room temperature and its crystal structure and crystal graph details will be published in a forthcoming paper.[70] In short, the crystal structure has spacegroup $P2_1/c$ with Z = 4, **a** = 8.21 Å, **b** = 8.85 Å, **c** = 21.79 Å and β = 92.79°. The crystal graph bonds are listed in Table 3.1. These bonds, calculated with respect to vacuum using the Dreiding forcefield, are scaled so that the sum of the bonds is equal to the dissolution enthalpy in heptane of 10.0 kcal·mol^{-1}. For further computational details the reader is referred to [70].

3.4.1 Connected nets, attachment energies and steps on Venlafaxine

The FACELIFT routine gives the connected nets and attachment energies in Table 3.2. Combining all steps determined with STEPLIFT for each face to get the Wulff constructions of the 2D nuclei leads to the Wulff 2D island energies, listed in the same table.

Venlafaxine has a plank-like growth morphology with the crystallographic orientations {002}, $\{\bar{1}01\}$ and {012}, and experimental morphological importance in that order with {002} being the largest face, in case of 2D-nucleation growth. The corresponding experimental growth morphology is shown in the left hand image of Figure 3.7(a). The image on the right hand in this figure has a different aspect ratio as a result of the {002} faces growing relatively fast with a spiral growth mechanism [70]. The attachment energies can be used to

Table 3.2: The connected net orientations, lowest attachment energies and average step energies ($\bar{\epsilon}_{st}$) of Venlafaxine. No entry in the average step energy column means that there is no 2D Wulff island with an energy larger than zero, i.e. the criterion for non-rough growth in Eq. 3.2 is not fulfilled. The {001} orientation consists of {002} sublayers, related by inversion symmetry. Steps on connected nets in this orientation show interlacing and have been calculated using the approach of Section 3.2.5.

(hkl)	E_{att} [kcal·mol^{-1}]	$\bar{\epsilon}_{st}$ [cal·mol^{-1}·Å^{-1}]
$\{002\}_{int}$	-9.52	798.87
$\{\bar{1}01\}$	-14.82	452.85
$\{01\bar{2}\}$	-19.17	302.19
$\{\bar{1}1\bar{1}\}$	-25.03	150.15
$\{\bar{1}0\bar{3}\}$	-26.80	117.49
$\{110\}$	-24.22	90.95
$\{\bar{1}0\bar{1}\}$	-20.01	73.25
$\{1\bar{1}2\}$	-25.98	69.50
$\{11\bar{1}\}$	-25.71	58.19
$\{01\bar{1}\}$	-19.04	25.19
$\{11\bar{2}\}$	-27.61	-
$\{\bar{1}1\bar{4}\}$	-32.38	-
$\{1\bar{1}3\}$	-29.18	-

create an attachment energy morphology. This predicted morphology is displayed in Figure 3.7(b). When compared to the experimental morphology, the attachment energy morphology is quite different from the experimental morphology. For one, the experimental morphology is not as rich as the prediced attachment energy morphology: {111}, {110}, {101} and {011} are predicted but not observed. On the other hand, {012} is observed, but not predicted. Furthermore, the {002} orientation has too low a morphological importance and that of {011} is too high, resulting in a too thick square shape, whereas the experimental morphology is thinner and plank-like.

The predicted growth morphology at $\Delta\mu/kT = 4.0$ is shown in Figure 3.7(c). In this Figure, the predicted shape is elongated plank-like, bounded by the {002}, $\{\bar{1}01\}$ and {012} orientations, corresponding much better with the experimentally observed shape. The result at this value for the driving force showed a good correspondence to the experimentally observed morphology (left hand image in Figure 3.7(a)) and when the driving force is lowered, the predicted morphologies become more elongated in the **b**-axis direction, the longest direction in the crystal habit, which was also observed experimentally. The approximation applied to the {002} orientation, which is interlaced, seems to be adequate as the aspect ratio is predicted well.

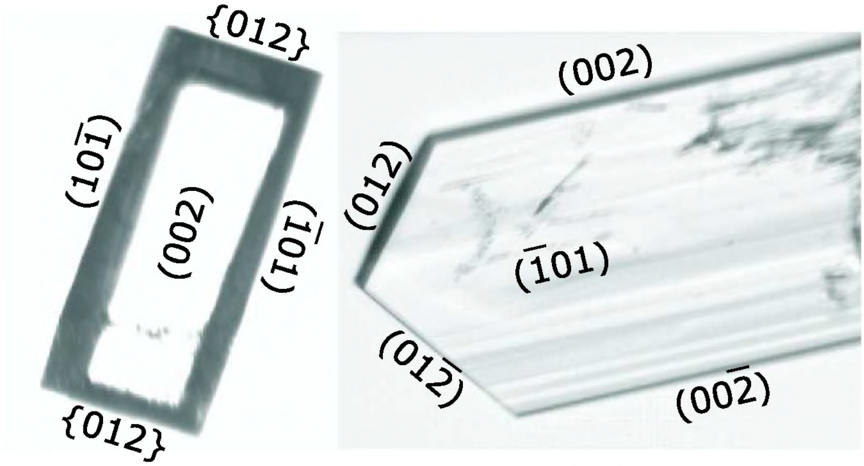

(a) Experimentally observed morphology in heptane solution; in the left hand image all faces grew via a 2D-nuclation mechanism, while for the crystal in the right hand image the {002} orientation grew via a spiral growth mechanism

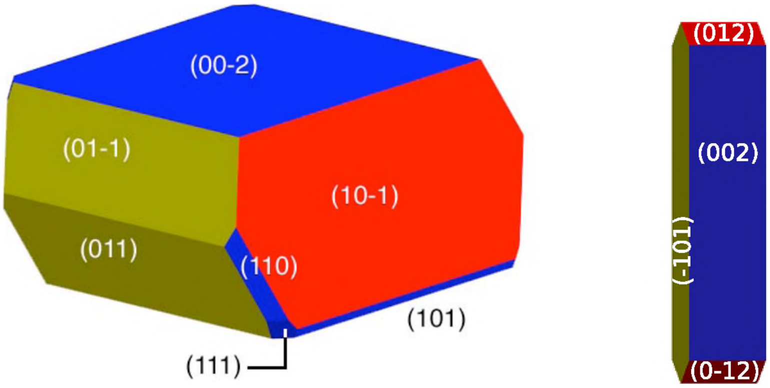

(b) Attachment energy morphology

(c) Step energy morphology at $\Delta\mu/kT$=4.0

Figure 3.7: Experimental growth morphology, attachment energy morphology and step energy morphology of Venlafaxine. The experimental morphology has orientations {002}, {$\bar{1}$01} and {012}.

Table 3.3: Bonds used in the crystal graph of aspartame II-A after scaling to the enthalpy of dissolution in water. Symmetry-related bonds are not listed.

Bond	Energy [kcal·mol^{-1}]
$1^{[000]}$ - $3^{[01\bar{1}]}$	-2.68
$1^{[000]}$ - $1^{[00\bar{1}]}$	-2.40
$1^{[000]}$ - $3^{[00\bar{1}]}$	-1.72
$1^{[000]}$ - $2^{[01\bar{1}]}$	-1.59

3.5 Application to aspartame II-A

Aspartame is the methyl ester of a dipeptide consisting of L-phenylalanine and L-aspartic acid, and is used as a low-calorie artificial sweetener. Aspartame exhibits a very thin needle-like morphology and its crystal structure was determined by Hatada *et al.*, which was later named phase II-A having spacegroup $P4_1$, with $Z = 4$, $\mathbf{a} = \mathbf{b} = 17.69$ Å and $\mathbf{c} = 4.92$ Å.[71] Previous investigations using Monte Carlo growth simulations showed a good agreement between the simulated growth rates and the experimentally observed growth behavior.[30] Here we attempt to understand the growth morphology in terms of the step energies involved in the growth process.

3.5.1 Connected nets and steps on aspartame

The crystal graph as used in a Monte Carlo simulations study[30] is applied to STEPLIFT. The bonds used in the crystal graph are listed in Table 3.3. These interactions, calculated with respect to vacuum, are scaled so that the sum of all bonds is equal to the dissolution enthalpy in water of 8.38 kcal·mol^{-1}. The resulting connected nets and average step energies are listed in Table 3.4.

3.5.2 Aspartame growth rates and morphology

Aspartame II-A has a needle-like growth morphology, originating from a spherulite-type nucleation center (see Figure 3.8(a)). The long axis of the needle is parallel to the crystallographic **c**-axis, and previous Monte Carlo growth investigations have shown that all faces, except {010} and {110}, show fast growth, confirming the shape and growth direction of the needle. The attachment energy prediction, shown in Figure 3.8(b), does not represent the extreme needle-like morphology: a more block-like morphology is predicted. Using Eq. 3.9 we have calculated growth rates for all the orientations that have an average step energy $\bar{\epsilon}_{st}$ ¿ 0. The predicted morphology at $\Delta\mu/kT = 2.5$ is shown in Figure 3.8(c). It is clear that using calculated growth rates also leads to a fine needle morphology. Lower values for $\Delta\mu/kT$ lead to unrealistically thin needles.

Table 3.4: The connected net orientations, lowest attachment energies and average step energies ($\bar{\epsilon}_{st}$) of aspartame II-A. No entry in the average step energy column means that there is no 2D Wulff island with an energy larger than zero.

(hkl)	E_{att} [kcal·mol^{-1}]	$\bar{\epsilon}_{st}$ [cal·mol^{-1}·Å^{-1}]
$\{010\}$	-6.60	588.06
$\{\bar{1}10\}$	-8.79	548.60
$\{02\bar{1}\}$	-20.46	138.49
$\{1\bar{3}\bar{1}\}$	-22.18	50.17
$\{2\bar{3}\bar{1}\}$	-22.18	27.92
$\{0\bar{3}\bar{1}\}$	-20.33	13.24
$\{121\}$	-22.31	12.36
$\{\bar{3}1\bar{1}\}$	-24.10	8.43
$\{\bar{1}21\}$	-22.31	4.94
$\{0\bar{1}\bar{1}\}$	-20.46	0.00
$\{1\bar{1}\bar{1}\}$	-22.31	0.00
$\{2\bar{2}1\}$	-22.31	-
$\{3\bar{2}1\}$	-24.10	-

At $\Delta\mu/kT$=2.5, the needle is bounded by the $\{\bar{1}10\}$ side faces and the $\{02\bar{1}\}$ and $\{121\}$ top faces. These faces were also found from the Monte Carlo simulations, albeit at $\Delta\mu/kT$=1.5. As the crystal is non-centrosymmetric, the indices of the opposite needle tip face indices are different. Experimentally grown aspartame crystals have not been indexed, however, and do not show faceted needle tips, due to thermal and/or kinetic roughening.

3.6 Application to the polymorphic system of a yellow isoxazolone dye

The polymorphic system of a yellow isoxazolone dye has been studied using Monte Carlo growth simulations.[50]. Two readily made polymorphs are known, exhibiting very different morphologies (a third, very unstable, polymorph is not studied in thischapter).[72]. The two polymorphs are monotropically related, and the stable polymorph **I** (spacegroup P 2_1/n with Z = 4, **a** = 10.80 Å, **b** = 13.23 Å, **c** = 17.31 Å and β = 102.28°) has a block-like habit, whereas the metastable polymorph **II** (spacegroup P 2_1 with Z = 4, **a** = 13.71 Å, **b** = 9.65 Å, **c** = 18.18 Å and β = 112.14°) grows as fine needles (see Figure 3.9). In the Monte Carlo study, the experimental dependence of the habit of both polymorphs on $\Delta\mu/kT$ was simulated using the MONTY program. From the simulations, it was found that at low $\Delta\mu/kT$ values the simulated growth rate curves for distinct faces of polymorph **I** cross, indicating a strong dependence of the morphology on $\Delta\mu/kT$. For polymorph **II** it was shown that all faces grow rough, except $\{\bar{1}01\}$,

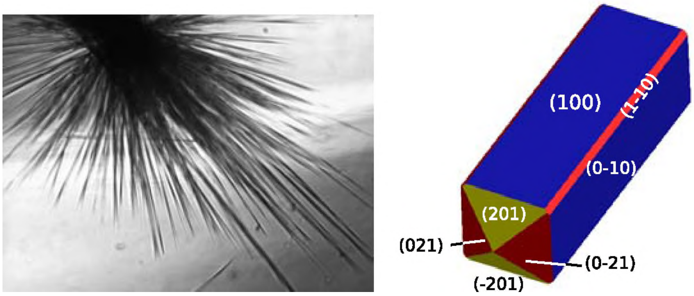

(a) Experimental morphology in aqueous solution

(b) Attachment energy morphology

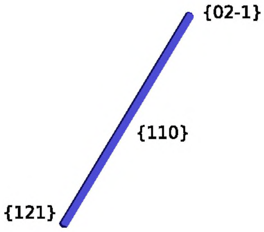

(c) Step energy morphology

Figure 3.8: Experimental morphology, attachment energy and step energy morphology of aspartame II-A. Experimentally, thin needles grow from a spherulite nucleation center. The attachment energy morphology is somewhat elongated, but it is too block-like. The step energy morphology, at $\Delta\mu/kT$=2.5, corresponds much better to the experimentally observed morphology.

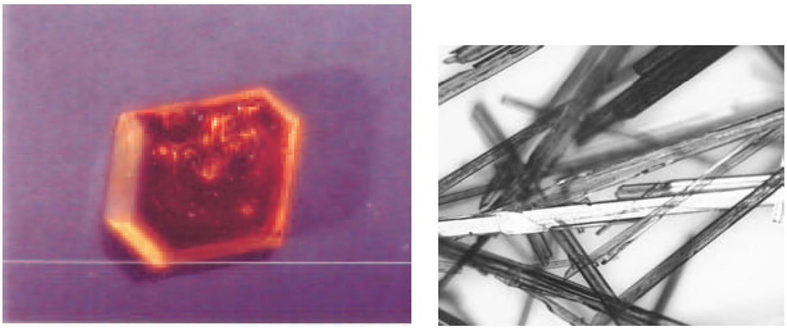

Figure 3.9: The experimental morphologies for the yellow dye polymorphs **I** (left) and **II** (right) grown in methanol solution. The stable polymorph **I** grows with a block-like habit bounded by $\{\bar{1}01\}$, $\{\bar{1}10\}$, $\{011\}$, and – at lower driving force – $\{00\bar{2}\}$, $\{10\bar{1}\}$ and $\{11\bar{1}\}$. The metastable polymorph grows at low driving force as flat needles with large $\{00\bar{1}\}$ facets and small $\{100\}$ and $\{10\bar{1}\}$ facets; at higher driving forces no facets can be discerned.

$\{100\}$ and $\{001\}$. As these three faces are all in the $(h0l)$ zone, the growth rate is high in the b-direction, explaining the needle morphology. Experimentally, form **II** only nucleates heterogeneously, on foreign particles or on the wall of the crystallisation vessel. Again, we apply the STEPLIFT procedure to the crystal graphs used in the Monte Carlo simulations. For further detail, the reader is referred to refs [50, 72]. The bonds listed in Table 3.5 are, again, scaled to the dissolution enthalpy in methanol of 18.9 kcal·mol^{-1} and 17.9 kcal·mol^{-1} for polymorph **I** and **II** respectively. The connected net orientations and average step energies obtained using Eq. 3.6 are listed in Table 3.6.

The morphologies predicted using the attachment energy method are displayed in Figure 3.10. The agreement between the experimentally observed morphology and the attachment energy morphology is reasonable for polymorph **I**. The large faces $\{\bar{1}01\}$ and $\{011\}$ are predicted by the attachment energy method, whereas only the smaller $\{\bar{1}10\}$ faces are not predicted. For polymorph **II** however, a plank-like morphology is predicted from the attachment energies, as opposed to the needle-like morphology that is found experimentally.

The morphologies predicted using STEPLIFT for form **I** and **II** are shown in Figure 3.11. The morphology predicted for the stable form **I** shows at $\Delta\mu/kT$ = 15 a flat prism shape with $\{\bar{1}01\}$ and $\{011\}$ and at $\Delta\mu/kT = 90$ the predicted habit is bounded by the $\{\bar{1}01\}$, $\{011\}$, $\{101\}$, $\{002\}$ and $\{110\}$ faces. At these higher driving forces, the predicted morphology is corresponding very well to the experimentally observed morphology, which is found at low supersaturation. The flat prism, calculated at low driving force, is found at higher experimental supersaturations. The very high values of $\Delta\mu/kT$ used in this prediction are due to the high nucleation barrier on $\{\bar{1}01\}$, which was also found from the Monte Carlo simulations in which this face did not show any growth up to a value of $\Delta\mu/kT = 8.8$.

Table 3.5: Crystal graph bonds of the isoxazolone dye form **I** (left) and **II** (right). These bonds are scaled to the enthalpy of dissolution in methanol. Symmetry-related bonds are not listed. Some entries do not match those in [50], which is due to a misprint in that reference.

Bond	Bond energy [kcal·mol^{-1}]	Bond	Bond energy [kcal·mol^{-1}]
$1-1[\bar{1}00]$	-1.25	$1-2[000]$	-9.51
$1-2[\bar{1}\bar{1}0]$	-3.36	$1-2[010]$	-11.17
$1-2[0\bar{1}0]$	-1.69	$1-3[\bar{1}00]$	-1.45
$1-3[\bar{1}\bar{1}1]$	-10.00	$1-3[000]$	-1.69
$1-3[\bar{1}01]$	-3.01	$1-4[\bar{1}\bar{1}0]$	-1.12
$1-3[0\bar{1}1]$	-1.69	$1-4[\bar{1}0\bar{1}]$	-1.72
$1-4[\bar{1}\bar{1}0]$	-1.05	$1-4[\bar{1}00]$	-3.27
$1-4[\bar{1}00]$	-4.19	$1-4[000]$	-2.62
		$2-4[\bar{1}\bar{1}0]$	-3.25

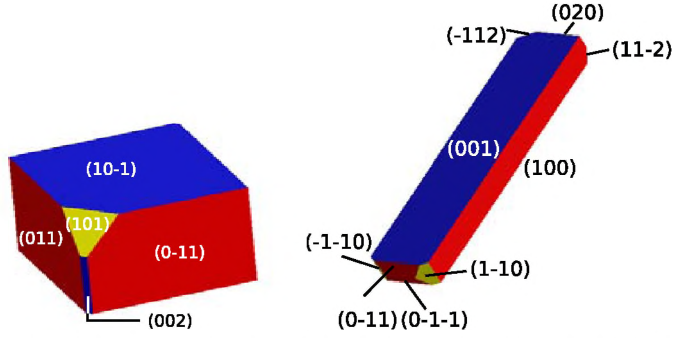

(a) Attachment energy morphology polymorph **I**

(b) Attachment energy morphology polymorph **II**

Figure 3.10: Attachment energy morphologies of two polymorphs of the yellow isoxazolone dye. The attachment energy morphology corresponds reasonably for polymorph **I**, but the plank-like morphology of polymorph **II** does not reproduce the needle-like morphology observed experimentally.

Table 3.6: All orientations with a connected net, attachment energies and average step energies of polymorph **I** (left) and polymorph **II** (right). Orientations with subscript *"int"* have 2D island energies calculated with the approximation used for orientations that show interlacing (see Section 3.2.5).

(hkl)	E_{att} [kcal·mol^{-1}]	$\bar{\epsilon}_{st}$ [cal·mol^{-1}·Å^{-1}]
$\{\bar{1}01\}$	-15.15	1,101.92
$\{011\}$	-26.59	675.54
$\{00\bar{2}\}_{int}$	-41.16	437.27
$\{\bar{1}0\bar{1}\}$	-42.82	312.23
$\{\bar{1}10\}$	-35.00	235.13
$\{11\bar{1}\}$	-34.02	159.99
$\{01\bar{2}\}$	-43.66	118.56
$\{\bar{1}13\}$	-52.05	59.63
$\{\bar{1}1\bar{1}\}$	-43.60	0.00
$\{3\bar{1}\bar{2}\}$	-64.60	-
$\{212\}$	-65.15	-
$\{21\bar{2}\}$	-55.42	-
$\{\bar{2}\bar{1}\bar{1}\}$	-58.15	-
$\{1\bar{1}\bar{4}\}$	-62.47	-
$\{21\bar{3}\}$	-59.41	-
$\{0\bar{1}\bar{3}\}$	-62.45	-
$\{\bar{2}11\}$	-48.09	-
$\{10\bar{3}\}$	-58.75	-
$\{\bar{2}10\}$	-57.10	-
$\{\bar{1}\bar{1}2\}$	-43.04	-
$\{\bar{1}\bar{1}\bar{2}\}$	-54.79	-
$\{21\bar{4}\}$	-63.73	-

(hkl)	E_{att} [kcal·mol^{-1}]	$\bar{\epsilon}_{st}$ [cal·mol^{-1}·Å^{-1}]
$\{001\}$	-3.44	1,274.67
$\{100\}$	-8.62	565.42
$\{020\}_{int}$	-56.38	131.31
$\{\bar{1}\bar{1}0\}$	-34.55	106.07
$\{\bar{1}\bar{1}1\}$	-35.26	42.67
$\{2\bar{1}\bar{1}\}$	-41.43	29.03
$\{\bar{2}21\}$	-61.77	24.86
$\{\bar{1}\bar{2}1\}$	-58.23	15.98
$\{101\}$	-57.86	-
$\{20\bar{1}\}$	-58.29	-
$\{\bar{2}12\}$	-42.11	-
$\{\bar{3}11\}$	-62.10	-
$\{10\bar{1}\}$	-18.19	-
$\{0\bar{2}1\}$	-61.77	-
$\{01\bar{1}\}$	-35.26	-
$\{\bar{2}10\}$	-49.38	-
$\{\bar{1}1\bar{2}\}$	-61.44	-
$\{1\bar{1}\bar{2}\}$	-42.11	-
$\{0\bar{1}2\}$	-62.37	-
$\{2\bar{1}1\}$	-54.77	-
$\{1\bar{1}1\}$	-49.12	-

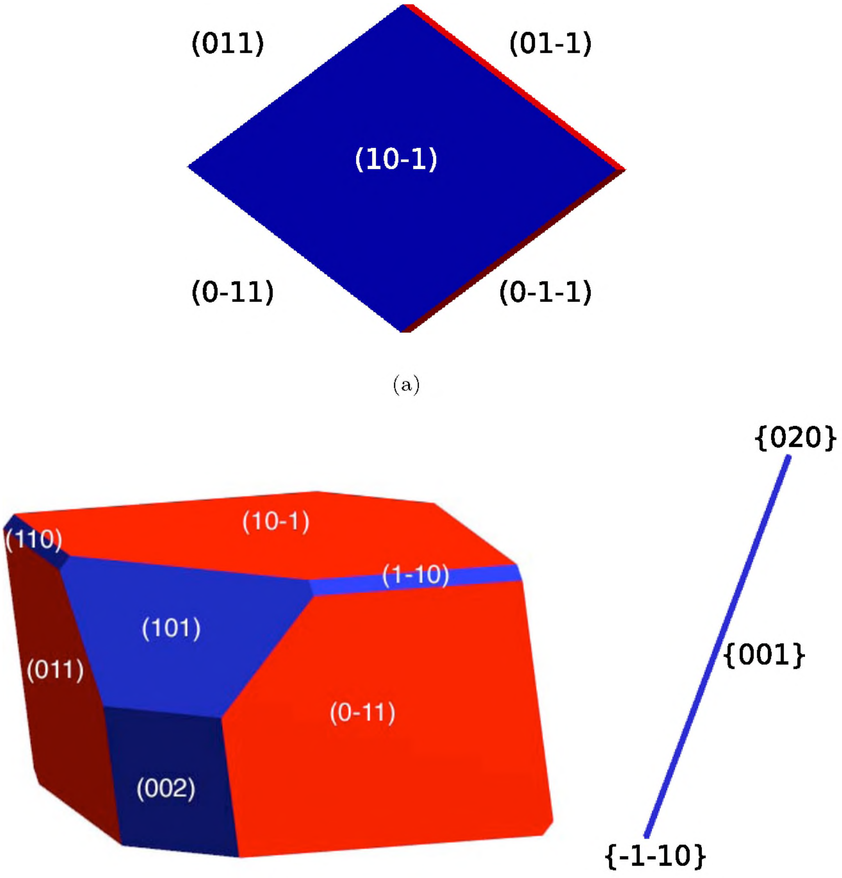

(a)

(b)

(c)

Figure 3.11: Calculated morphologies for the two forms of the yellow isoxazolone dye using STEPLIFT. Figure 3.11(a) shows the calculated habit of the stable form **I** at $\Delta\mu/kT = 15$, where a flat prism-like habit is predicted. Figure 3.11(b) shows the predicted morphology at $\Delta\mu/kT = 90$ and Figure 3.11(c) shows the metastable form **II** predicted habit at $\Delta\mu/kT = 3.5$.

The needle morphology of form **II** is not reproduced very well. Although at $\Delta\mu/kT = 3.5$ a needle shape is predicted, it is a two-dimensional crystal as the $\{001\}$ faces have a very low growth rate, due to a high nucleation barrier on that face. This was also found in the Monte Carlo simulations, as this face only showed growth above $\Delta\mu/kT = 8.0$. At these higher $\Delta\mu/kT$ values the growth rate of the $\{100\}$ faces is so high compared to $\{001\}$ that a flat plate-like crystal is predicted (not shown), as opposed to the needle-like shape observed experimentally. Still, the aspect ratio of the step energy morphology of polymorph **II** corresponds much better to the experimentally observed needle-like morphology, when compared to the attachment energy prediction. The effect of the approximation applied to the $\{020\}$ orientation, which shows interlacing, cannot be tested well as this is a fast growing direction of the needle tip.

3.7 Discussion

The first and most important point of discussion is the neglect of kinks on the steps. The problem of finding step configurations for any crystal structure is complex, and the limitation to steps without kinks has proved to be a necessary simplification, postponing the study of the influence of kinks to future investigations. The calculation of kink energies on steps is conceptually similar to the calculation of step energies on surfaces, but one dimension lower. The roughening behavior of steps is different compared to that of surfaces however, as steps are always roughened. This makes the application of the method for calculation of step energies to the calculation of kink energies much less straightforward.

The dependence of the step energy on the size of the island is not taken into account in this chapter. The islands are assumed to be large enough for corner effects to be negligible. Because kinks are neglected, the limited configurational entropy at small island sizes is also not treated. Furthermore, the step *free* energy is a function of the driving force for crystallization: one of the criteria for kinetic roughening is the vanishing of the step free energy at a high enough driving force.[27, 73] As the influence of kinks is not treated, kinetic roughening is beyond the scope of thischapter. Therefore the method and results presented are expected to be applicable to crystal orientations that have not too small 2D nuclei. Nevertheless, orientations that do turn out to have small step energies as a result of the present approach will still have relatively small 2D nuclei and therefore, will grow fast. An example are the top faces of aspartame and the metastable polymorph of the yellow dye. These faces all grow kinetically rough at the driving forces where crystals are formed experimentally (see Figures 3.8(a) and 3.9(a)).

Using equation 3.7 for the calculation of growth rates in dependence of the driving force for crystallization implies a number of assumptions. The formula is derived for cubic crystal structures and circular nuclei. In our case, the crystal structure has arbitrary symmetry, and the nuclei will not be circular, but can have any shape. Also, it is assumed that the kinetic constant for integration into the step, β_{st}^{hkl}, is the same for all (hkl) and all step orientations. As this kinetic constant is composed of contributions of surface diffusion and integration kinetics, this assumption might be justified for all step orientations on a single (hkl) surface, but will need refinement for different surface diffusion behavior on different (hkl) surfaces. Such detailed investigations are, however, beyond the scope of this.

By using the crystal growth theories, we have introduced a method for semi-quantitative treatment of the $\Delta\mu/kT$ dependence of the growth morphology. The driving force for crystallization, however, at which some of the predicted morphologies were made in this chapteris rather high, e.g. $\Delta\mu/kT$=4.0 for Venlafaxine and even 15 and 90 for the isoxazolone polymorph **I**. Experimentally, these kind of driving forces will not be obtained for growth from solution. The question arises, what is the significance of these high driving force values. One of the explanations may be that this indicates a different kind of growth mechanism to be favoured, for instance spiral growth, or a reentrant corner mechanism from a contact nucleation site. The need to consider spiral growth was shown for the growth of polycenes[32]. Also for other compounds sometimes high driving forces were used in the 2D nucleation simulations.[9, 31, 50] Why the simulations need these high driving forces is still unclear though. It may be related to the limited simulation times and/or relatively small simulation size, but this needs more clarification. For now, however, we need to conclude that the experimental driving force and the one used in the simulations and also in the method proposed here, are not always easily comparable.

For very complex crystal structures, especially those with a large number of molecules in the unit cell, the number of connected nets can increase rapidly. As the STEPLIFT routine depends on the number of connected nets N as $\mathcal{O}\left(N^2\right)$, the computational expense can become large for these systems. By carefully choosing the size of the crystal graph, and by limiting the number of connected nets used in the STEPLIFT analysis, these systems can still be treated.

One of the major advantages of using STEPLIFT is the speed of calculation. Generally, the examples given in this chaptertake under a minute to compute on a modern workstation. Compared to the crystal growth simulations done with MONTY this is an enormous decrease in demand for computing power, as the MONTY simulations can take several hours to several days to complete, depending on the complexity of the crystal graph. The speed of calculation therefore enables the use of STEPLIFT as a tool in polymorph prediction, which is currently mainly done using attachment energy-based methods.[74] Polymorph prediction generally generates a large number of possible crystal structures, all within a few kcal·mol^{-1} in total energy. New methods must be used to assess the likelihood of such hypothetical crystal structures actually forming in a crystallization experiment, and the predicted growth morphology, especially in dependence of driving force, may give additional insight in the formation probability of polymorphs.

3.8 Conclusions

The step free energy is one of the fundamental parameters in crystal growth. The formation of a 2D nucleus depends on the amount of step free energy it takes to create the nucleus. In this chapteran automated procedure has been introduced that calculates all lowest energy steps on all connected orientations of a given crystal structure for which a crystal graph is calculated. The steps found are subsequently combined to create the minimum energy shape of a 2D island using the Wulff construction. The average step energy can be derived from this shape, and can be used as a semi-quantitative parameter in expressions for the growth rate during 2D nucleation.

Given the assumptions made for the neglect of kinks and with respect to the kinetic step coefficient β_{st}^{hkl}, it is remarkable to see that the application of the STEPLIFT method gives such good results for the three examples provided. For the application to aspartame and Venlafaxine, the results correspond very well to the experimentally observed morphology. The third example indicates that the growth behavior used for the calculation, i.e. only 2D nucleation, may be too simple for some crystal structures. For the needle-shaped metastable form **II** of the isoxazolone dye a heterogeneous nucleation mechanism is found experimentally, indicating a high 3D homogeneous nucleation barrier. When the crystal has nucleated however, growth proceeds rapidly in the direction of the needle axis. This was also found from the calculated growth rates, but the very low calculated growth rate in the $\{001\}$ direction gave a very flat needle-like shape. The stable polymorph did not show a correct dependence of the habit on $\Delta\mu/kT$; at (very) high driving forces the predicted habit matches the one observed experimentally at low driving force and vice versa. Also the driving forces at which some of the predictions were done are much higher than those used experimentally. The origin of this discrepancy is still unclear.

The STEPLIFT method offers a new tool in the prediction of crystal growth morphology. It is an improvement to the attachment energy method. The STEPLIFT method combines speed of calculation with a genuine mechanism for crystal growth, e.g. two-dimensional nucleation barriers, as well as the possibility to semi-quantitatively determine the driving force dependence of the morphology. Other growth mechanisms, besides the 2D nucleation studied in this chapter, are the subject of further investigation. Besides as a fast morphology prediction tool, the speed of calculation also enables the future use of STEPLIFT as an aid in polymorph prediction.

Chapter 4

Polymorph formation studied by 3D nucleation simulations I. Method development and validation using the Kossel model

4.1 Introduction

Nucleation is the first step in a crystallization process and involves random attachment and detachment of growth units (GUs) to a cluster of GUs. When a cluster has reached the size n for which the frequencies of attachment and detachment are equal, it has reached its critical size, n^*, and is called the nucleus, or critical nucleus. It was shown by ter Horst et al. that the probability $P(n)$ of a cluster of predetermined size n to grow out to macroscopic size can be related to the Zeldovich factor and the size of the nucleus.[75] The nucleus, having equal attachment and detachment probabilities, was also shown to have equal probability to grow out or decay, i.e. $P(n^*) = \frac{1}{2}$. Based on this property they developed a method to determine the critical nucleus size and the Zeldovich factor from Monte Carlo simulations. This growth probability method was applied to nucleation of a droplet in water vapor[75], 2D nucleation[76] and to the nucleation of terephthalic acid, using a modified Kossel model, allowing for an a priori product quality prediction[77].

In this chapter the growth probability method is combined with a general Monte Carlo crystal growth simulation method. Crystal growth simulations for any crystal structure, in any crystallographic orientation were first reported by Boerrigter et al., using the MONTY simulation package.[9] This program was developed to calculate the growth rate of any facet of a crystal structure for which a crystal graph had been calculated. Here, it forms the starting point of the development of simulations of cluster growth, which, together with the growth probability method, allows for the determination of the nucleus size as a function of the driving force, $\Delta\mu/kT$, and the nucleus interfacial energy.

4.2 Theoretical background

4.2.1 Nucleation work

The nucleation rate J is the number of crystals generated per unit of time and volume and is according to classical nucleation theory (CNT) given by[78]

$$J = zf^* C_0 \exp\left(-\frac{W^*}{kT}\right) \tag{4.1}$$

where z is the Zeldovich factor, f^* is the attachment frequency of molecules to the nucleus, C_0 the concentration of nucleation sites, W^* the nucleation work, k the Boltzmann factor and T the temperature. In order to predict the nucleation rate, an accurate prediction of the nucleation work W^* is required.

The work W for creating a cluster of size n is given by

$$W = -n\Delta\mu + \phi(n) \tag{4.2}$$

in which $\phi(n)$ is the excess free energy of the n-sized cluster. This quantity is generally expressed as

$$\phi(n) = A_n\sigma_n = c_n\sigma_n(v_0 n)^{\frac{2}{3}} \tag{4.3}$$

with the interfacial energy σ_n of an n-sized cluster, A_n the surface area, v_0 the molecular volume and c_n a numerical shape factor, which for a spherical cluster is equal to $(36\pi)^{\frac{1}{3}}$ and for a cubic cluster is equal to 6.

In case of a crystalline compound however, the interfacial energy is anisotropic with respect to the surface orientation. The excess energy of a crystalline cluster is therefore a weighed average of the surface energy of all interfacial orientations present on the cluster. To describe nucleation behavior it is then more convenient to use a reduced nucleation parameter Γ as the weighed sum over all interfaces i, with interfacial energy σ_i and shape-factor c_i, at the cluster surface.[79]

$$\phi(n) = \sum_i c_i\sigma_i(v_0 n)^{\frac{2}{3}} = \Gamma n^{\frac{2}{3}}. \tag{4.4}$$

This nucleation parameter thus contains the interfacial energy and the shape factor. In CNT, these are, for homogeneous nucleation, assumed to be constant with respect to cluster size and equal to σ_∞ and c_∞ respectively, i.e. they are not a function of orientation, n or $\Delta\mu$ and have the same value as that of a macroscopically large crystal. The nucleation parameter is therefore assumed to be constant as well. Setting $\frac{dW}{dn}$ to zero and solving for the cluster with critical size n^* (i.e. the nucleus) results in the Gibbs-Thomson equation:

$$n^* = \frac{8}{27}\left(\frac{\Gamma}{kT}\frac{kT}{\Delta\mu}\right)^3 = \frac{8v_0^2}{27}\left(\frac{c_\infty\sigma_\infty}{\Delta\mu}\right)^3, \tag{4.5}$$

which describes the nucleus size n^* as a function of the nucleation parameter and the driving force. For homogeneous nucleation the nucleation work, $W^* = W(n^*)$, has a very simple relation with $\Delta\mu/kT$ in CNT:

$$\frac{W^*}{kT} = \frac{1}{2}n^*\frac{\Delta\mu}{kT}. \tag{4.6}$$

4.2.2 The growth probability method

In a supersaturated environment, a given cluster of n molecules changes its size randomly as a result of successive attachments and detachments. As these are random events, a given n-sized cluster can grow and reach macroscopic size only with a certain probability $P(n)$.[75] This growth probability of an n-sized cluster is a function of the cluster size n, the nucleus size n^* and a numerical factor β between 0 and 1 and is given by

$$P(n) = \frac{1}{2}\left[1 + \operatorname{erf}\left(\beta(n - n^*)\right)\right]. \tag{4.7}$$

The numerical factor β is related to the Zeldovich factor z, which is present in the pre-exponential factor in the nucleation rate equation, according to

$$\beta = \pi^{\frac{1}{2}}z. \tag{4.8}$$

For 3D homogeneous nucleation, CNT gives an expression for β[78]

$$\beta = \left(\frac{\Delta\mu}{6kTn^*}\right)^{\frac{1}{2}}. \tag{4.9}$$

By determining the growth probability as a function of the initial cluster size, n, and the dimensionless driving force for crystallization, $\Delta\mu/kT$, the nucleus size can be determined as a function of $\Delta\mu/kT$.

4.3 Methods

4.3.1 Simulating cluster growth

To simulate 3D nucleation for any crystal structure, the Monte Carlo crystal growth simulation program MONTY[9] was adapted to simulate 3D nucleation. This program simulates crystal growth in a lattice system, based on a graph representation of the crystal structure.

Originally, MONTY is intended to be used for simulating crystal growth on specific crystallographic orientations (hkl).[9, 30, 31, 50, 52] To this end, a simulation box is created from a number of unit cells. Periodic boundary conditions are applied in the **a**- and **b**-direction; growth takes place in the **c**-direction. The initial starting configuration is a number of crystalline layers onto/from which growth units (GUs) can attach/detach.

To simulate 3D nucleation, the two-dimensional periodic boundary conditions are removed, and the initially empty simulation box is taken suitably large, to avoid growth beyond the boundaries. An initial cluster of predetermined size is placed in the centre of the simulation box and a simulation is run. To get an initial cluster of certain size the method uses an initialization routine that builds the cluster starting from a single GU. All the neighboring GUs that this GU connects to, i.e. has bonds to, are consecutively added. Next, all their neighbors are added, and so on, until the desired cluster size is reached. Generally, this leads to a more or less spherical cluster.

Next, to find the energetically optimal shape of the cluster under the simulation conditions chosen, each simulation run is preceeded by an equilibration simulation with a constant number of GUs using a Metropolis-type algorithm.[80, 81] Briefly, at each Monte Carlo move a randomly selected GU is moved to a different location on the initial cluster according to the following conditions:

$$\Delta E = E_{\text{final}} - E_{\text{initial}} = \begin{cases} < 0 & \text{move accepted} \\ > 0 : & e^{-\Delta E/kT} \begin{cases} > R & \text{move accepted} \\ < R & \text{move rejected} \end{cases} \end{cases} \tag{4.10}$$

in which R is a random number between 0 and 1. The difference in broken bond energy, $E_{\text{final}} - E_{\text{initial}}$ is calculated from the final and initial broken bond configurations of the GU being moved. These and subsequent simulations are all run at 300K, which is representative enough for typical solution growth situations.

After the equilibration run, a simulation run is performed at a specific driving force using the original MONTY event algorithm, which uses an n-fold way algorithm.[9, 82]. This algorithm was chosen for efficiency, as at each Monte Carlo event, a move will be accepted. In contrast, for a Metropolis-type algorithm, moves are not accepted when the conditions for that move are not met.

For crystal growth, especially at low driving force, the growth is often limited by a barrier for nucleation. Using a Metropolis algorithm in that case could result in most attempted moves being rejected, which would lead to very long simulation times.

A simulation run is stopped if the cluster is reduced to a size of a single GU (the cluster decays) or when the cluster has reached a size for which the growth probability, determined in earlier simulations, is unity (the cluster grows out). For a specific initial cluster size n at a certain driving force, the growth probability is given by the fraction of successful simulation runs. Fitting the growth probabilities for different initial cluster sizes determined at a given driving force to Eq. 4.7 results in the nucleus size n^* as well as β at that driving force. These values can then be used together with Eq. 4.1 and 4.6 to calculate the nucleation rate as a function of the driving force.

4.4 Application to the Kossel model

To validate the methodology and the automatic routines, the Monte Carlo growth simulations using the growth probability method were applied to the Kossel model for three different bond strengths, $\phi/kT = 2$, $\phi/kT = 1.33$ and $\phi/kT = 1$. The simulations were performed using the 'random rain' probability scheme[21] at 300K. All simulations were preceded by a relaxation period of 10000 MC events, and were performed 1000 times to determine the growth probability as the fraction of successful growth attempts. In the following two sections, a cluster of 231 GUs is studied. This initial size was chosen because it forms a completed octahedron for the Kossel model, exposing the unstable $\{111\}$ faces.

4.4.1 The initial cluster shape

When the initialization routine is used for the Kossel model, initial clusters of relatively high surface energy are created. This is caused by the fact that clusters are built up starting from a single GU. This GU's neighbors are then added to the cluster and in the next step, their neighbors are added, and so forth, until the desired cluster size is reached. For the Kossel model, this results in an octahedron with the $\{111\}$ faces exposed. These facets, which are K-faces, expose three broken bonds per GU at the surface, as opposed to the stable $\{001\}$ facets, which expose only a single broken bond. An example of such an octahedral cluster is shown in Figure 4.1(a).

4.4.2 Relaxation at a constant number of GUs

The surface energy as a function of relaxation time is shown in Figure 4.2. Here it can be seen that for this octahedral Kossel cluster, having an initial size of 231 GUs, the surface energy quickly drops in the beginning of the relaxation

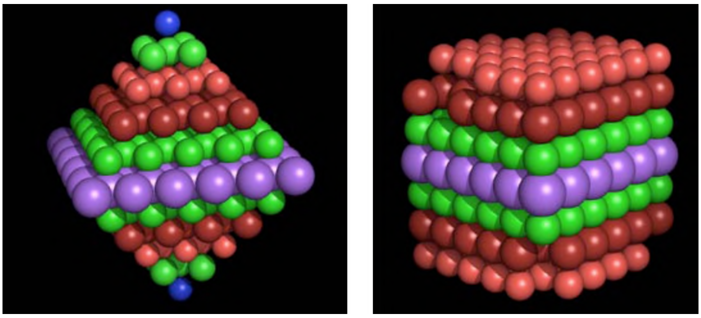

(a) Initial cluster (b) Relaxed cluster

Figure 4.1: A cluster of 231 GUs forms a complete octahedron for the Kossel model. Upon relaxation, this energetically unfavorable shape is converted to a cubic shape. See also the plot of the surface energy as a function of relaxation time in Figure 4.2.

stage, while later on it slowly reaches its final value, which belongs to a more cube-like cluster, as shown in Figure 4.1(b).

4.4.3 Determination of Γ/kT for different bond strengths

For the Kossel model, the nucleation parameter Γ/kT of a cubic and spherical cluster can be calculated using Eq 4.5:

$$\Gamma/kT = \frac{c_\infty \sigma_\infty}{kT} \tag{4.11}$$

using the shape factors c_∞ for a spherical and cubic cluster: i.e. $(36\pi)^{\frac{1}{3}} \approx 4.84$ and 6, respectively. The surface energy σ_∞ is taken to be equal to ϕ, which corresponds to the single bond exposed on the $\{001\}$ faces. For an infinitely large cubic cluster this is the correct bond strength; for a spherical cluster taking $\sigma_\infty = \phi$ may be an underestimate, due to the kink sites at the surface of a sphere. The resulting theoretical values for Γ/kT are listed in Table 4.1.

A few of the results of the simulations are shown in Figure 4.3, where the growth probability $P(n)$ is plotted as a function of initial cluster size n, for three different values of the driving force $\Delta\mu/kT$. The fitted lines were obtained using Eq. 4.7.

Using all simulations, comparable to the ones shown in Figure 4.3, the nucleus size was determined as a function of driving force. In Figure 4.4 these results are plotted, together with theoretical lines for a cubic cluster and a spherical cluster.

By fitting the Gibbs-Thomson equation to the simulation results shown in Figure 4.4, the Γ/kT values were obtained. These are listed in Table 4.1.

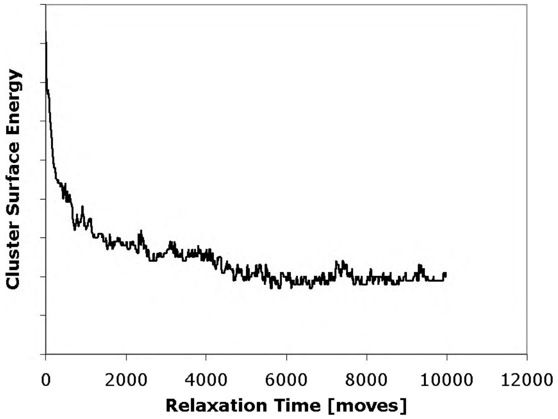

Figure 4.2: Cluster surface energy as a function of relaxation time. The initial part shows a quick drop in surface energy, as the initial surface energy is relatively high, due to the octahedral shape of the Kossel cluster, which exposes the unfavorable {111} facets. After the initial quick drop, the surface energy slowly converges to a value where further relaxation does not significantly alter the cluster surface energy.

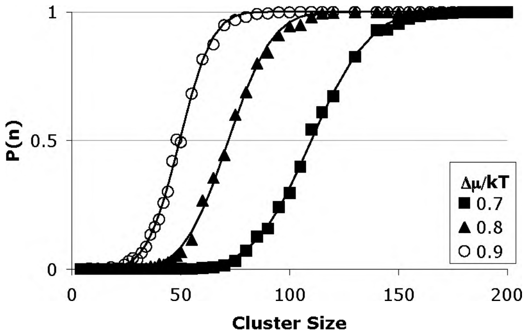

Figure 4.3: Growth probability $P(n)$ as a function of initial cluster size for the Kossel model with $\phi/kT = 1$.

Table 4.1: The theoretical and fitted values of Γ/kT for cubic and spherical clusters for three bond strengths of the Kossel model.

Bond strength ϕ/kT	1.0	1.33	2.0
Γ/kT (cubic clusters)	6	8	12
Γ/kT (spherical clusters)	4.84	6.43	9.67
Γ/kT (obtained from fit)	5.05	7.66	12.02

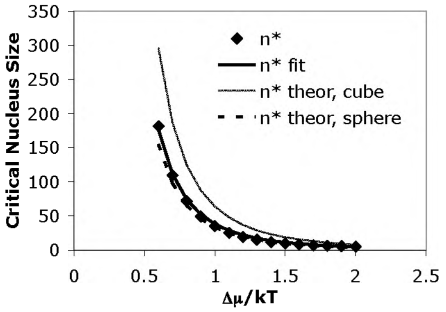

(a) $\phi/kT = 1$

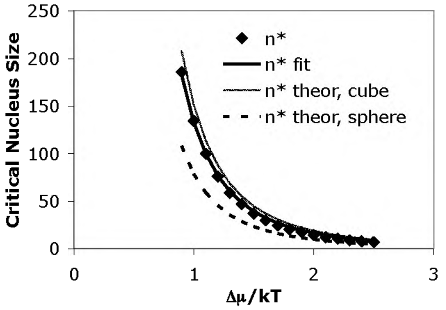

(b) $\phi/kT = 1.33$

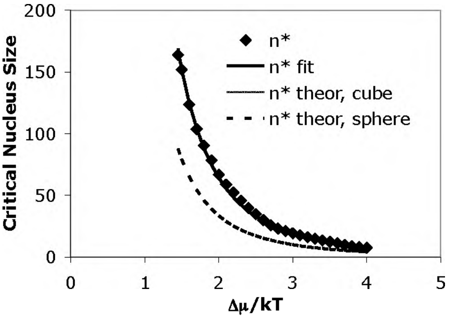

(c) $\phi/kT = 2$

Figure 4.4: Critical nucleus size as a function of driving force for three different bond strengths of the Kossel model. Theoretical lines are shown for cubic and spherical clusters, based on Eq. 4.11 In Figure 4.4(c) the values for the theoretical cubic cluster and the fitted line overlap.

4.5 Discussion

The initialization scheme used for the simulations is twofold. A cluster of desired size is created, followed by a relaxation step, where the cluster is allowed to relax. When this scheme is applied to the Kossel model, the initial shape of the clusters is octahedral, with exposed $\{111\}$ facets: an energetically unfavorable configuration. The relaxation step, however, quickly resolves this unfavorable configuration and relaxes the cluster to the more favorable cubic shape, where mainly the $\{001\}$ facets are exposed. The relaxation step is therefore necessary to start the actual simulation with an energetically favorable configuration. An added benefit of this scheme is that the simulation is not always started with exactly the same cluster configuration, but that an ensemble of favorable configurations is sampled during the simulation. The validity of the newly developed method is illustrated by the results of the simulations, as shown in Figures 4.3 and 4.4, together with the values for Γ/kT obtained from fitting the Gibbs-Thomsom equation. For the bond strength of ϕ/kT=2, the results agree very well with the classical nucleation theory: the interfacial energy found compares very well with the theoretical value. For lower bond strengths, the results show that a cubic cluster configuration becomes less likely. At the lowest bond strength of $\phi/kT = 1$ the results agree more with a spherical cluster.

This result can also be understood in terms of roughening. On large flat faces, roughening takes place when the step free energy is zero (thermal roughening) or when, at high $\Delta\mu/kT$, the 2D nucleus size is equal or smaller than a single growth unit (kinetic roughening). When the bond strength for the Kossel model is low, these roughening phenomena will already take place at moderate temperature and driving force. For small clusters, roughening will take place at even lower temperature or driving force, because of the small size of the clusters. Therefore, the transition at lower bond strength to a more spherical cluster also indicates that the cluster surface roughens and adopts the shape with the lowest interfacial energy, i.e. a sphere.

4.6 Conclusions

Nucleation proceeds via attachment and detachment of molecules to a small cluster. In order to study this phenomenon computationally, simulations of small clusters growing out to macroscopic size or decaying were implemented in the MONTY simulation software. Care was taken to start with an energetically favorable cluster configuration by allowing the initial cluster to relax at a constant number of growth units. It was shown that for the Kossel model, even when starting with a quite unfavorable configuration, the relaxation step allowed the cluster to relax to an energetically favorable configuration. The results obtained for the Kossel model show the validity of the method implemented. For the higher bond strength, $\phi/kT = 2$, the cluster shape confirms to the theoretical shape of a cubic cluster and the interfacial energy found agrees very well with the theoretical value. The results for lower bond strengths show that the clusters adopt a more spherical shape, especially at the lowest bond strength simulated, $\phi/kT = 1$. Concluding it can be said that combining the growth probability method with the Monte Carlo crystal growth simulations allows for the determination of nucleus size, interfacial energy and nucleation rates for any crystal structure. In the next chapter the method will be applied to the prediction of polymorph nucleation rates, in an effort to determine the nucleation behavior and optimal nucleation conditions for different polymorphs of a compound.

Chapter 5

Polymorph formation studied by 3D nucleation simulations II. Application to a yellow isoxazolone dye, paracetamol and L-glutamic acid

5.1 Introduction

Organic materials, like pharmaceuticals, dyes and other compounds, may crystallize in multiple crystal structures called polymorphs. For applications it is essential to control this behavior and to select a specific polymorph, but it remains difficult to predict the relevant parameter values for that. The formation of different polymorphs depends on a number of parameters, the rate of nucleation being an important one. A commonly used rule for polymorph formation is Ostwald's rule of stages, which states that during the formation of a crystalline phase, the thermodynamically least stable phase forms first, which later transforms into the most stable phase, possibly through phases of intermediate stability.[83] There are, however, examples known of systems that do not follow this rule of stages, and it is generally accepted that the rule indeed does not apply to every system, for instance in the case where polymorphs nucleate at the same time, i.e. concomitantly.[84]

Nucleation of polymorphic systems has been studied computationally for simple models [85] and for the small molecules nitrogen and carbon dioxide[86, 87]. Also in these studies, Ostwald's rule is not always obeyed[86] as the molecular dynamics (MD) simulations of carbon dioxide crystallization show that it crystallizes directly into its most stable polymorph.

More complex, organic crystals are still beyond the scope of MD simulations due to the computational cost involved. Therefore, in this chapter we combine two relatively fast methods, Monte Carlo simulations of crystal growth and a growth probability method, and apply these methods to complex crystalline systems showing polymorphism. The combination of the two methods enables us to study the growth probability of small crystalline clusters for different polymorphic systems as a function of driving force for crystallization, $\Delta\mu/kT$. This leads to a prediction of the driving force dependence of the nucleation rate of each polymorph. The method will lead to a prediction of the conditions under which certain polymorphs can be produced and concomitant nucleation can be prevented and thus to an a priori product quality prediction.[77]

It will be shown that the growth probability can be used to determine the nucleus size as a function of the driving force for crystallization in case of 3D homogeneous nucleation. The growth probability method has been used to study homogeneous nucleation of a liquid droplet in a vapor[75], 2D nucleation of simple model systems[76] and a theoretical study on homogeneous nucleation of terephthalic acid polymorphs[77], using a modified Kossel model. In the previous chapter Monte Carlo growth simulations were combined with the growth probability method to be able to study cluster growth probability as a function of initial cluster size and driving force. Here, the method is applied to three 'real' crystals showing polymorphism. It will be shown that the method is very well-suited to reproduce the nucleation behavior observed experimentally for these systems.

5.2 Comparing different polymorphs

The driving force for crystallization, $\Delta\mu$, is given by the difference in chemical potential between molecules in the fluid phase and molecules in the solid phase:

$$\Delta\mu = \mu^f - \mu^s, \tag{5.1}$$

such that when $\Delta\mu$ is positive, crystallization will take place. Now, when comparing two or more polymorphs, the chemical potential in the solid phases is different. For a dimorphic system at a certain concentration in the solution, we can write:

$$\Delta\mu_1 = \mu^f - \mu_1^s \tag{5.2}$$

$$\Delta\mu_2 = \mu^f - \mu_2^s \tag{5.3}$$

This means that experimentally, at a given solution concentration, molecules experience a different driving force for crystallization towards the stable phase 1 compared to the metastable phase 2. A clear example can be given when $\Delta\mu_1$ is taken to be positive and $\Delta\mu_2$ negative: the metastable polymorph will dissolve while the stable polymorph is formed. If we want to compare the outcome of the growth probability method for two polymorphs, we have to adjust for this difference.

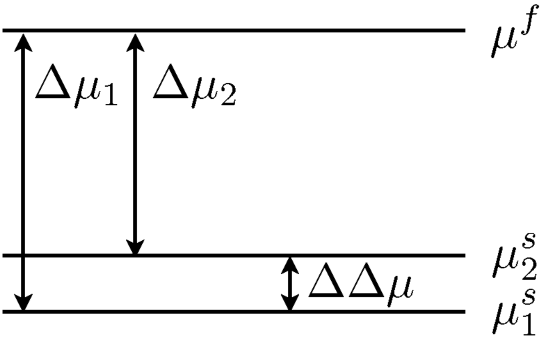

Figure 5.1: The definition of the various $\Delta\mu$ values for different polymorphs

To express $\Delta\mu_1$ and $\Delta\mu_2$ by a single driving force $\Delta\mu$, in accordance with Eq. 5.1 and 5.2, they are represented as (see also Figure 5.1):

$$\begin{aligned}\Delta\mu_1 &= \Delta\mu \\ \Delta\mu_2 &= \Delta\mu - \Delta\Delta\mu\end{aligned} \tag{5.4}$$

where $\Delta\mu \equiv \mu^f - \mu_1^s$ and $\Delta\Delta\mu \equiv \mu_2^s - \mu_1^s$.

With this presentation of $\Delta\mu_1$ and $\Delta\mu_2$, the nucleation rates of both polymorphs at a given $\Delta\mu$ value can be compared as if it were an experiment at a given concentration, where each polymorph experiences it's own $\Delta\mu$. The difference in $\Delta\mu$ is approximated by the difference in heat of dissolution, $\Delta_{diss}H$, for both polymorphs.

5.3 Calculation of crystal graphs

The MONTY program uses the crystal graph representation of a crystal structure. In a crystal graph the growth units (i.e. molecules, ions) are represented by graph vertices and the pairwise interactions between growth units are represented by graph edges. The graph edges' weight represents the strength of the interaction. To calculate the pairwise interactions between the molecules in the crystal structure, we use the Dreiding forcefield[88] in Cerius^2[89] with partial atomic charges calculated using a restricted electrostatic potential (RESP) fitting method.[90] We use this RESP method to come to a single set of partial atomic charges for all conformers of all polymorphs of a given molecule. Changing the conformation of a molecule is usually associated with a slight change in charge distribution. Having a single set of partial atomic charges for all conformations enables us to directly compare energies between the different polymorphs, instead of having to estimate or ignore the energy associated with a change in charge distribution.

The molecules' partial atomic charge distribution is calculated with respect to vacuum. After calculation of the charges, the molecules are placed at their original site in the crystal structure. The crystal structure geometry is then optimized using Ewald summation for the van der Waals and Coulombic contributions. After this optimization, all pairwise interactions within a certain cutoff radius are calculated. The sum of all interactions is scaled to be equal to the enthalpy of dissolution of the particular polymorphic form; only scaled interactions that have a magnitude above kT are used in the crystal graph.

5.4 Crystal structures and crystal graphs

5.4.1 Yellow isoxazolone dye

In a previous study, the polymorphic behavior of two polymorphs of an isoxazolone dye was studied experimentally as a function of the supersaturation.[72] It was found that the metastable polymorph **II** is kinetically favored, as a fast cooling rate exclusively leads to the formation of needle-like crystals of this polymorphic form. Lower driving forces combined with slow cooling rates yield the stable polymorphic form **I**. The crystal morphologies were studied experimentally and compared to 2D nucleation crystal growth simulations done with MONTY and they were found to correspond well[50] so that this system was an obvious choice to use in the study of the 3D growth probability. The crystal graph of this study was used unaltered here: the crystal graph details are listed in Table 5.1. For the comparison of the nucleation rates of the two polymorphs a value of $\Delta\Delta\mu$ of $1.6kT$ was used, as the dissolution enthalpies differ by 1.0 kcal·mol^{-1}.[72]

5.4.2 Paracetamol

Paracetamol, a well-known analgesic drug, is used worldwide in the production of pain-relief tablets. It has also become a well-studied pharmaceutical solid. Three polymorphs are known, of which the stable monoclinic form **I** is marketed worldwide. The orthorhombic form **II**[91, 92, 93] is interesting for pharmaceutical applications, as its tabletting properties are superior to form **I**. The third polymorph is very unstable, and its structure has not been determined experimentally. Recently a number of likely structures were determined computationally using polymorph prediction[15], and one of the predicted structures (AK6) "gave a calculated powder pattern that closely matched the observed powder pattern for form **III**".[94] In the present study we consider forms **I** and **II**.

As the enthalpy of dissolution in water is only known for form **I**, it is estimated for form **II** by subtracting the difference in enthalpy of fusion:

$$\Delta_{diss}H(\mathbf{II}) \approx \Delta_{diss}H(\mathbf{I}) - \Delta\Delta_{fus}H$$

Table 5.1: Crystal graph bonds with respect to vacuum of the isoxazolone dye form **I** (left) and **II** (right). The first entry in the left table is read as a bond that goes from GU 1 to GU 3, translated along $[\bar{1}\bar{1}1]$ on the lattice basis.

Form **I**		Form **II**	
Bond	Bond energy [kcal·mol^{-1}]	Bond	Bond energy [kcal·mol^{-1}]
1-3$[\bar{1}\bar{1}1]$	-21.05	1-2[010]	-22.00
1-4$[\bar{1}00]$	-8.81	1-2[000]	-18.72
1-2$[\bar{1}\bar{1}0]$	-7.07	1-4$[\bar{1}00]$	-6.44
1-3$[\bar{1}01]$	-6.33	2-4$[\bar{1}\bar{1}0]$	-6.39
1-3$[0\bar{1}1]$	-3.56	1-4[000]	-5.16
1-2[000]	-3.55	1-4$[\bar{1}0\bar{1}]$	-3.38
1-1[100]	-2.64	1-3[000]	-3.33
1-4$[\bar{1}\bar{1}0]$	-2.21	1-3$[\bar{1}00]$	-2.86
		1-4$[\bar{1}\bar{1}0]$	-2.21

Table 5.2: Experimental and optimized lattice parameters for two polymorphs of paracetamol (spacegroup $P2_1/a$ with $Z = 4$ and $P2_1/a\ 2_1/b\ 2_1/c$ with $Z = 8$) and two polymorphs of L-glutamic acid (both forms with spacegroup $P2_12_12_1$ and $Z = 4$).

Crystal structure	**a**(Å)	**b**(Å)	**c**(Å)	β
Paracetamol (monoclinic) HXACAN01	12.93	9.40	7.10	115.9^o
– optimized	13.24	9.30	7.27	117.5^o
Paracetamol (orthorhombic) HXACAN08	7.41	11.84	17.16	
– optimized	7.24	12.06	17.26	
L-glutamic acid ($\boldsymbol{\alpha}$) LGLUAC03	10.28	8.78	7.07	
– optimized	10.34	8.49	7.87	
L-glutamic acid ($\boldsymbol{\beta}$) LGLUAC03	5.16	17.30	6.95	
– optimized	5.19	17.85	6.78	

Table 5.3: Crystal graph bonds with respect to vacuum of monoclinic (left) and orthorhombic paracetamol (right).

Monoclinic Paracetamol (**I**)		Orthorhombic Paracetamol (**II**)	
Bond	Bond energy [kcal·mol^{-1}]	Bond	Bond energy [kcal·mol^{-1}]
1-1[001]	-2.35	1-3[000]	-4.28
1-2[000]	-4.01	1-4[000]	-3.10
1-3[$1\bar{1}1$]	-3.91	1-5[$\bar{1}00$]	-7.21
1-3[100]	-2.80	1-5[000]	-6.04
1-3[101]	-8.81	1-6[000]	-8.24
1-4[101]	-9.90	1-7[000]	-9.63
1-4[000]	-9.41	1-8[000]	-2.53

Using this simple equation, the two enthalpies of dissolution in water used are 5.37 kcal·mol^{-1} and 5.01 kcal·mol^{-1} for forms **I** and **II** respectively, calculated using the enthalpies of fusion of 6.92 kcal·mol^{-1} and 6.56 kcal·mol^{-1} respectively.[95] In the determination of the nucleation rates a value for $\Delta\Delta\mu$ of 0.36 kcal·mol^{-1}, or 0.6 kT was used.

The crystal structures of paracetamol (Cambridge Structural Database reference codes HXACAN01 and HXACAN08) were minimized using the procedure outlined before. The results of the minimization and the crystal graph are listed in Tables 5.2 and 5.3.

5.4.3 L-glutamic acid

L-glutamic acid is an amino-acid industrially prepared by fermentation. It is a well-studied polymorphic compound with two distinct polymorphs, $\boldsymbol{\alpha}$ and $\boldsymbol{\beta}$. The metastable $\boldsymbol{\alpha}$ form has a prismatic crystal morphology, whereas the stable $\boldsymbol{\beta}$ form has an elongated plate-like shape.

The dissolution enthalpy was measured by Sakata et al. to be 5.55 kcal·mol^{-1} for the $\boldsymbol{\alpha}$ form and 5.15 kcal·mol^{-1} for the $\boldsymbol{\beta}$ form. This leads to a $\Delta\Delta\mu$ difference of 0.67 kT when comparing the nucleation rates.

The crystal structures of L-glutamic acid (LGLUAC03 and LGLUAC11) were minimized using the procedure outlined before. The original and minimized lattice parameters are listed in Table 5.2. All optimized lattice parameters are within 5% of the original lattice parameters, except for the optimized **c**-axis of the $\boldsymbol{\alpha}$ form of L-glutamic acid that changed 11% in length. This unusually large deviation upon minimization may be due to the zwitterionic nature of the molecule in the solid. As the molecular charges are obtained from the molecule in the gasphase, the partial charges on the deprotonated carboxylic acid group and the protonated ammonium group may not accurately represent

Table 5.4: Crystal graph bonds with respect to vacuum of L-glutamic acid α (left) and β (right).

L-glutamic acid α form		L-glutamic acid β form	
Bond	Bond energy [kcal·mol^{-1}]	Bond	Bond energy [kcal·mol^{-1}]
1-2[000]	-32.90	1-2[$\bar{1}\bar{1}0$]	-29.39
1-3[000]	-15.97	1-2[$0\bar{1}0$]	-23.61
1-4[000]	-24.01	1-3[000]	-17.94
1-4[010]	-11.55	1-4[001]	-6.35
1-1[011]	-2.27	1-1[100]	-8.81
1-1[010]	-2.35	1-2[$\bar{1}\bar{1}\bar{1}$]	-2.62
1-4[$01\bar{1}$]	-2.79	1-3[001]	-3.39

the 'real' partial charges in the solid. The magnitude of the partial charges on these groups is reasonable, however, with -0.67 and +0.48 on the carboxylic and the ammonium groups, respectively. The effect of this possible inaccurate representation is limited, as the results of the simulations are of a qualitative nature, rather than quantitative. The crystal graph bonds are listed in Table 5.4.

5.5 Results and discussion

5.5.1 Equilibration of clusters of the isoxazolone dye polymorphs

The simulation procedure starts with the equilibration of the initial cluster. To illustrate the benefits and necessity of this equilibration step in the simulation procedure, clusters of the two polymorphs of the yellow isoxazolone dye with an initial size of 100 GUs were equilibrated and then grown out to a final size of 300 GUs. The results are displayed in Figure 5.2. In the Figure the initial, equilibrated and final cluster shapes are displayed. It can be seen that the initial cluster for polymorph **II** contains more kink sites, compared to the equilibrated cluster. For polymorph **I** the cluster has a less spherical shape, compared to the equilibrated cluster. The grown clusters show the difference in growth morphology: polymorph **I** has a final shape as indicated by the thin black lines in the figure and polymorph **II** has a needle shape; it effectively only grew in the needle direction.

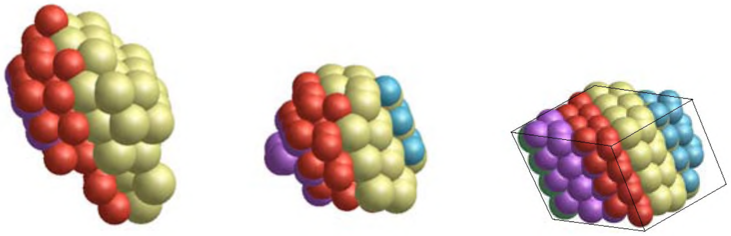

(a) Initial cluster form I (b) Equilibrated cluster form I (c) Grown cluster form I

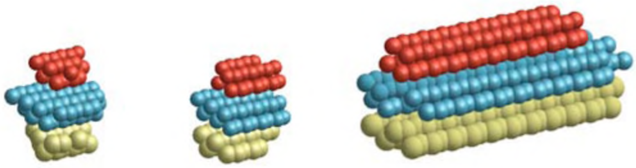

(d) Initial cluster form II (e) Equilibrated form II (f) Grown cluster form II

Figure 5.2: Initial, equilibrated and grown clusters of two polymorphs of the yellow dye. The colors of the GUs are merely added to clearly show the structure in the clusters.

5.5.2 Nucleation of the yellow isoxazolone dye polymorphs

The nucleation results for polymorphs **I** and **II** are shown in Figures 5.3 and 5.4. A clear difference can be observed as the metastable polymorph **II** nucleates at lower $\Delta\mu/kT$ than the stable polymorph **I**. In Figure 5.4, the solid lines, fitted to the Gibbs-Thomson equation 4.5 cross at low values of $\Delta\mu/kT$. This indicates a favored formation of the stable polymorph at lower driving forces. The value at which the extrapolated lines cross lies around $\Delta\mu$=2.5 kT. The values for Γ/kT (see Eq. 4.5), resulting from the fit of the nucleation results, are listed in Table 5.5.

There is a large difference in interfacial energy between the two polymorphic forms, which is caused by the fact that the metastable polymorph **II** has a needle-like morphology. Most of the surface of the needle is composed of crystallographic orientations that have very low interfacial energy, as compared to the orientations at the needle tip. Consequently, a considerably lower Γ/kT value can be realized through the anisotropic shape. In contrast, for the stable polymorph **I**, there is not a particular orientation that has much lower interfacial energy and therefore, its shape is more isotropic and the Γ/kT value higher. Thus the origin of the more favorable nucleation of the metastable phase is its lower surface energy due to its anisotropic shape.

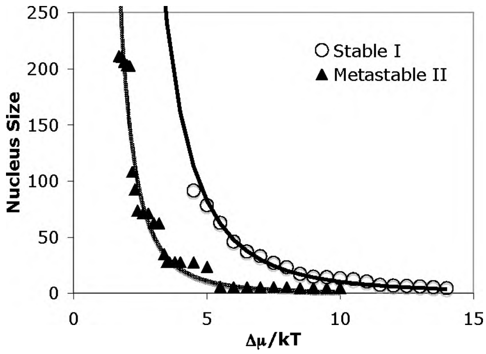

Figure 5.3: Nucleus size (i.e. the size of the critical cluster) for polymorphs **I** and **II** of the isoxazolone dye as a function of driving force $\Delta\mu/kT$. The fitted lines were obtained using the Gibbs-Thomson equation 4.5 with Γ/kT as a fitting parameter.

The needle shape is probably also the cause for the large deviations of the simulation results from the fitted line in Figure 5.3. Forming steps and islands on the side faces of the needle is energetically very unfavorable. The deviations may therefore be a result of statistical fluctuations, but could also be caused by the starting configuration for the simulations, since the size of the side faces is a function of the initial cluster size, making the behavior of the nucleus size with respect to $\Delta\mu/kT$ quite discontinuous.

During the simulation of the stable polymorph **I**, within 10^7 MC steps some simulation runs did not progress beyond certain cluster sizes, which were larger than the initial cluster, but smaller than clusters for which the growth probability was unity (i.e. the condition for successful nucleation and termination of the simulation run). Detailed inspection of these clusters showed that they corresponded to facetted nanocrystallites that did not grow further due to the 2D nucleation barrier on the facets of the crystallites (such a nanocrystallite is displayed in Figure 5.2c). These crystallites represent local minima in the free energy as a function of cluster size, and due to the energetics of the system result in a high 2D nucleation barrier. Simulation runs of clusters that did not grow out to their final size were taken to be successful. This may underestimate the nucleus size as a function of $\Delta\mu/kT$, but, when looking at the results obtained for the stable polymorph of the yellow isoxazolone dye, this does not lead to a major shift in nucleation behavior. If anything, the curves in Figures 5.3 and 5.4 of polymorph **I** would be shifted to higher $\Delta\mu/kT$ values, making the difference between the two polymorphs even greater. This high 2D nucleation barrier for facetted nanocrystallites was not observed for any of the other systems studied.

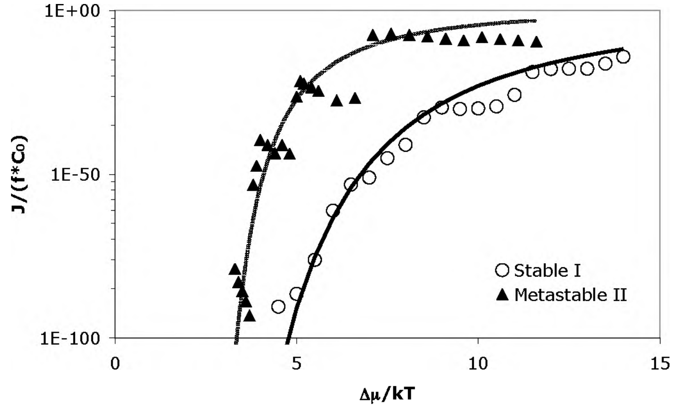

Figure 5.4: Nucleation rates for polymorphs **I** and **II** of the yellow dye. A value for $\Delta\Delta\mu$ of $1.6kT$ was used, shifting the metastable polymorph to higher $\Delta\mu/kT$ values. The extrapolated fit lines cross at around $\Delta\mu/kT$=2.5.

Table 5.5: The values of Γ/kT for both polymorphs of the yellow isoxazolone dye.

Polymorph	Γ/kT
Stable form **I**	32.67
Metastable form **II**	16.76

5.5.3 Nucleation of two polymorphs of paracetamol

Experimentally, the nucleation behavior in solution of paracetamol seems to favor the formation of the stable monoclinic form under all circumstances. The orthorhombic form can be obtained from the melt, and these crystals are used to seed solutions of paracetamol in benzyl alcohol and industrially methylated spirits.[91] The latter solvent was used to obtain laboratory-scale amounts of the orthorhombic form of paracetamol, but the yields were low, about 30%, as the monoclinic form started to crystallize at that point.

Using the same procedure as above, the nucleus size was determined and fitted to the Gibbs-Thomson equation (Figure 5.5). The nucleation rates are shown in Figure 5.6. It can be seen in the Figure, that the nucleation process favors the stable monoclinic form **I** over the metastable orthorhombic form **II**. Interestingly, in the high $\Delta\mu/kT$ region of the Figure, which is displayed in Figure 5.6(b), a clear deviation from the fitted line towards lower nucleation rates for the orthorhombic form can be seen, seemingly leading to non-crossing curves, even at high driving forces. This indicates that the assumption of constant interfacial energy with respect to the nucleus size, as implied in Eq. 4.5, does not hold for nuclei smaller than about 10 molecules. At the same time it also indicates that the classical nucleation theory holds, even down to a nucleus

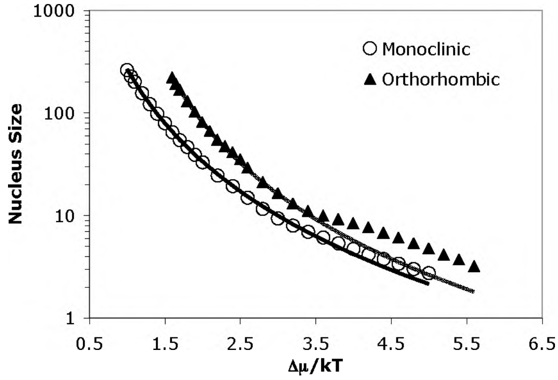

Figure 5.5: The nucleus size for two polymorphs of paracetamol.

Table 5.6: The values of Γ/kT for both polymorphs of paracetamol.

Polymorph	Γ/kT
Monoclinic stable form **I**	9.68
Orthorhombic metastable form **II**	9.95

as small as 10 molecules. This deviation supports the difficulties in preparing orthorhombic paracetamol[91], as it supports the claim that the orthorhombic form has a substantially higher nucleation barrier.

There is no significant difference in the Γ/kT values for both polymorphs (see Table 5.6), which means that the surface energy of the nucleus is not determining which polymorph is formed, but rather the different $\Delta\mu$ values for the two polymorphs. As a consequence, the orthorhombic form will not be formed easily.

5.5.4 Nucleation of the L-glutamic acid polymorphs

The crystallization behavior of L-glutamic acid seems to depend mostly on stirring in the crystallization vessel. When a supersaturated solution is stirred, the metastable α polymorph forms mostly, whereas β forms in stagnant solutions.[96, 97] This behavior is ascribed to the fact that α grows faster, whereas β has the higher nucleation rate. In a stirred solution, α crystals reach the critical size for attrition first, which results in a large number of secondary nuclei being formed, leading to the formation of α L-glutamic acid. In contrast, when the solution is not stirred, secondary nucleation does not take place, and β L-glutamic acid is formed. As the method used in this chapter cannot simulate the effects of attrition, the results are thought to best represent the situation of a stagnant solution. There are also a number of reports that show the solution-mediated solid state transformation of α to β, for instance in [98, 99].

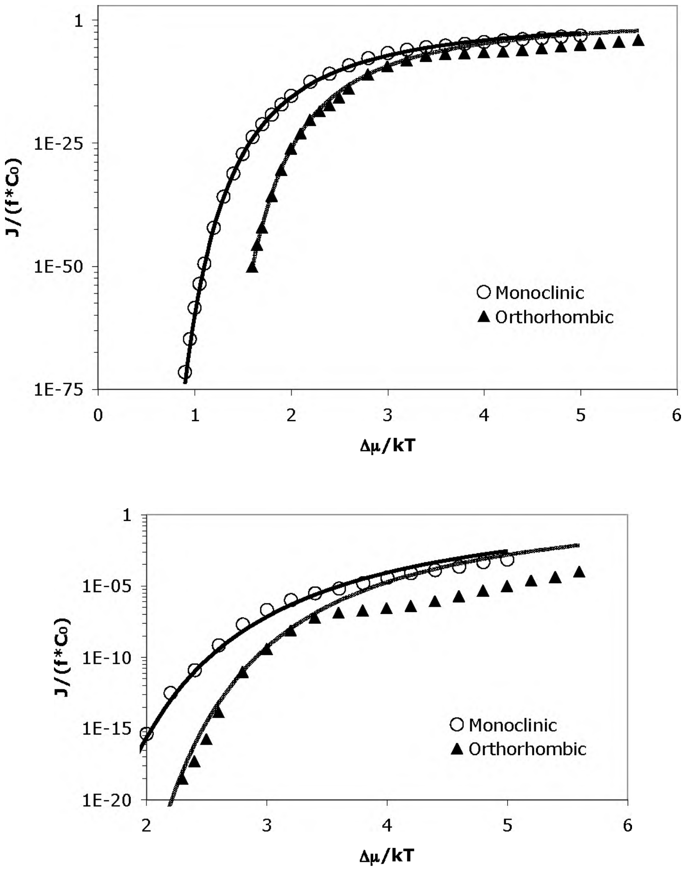

Figure 5.6: The nucleation rates for the two polymorphs of paracetamol. A value for $\Delta\Delta\mu$ of 0.6 kT was used. The second graph shows a clear deviation to lower rates from the fitted line for the orthorhombic form at higher driving forces.

The results of the growth probability method applied to the L-glutamic acid system are shown in Figures 5.7 and 5.8 and it can be seen that, although the nucleus size as a function of $\Delta\mu/kT$ is not very different for the two polymorphs, the nucleation rates indicate that the formation of $\boldsymbol{\beta}$ L-glutamic acid is favored over the formation of the $\boldsymbol{\alpha}$ form. There is no clear difference in the Γ/kT values for both polymorphs (see Table 5.7), again indicating the favorable formation of the stable polymorph directly, due to the difference in $\Delta\mu$.

In a recent paper, Hammond et al. present the results of the calculation of energies of clusters of various sizes of $\boldsymbol{\alpha}$ and $\boldsymbol{\beta}$ L-glutamic acid.[100] Their method comprises of the creation of clusters of various sizes in the shape of the macroscopic crystal, which was predicted using the attachment energy method. Compared to our results, where the $\boldsymbol{\beta}$ form is formed directly, the results of that study are surprising, as they show that minimized clusters of less than 200 molecules and not-minimized clusters of less than 50 molecules of $\boldsymbol{\alpha}$ L-glutamic acid have lower energy than those of $\boldsymbol{\beta}$ L-glutamic acid.[100] It seems reasonable, though, to include the statistical process of attachment and detachment of molecules in the determination of nucleation rates, as is done in the growth probability method. When this process is included, the results are indeed consistent with the direct formation of $\boldsymbol{\beta}$ L-glutamic acid from stagnant solutions.

5.5.5 The role of $\Delta\Delta\mu$ and Γ

The main result of this chapter is that the Γ/kT values can be determined from the simulations and the growth probability method. When the Γ/kT values of two polymorphs are comparable, the discriminating factor between polymorph nucleation rates is largely due to the $\Delta\Delta\mu$ term, as it is in the examples of paracetamol and L-glutamic acid. In other words, the difference in nucleation behavior is in that case not caused by a difference in surface energy, but only due to the difference in bulk chemical potential, $\Delta\Delta\mu$. It has been made clear that the $\Delta\Delta\mu$ term originates from the thermodynamic treatment of the system with two polymorphs forming in the same solution. Practically, the difference in $\Delta\mu$ was approximated by the difference in dissolution enthalpy, which can only be measured using adequate samples of both polymorphs, in which case the simulations might be of reduced value for prediction of favorable conditions under which the polymorphs can be made, since by then, experimental data is available. It has also been shown that the difference in enthalpy of fusion can be used when solution data are not available, which opens up the possibility of using e.g. DSC data to come to an approximate $\Delta\Delta\mu$ value. Using DSC, different polymorphs and their heat of fusion may be obtained from interconversion or from cooling a molten sample, so this can be a situation in which these simulations have more practical value. Unfortunately, forcefields are generally not yet accurate enough to predict $\Delta\Delta\mu$ values or differences in dissolution enthalpy.

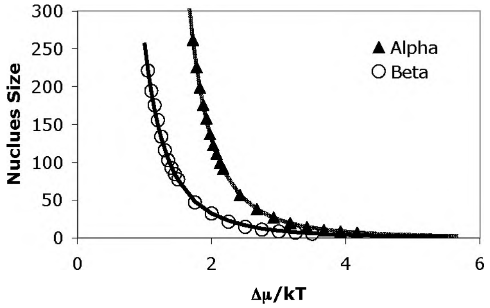

Figure 5.7: The nucleus size for two polymorphs of L-glutamic acid.

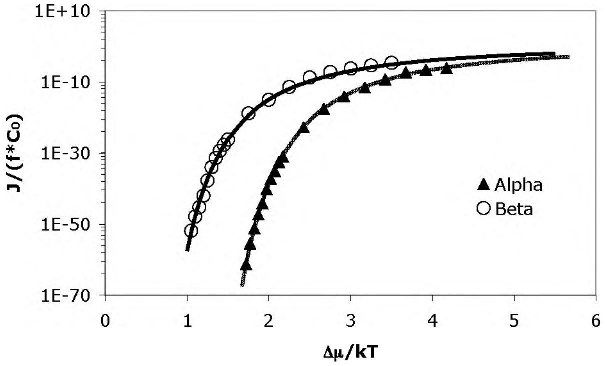

Figure 5.8: The nucleation rates for the two polymorphs of L-glutamic acid. A value for $\Delta\Delta\mu$ of 0.67 kT was used.

Polymorph formation, as studied in this chapter, is thus governed by either a difference in bulk chemical potential, or by a difference in interfacial energy. It is useful to know which parameter is of influence, as differences in interfacial energies between polymorphs can be manipulated advantageously by choosing a solvent carefully. When bulk chemical potential is the dominant factor in polymorph nucleation, other routes towards polymorph selection may be applied. As an example, the case of L-glutamic acid demonstrates that although the nucleation rate of the β form is highest, the higher growth rate of the α form can be used to form that polymorph by ensuring that its nuclei reach their critical size for attrition and hence secondary nucleation first.

Table 5.7: The values of Γ/kT for both polymorphs of L-glutamic acid.

Polymorph	Γ/kT
α metastable form	10.08
β stable form	9.54

5.6 Conclusions

The use of the growth probability method for predicting 3D homogeneous nucleation rates has been highlighted using three examples of experimentally well-characterized organic compounds. In all three cases the experimental crystallization behavior shows results similar to the simulations. In the first case, the metastable form of the yellow isoxazolone dye has a clear kinetic advantage compared to the stable polymorph at higher driving forces, which is in accordance with Ostwald's rule of stages. In this case the kinetic advantage is due to a lower interfacial energy of the nucleus of the metastable polymorph, that more than compensates the difference in bulk chemical potential. The two other cases, of paracetamol and L-glutamic acid, show a behavior that is not consistent with Ostwald's rule, i.e. the stable polymorph is formed directly in favor of the metastable polymorph, both experimentally as well as in the simulations. For these cases the interfacial energies are comparable. The fact that the stable polymorph is formed in spite of the rule of stages, can thus be explained in terms of the crystal structure, the interactions between growth units, driving force for crystallization and the growth behavior of small crystalline clusters, which results in values for the Γ/kT parameter used in the description of nucleation. These parameters all seem to be important in the correct description of the problem; other factors like detailed kinetics of growth unit incorporation and solvent interactions can be neglected for the examples shown.

In the case where the difference in bulk chemical potential determines which polymorph is formed, the solvent interactions may indeed be neglected. In other cases, where the interfacial energy determines polymorph formation, solvents may be employed to modify interfacial energies in such a way that the formation of the desired polymorph can be promoted, or other phenomena, like secondary nucleation, can be used to selectively form the desired polymorphic form.

The method is well-suited to be adopted in the screening of polymorphs and the determination of conditions for preparation of certain polymorphs. As it is known that polymorphs may nucleate concomitantly, the use of the method can help in determining conditions for which this unwanted behavior can be prevented. Also, in the computational prediction of polymorphism, the incorporation of nucleation behavior can give an additional tool to discriminate between the often large set of possible crystal structures.

Chapter 6

Towards rational design of tailor-made additives using growth site statistics

6.1 Introduction

The shape of crystallites is an important property of solid crystalline materials that influences a number of important other properties of the material, for instance dissolution rate, flowing, filtering and drying characteristics, compacting, milling and dust formation.[2] For processing purposes, the desired shape of crystalline particles is isotropic, as this shape has favorable flowing, filtering and drying properties. The shape of crystallites is, however, determined by the conditions during growth and of course by the crystal structure; different polymorphs can lead to very different habits.[33, 101] It is well-known that the crystal habit is a function of the driving force for crystallization, so temperature and concentration profiles during crystallization are parameters that can influence the final crystal habit. In the case of seeding crystallization, the initial shape of the seeds can also play a role in the final shape of the crystallites.[17, 102]

Apart from process parameters, like temperature and concentration, the crystal habit can be influenced using habit modifiers, molecules that selectively inhibit or promote growth of certain crystal faces, thereby changing the shape of the final crystal.[103, 104] A large number of examples are known in which molecules that are structurally similar to the material being crystallized influence the crystal morphology. For instance, a set of additives are reported to influence the growth of benzamide[103], each additive in a different growth direction: benzoic acid blocks growth of benzamide in the **b**-axis direction, and *p*- and *o*-toluamide block growth in the **a**-axis and the **c**-axis direction, respectively. Another example is the influence of biuret, i.e. $NH_2C(=O)NHC(=O)NH_2$, the dimer byproduct of urea synthesis, on the growth of urea ($NH_2C(=O)NH_2$). Biuret has been found to have a dramatic influence on the growth rate of the

(001) face, but does not influence the growth rate of the (110) face, making the habit of urea much less needle-like. A twofold explanation was given by Davey et al.[105], where firstly the fewer hydrogen-bonding possibilities towards adsorbed biuret on the (001) face led to less adsorption of urea on this face. Secondly, as the (001) face grows by a spiral growth mechanism, growth was completely stopped when the average separation of the biuret impurities was of the order of the critical curvature of the spiral.

As a final example, the selective adsorption of chiral molecules onto specific faces of centrosymmetric crystals has been used to directly assign the absolute configuration of these molecules. An example of this method was given by Weissbuch et al., where R- or S-threonine was adsorbed at a racemic crystal of (R,S)-serine.[106] The extra methylgroup present in the enantiomerically resolved threonine blocks either the (011) and $(01\bar{1})$ faces when using R-threonine, or the $(0\bar{1}1)$ and $(0\bar{1}\bar{1})$ faces when using S-threonine, thus enabling the absolute assignment of the configuration of the threonine molecules.

In the case where the intentional addition of these habit modifiers achieves the goal of improving product quality, one can speak of tailor-made additives[103], i.e. additives for crystallization that have been optimized to influence crystal growth in a well-defined way. Often, these tailor-made additives are largely isostructural with the molecule that crystallizes, only to replace a specific favorable interaction with a disruptive group, for instance replacing a favorable N-H $\cdots$ O by a repulsive O $\cdots$ O interaction, or by introducing a bulky substituent that blocks the addition of more growth units to a certain face. Benzoic acid on benzamide is an example of the former case; *p*- and *o*-toluamide on benzamide of the latter.

The large volume of literature reporting on tailor-made additives[107] almost exclusively treats the chemical similarity between flat surfaces (hkl) in contact with the tailor made additives. It is, however, well-known that layer-by-layer growth does not take place at flat surfaces directly, but by first creating a two-dimensional nucleus on the flat surface. When such a nucleus is large enough, it will grow out by attachment of growth units to the edges of the nucleus. This means that the impurities or habit modifiers will adsorb at the step configurations that make up the edge of the growing island, thus retarding the advancement of the step on the surface. The same applies for spiral growth and step flow growth, having a permanent source of steps. Moreover, in the case of strongly anisotropic morphologies, like needles and thin platelets, the shape of the crystal is not only determined by slow growing faces. For instance in the case of needles, the fast growing top faces often are far from being flat. These rough faces show a lot of steps and kinks. Rather than selecting additives on their binding properties to flat surfaces, it would be better to first identify the most important binding sites during growth.

In this chapter a new theoretical approach and method to identify the configurations and statistics of such growth site configurations from detailed Monte Carlo simulations is presented. This is done by monitoring the creation and annihilation of growth sites as a result of the attachment and detachment of growth units. As all possible growth site configurations are used, both surface-bound and step-bound growth sites are taken into account, as well as other configurations, for instance kinks. This then allows for the identification of a set of growth site configurations that are important during growth on a certain orientation (*hkl*), and by comparison with similar simulations on other orientations the relative importance and selectivity of growth site configurations can be quantified. The outcome is an ensemble of growth site configurations that can form the basis for the design of new tailor-made additives using molecular design methods, e.g. by docking techniques. The latter is not treated here.

The method is applied to an anisotropic Kossel crystal as a model system and to aspartame II-A as an example of a real crystal for which the morphology imposes problems during downstream processing, in an effort to identify growth site configurations that can be blocked to change the extreme needle morphology of this compound.

6.2 Growth site theory

In the Monte Carlo crystal growth simulations, the crystal is represented by a lattice periodic model called the crystal graph, in which the graph vertices represent growth units, and the graph edges represent pairwise interactions between growth units.[19] The crystal surface, on which growth takes place, is then an arbitrary cut through the crystal graph with an (average) orientation (*hkl*).

A growth site is an unoccupied site on the crystal surface. According to the definition of the crystal graph, it has a number of neighbors an attaching growth unit can connect to. These neighboring growth units can be either present or absent, and as each growth unit has a specific number of bonds/neighbors, the total number of possible growth site configurations is 2^M with M the number of neighbors of that growth unit. Configurations are labeled with a binary number, indicating the number of neighbors present. For instance, if, according to the crystal graph, the growth site is surrounded by neighbors 1, 2 and 5 out of 8 possible neighbors, the binary representation of this configuration is '00010011', or, when expressed as a decimal number, 19. All possible growth site configurations include the configuration with no neighbors, i.e. configuration 0 (zero), which is a site in the bulk parent phase, and the configuration where all neighbors are present, an inclusion in the bulk of the crystal, which is configuration $2^M - 1$. It is important to note that the site with configuration 0 (a site in the parent phase) is not a growth site, i.e. growth only takes place *at* the crystalline surface, obeying a solid-to-solid growth condition. Growth on an inclusion site ($2^M - 1$), however, is allowed. As the growth site label only depends on which neighbors surround it, the label does not depend on the crystalline orientation (*hkl*) being simulated.

6.2.1 The site- and collateral effect

During crystal growth simulations a growth unit may attach to the surface, or detach from the surface. These processes are governed by the Monte Carlo attachment and detachment probabilities. When a growth unit attaches itself to the surface at a growth site with configuration p, a number of processes happen: firstly, the number of growth sites with configuration p (X_p) is reduced by one. Secondly, all its neighboring sites will also change their configuration, due to the attachment of the growth unit. The first process is called the 'site effect', the second process the 'collateral effect'. Thus the overall change in number of growth sites with configuration i is given by:

$$\Delta X_i = \Delta_s X_i + \Delta_c X_i \qquad \forall\, i = 0 \ldots 2^M - 1 \tag{6.1}$$

where ΔX_i is the overall change in the number of growth sites with configuration i, $\Delta_s X_i$ its site contribution due to attachment of a growth unit of configuration i and $\Delta_c X_i$ the change due to the collateral effect.

The site effect for all configurations i due to an attachment or detachment at a configuration p is given by:

$$\Delta_s X_i = \pm\delta_{ip} \tag{6.2}$$

where δ_{ip} is the Kronecker delta. Upon attachment of a growth unit at a site with configuration p, $\Delta_s X_p = -1$. When a growth unit detaches from that site, $\Delta_s X_p = +1$. $\Delta_s X_i = 0$ for all configurations other than p.

The collateral effect takes place when, due to a neighboring growth unit's attachment, a growth site changes configuration from q to r. The collateral effects are given by:

$$\Delta_c X_i = \pm(\delta_{ir} - \delta_{iq}) \tag{6.3}$$

Upon attachment $\Delta_c X_i = +(\delta_{ir} - \delta_{iq})$ and upon detachment $\Delta_c X_i = -(\delta_{ir} - \delta_{iq})$.

For sites with configuration 0 (zero) there is only a collateral effect, when due to growth of a growth unit at a growth site with configuration $p > 0$, a neighboring site with configuration $q = 0$ is changed to a growth site with configuration $r > 0$. In this way, new growth sites are introduced in the system. Growth sites are removed from the system when a growth unit attaches itself on a growth site, or when a growth unit is etched in such a way that a neighboring growth site changes its configuration from $r > 0$ to $q = 0$ as a collateral result. As growth site configurations always change from q to r or vice versa, the sum of all collateral effects will be zero for each event:

$$\sum_{i=0}^{2^M-1} \Delta_c X_i = 0 \tag{6.4}$$

After N events of either attachment or detachment, the total change in site configurations is given by

$$\Delta X_i(N) = \Delta_s X_i(N) + \Delta_c X_i(N) \qquad \forall\, i = 0 \ldots 2^M - 1 \tag{6.5}$$

6.2.2 Steady state situations

For a steady state situation, the average number of growth sites with configuration i for $i = 1 \ldots 2^M - 1$ does not change for a simulation run over a large enough number of events, i.e.:

$$\lim_{N \to \infty} \langle \Delta X_i(N) \rangle = 0 \qquad \forall\, i = 1 \ldots 2^M - 1 \tag{6.6}$$

This implies that, when using Eq. 6.5, for large enough N and omitting the limit for brevity,

$$\langle \Delta_s X_i(N) \rangle = -\langle \Delta_c X_i(N) \rangle \qquad \forall\, i = 1 \ldots 2^M - 1 \tag{6.7}$$

which, in turn, implies

$$\left\langle \sum_{i=1}^{2^M-1} \Delta_s X_i \right\rangle = -\left\langle \sum_{i=1}^{2^M-1} \Delta_c X_i \right\rangle . \tag{6.8}$$

As from Eq. 6.4 it follows that

$$\sum_{i=1}^{2^M-1} \Delta_c X_i = -\Delta_c X_0, \tag{6.9}$$

we can write

$$\left\langle \sum_{i=1}^{2^M-1} \Delta_s X_i \right\rangle = \Delta_c X_0, \tag{6.10}$$

which simply means that the average number of growth sites converted to etch sites is equal to the number of newly introduced growth sites in the system, when a steady state has been reached.

6.2.3 Flow

The collateral effect can also be thought of as a flow process, where, due to the attachment of a growth unit, neighboring growth sites flow from their original configuration q to a new configuration r. Not all changes of configuration q to r are possible, all possible pathways are defined from the crystal graph connectivity. We can now define a flow f_{qr} that connects two configurations:

$$f_{qr} = \begin{cases} 1 & \text{for the transition } q \longrightarrow r \\ 0 & \text{if there is no transition} \\ -1 & \text{for the transition } q \longleftarrow r \end{cases} \qquad \text{with } q < r \tag{6.11}$$

The total flow after N events is given by $f_{qr}(N) = \sum_{n=1}^{N} f_{qr,n}$ and, due to the nature of the flow, the total sum of the collateral change can also be computed from the net flow, i.e. the difference between the sum of flows leading to i and the sum of flows leading from i:

$$\Delta_c X_i(N) = \sum_{j=1}^{i-1} f_{ji}(N) - \sum_{j=i+1}^{2^M-1} f_{ij}(N) \tag{6.12}$$

6.2.4 Contribution of a growth site configuration to the growth process

It is clear that during a simulation on a surface (hkl), some growth site configurations will have a relatively high probability of being formed, due to the crystallographic structure and interaction energies as described by the crystal graph. To quantify the relative importance of a growth site with configuration k in the growth process of a surface (hkl), a contribution value is computed by comparing the 'normal' situation to a situation where that growth site configuration k is excluded from the growth process. To exclude k, $\Delta_s X_k$ is set to zero and the outgoing flows f_{kr} are removed. Removing these flows f_{kr} has the effect that all growth site configurations r that can be formed by a collateral effect originating at k will be formed less often. Defining the sum S_r of all collateral changes leading to r as

$$S_r = \sum_{j=1}^{r-1} f_{jr}(N), \tag{6.13}$$

upon exclusion of k the sum changes from S_r to $S'_{k,r}$:

$$S'_{k,r} = S_r - f_{kr}. \tag{6.14}$$

In case f_{kr} is largely responsible for the formation of r by the collateral effect, the change in the sum will be high. The new value of the site effect $\Delta_s X_i(N)$ when the growth configuration k is excluded is denoted as $\Delta_{s,e} X_{k,i}(N)$ and is defined as:

$$\Delta_{s,e} X_{k,i}(N) = \Delta_s X_i(N) \frac{S'_{k,i}}{S_i}. \tag{6.15}$$

The contribution value of the growth site with configuration k is now defined as:

$$C_k = \frac{\sum_{i=1}^{2^M-1} \Delta_s X_i(N) - \sum_{i=1}^{2^M-1} \Delta_{s,e} X_{k,i}(N)}{\sum_{i=1}^{2^M-1} \Delta_s X_i(N)}. \tag{6.16}$$

When $\sum_{i=1}^{2^M-1} \Delta_s X_i(N)$ is equal to $\sum_{i=1}^{2^M-1} \Delta_{s,e} X_{k,i}(N)$, the exclusion has no effect and the contribution will be zero. In the limiting case that the configuration k is exclusively responsible for the growth, $\sum_{i=1}^{2^M-1} \Delta_{s,e} X_{k,i}(N) = 0$ and the contribution C_k will be unity.

The sum of all contributions is then given by

$$0 \leq \sum_{i=1}^{2^M-1} C_i \leq 2^M - 1. \tag{6.17}$$

When the sum of all contributions is low with respect to $2^M - 1$, the growth process is selective, i.e. it makes use of only a few energetically favorable growth configurations. When the total contribution is high, a large number of growth site configurations take part in the growth process.

6.2.5 Towards rational design of new tailor-made additives

The contribution value can be computed for each growth site configuration. Its value depends on the face (hkl) for which a simulation has been run. As each individual contribution value is between 0 and 1, the contributions can be compared directly. Two things can be learned from this comparison. First of all, which growth site configurations are important for which faces, and more importantly, whether certain growth sites are specifically used in the growth process of a certain face. This then enables the use of the contribution value as a quantitative parameter for the design of new tailor-made additives when a set of growth site configurations can be selected that is both important in the growth process on one face, but when blocked by a well-designed additive, will have a limited effect on the growth process of other faces.

6.3 Application to an anisotropic Kossel model

The simplest of crystal growth models, the Kossel model, is too simple to illustrate the different aspects of the growth site theory and its applications. Due to the high symmetry of the Kossel model (space group P$m\bar{3}m$), the structure has only one flat face crystallographic form, $\{001\}$. Therefore, no difference in contribution value will be determined.

Because of the fact that the Kossel model is too simple, a more complex model has to be used.[108] To illustrate the different parameters of the growth site theory (see Section 6.2), an *anisotropic* Kossel model is used, which was also used earlier for fundamental crystal growth studies.[25, 26, 48] The graph of this model, having spacegroup P$mm2$, is displayed in Figure 6.1, and consists of two growth units, 1 and 2, and three different bonds, ϕ_a, ϕ_p and ϕ_q. The bond strengths are defined as:

$$\begin{aligned} \phi_p &= \frac{\delta 2\phi_a}{1+\delta} \\ \phi_q &= \frac{2\phi_a}{1+\delta} \end{aligned} \tag{6.18}$$

where δ is the anisotropy parameter, defined through $\phi_p{=}\delta\phi_q$. When $\delta = 1$, all the bonds are equal to ϕ_a.

The anisotropic Kossel model has three forms that are F-faces, $\{001\}$, $\{011\}$ and $\{100\}$, for which the contribution values and site- and collateral effect values were determined from Monte Carlo simulations. In the following, only the surface adatoms and f-step adatoms[68], which are oriented along a periodic bond chain, are considered. Although the theory and the software routines take all configurations into account, studying steps in other directions and kink sites in detail would confound this example, for which the objective is to show the trends calculated using the growth site theory match the trends expected, based upon the calculation of f-step-, slice and attachment energies.

6.3.1 Simulation details

Monte Carlo simulations were performed using the MONTY crystal growth simulation program[9], expanded with routines that monitor the creation and annihilation of growth sites. The probabilities used for these simulations are called “random rain”, which means that the growth probability is determined by the driving force $\Delta\mu/kT$, and the etch probability is determined by the strength with which growth units are bound to the surface. This probability scheme has been shown to give good results for the simulation of crystal growth from solution.[21]

On all F-face orientations a set of 7 Monte Carlo growth simulation runs were performed for $\Delta\mu/kT$ values between 0.25 and 5.0 and for δ=0.2 to 1.0.

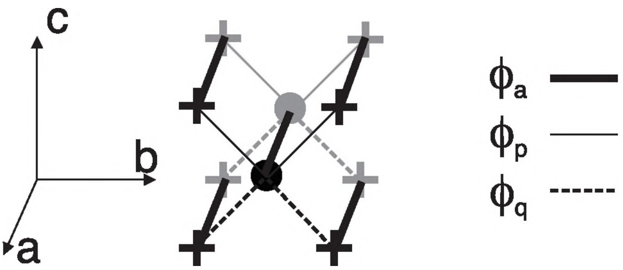

Figure 6.1: The crystal graph of the anisotropic Kossel model. There are two growth units, A and B, which have three different bonds, ϕ_a, ϕ_p and ϕ_q, defined as ϕ_a=(ϕ_p+ϕ_q)/2 and ϕ_p = $\delta\phi_q$, with δ the anisotropy parameter.

The bond strength ϕ_a was set to $2kT$. The simulation surface size was set to 50x50 unit cells and the length of the simulation was 10^7 events with 10^5 initial relaxation events. The crystal growth mechanism used was 2D nucleation in all cases. At each $\Delta\mu/kT$-value and for each orientation the final contribution values for all configurations were averaged over the 7 simulation runs. The resulting data set is quite substantial, therefore, the results are only discussed here for the {001} orientation. The results for the {100} and {011} orientations can be found in the Appendix.

6.3.2 Anisotropic Kossel (001) orientation

The (001) orientation is a special orientation, that behaves as an S-face at $\delta = 1.0$, due to symmetry roughening.[48] At $\delta < 1.0$, the symmetry-roughening effect is lost, but some step energies are still much lower than expected based on the attachment energy. The (001) orientation has two connected nets. At $\delta < 1.0$, there is one weaker net in which the ϕ_p bonds are the connected net slice bonds and the ϕ_q bonds are the connected net attachment bonds. The second, stronger, connected net has the ϕ_q bonds as the connected net slice bonds and the ϕ_p bonds as the connected net attachment bonds. At $\delta < 1.0$, the second connected net, having the ϕ_q slice bonds, is expected to dominate the surface configuration during growth.

The two connected nets both have a single "surface adatom" growth unit configuration, displayed in Figure 6.2. At lower $\Delta\mu/kT$ their contribution values are very different (see Figure 6.3), and as δ becomes larger, the difference becomes smaller. This is in line with expectations, as the difference in the stability of the connected nets becomes smaller at larger δ values.

On the (001) surface there are two f-step directions, <100> and <010>, that are oriented along a periodic bond chain. In total, there are six different f-step adatom growth site configurations for the (001) orientation, labeled A-F, which are shown in Figure 6.4. These six adatom configurations can be paired to form three types of configurations: A and B, C and D and E and F. The <100> step

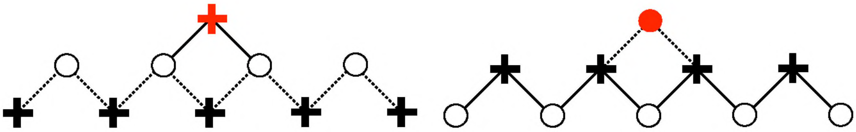

(a) Configuration A (b) Configuration B

Figure 6.2: [100]-projections of the anisotropic Kossel crystal graph showing the two adatom configurations of the (001) orientation. The grey growth units represent a growth site, both having two bonds to bind to the surface. The remaining four broken bonds of the growth site are not drawn.

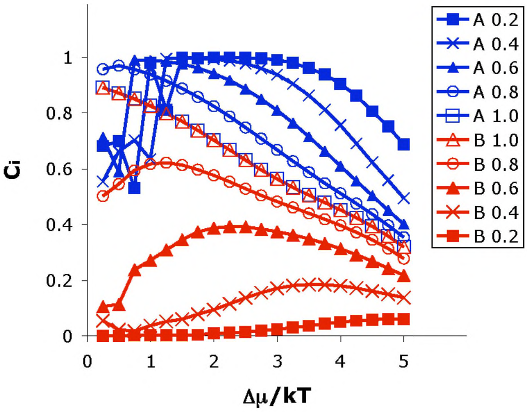

Figure 6.3: The anisotropic Kossel (001) contribution values of the surface adatoms as a function of $\Delta\mu/kT$ for different δ values. The configurations labels A and B correspond to the configurations in Figure 6.2. The "noise" at low $\Delta\mu/kT$ (mainly for the A configurations) is due to the fact that no net growth takes place at these driving forces.

has configurations C and D, whereas the <010> step has configurations A, B, E and F. Looking at the contribution values as a function of $\Delta\mu/kT$ for different δ (see Figure 6.5), the <100> step is clearly more important than the <010> step, which is logical as the <100> step energy is lower due to symmetry weakening. Also, at low δ, the steps on the weaker connected net (configurations A and F) have lower contribution than the configurations on the stronger connected net (configurations B and E).

6.3.3 Comparison of surface and step growth site configurations

In the introduction the claim was made that growth takes place predominantly at step edges, as opposed to on flat surfaces, which implies that the adsorption of tailor-made additives should be studied at step edges, as well as on flat

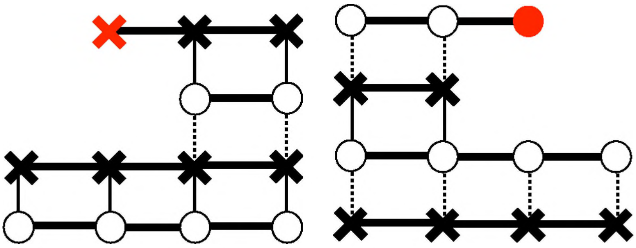

(a) <010> configuration A

(b) <010> configuration B

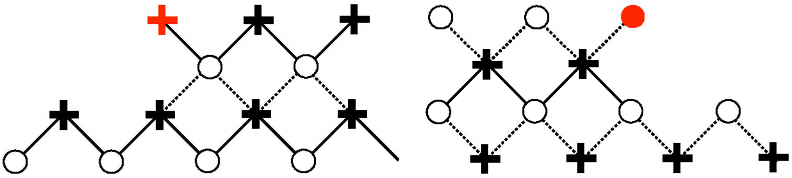

(c) <100> configuration C

(d) <100> configuration D

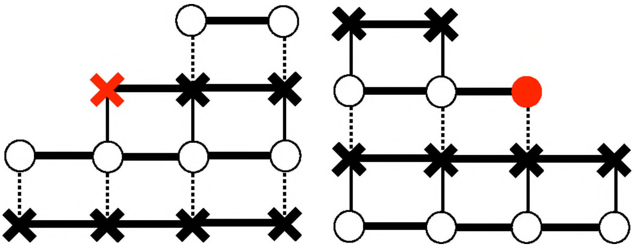

(e) <010> configuration E

(f) <010> configuration F

Figure 6.4: Side views of examples of the six different growth site configurations for the adatoms at the <010> and <100> f-steps on the (001) orientation of the anisotropic Kossel model. Each of these growth site configurations has a single symmetry related growth site configuration (not shown) as a result of mirror symmetry.

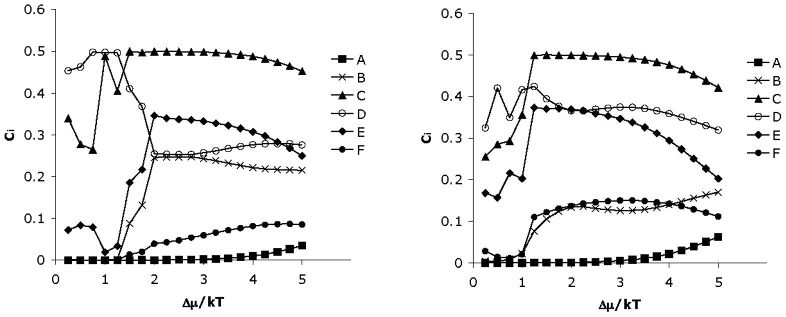

(a) $\delta = 0.2$ (b) $\delta = 0.4$

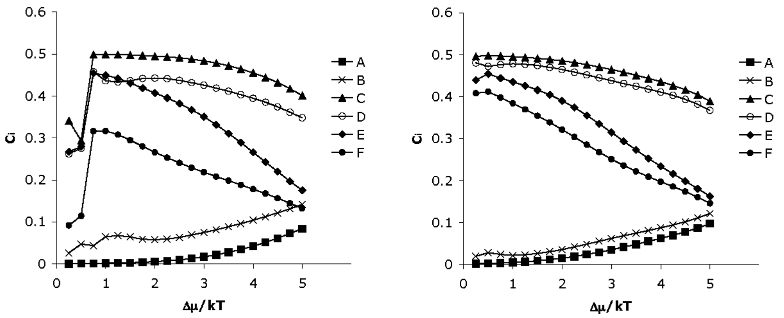

(c) $\delta = 0.6$ (d) $\delta = 0.8$

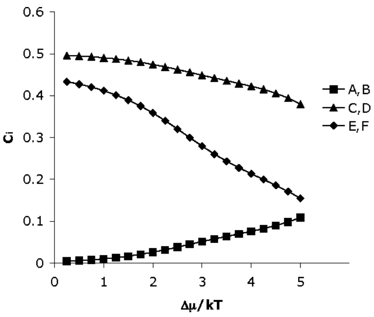

(e) $\delta = 1.0$

Figure 6.5: The (001) contribution values of the step adatoms as a function of $\Delta\mu/kT$ for different δ values. The configurations labels A-F correspond to the configurations in Figure 6.4.

surfaces. Using the results obtained in the previous sections, this claim can now be quantified for each orientation of the anisotropic Kossel model. To do so, the sum of the contribution of all growth site configurations are plotted in Figure 6.6 as a function of $\Delta\mu/kT$ and δ, both for the surface sites and the step adatom sites.

As can be seen from the Figure, the total contribution of the step-bound growth site configurations is either higher or equal to that of the surface-bound growth site configurations. Although the individual step growth site configurations generally have a lower contribution than the surface growth site configurations, the number of step growth site configurations is higher, leading to a higher overall contribution to the growth process.

6.4 Application to Aspartame II-A

Aspartame is the methylester of the dipeptide of L-phenylalanine and L-aspartic acid, and is used worldwide as an artificial sweetener, as it is about 200 times as sweet as sugar. The II-A phase of aspartame has a very thin needle-like morphology and the crystal structure, as determined by Hatada *et al.*, has spacegroup $P4_1$, with $Z = 4$, $\mathbf{a} = \mathbf{b} = 17.69$ Å and $\mathbf{c} = 4.92$ Å.[71] As a result of detailed investigations, the habit of aspartame could be explained from the fact that the side faces of the needle ($\{110\}$) have a much higher 2D nucleation barrier than the top faces; both from Monte Carlo simulations[30, 109] and from detailed investigations of the stepenergies[49], it was found that the difference in growth rate as a function of $\Delta\mu/kT$ between the $\{201\}$ and $\{\bar{1}2\bar{1}\}$ top faces and the $\{110\}$ side faces is very large, thus explaining the extreme needle morphology.

6.4.1 Crystal structure and crystal graph

The crystal structure of aspartame II-A contains two water molecules per unit cell. It has been found, however, that these water molecules do not play a major stabilizing role in the crystal structure, and could be omitted in the calculation of the crystal graph.[30] Four unit cells of the crystal structure without water are shown in Figure 6.7; the fourfold axis is perpendicular to the plane of the paper. The crystal graph bonds were scaled with respect to the dissolution enthalpy in water ($\Delta_{diss}H = 8.38$ kcal·mol^{-1}), and the resulting crystal graph bonds are listed in Table 6.1. Each of the four growth units has 8 different bonds, which in total gives $4 \cdot 2^8 = 1024$ possible configurations.

6.4.2 Aspartame contribution values

Experimentally, the needle tips of aspartame are not faceted, but rounded, indicating a rough growth mode. From the earlier Monte Carlo simulations it was found that the $\{201\}$ and $\{\bar{1}2\bar{1}\}$ top faces grow slowest compared to all other top faces. To be able to study the contribution value difference between the

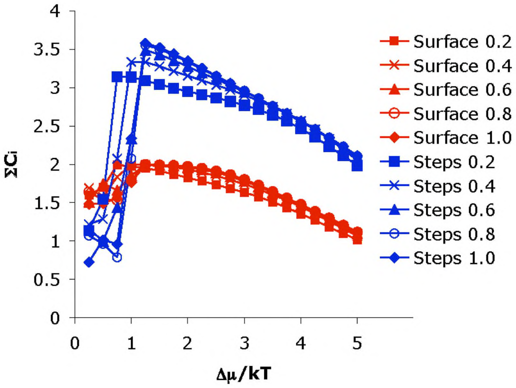

(a) (100) orientation

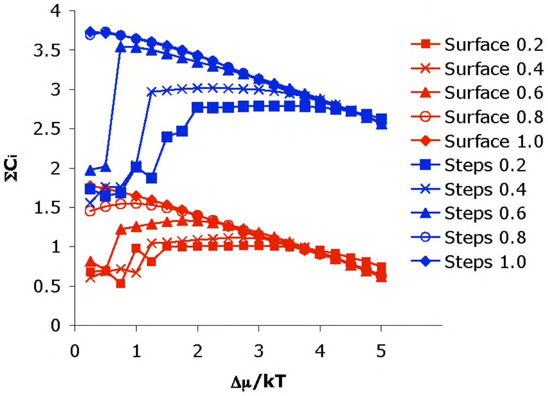

(b) (001) orientation

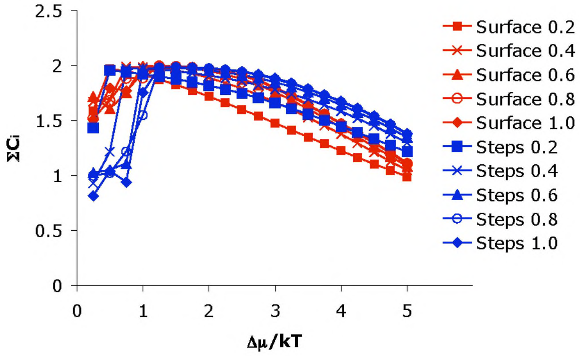

(c) (011) orientation

Figure 6.6: Summed contributions of the surface and step growth site configurations for various δ-values for the three F-faces of the anisotropic Kossel model.

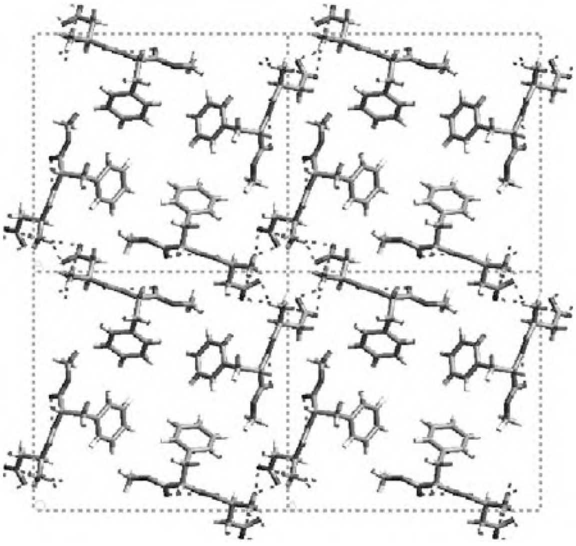

Figure 6.7: Four unit cells of the crystal structure of aspartame, viewed along the c-axis.

Table 6.1: Bonds used in the crystal graph of aspartame II-A after scaling to the enthalpy of dissolution in water. Symmetry-related bonds are not listed.

Bond	Energy [kcal·mol^{-1}]
$1^{[000]}$ - $3^{[01\bar{1}]}$	-2.68
$1^{[000]}$ - $1^{[00\bar{1}]}$	-2.40
$1^{[000]}$ - $3^{[00\bar{1}]}$	-1.72
$1^{[000]}$ - $2^{[01\bar{1}]}$	-1.59

top faces and the side faces, the contribution differences of the top orientations $\{201\}$ and $\{\bar{1}2\bar{1}\}$ taken togeter as one set ('top') and the side orientations $\{110\}$ as another set ('side') were determined. Due to symmetry, this implies that four side faces and eight top faces are considered. The general expression for the contribution value difference of two such sets $\{x\}$ and $\{y\}$ is

$$\Delta_{[(h_1k_1l_1)..(h_mk_ml_m)],[(h_{m+1}k_{m+1}l_{m+1})..(h_nk_nl_n)]}C_i = \frac{1}{m}\sum_{x=1}^{m} C_{i(h_xk_xl_x)} - \frac{1}{n-m}\sum_{y=m+1}^{n} C_{i(h_yk_yl_y)}. \tag{6.19}$$

Note that there is no symmetry in the labeling of growth site configurations, which means that symmetrically related growth site configurations have different labels. As simulations are only performed for one orientation of a crystallographic form, this means that the results of this single simulation do not treat all symmetry-related growth site configurations equally. Using symmetry operators, a list of symmetry-related growth site configurations was created for the symmetry-related faces that were not simulated. Thus a complete list of orientations and their respective growth site configuration contributions could be made and used to calculate $\Delta_{[top],[side]}C_i$ for the simulates top and side faces.

In Figure 6.8, $\Delta_{[top],[side]}C_i$ is plotted for descending values of $\Delta_{[top],[side]}C_i$. It can be seen that there are quite a number of differences, both positive and negative. The total number of configurations with $|\Delta_{[top],[side]}C_i| > 0.05$ is 124, which means that the majority of configurations (about 900 out of 1023) have a comparable contribution on the top faces, as compared to the side faces.

6.4.3 Statistics of configurations

The configurations with $|\Delta_{[top],[side]}C_i| > 0.05$ have some interesting features, with respect to the frequency of the individual bonds being used. To quantify this, three sets of $\Delta_{[top],[side]}C_i$-values were made: the first set with $\Delta_{[top],[side]}C_i > 0.05$ (left part of the graph in Figure 6.8), the second set with $\Delta_{[top],[side]}C_i < -0.05$ (right part of the graph in Figure 6.8) and a 'control' set with values of $-0.05 < \Delta_{[top],[side]}C_i < 0.05$. The weighed (with the $\Delta_{[top],[side]}C_i$-value) frequencies of the eight bonds involved are plotted in Figure 6.9. As can be seen from the Figure, there is a difference between the two extremes ($\Delta_{[top],[side]}C_i < -0.05$ and $\Delta_{[top],[side]}C_i > 0.05$) and the middle part of the graph in Figure 6.8. The two extremes display a clear trend in two bonds being more important than the other bonds, whereas for the configurations in the middle, there is no such trend: all bonds are being used as frequently as the others. A first attempt at the design of tailor-made additives that block the top-faces from growing would be to look for additives that bind to configurations having these high-frequency bonds and that have sterical or electrostatic blocking substituents at other sites in the molecule.

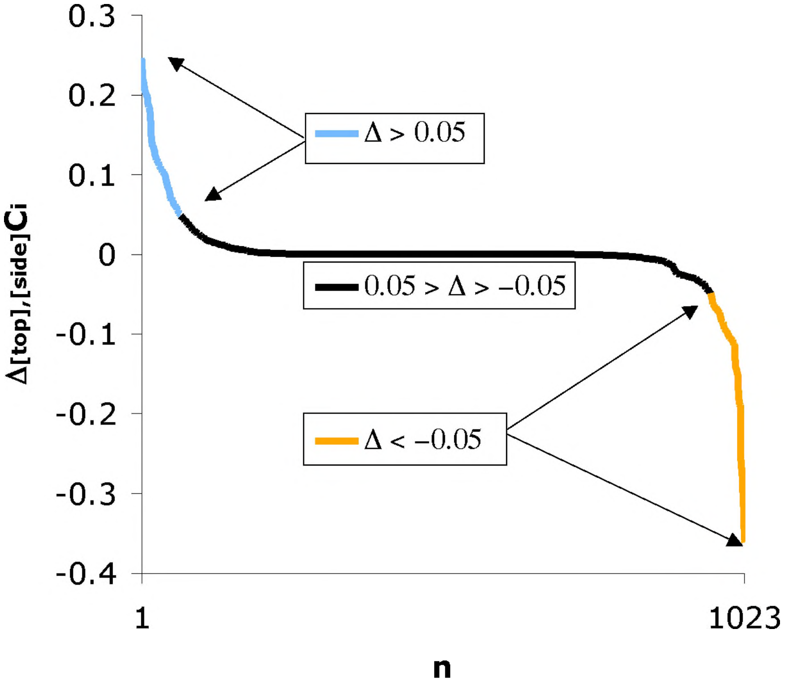

Figure 6.8: $\Delta_{[top],[side]}C_i$ plotted in descending values at $\Delta\mu/kT$=1.5. i is the configuration number between 1 and 1023; the n-values differ from the index i as a result of the rearrangement to descending $\Delta_{[top],[side]}C_i$-values.

6.4.4 Exclusion of important configurations

For aspartame phase II-A the important configurations of the side faces and the top faces have been identified (see Figure 6.8). To see the effect of excluding these configurations in a MONTY simulation, two sets of simulations were performed, one in which the growth probability of the configurations with $\Delta_{[top],[side]}C_i > 0.05$ were set to zero and another where the growth probability of the configurations with $\Delta_{[top],[side]} < -0.05$ were set to zero. The results of these simulations, and the comparison to a situation in which no configurations are excluded from the growth process are shown in Figure 6.10.

In Figures 6.10(a) and 6.10(c) it can be clearly seen that the exclusion of configurations having $\Delta_{[top],[side]}C_i < -0.05$, i.e. where the configuration contribution is high on the side faces compared to the top faces, has a large impact on the growth rates of the side faces. The 2D nucleation barrier is increased, which means that growth starts to take place only at higher driving force, and when growth takes place, the growth rate is much lower compared to a situation where no configurations are excluded. The impact of the exclusion on the top faces, however, is much smaller (Figure 6.10(c)). The growth rates are lowered somewhat for the top faces, but to a much lesser degree as the side faces.

Interestingly, exclusion of the configurations having $\Delta_{[top],[side]}C_i > 0.05$ has no significant effect on the growth rates of either the side or the top faces (see Figures 6.10(b) and 6.10(d)). Although these configurations have a higher contribution on the top faces, the fact that these top faces show rough growth means that when certain configurations are excluded, the growth process will apparently find other pathways to grow, without being slowed down. This interesting result means that the method proposed in this chapter should work best when faces that should be blocked are flat, i.e. show layer-by-layer growth instead of rough growth. Such a general rule was already proposed by Berkovitch-Yellin et al.[103]

6.5 Conclusions

From Monte Carlo crystal growth simulations on specific crystal orientations (hkl), the statistics of formation and annihilation of growth sites and their configurations can be obtained for that orientation. Using the growth site statistics, as outlined in this chapter, the contribution of each growth site configuration to the growth process can be quantified for all orientations. The ensemble of configuration contributions that is thus obtained can be used as a starting point for the rational design of effective tailor-made additives. By choosing configurations that have a large difference in contribution value for different orientations, the effect of the tailor-made additives can be targeted to specific orientations while other orientations remain unaffected.

Because the Monte Carlo simulations allow for the determination of the contribution as a function of $\Delta\mu/kT$, this dependency will allow for a proper choice of driving force, at which the blocking effect and selectivity of tailor-made additives are optimal.

The growth site theory was applied to two systems, an anisotropic Kossel model and a ‘real’ crystal, aspartame phase II-A. The anisotropic Kossel model was used to test the theory and related software routines, as the trends for the dependence on $\Delta\mu/kT$ and the anisotropy can be understood without great difficulty. To that end the contribution values were determined at different anisotropy values as a function of $\Delta\mu/kT$. Two clear trends could be distinguished: the dependence on $\Delta\mu/kT$ shows that as $\Delta\mu/kT$ increases, more and more growth site configurations are involved in the process, which indicates a rougher growth mode, leading to a smaller difference in contribution values of different site configurations. The dependence on δ shows that as the anisotropy increases, the system tends to use more and more the surface and step configurations that are becoming energetically more favorable. Both trends are in line with expectations for this system and show the validity of the method.

The comparison of the total contribution value of surface adatom growth site configurations vs. f-step adatom growth site configurations shows that the surface adatoms are important in the growth process, but that the contribution of the f-step adatom growth site configurations have a higher or equal overall contribution to the growth process. In this specific example we have not taken growth site configurations for step orientations that are not along a PBC direction (i.e. steps that are not f-steps) and kinks into account. The result, however, offers already a further justification for looking beyond surface adatom configurations for the design of tailor-made additives.

In this chapter, only 2D nucleation was considered as growth mechanism. In other growth mechanisms, like spiral growth or step flow, steps will have an even more important role. In spiral growth, addition of growth units takes place at the steps forming the spiral arms. In step flow, as growth units are added to the step front, the steps move over the growing surface. As both growth mechanisms have a permanent step source, it is expected that the contribution of step growth site configurations will be even higher, as compared to the contributions found for 2D nucleation.

For aspartame II-A it was found that certain growth site configurations have a higher contribution on the top faces, as compared to the side faces of the aspartame needles, and vice versa for other growth site configurations. These specific configurations were then found to also have some bonds that are present more often than the configurations without great top-side differences. This is an indication that there is a difference in the contribution of the growth sites that are involved in the growth process in the direction of the needle and growth sites that are involved in growth in the direction perpendicular to the needle. Using simulations in which the configurations that have higher contribution on the side faces on the one hand or higher contribution on the top faces on the other hand were excluded, it was shown that the blocking strategy works very well for faces that show layer-by-layer growth. Faces that show rough growth are able to find other pathways in the growth process without being slowed down considerably.

To conclude, a general method has been presented for the determination of the growth site configurations that play a role in the crystal growth process, and it has been shown how the statistics of these configurations can be used to start a rational design of tailor-made additives that are selective in affecting the growth of chosen crystal facets. Initial simulations show that the method works best for faces showing layer-by-layer growth.

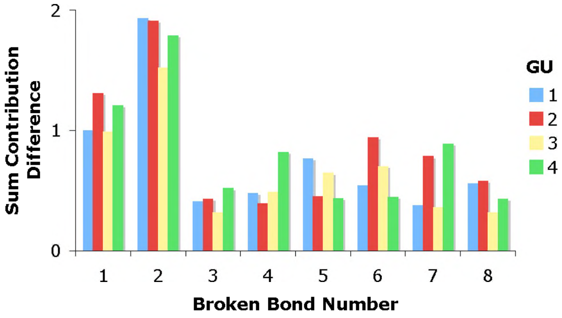

(a) $\Delta_{[top],[side]}C_i > 0.05$

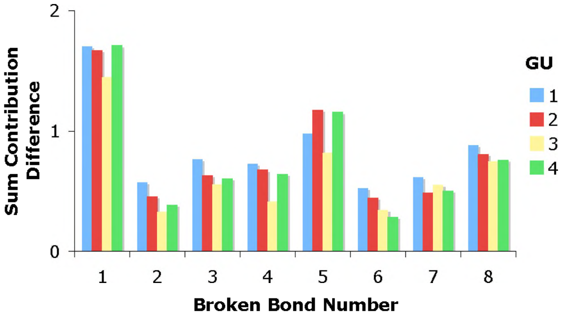

(b) $\Delta_{[top],[side]}C_i < -0.05$

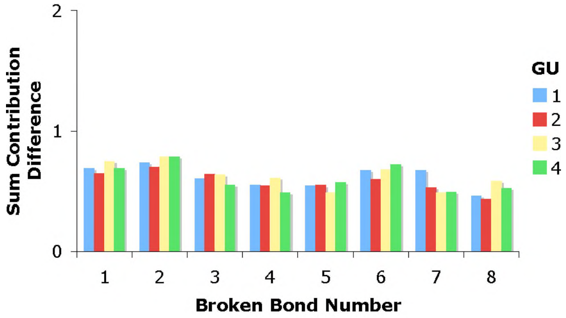

(c) $-0.05 < \Delta_{[top],[side]}C_i < 0.05$

Figure 6.9: The sum of the $\Delta_{[top],[side]}C_i$-values versus the broken bond number for the three domains of $\Delta_{[top],[side]}C_i$-values of Figure 6.8; the colors indicate the growth unit identity. In Figure 6.9(a) bond 1 and 2 have higher weighed contribution values compared to the other bonds. In Figure 6.9(b) bonds 1 and 5 have higher weighed contribution values and in Figure 6.9(c), in which the configurations with $-0.05 < \Delta_{[top],[side]}C_i < 0.05$ are plotted, there is no preferential bond in the configurations.

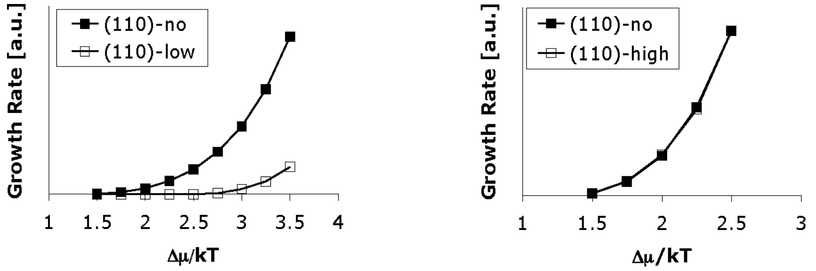

(a) Side faces growth rates with configurations having $\Delta_{[top],[side]}C_i < -0.05$ excluded

(b) Side faces growth rates with configurations having $\Delta_{[top],[side]}C_i > 0.05$ excluded

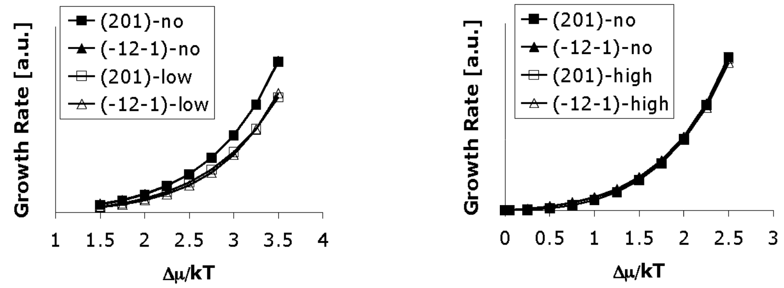

(c) Top faces growth rates with configurations having $\Delta_{[top],[side]}C_i < -0.05$ excluded

(d) Top faces growth rates with configurations having $\Delta_{[top],[side]}C_i > 0.05$ excluded

Figure 6.10: Simulation results for aspartame phase II-A with excluded configurations. The legends with "-no" added refer to a situation with no exclusion, the legends with "-high" added refer to the situation in which configurations having $\Delta_{[top],[side]}C_i > 0.05$ are excluded and legends with "-low" refer to the situation in which configurations having $\Delta_{[top],[side]}C_i < -0.05$ are excluded. Figure (a) thus shows the growth rates of the side faces for a normal situation and a situation where configurations having $\Delta_{[top],[side]}C_i < -0.05$ are excluded and (b) shows growth rates of the side faces for a normal situation and a situation where configurations having $\Delta_{[top],[side]}C_i > 0.05$ are excluded. Figures (c) and (d) show the same for the top faces. The scales for (a) and (b) differ from the scales of (c) and (d).

Appendix

Anisotropic Kossel (100) orientation

The (100) orientation of the anisotropic Kossel model is the closest to a classical Kossel (100) F-face. The (100) connected net slice consists of the ϕ_p and ϕ_q bonds; the ϕ_a bonds are the bonds between the (100) connected nets. An A or B adatom (see Figure 6.11) is bound to the surface with a single ϕ_a bond and has 5 broken bonds: one ϕ_a, two ϕ_p and two ϕ_q. Steps on the (100) orientation occur in the <001>, <010>, <011> and <01$\bar{1}$> directions, and these step configurations are displayed in Figure 6.12. The contribution values are plotted as a function of $\Delta\mu/kT$ for different δ-values in Figures 6.13 and 6.14.

Because both the A and B surface adatoms have the same configuration of 5 broken bonds, their contribution values are the same at each δ value. As is the case with most contribution values, the dependence on $\Delta\mu/kT$ generally reflects the transition from 'clean' layer-by-layer growth to a more rough growth mode. This can be seen by the fact that the contribution of favorable growth sites decreases with $\Delta\mu/kT$, and energetically more unfavorable growth sites become more important in the growth process.

The five different step configurations, labeled A-E in Figure 6.12, can be thought of as two types: the first type of the <011> and <01$\bar{1}$> steps, labeled A and B, and the second type of the <001> and <010> steps, labeled C-E. Apart from small deviations between A and B at low δ, the first type behaves the same, independent of δ. The second type, with configurations C-E, does depend on δ: the C configuration has high contribution at low δ as it only has two broken ϕ_p bonds, which is very favorable at low δ. The D configuration behaves oppositely, it has two broken ϕ_q bonds, which is unfavorable at low δ. The E configuration has one broken ϕ_p bond and one broken ϕ_q bond, and has a contribution that is in between that of C and D. As δ goes to unity, the difference between C, D and E become less pronounced and at $\delta = 1.0$, their contribution values are the same.

Anisotropic Kossel (011) orientation

The (011) orientation also has two surface adatom growth site configurations, displayed in Figure 6.15. The contribution of these is not the same, although the differences at higher δ are negligible. As the configuration of both adatoms is slightly different, it is expected to be more pronounced at lower δ values. This trend is also found from the simulations and is displayed in Figure 6.16. There are two important step directions on (011), <100> and <011>. Four different configurations can be found for the <100> steps, two other configurations belong the <011> step. These six configurations are all displayed in Figure 6.17. Figure 6.18, finally, displays the step adatom growth site contributions for the (011) configurations.

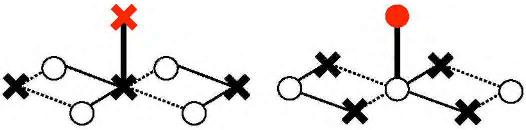

Figure 6.11: The two adatom configurations on the (100) face of the anisotropic Kossel model.

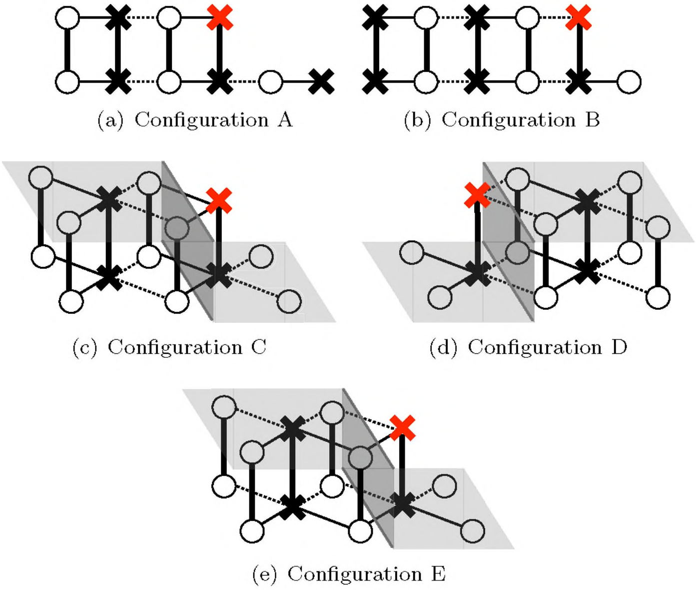

(a) Configuration A

(b) Configuration B

(c) Configuration C

(d) Configuration D

(e) Configuration E

Figure 6.12: Five examples of the five possible step configurations on the (100) face of the anisotropic Kossel model. The growth unit in grey is the step adatom growth site configuration. For all five configurations there are symmetry-related configurations due to the spacegroup symmetry; these configurations are not displayed.

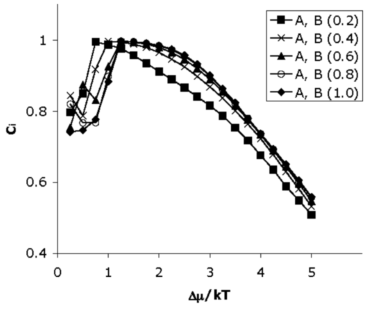

Figure 6.13: The (100) contribution values of the surface adatoms as a function of $\Delta\mu/kT$ for different δ values. The configurations labels A and B correspond to the configurations in Figure 6.11. Note that the region of $\Delta\mu/kT$ below about 1.0 is where growth on the surface is very rare and contribution values are not very reliable.

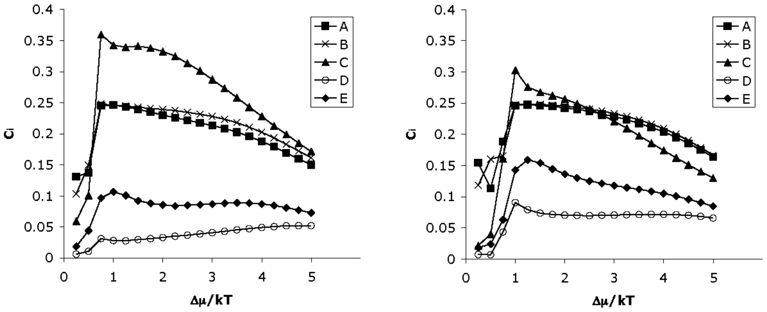

(a) $\delta = 0.2$ (b) $\delta = 0.4$

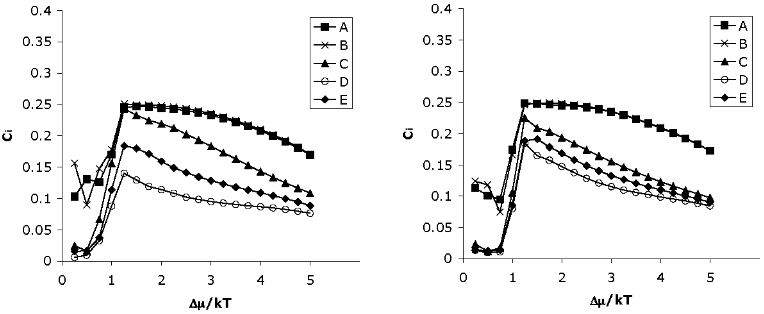

(c) $\delta = 0.6$ (d) $\delta = 0.8$

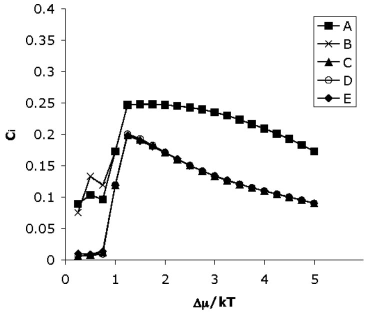

(e) $\delta = 1.0$

Figure 6.14: The (100) contribution values as a function of $\Delta\mu/kT$ for different δ values. The configuration labels A-E correspond to the configurations in Figure 6.12.

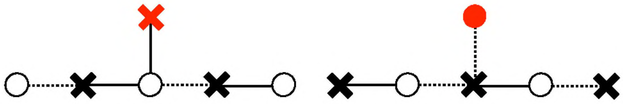

Figure 6.15: The two surface adatom growth site configurations on the (011) surface

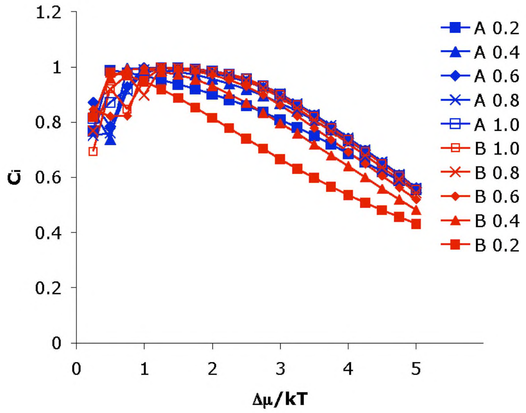

Figure 6.16: The (011) contribution values of the surface adatoms as a function of $\Delta\mu/kT$ for different δ values. The configurations labels A and B correspond to the configurations in Figure 6.15.

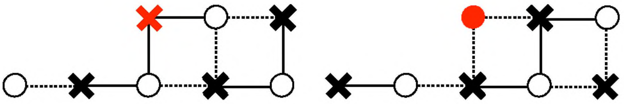

(a) Configuration A (b) Configuration B

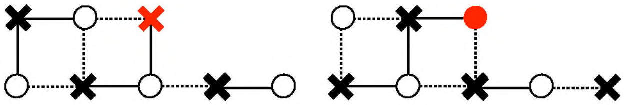

(c) Configuration C (d) Configuration D

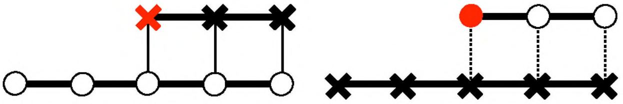

(e) Configuration E (f) Configuration F

Figure 6.17: The six step adatom growth site configurations representing steps on the (011) surface.

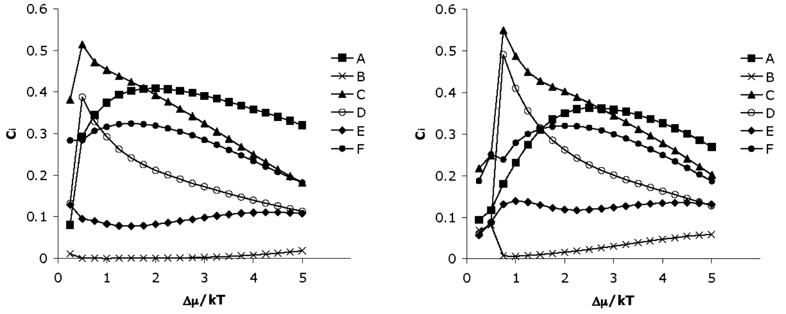

(a) $\delta = 0.2$ (b) $\delta = 0.4$

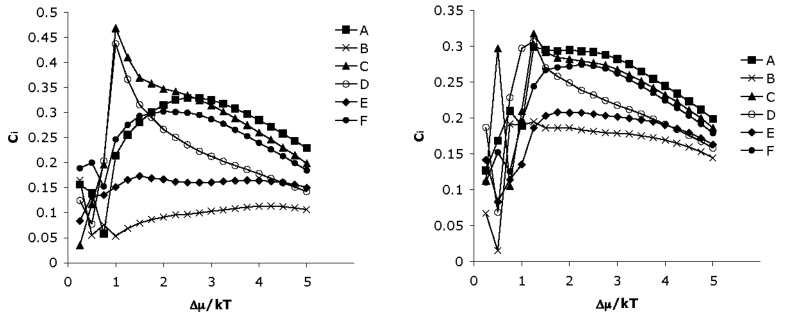

(c) $\delta = 0.6$ (d) $\delta = 0.8$

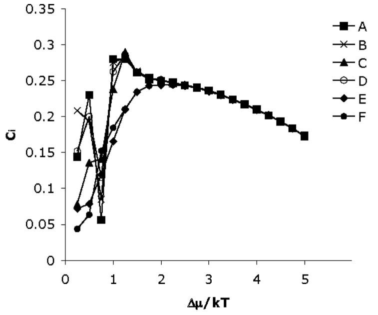

(e) $\delta = 1.0$

Figure 6.18: The (011) step adatom contribution values as a function of $\Delta\mu/kT$ for different δ values. The configuration labels A-F correspond to the configurations in Figure 6.17.

Chapter 7

Experimental and computational growth morphology of two polymorphs of a yellow isoxazolone dye

7.1 Introduction

Crystallization is often the only viable step for separation and purification, both in small and large scale processes. The crystal morphologies obtained are strongly dependent on the crystal structure, and different polymorphs of the same compound may have very different habits. Both the ability to exert control over the formation of a desired polymorph, as well as the ability to influence the morphology of that polymorph are desired by industry to optimize the processing of crystalline compounds.[110, 1] Generally it can be said that the morphology desired in a crystallization process is a block-like habit, which ensures good flow, drying and filtering properties. Needles and platelets on the other hand tend to block filters and do not dry and flow very well. Therefore, besides a fundamental interest, a thorough understanding of the mechanism behind the formation of crystal shape is also essential for applications in industry.

Crystal morphology modeling often uses crude approximations. For instance, the Bravais, Friedel, Donnay and Harker (BDFH) model relies solely on the unit cell parameters and the crystal's spacegroup.[3, 4] The more sophisticated attachment energy model uses the energy released when two layers of the crystal structure are brought together and relates this to the growth rate of the corresponding crystallographic orientations.[5, 6, 7, 8] In reality however, layer-by-layer crystal growth is observed to proceed via the two-dimensional nucleation and further growth of small islands or via the addition of growth units to spiral arms originating from a dislocation. These surface processes of the growth mechanism are not incorporated in the two models described above.

A second shortcoming of the often used attachment energy model is the inability to model the depence of crystal morphology on the supersaturation during growth. It has been shown for a number of compounds that the supersaturation can determine the morphology to quite an extent.[52, 111, 112, 113]

To integrate the field of crystal morphology modeling and the world of Monte Carlo growth simulations, the program MONTY was developed.[9] This program is able to simulate crystal growth in any crystallographic orientation using the structure's crystal graph. Crystal growth is thus modeled as an atomistic surface phenomenon, with probabilities for attaching and detaching growth units based on their local bonding topology as well as on crystallization parameters like temperature and supersaturation. Also, the crystallization mechanism simulated can be varied in MONTY from 2D-nucleation to step flow and spiral growth.

The integration of different approaches towards crystal morphology modeling – attachment energy, step energy, statistical mechanics, Monte Carlo techniques – is a continuing effort to create a set of tools geared towards the automation of morphology prediction. The Monte Carlo growth simulations are based on the lattice-gas model of the crystal structure, as the length scales involved in simulating crystal growth are not yet accessible to off-lattice models in terms of computing time. For the attachment energy and step energy, relaxation and possible surface/step reconstruction can play a role. These phenomena, although not as a function of supersaturation, can be studied with the MARVIN program.[114] Another important aspect in crystal growth is the influence of impurities. Impurities can be studied in the attachment energy model in the program HABIT95, which can study the influence both of impurities and vacancies on the attachment energy.[115] Neither impurities, nor surface relaxation or reconstruction are incorporated in the MONTY program. The program uses a bulk termination as the surface structure.

In this chapter we report on the crystal structure, experimental crystal habit and computational prediction of the morphology for two polymorphs of a yellow isoxazolone-based dye used in the photographic industry. The molecule's structure is shown in Figure 7.1. The extended conjugated ring system absorbs light in a specific region of the visible spectrum, which explains the use of this compound in the photographic industry.

The two polymorphs of the dye exhibit very different morphologies: polymorph I grows as blocks whereas polymorph II grows as fine needles. Also, for both polymorphs the morphologies depend on the supersaturation during growth. The shortcomings of the attachment energy model are highlighted using these two polymorphs.

The MONTY program is used to simulate crystal growth on the faces of the two polymorphs of the yellow dye studied. The outcome of the simulations shows the block-like morphology of polymorph I and its strong dependence on supersaturation. For polymorph II, the simulations show its fine needle morphology, its dependence on supersaturation and the roughening of the top faces, explaining the fast growth in the direction of the needle.

7.2 Materials and methods

The pure isoxazolone dye was provided by Agfa Gevaert N.V. and used as received; the solvent used was methanol of p.a. quality (Merck). Solutions were prepared by first dissolving a well defined amount of dye in methanol, followed by filtrating the solution over a 0.22 μm Millipore filter and finally putting the solution in a closed glass vessel. This vessel was placed in a cell connected to a Julabo F25 waterbath ($\Delta T = 0.01^\circ$C) to stabilize and control the solution temperature. The temperature was measured with a PT100 resistance thermometer ($\Delta T = 0.01^\circ$C). Nucleation and crystal growth in the vessel could be monitored *in situ* with an optical microscope.

The crystals were nucleated from the methanol solution by lowering the temperature. To avoid exhaustion of the solution during growth, the crystals were dissolved again until a single small crystal remained. Next, the temperature was lowered again until the desired supersaturation was reached. Pictures were taken at well-defined intervals to determine the growth rate of each facet. These measurements were done at constant temperature, averaged over time and repeated twice using different solutions. Although the solution was not stirred, we assume that the concentration in the vessel was constant during growth.

7.3 Computational methods

Crystal growth simulations were performed using the Monte Carlo growth simulation program MONTY.[9] This program performs growth simulations on any crystal structure using its crystal graph. In the crystal graph the molecules are reduced to the growth units and are represented by the graph vertices. The graph also contains the pairwise interactions between the growth units, making up the graph edges. As the crystal structure is three-dimensionally periodic, the result is an infinite undirected weighted three-dimensionally periodic graph.

It has been shown that for crystal graphs that are more complicated than the Kossel model, the local bonding topology in step edges on the surface of a growing crystal can be responsible for unexpectedly low step energies.[48] As the steps determine the growth process to a large extent, the ease with which they can be formed is crucial for the correct modeling of the crystal growth. This process is inherently present in the simulations performed, as this bonding is present in the crystal graph.

The Monte Carlo “random rain” probability scheme used in the MONTY simulations ensures microscopic reversibility. This particular probability scheme has been shown to give good results for the simulations of solution growth.[21]

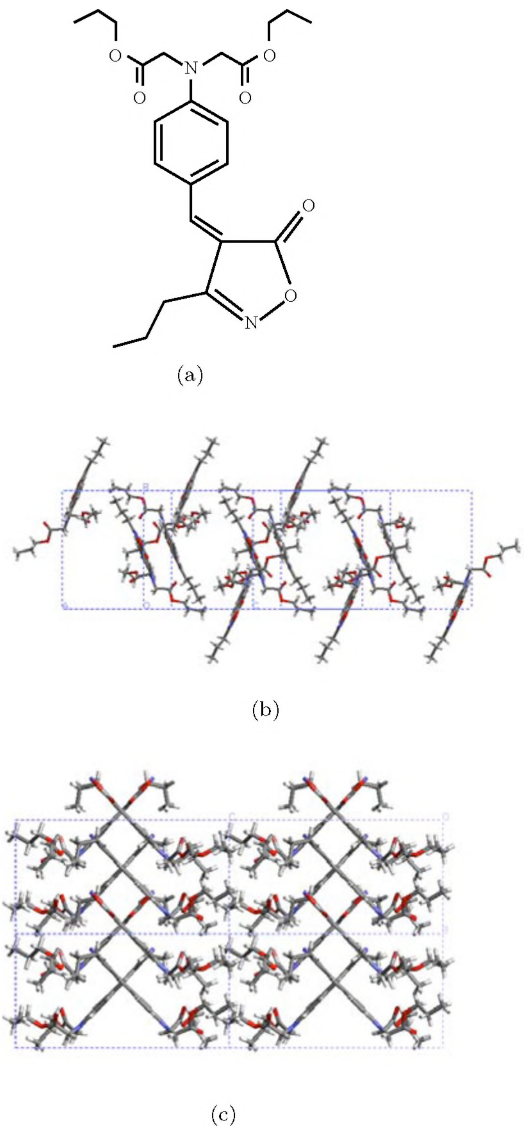

(a)

(b)

(c)

Figure 7.1: Molecular structure (a) and crystal packing of the yellow isoxazolone dye. Polymorph I (viewed along the [201] direction) packs in anti-parallel dimers (b) and polymorph II (viewed along the [100] direction) packs in sheets of parallel-packed molecules(c). For polymorph II the corrected crystal structure is shown.

In the remainder of this section the determination of the crystal graph and the way the simulations are performed are elaborated in further detail.

7.3.1 Determination of the crystal graph

The crystal structures were determined from single crystal X-ray diffraction, as described below. The crystal structure of the metastable polymorph showed – due to disorder – a large overlap of one of the acetic acid propylester chains with that of its counterpart growth unit generated by the mirror symmetry. The experimentally determined spacegroup $Cmc2_1$ did not allow for the necessary correction to obtain a valid molecular layout. A workaround was found in removing the mirror plane symmetry from the spacegroup symmetry elements, effectively lowering the spacegroup to $P2_1$. The disordered tails were then reconstructed after which a correct molecular layout was obtained. The chains were relaxed by means of partial structure minimization; thereby allowing for the calculation of representative interaction energies. Obviously, the asymmetric unit in this new structure contains two molecules. All following references to the structure of polymorph II will reflect this new structure.

The molecules' geometry was optimized at the 6-31G* level using the program Gaussian, versions 94[116] and 98[117]. Electrostatic potential-derived charges were obtained using a restricted electrostatic potential (RESP) fitting method, as described by Cornell *et al.*[90] using a modified procedure after Pigache *et al.*[118] The molecular electrostatic potentials (MEP) of the three different conformations were fitted to a single set of charges, to be able to compare lattice energies of the different polymorphs directly, instead of having to calculate, estimate or ignore the energy for changing the charge distribution in the molecule. These fit results were compared to fits obtained by a standard ESP charge fitting procedure in which a set of charges was obtained for each individual conformation.

The Dreiding v2.21 forcefield was used to optimize the crystal structure geometry using Ewald sums for the van der Waals and Coulomb interactions. The pairwise interactions between the growth units (molecules) in the crystal structure were determined using a direct calculation of the van der Waals and Coulomb interactions without a cutoff and with a constant dielectric constant ϵ_r. In Cerius^2[89], the default value of ϵ_r in the implementation of the Dreiding forcefield scales inversely with the distance to accomodate for polar environments. As we are interested in vacuum energies, the ϵ_r was taken constant.

7.3.2 Monte Carlo growth simulations

The results from the connected net analysis using the program Facelift[65] were used to select crystallographic orientations (hkl) on which to perform the growth simulations. The Facelift algorithm computes all orientations for which connected nets exist; these orientations have relatively low surface energy and have a high probability to show up in the crystal morphology. Orientations that have no connected nets grow rough and generally relatively fast and will not be considered here.[19, 48, 61] For all simulations a 2D-nucleation, or *birth and spread*, model was used, because spiral growth was never observed in the crystal growth experiments performed. For polymorph II, all orientations selected in the new spacegroup $P2_1$ conform to the spacegroup selection rules of the original spacegroup $Cmc2_1$.

For each orientation (hkl) the birth and spread simulations were performed on a grid of 100 x 100 unit cells with periodic boundary conditions. The simulations were all performed at a temperature of 300 K and at relative driving forces $(\Delta\mu/kT)$ between 0 and 6.0 with steps of 0.4 in between. The $\{\bar{1}01\}$, $\{011\}$ and $\{110\}$ orientations of polymorph I and the $\{h0l\}$ orientations of polymorph II were simulated between 0 and 12.0 to observe the onset of 2D-nucleation. In order to study the roughening behaviour of the fast-growing orientations of polymorph II, the orientations $\{hkl\}$ with $k \neq 0$, i.e $\{110\}$, $\{211\}$, $\{1\bar{1}\bar{1}\}$, and $\{011\}$, were simulated in detail for relative driving forces of 0 to 0.5 with steps of 0.05 in between. A simulation run consisted of an equilibration stage of 10^5 Monte Carlo events at the driving force selected, after which the simulation of $2 \cdot 10^7$ MC events was started.

The crystal graph bond strengths were scaled with respect to the experimentally determined enthalpy of dissolution, to account for the fact that solution growth is simulated. In this case the enthalpies were 18.9 kcal·mol^{-1} and 17.9 kcal·mol^{-1} for polymorphs I and II respectively. After scaling, bonds with a bond strength below 2 kcal·mol^{-1} have bondstrength below kT, and were therefore discarded.

7.4 Results

7.4.1 Crystal structure determination

Crystals of high quality and good size were selected for single crystal X-ray diffraction. The bulk structure of both polymorphs was determined using a Siemens P4-PC diffractometer and MoKα ($\lambda = 0.71073$Å) at 289K. The structure of polymorph I could be characterized fully with an R-value of 6.59% (for 1975 reflections with $I > 2\sigma(I)$). The structure of polymorph II could only be solved and refined in the space group $Cmc2_1$. Its fine needle morphology, a limited diffraction pattern (1.0 Å resolution) and structural disorder inhibited refinement beyond an R-value of 19%. At this level of refinement some of the acetic acid propyl ester side-chains of symmetry-related molecules are overlapping. Further refinement of this disorder was not possible. Assigment of the space group and possible twinning were checked. As already mentioned in the section on the crystal graph, to correct for this, the mirror-plane symmetry was removed from the crystal structure. This correction lowers the symmetry, giving a $P2_1$ spacegroup with two molecules in the asymmetric unit cell. The

Table 7.1: Crystallographic data used for the crystal graph

	Polymorph I	Polymorph II (uncorrected)	Polymorph II (corrected)
	monoclinic $P2_1/n$	orthorombic $Cmc2_1$	monoclinic $P2_1$
a (Å)	10.801(4)	33.67	13.71
b (Å)	13.229(4)	13.71	9.65
c (Å)	17.310(6)	9.65	18.18
$\alpha(^o)$	90	90	90
$\beta(^o)$	102.28(2)	90	112.14
$\gamma(^o)$	90	90	90
Z	4	8	4
V (Å^3)	2416.8(14)	4455	2226.95

new crystallographic axes a_2, b_2 and c_2 expressed in the old axes a_1, b_1 and c_1 were defined as follows: $a_2 = b_1$, $b_2 = -c_1$ and $c_2 = \frac{1}{2}(b_1 - a_1)$. The crystal data of polymorph I and the experimentally determined and corrected data of polymorph II are presented in Table 7.1.

7.4.2 Crystal growth and observed morphologies

To nucleate polymorph I within accessible experimental time, a relative supersaturation (σ) of at least 1.6 is necessary. One to ten separate single crystals then start to grow per cm^3. Depending on the relative supersaturation during growth, several morphologies are observed, which means that the relative growth rates are not constant. The measured indices are presented in Figure 7.2 and the different morphologies as a function of the relative supersaturation during growth in Figure 7.3. The average measured growth rates are displayed in Figure 7.6. The $\{11\bar{1}\}$ facets are present up to a relative superaturation of 0.30; $\{002\}$ and $\{101\}$ are visible up to $\sigma = 0.40$, whereas the $\{10\bar{1}\}$, $\{011\}$ and $\{110\}$ are always present. The first three faces start to grow fast at their treshold supersaturations and grow out of the crystal very quickly.

The nucleation of polymorph II occurs within accessible experimental time at a relative supersaturation of 1.2; optical microscopy shows that this happens by contact nucleation on the glass or on foreign particles. In this case, hundred to several thousand needles per cm^3 nucleate in clusters. At higher relative supersaturations, above 2.5, the crystals nucleate heterogeneously as spherulites. Only when an anti-solvent like water is used to obtain an extremely high supersaturation, separate micron-sized crystals of this polymorph nucleate homogeneously. Figure 7.4 shows the measured indices of this polymorph. The changes in morphology as a function of the relative supersaturation during growth can be found in Figure 7.5. The averaged growth rates are plotted in Figure 7.7. The growth of the $\{001\}$ facets was too slow to be measured using the method

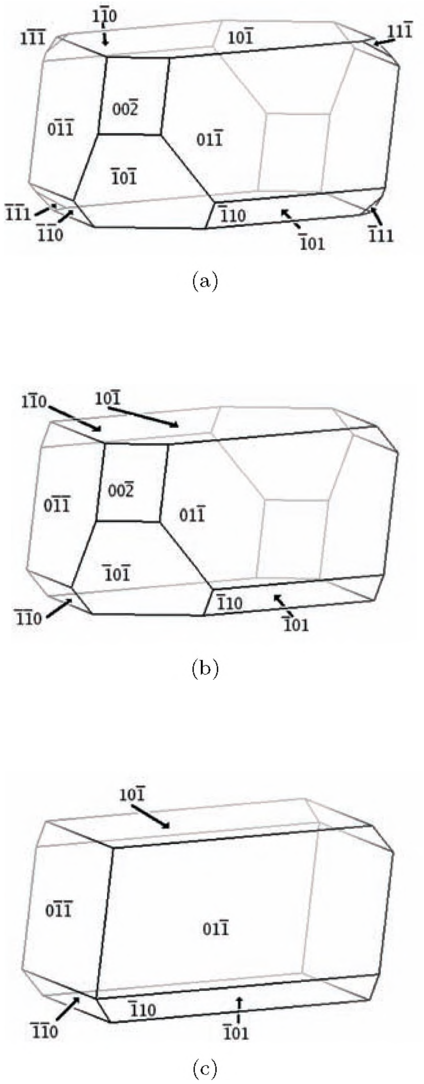

(a)

(b)

(c)

Figure 7.2: Schematic morphology to show the measured indices for polymorph I at low supersaturation (a). Above $\sigma = 0.30$ the small $\{11\bar{1}\}$ faces dissappear (b) and above $\sigma = 0.40$ only the faces $\{10\bar{1}\}$, $\{011\}$ and $\{110\}$ remain (c).

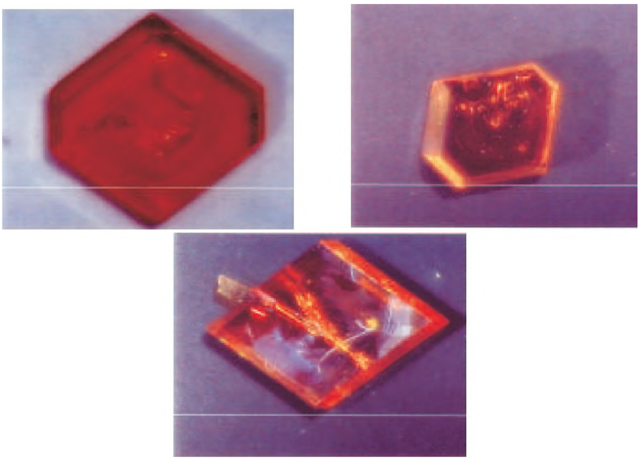

Figure 7.3: Observed morphologies polymorph I at $\sigma < 0.3$ (left), $0.3 \leq \sigma \leq 0.4$ (middle) and $\sigma > 0.4$. All crystals have a width of 1-2 cm and a thickness of 0.3-0.5 cm.

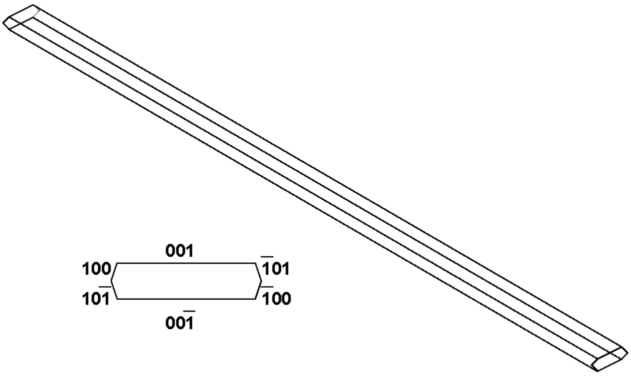

Figure 7.4: Schematic morphology to show the measured indices for polymorph II. The lower left corner shows the indices for a projection along the needle axis. The top of the needle is always rounded.

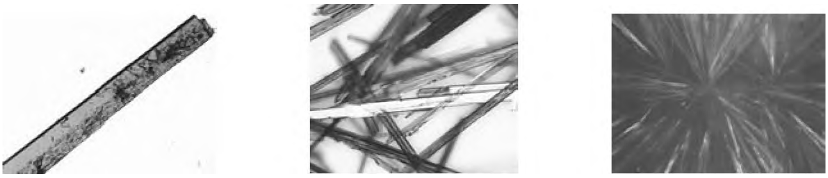

Figure 7.5: Observed morphologies polymorph II at low (left), medium (middle) and high (right) supersaturation. Needle length 1 cm, width 0.1 - 0.5 mm and thickness 0.1 mm.

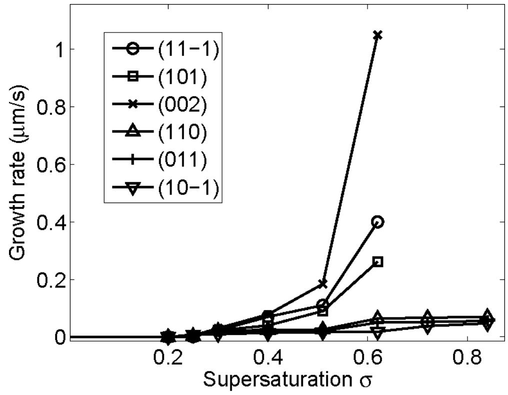

Figure 7.6: Average growth rates for polymorph I. Error bars are smaller than the symbols used.

described. The $\{10\bar{1}\}$ facets were only present when the growth rate was near zero for several days. The top of the needle was always rounded. The $\{100\}$ facets are present up to a relative supersaturation of 0.20; $\{001\}$ was present up to $\sigma = 0.29$. Above this latter supersaturation, no faceted orientations are observed. The growth rates for orientations displayed at too high values for the facets to be present were obtained by measuring the rate at which an orientation grows out of the crystal. In this case the facet still grows as a flat face, but too fast to be present at the end of the growth.

7.4.3 The crystal graph

For all conformations the molecular electrostatic potential (MEP) was determined using the method described above. The MEPs were fitted to a single set of charges as well as individual sets of charges for each conformer. The differences between charges fitted to a single MEP and the charges fitted to the three MEPs were smaller than 0.1 unit charge for all atoms. The relative rms values, which reflect the quality of the fit of the ESP charges to the quantum mechanically determined MEP, are displayed in Table 7.2. As can be seen from the relative root mean square deviations (RRMS), fitting a single MEP does not give a worse fit than fitting three MEPs simultaneously.

The total lattice energies of the two polymorphs, obtained after minimization of the crystal structure, were -44.0 kcal·mol^{-1} and -37.6 kcal·mol^{-1} for

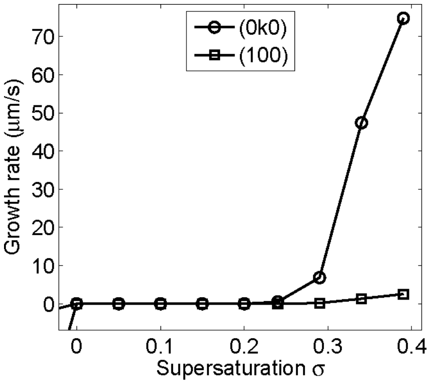

Figure 7.7: Average growth rates for two side faces of polymorph II. Error bars are smaller than the symbols used. The $\{10\bar{1}\}$ orientation has zero growth rate at $\Delta\mu/kT = 0$ and could not be measured at other driving forces. The growth rate of $\{001\}$ was zero for all measured driving forces.

Table 7.2: Restricted Electrostatic Potential (RESP) fitting results. Relative root mean square deviation is defined as in[90]

	ESP relative RMS
Polymorph I	0.102
Polymorph II, molecule A	0.112
Polymorph II, molecule B	0.106
Combined MEPs	0.111

Table 7.3: Crystal graph bonds before scaling (i.e. with respect to vacuum) for polymorph I (left table) and polymorph II (right table). All symmetrically equivalent bonds have been omitted. The first bond is between molecule 1 and molecule 3 in the neighbouring unit cell in the $[\bar{1}\bar{1}1]$ direction with respect to the crystallographic axes.

Form **I**		Form **II**	
Bond	Bond energy [kcal·mol^{-1}]	Bond	Bond energy [kcal·mol^{-1}]
1-3$[\bar{1}\bar{1}1]$	-21.05	1-2[010]	-22.00
1-4$[\bar{1}00]$	-8.81	1-2[000]	-18.72
1-2$[\bar{1}\bar{1}0]$	-7.07	1-4$[\bar{1}00]$	-6.44
1-3$[\bar{1}01]$	-6.33	2-4$[\bar{1}\bar{1}0]$	-6.39
1-3$[0\bar{1}1]$	-3.56	1-4[000]	-5.16
1-2[000]	-3.55	1-4$[\bar{1}0\bar{1}]$	-3.38
1-1[100]	-2.64	1-3[000]	-3.33
1-4$[\bar{1}\bar{1}0]$	-2.21	1-3$[\bar{1}00]$	-2.86
		1-4$[\bar{1}\bar{1}0]$	-2.21

polymorphs I and II respectively. This large difference between lattice energies indicates that polymorph I is more stable than polymorph II. On the other hand, the enthalpies of dissolution, measured at room temperature, differ by merely 1.0 kcal·mol^{-1}, indicating that the lattice energy determined computationally is overestimating the difference in stability of the polymorphs. This is probably due to the use of the Dreiding force field that does not calculate the intermolecular interactions to a high degree of accuracy. The resulting bonds of the crystal graph are listed in Table 7.3.

7.4.4 Attachment energy morphology

From the connected nets and their corresponding attachment energies, found with the program FACELIFT, the attachment energy morphologies were constructed. The attachment energies for both crystal structures are shown in Table 7.4. The resulting morphologies are shown in Figure 7.8. The attachment energy morphology of polymorph I is reasonable, although the forms $\{11\bar{1}\}$ and $\{110\}$ are not predicted. For polymorph II, the prediction is worse however. The aspect ratio of the predicted habit is approximately 5, whereas we find aspect ratios of 20-100 experimentally. Furthermore, the $\{10\bar{1}\}$ orientations are not predicted, and the top is predicted to be faceted. The dependence of both habits on supersaturation during growth found experimentally, is not incorporated in this model.

Table 7.4: All orientations with a connected net and the attachment energies in kcal·mol^{-1} of the strongest connected net of polymorph I (left) and polymorph II (right)

hkl	U^{att}	*hkl*	U^{att}
$\{1\bar{1}\bar{2}\}$	-70.47	$\{\bar{1}0\bar{1}\}$	-65.07
$\{\bar{1}01\}$	-21.56	$\{0\bar{1}2\}$	-82.38
$\{1\bar{1}1\}$	-51.58	$\{1\bar{1}2\}$	-92.84
$\{\bar{1}\bar{1}0\}$	-55.05	$\{\bar{1}14\}$	-107.17
$\{0\bar{1}\bar{1}\}$	-47.47	$\{10\bar{3}\}$	-99.70
$\{1\bar{1}\bar{3}\}$	-89.37	$\{00\bar{2}\}$	-71.46
$\{111\}$	-69.42		

hkl	U^{att}	*hkl*	U^{att}
$\{011\}$	-68.53	$\{\bar{2}01\}$	-108.88
$\{00\bar{1}\}$	-9.30	$\{0\bar{2}0\}$	-106.99
$\{10\bar{1}\}$	-22.61		
$\{1\bar{1}0\}$	-64.17		
$\{100\}$	-20.96		
$\{1\bar{1}\bar{1}\}$	-65.55		
$\{\bar{2}\bar{1}\bar{1}\}$	-76.22		

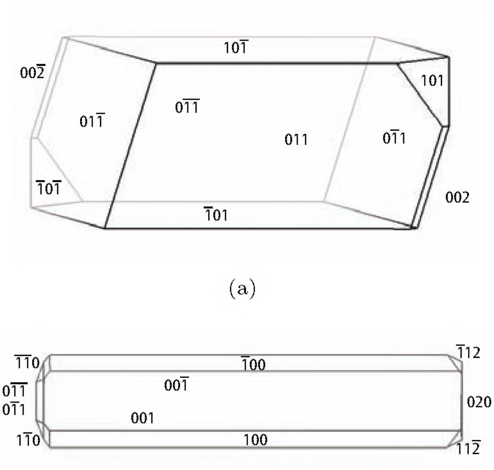

(a)

(b)

Figure 7.8: The predicted morphologies based on the attachment energy model of polymorph I (a) and polymorph II (b).

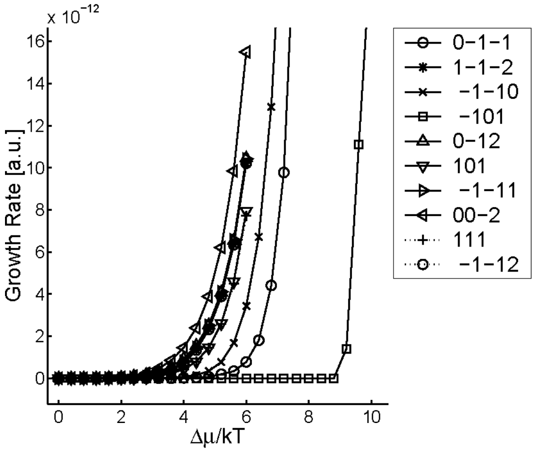

(a)

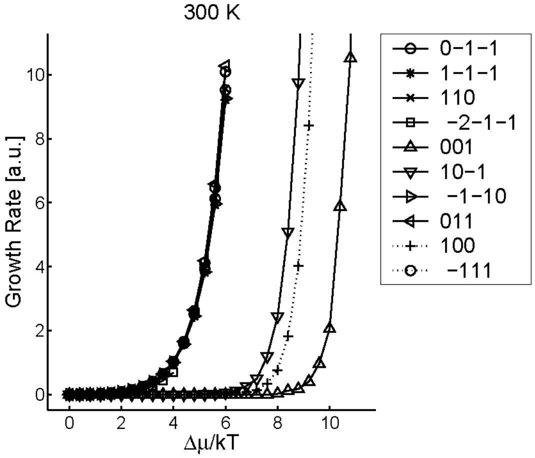

(b)

Figure 7.9: Growth simulations of polymorph I (a) and polymorph II (b)

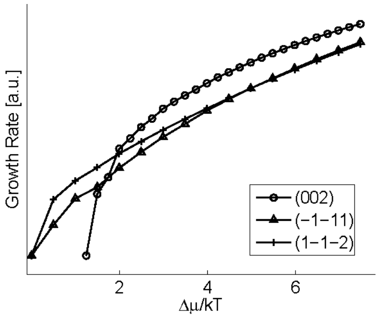

Figure 7.10: The low driving force regime of polymorph I. In this plot it can be seen that the orientations $\{002\}$ and $\{\bar{1}\bar{1}1\}$ grow slowly at low driving force, but cross the line of $\{\bar{1}\bar{1}2\}$ at $\Delta\mu/kT = 0.7$ and 2.1 respectively. This means that the relative morphological importance of these two orientations compared to the $\{\bar{1}\bar{1}2\}$, a crystallographic orientation that is never observed, is high at low driving force and becomes lower at high driving force.

7.4.5 Growth simulations

For the Monte Carlo simulations of both polymorphs, the crystallographic orientations with a connected net attachment energy larger than -85 kcal·mol^{-1} (i.e. lower absolute energies) were selected. The results of the growth simulations are shown in Figure 7.9.

Polymorph I

The growth simulations in Figure 7.9(a) show that $\{10\bar{1}\}$ is the orientation with the highest 2D-nucleation barrier; its growth starts between $\Delta\mu/kT = 8.8$ and 9.2. All other orientations start to grow at lower $\Delta\mu/kT$. This value can not be compared with the experimental observation for the nucleation, as the nucleation process is a 3D nucleation, whereas we are simulating 2D-nucleation only.

In the low $\Delta\mu/kT$ regime we have found in our simulations that the orientations observed at low supersaturations grow slow, but grow out of the morphology at higher driving forces: the lines in the graph cross. This crossing of lines indicates a (strong) dependence of the habit on the supersaturation, a phenomenon that has been described earlier for paracetamol.[52] This behaviour is displayed in the logarithmic plot in Figure 7.10, where the growth rate of $\{002\}$ is negligible compared to that of the other orientations up to $\Delta\mu/kT = 0.6$. Above this value, the growth rate is increasing much faster than the other two orientations plotted. Also, albeit less dramatically, the curve of $\{\bar{1}\bar{1}1\}$ crosses the curve of $\{\bar{1}\bar{1}2\}$ at around $\Delta\mu/kT = 2.0$. This is in line with the fact that these orientations are observed experimentally at low supersaturations, see Figure 7.2.

The order in which the two orientations disappear from the morphology is not correct however. And as for the $\{101\}$ orientation, this orientation's simulated growth rate is always relatively slow, but faster than the $\{10\bar{1}\}$, $\{011\}$ and $\{110\}$ orientations. As $\{101\}$ is also the last orientation that grows out of the experimental morphology at higher supersaturation, this agrees with the results found from the simulations. The three forms left at high supersaturation, $\{\bar{1}\bar{1}0\}$, $\{0\bar{1}\bar{1}\}$ and $\{10\bar{1}\}$ also have the highest 2D-nucleation barrier in the simulations.

It can be seen from the simulations of polymorph I, that the growth rate of the slowest growing orientation $\{10\bar{1}\}$ is zero until very high driving force values. All other orientations already grow very fast when this orientation just starts to grow. Experimentally it was observed that the $\{10\bar{1}\}$ surface growth rate depended on the presence of impurities in the form of small foreign particles or small crystallites. Repeated growing and etching showed islands appearing and disappearing at the same location of the crystal surface, indicating a pinned source of steps. It is unclear however if the presence of these impurities is the cause of the discrepancy between the observed and simulated growth rates.

Polymorph II

For polymorph II a very clear difference between orientations in the $\{h0l\}$ zone and orientations with $k \neq 0$ can be seen in Figure 7.9(b). All orientations with $k \neq 0$ have a non-zero growth rate already at the lowest driving force simulated (see Figure 7.11), in contrast to the $k = 0$ zone. In Figure 7.12 two simulated surfaces are shown. Figure 7.12a shows the surface of the (001) orientation at $\Delta\mu/kT = 10.8$, a value at which the surface is showing step flow as a result of 2D-nucleation. As can be seen from the picture, the surface is very flat, showing only a few steps. The (011) orientation however shows a rough surface already at $\Delta\mu/kT = 0.3$ as can be seen in Figure 7.12b. Similar pictures can be obtained for other top face orientations. This means that the crystal grows rough in all orientations with $k \neq 0$ and therefore growth in the b-direction will be much faster. As a result a needle is formed in the direction of the **b**-axis, with rounded needle tips, due to the rough growth.

The finer details of the experimental observations are replicated in the simulation as well: comparing the sequence in which the side facets disappear from the morphology in the experiment, $\{10\bar{1}\} < \{100\} < \{001\}$, it is found that this sequence is the same for the three $\{h0l\}$ orientations simulated.

7.5 Conclusions

The attachment energy model fails to predict the needle-like morphology of polymorph II. Also, as this is not incorporated in the model, it can not predict the observed dependence on the supersaturation during growth of the morphology of both polymorphs. The failure of the attachment energy model for the prediction of the needle morphology of polymorph II is caused by the fact that

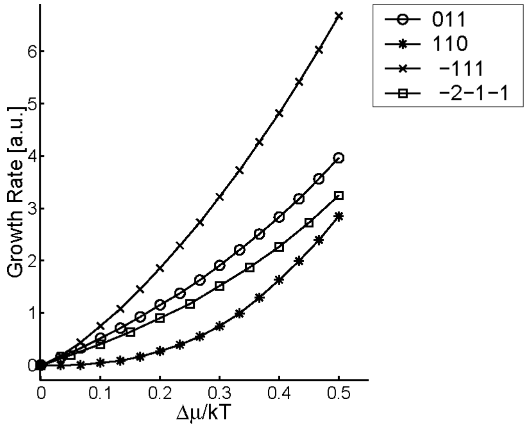

Figure 7.11: The low supersaturation regime of polymorph II. The orientations (hkl) with $k \neq 0$ all lack a clear 2D-nucleation barrier.

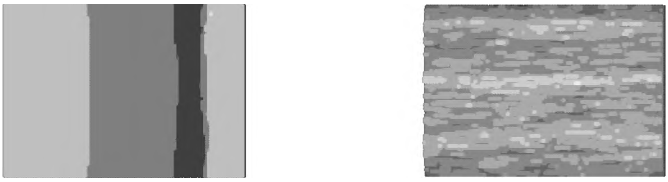

(a) (b)

Figure 7.12: Surfaces of polymorph II showing the difference in surface roughness of two orientations, a) the (001) orientation with a flat surface with some steps (oriented along the needle direction) at $\Delta\mu/kT = 10.8$ and b) the (011) orientation with a rough surface already at $\Delta\mu/kT = 0.3$. Lighter values indicate higher regions.

the attachment energy model describes crystal growth as the coming together of complete layers of particles, whereas in reality, crystal growth is a process of individual particles coming together to form the bulk structure. In this 'atomistic' description of crystal growth, the energetics for growth are determined by the individual bonding patterns of particles attaching to a growing crystal surface, rather than the attachment energy of a whole layer.

To study crystal growth as a an 'atomistic' process, we have used a kinetic Monte Carlo simulation program that is able to simulate growth for any crystal structure, using the structure's crystal graph. When we study the crystal growth of the two polymorphs of the yellow isoxazolone dye, we find that the simulations are able to predict the needles of polymorph II: the needle's long axis is along the **b**-axis and all crystallographic orientations (hkl) with $k \neq 0$ grow rough and therefore much faster than the orientations that are not in that crystallographic zone, effectively predicting a needle.

For polymorph I it has been found that the facets that are present at low supersaturations have a low simulated growth rate at low driving force values. At higher driving forces, these orientations grow much faster, causing the growth rate curves to cross (see Figure 7.10).

The unusually high growth rates of certain orientations in polymorph II and the dependence of growth morphology on supersaturation for both polymorphs can be understood in terms of energetics of individual bonding patterns of particles attaching to certain orientations. For the *birth and spread* simulations used, these patterns ultimately determine the 2D-nucleation barrier and the growth rate. The stability of the nuclei formed is based on the bonding energy differences in the edge of the nucleus. These subtle energy differences are inherently present in the kinetic Monte Carlo simulations, as these simulations are based on the crystal graph, in which the bonding in the crystal structure is described.

Chapter 8

Experimental and computational morphology of three polymorphs of the free base of Venlafaxine. A comparison of morphology prediction methods.

8.1 Venlafaxine

Venlafaxine is a bicyclic phenylethylamine-based anti-depressive drug, which is believed to work by simultaneously blocking the re-uptake of neuronal norepinephrine and serotonin.[69] The Venlafaxine molecular structure is shown in Figure 8.1. It is administered as a racemic mixture, and the crystals of this mixture are the subject of the research reported on in this chapter.

Recently it has been found that the free base of Venlafaxine has superior processing characteristics over the hydrochloric acid salt, which is marketed

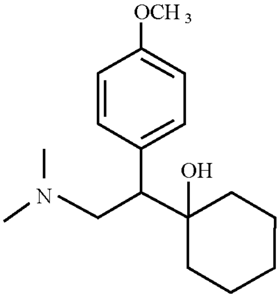

Figure 8.1: Molecular structure of Venlafaxine

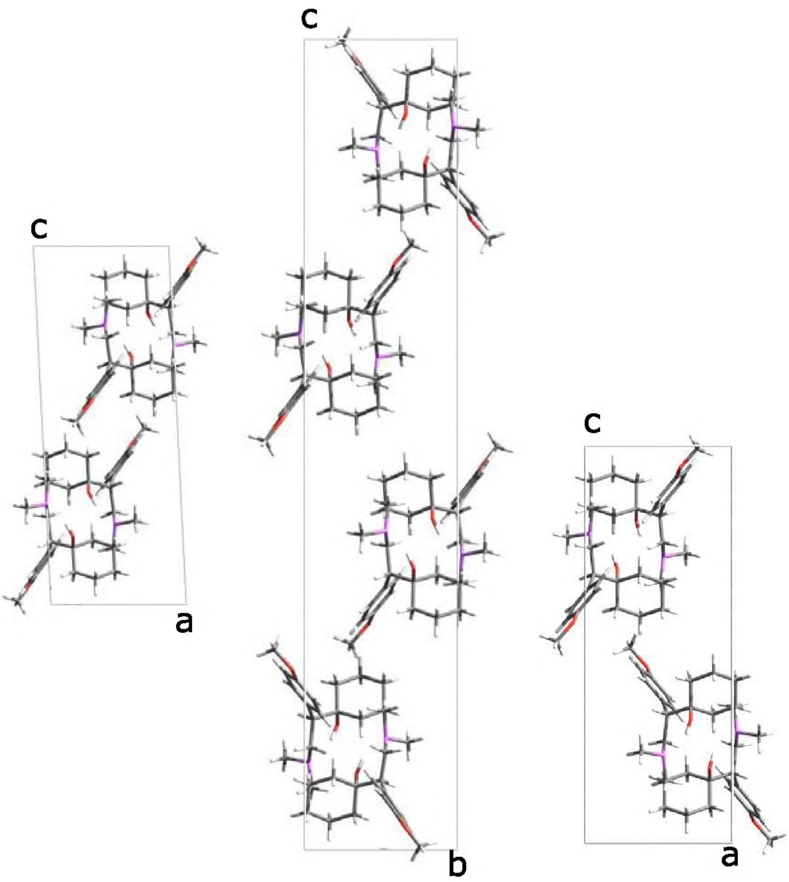

Figure 8.2: Crystal structures of phase **I** (left), phase **II** (middle) and phase **III** (right). The packing similarities can be seen, conceptually, as phase **II** being built up of layers of phase **I** and **III**.

worldwide. The free base is easier to handle as it is less aggressive towards equipment etc. compared to the hydrochloric acid salt. Also, the free base shows a low solubility and low dissolution rate in water, and is therefore suitable for the formulation of extended release dosage forms.[119] In the study of the free base, three polymorphs have been found, which are enantiotropically related.[120] Phase **I** is stable at room temperature, and can be converted into phase **II** above approximately 40°C. Phase **I** and phase **II** can be converted into phase **III** above 60°C.

It can be seen from Figure 8.2 that the crystal structures[120] of the three polymorphs are strongly related. When viewed along the **b**-axis, the unit cell of phase **I** consists of four molecules whose methoxyphenyl rings are oriented in a parallel fashion. In the crystal structure of phase **III**, the molecules stack with the methoxyphenyl rings in mutually perpendicular orientation. In the crystal structure of phase **II** these patterns of phase **I** and **III** are both incorporated; phase **II** can be thought of to be built of {002} layers of phase **I** and phase **III**. It must be noted, however, that this comparison only holds at a conceptual level, as due to packing details the crystal structures can not be overlaid exactly.

Thus all polymorphs are built up of two types of layers, and each layer consists of enantiopure molecules (R or S). The polymorphs differ in the way that the R- and S-layers are stacked. Phases **I** and **II** are racemates, having spacegroup $P2_1/n$ and $P2_1/c$ respectively. Phase **I** stacks with alternating R- and S-layers; Phase **II** with two R-layers followed by two S-layers.

Interestingly, phase **III** has spacegroup $P2_12_12_1$, a chiral spacegroup. Phase **III** can, however, be obtained from racemic solutions. It was shown using enantiomeric etch experiments[120], that phase **III** is a conglomerate, built up of enantiopure macroscopic R- and S-layers: upon immersion of a crystal of phase **III** in a supersaturated solution of one enantiomer, the other enantiomer is etched away, and μm-thick layers of enantiopure material are left. The enantiomeric enrichment of the remaining solid was proven by determination of the optical rotation of a crystal dissolved after etching.

As all polymorphs are enantiotropically related, the solid state conversion of phase **I** and **II** to phase **III** at higher temperatures is very remarkable, as that implies large movements of molecules from a molecularly racemic configuration to an enantiomeric conglomerate. Still, the etch experiments showed that a crystal that had been transformed from phase **I** to phase **III** is indeed a conglomerate of enantiopure material. For further details, the reader is referred to Reference [120].

In this chapter the results are presented of a morphology prediction study for the three polymorphs of Venlafaxine using three morphology prediction methods: BFDH, attachment energy and Monte Carlo growth simulations. A comparison with the morphologies observed experimentally is made. It is found that the predictions based on the Monte Carlo growth simulations are semi-quantitative for phases **I** and **II**; for phase **III** the overall shape is reproduced, but some predicted indices do not match the indices observed experimentally.

8.2 Computational methods

8.2.1 Calculation of the crystal graphs

The crystal graphs were calculated using crystal structures obtained from single crystal X-ray diffraction.[120] The geometries of the molecular conformations from the experimental structures were optimized using Gaussian 94 with an HF/6-31G* basis set.[116] A self-consistent field (SCF) convergence criterion of 10^{-8} as well as a "Tight" minimization threshold was applied. Charges were fitted to the nuclei using a restricted electrostatic potential (RESP) charge fitting scheme.[90] This RESP procedure serves two goals: first of all, it is known that RESP charges are less sensitive to small perturbations in the geometry, that will happen when the crystal structure is minimized (*vide infra*). Secondly, the RESP procedure was applied to all polymorph conformers at the same time, in order to obtain a single charge set that describes all molecular electrostatic potentials. In this way lattice energies of the two polymorphs can be compared directly, instead of having to calculate, estimate or ignore the cost in energy for changing the charge distribution going from one conformation to the other. This procedure is based on the R.E.D. v1.0 procedure developed by Pigache *et al.*[118]

The molecular structures thus obtained were used to build the crystal structures, which were consecutively minimized using the Dreiding force field[88] and the "Smart Minimizer" of Cerius^2[89], with Ewald sums for the van der Waals and Coulomb contributions and high convergence settings.

Pairwise interactions were calculated using the Dreiding forcefield in the Cerius^2 program using a direct calculation of van der Waals and Coulomb contributions with a constant ϵ_r value. In contrast, the default value of ϵ_r in the Cerius^2 implementation of the Dreiding forcefield scales linearly with the distance, to approximate solvent effects in biomolecular systems.[88] Crystal graphs were created from all pairwise interactions up to a certain cutoff radius. The resulting interactions were then scaled so that their sum was equal to the dissolution enthalpy in heptane of each polymorph. Any scaled interactions with bond strength below a certain cutoff-value (usually kT) were discarded.

8.2.2 Attachment energy calculations

Once the energies of the bonds making up the crystal graph have been determined, attachment energies can be calculated from the crystal graph by the program FACELIFT.[65] This program finds all PBCs in the graph and subsequently combines them to form connected nets. The bonds that make up the connected net are the slice bonds; the bonds that attach connected nets to each other are the attachment energy bonds. The FACELIFT routine is also implemented in the Hartman-Perdok module of Cerius^2.[89]

8.2.3 Monte Carlo simulations

The MONTY simulations were performed on surfaces (hkl) for which a connected net was found using the FACELIFT program. All simulations were performed on a rectangular grid of unit cells parallel to the orientation(hkl). For all orientations a simulation box of 50×50 unit cells with lateral periodic boundary conditions was used. The sampling in the simulations was preceded by a period of relaxation, in which the surface was allowed to grow under the same driving force as during the simulation. This relaxation time was taken to be 100000 events in all simulations. The sampling to determine the growth rate was subsequently

Table 8.1: Lattice parameters and energies of the three phases before and after geometry optimization.

Structure	Spacegroup	Z	a [Å]	b [Å]	c [Å]	β	Lattice Energy [kcal·mol^{-1}]
Phase **I**	P 1 2_1/n 1	4	8.21	8.86	21.79	92.79	
– optimized			8.28	9.32	22.47	93.71	-28.6
Phase **II**	P 1 2_1/c 1	8	8.84	8.27	43.75	90.97	
– optimized			9.28	8.35	44.63	92.41	-28.9
Phase **III**	P 2_1 2_1 2_1	4	8.22	8.86	22.27	90.00	
– optimized			8.25	9.27	22.74	90.00	-28.8

done at least 500 times, with periods of 10000 events in between. When there was reason to believe that the simulations needed more sampling time, as judged from the development of height *vs.* number of events, the sampling time was increased to a maximum of 10000 sampling events all with 10000 moves in between. In order to prevent long equilibration times at low driving forces, the simulations were performed on the same surface for decreasing driving force, i.e. the final surface configurations at higher $\Delta\mu/kT$ were used as the initial surface configuration for simulations at lower $\Delta\mu/kT$.

8.3 Results and discussion

8.3.1 Crystal graph calculation

Using the methods outlined above, the energies of the crystal structures were minimized using a single charge set for all conformers of the three polymorphs. The resulting lattice parameters and lattice energies are listed in Table 8.1. The lattice energies are very close, and given the error associated with the force field, no stability ranking can be made on the basis of these energies. The similarity of the crystal structures, as shown in Figure 8.2, is reflected in the fact that these lattice energies are so close. Next, all pairwise interactions were calculated. For all phases the unscaled interactions below -1.5 kcal·mol^{-1} were used. The included bonds were subsequently scaled to the dissolution enthalpy.

This procedure resulted in crystal graphs in which the total number of bonds between the growth units is equal to 11 for phase **I** and 12 for phases **II** and **III**. The bonds not related by symmetry are listed in Table 8.2. It must be noted that for phase **II** the maximum number of bonds listed in this Table does not correspond to the total number of bonds between growth units, as some bonds are not present for all growth units. This is due to the fact that for this phase, the number of growth units in the asymmetric unit cell, Z', is equal to two.

Table 8.2: Crystal graph bonds for the three phases of Venlafaxine. In the first column the bond offset is listed, in the second the bond strength in kcal·mol^{-1}. For example, the first line indicates a bond going from GU 1 to GU 2 in the same unit cell. This bond has an unscaled strength of -7.81 kcal·mol^{-1} and a scaled bond strength of -3.20 kcal·mol^{-1}. Bonds that are related by symmetry are not listed.

Phase **I**			Phase **II**		
Bond	Unscaled	Scaled	Bond	Unscaled	Scaled
$1-2[000]$	-7.81	-3.20	$1-8[100]$	-8.13	-5.44
$1-3[010]$	-5.98	-2.45	$1-8[000]$	-7.58	-5.07
$1-2[100]$	-4.64	-1.90	$1-5[10\bar{1}]$	-5.83	-3.90
$1-3[000]$	-3.98	-1.63	$1-5[00\bar{1}]$	-4.78	-3.19
$1-1[\bar{1}00]$	-3.58	-1.47	$1-8[110]$	-4.54	-3.04
$1-1[0\bar{1}0]$	-2.58	-1.05	$1-8[010]$	-4.52	-3.02
$1-3[\bar{1}00]$	-1.67	-0.68	$1-1[0\bar{1}0]$	-3.49	-2.34
			$1-1[\bar{1}00]$	-2.54	-1.70
			$1-5[0\bar{1}\bar{1}]$	-1.60	-1.07
			$2-4[0\bar{1}0]$	-4.00	-2.67
			$2-2[0\bar{1}0]$	-3.20	-2.14
			$2-4[\bar{1}\bar{1}0]$	-2.75	-1.84
			$2-2[\bar{1}00]$	-2.72	-1.82

Phase **III**		
Bond	Unscaled	Scaled
$1-3[000]$	-7.59	-4.02
$1-3[100]$	-4.55	-2.41
$1-4[0\bar{1}1]$	-3.84	-2.04
$1-1[\bar{1}00]$	-3.50	-1.85
$1-1[0\bar{1}0]$	-2.70	-1.43
$1-4[001]$	-2.69	-1.42

8.3.2 Experimentally observed habits

Phase **I** exhibits two distinct morphologies, both displayed in Figure 8.3. The (*hkl*) indices were determined using an optical goniometer. Both morphologies have the faces $\{002\}$, $\{10\bar{1}\}$ and $\{012\}$, one has $\{002\}$ as the largest faces (Figure 8.3(a)), the other has $\{10\bar{1}\}$ as the largest faces (Figure 8.3(b)). The difference between the two habits is attributed to the presence of a dislocation on the $\{002\}$ face leading to a spiral growth mechanism for the crystals shown in Figure 8.3(b). The presence of the typical spiral growth pattern on the $\{002\}$ surface was confirmed experimentally using Differential Interference Contrast Microscopy (DICM) for the crystals having the morphology of Figure 8.3(b) and no spirals were found on the $\{002\}$ surface of the crystals having the morphology displayed in Figure 8.3(a). These microscopy images are displayed in Figure 8.4.

The indices of the experimental habit of phase **II** could not be determined using the optical goniometer, so the experimental habit, shown in Figure 8.5, has no indices. Still, it can be seen that also this phase has a plank-like shape, with similar top faces as phase **I**. The crystals of phase **II** consist of domains parallel to the basal face, which is, very likely, $\{002\}$ (*vide infra*). These domains were found using a polarization microscope as alternating extinct and bright striped patterns on the side faces, depending on the orientation of the crossed polarizers. These domains were interpreted as twin domains typical for the monoclinic spacegroup $P\ 1\ 2_1/c\ 1$ of this phase in combination with its layered crystal structure (see Figure 8.2). As a result we can conclude that the basal face is $\{002\}$ and the **b**-axis is parallel to the long axis of the crystals. The presence of these domains and the corresponding domain walls gives rise to a lot of macrosteps and striations on the side and top faces, as can be seen in the lower image of Figure 8.5. Such striations can act as sources for growth steps leading to vicinal orientations. This explains the problem with indexing the habit of phase **II**.

The experimental habit of phase **III** is also a flat plank-like shape, displayed in Figure 8.6. The indices are $\{002\}$ (the basal face), $\{101\}$ (side faces) and $\{012\}$ (top face).

8.3.3 Prediction of morphologies

BFDH

The morphologies were first predicted using the BFDH theory. The results for the three phases of Venlafaxine are displayed in Figure 8.7. As can be seen in these figures, the predicted morphologies of phase **I** and **III** are very similar, due to the fact that the lattice parameters are quite similar. Differences are mainly caused by the difference in spacegroup, $P2_1/c$ for phase **I** and $P2_12_12_1$ for phase **III**. As the unit cell of phase **II** has a **c**-axis that is about twice as long as the **c**-axes of phase **I** and **III**, the predicted shape of phase **II** is more plate-like. None of the predictions of the BDFH theory are very good however,

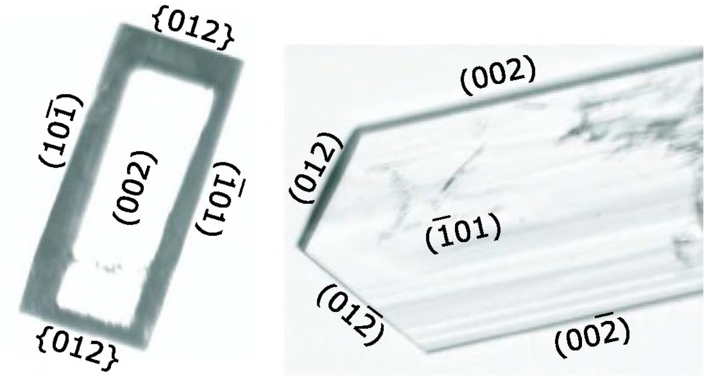

(a) (b)

Figure 8.3: Experimental habits of phase **I** grown from heptane solution. Figure 8.3(a) shows the rectangular morphology without a spiral pattern on {002}, Figure 8.3(b) shows the morphology with a spiral growth mechanism on {002}, leading to a more plank-like morphology with relatively large {$\bar{1}$01} faces.

as square shapes are predicted, instead of the experimentaly observed plank-like morphologies. Also, for phase **I** and **III**, the predicted shapes are too thick in the {002} orientations.

Attachment energies

For phase **I** the FACELIFT procedure results in a set of 170 PBCs and 63 connected nets in 13 crystallographic forms; for phase **II** however, these numbers are much higher because of the larger number of particles in the unit cell. For phase **II** 36922 PBCs and 4427 connected nets in 25 crystallographic forms were found. For phase **III**, 288 PBCs were found which could be combined to form 57 connected nets in 9 crystallographic forms.

The connected net attachment energies of phases **I**, **II** and **III** are shown in Table 8.3. The predicted morphologies obtained from these data are shown in Figure 8.8. This prediction is much better than that of the BFDH method; for phase **I**, the {002} and {10$\bar{1}$} orientations are both predicted correctly. The attachment energy of the {011} orientation is very close to that of {012} orientation, so the former is favored over the latter in the predicted morphology. The observed rectangular plank-like morphology is not reproduced, however, as the predicted morphology is almost square. Phase **II** also has an almost square attachment energy morphology, and orientations {002}, {100}, {$\bar{1}$02} and {011} are predicted. The third phase has the orientations {002}, {101} and {011} correctly predicted, and {110} predicted but not observed. The general shape is too thick and square, as opposed to the elongated plank-like shape of phase **III**, observed experimentally.

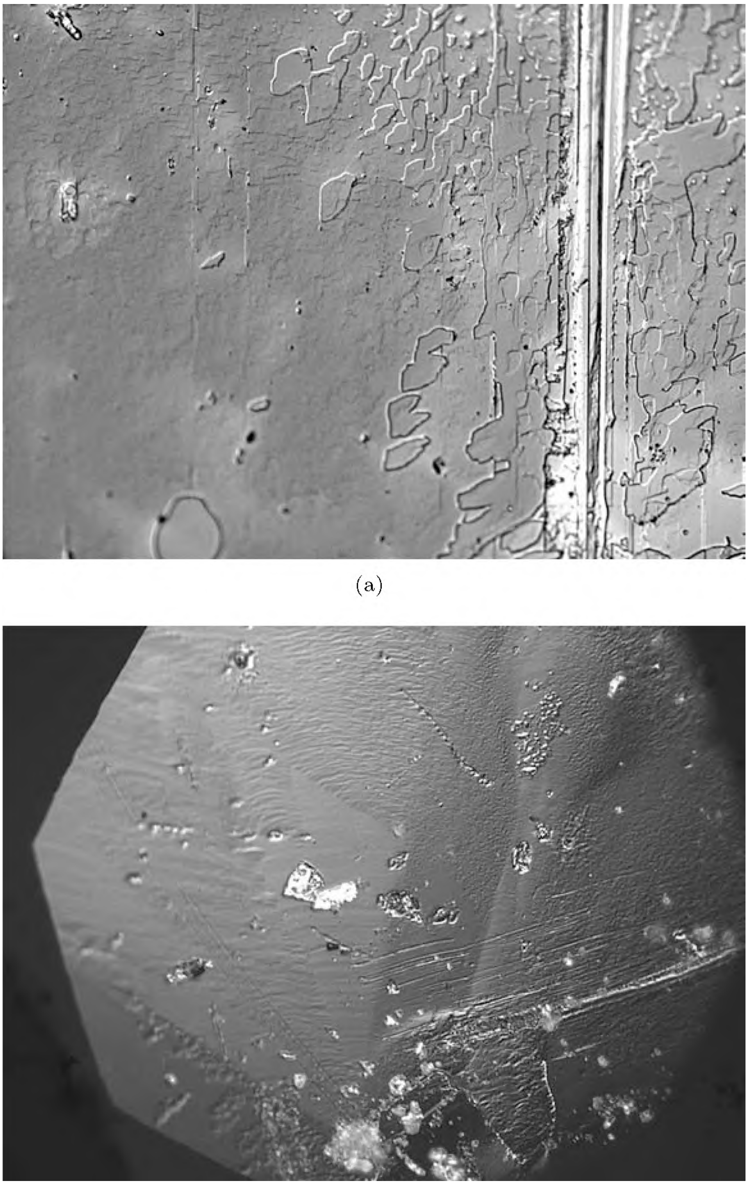

(a)

(b)

Figure 8.4: Differential interference contrast microscopy (DICM) images of phase **I** shows (a) the presence of 2D islands and (b) spiral growth hillocks. The magnification factor is 200x. These micrographs were taken of the {002} surface for samples corresponding to the two different morphologies as displayed in Figure 8.3.

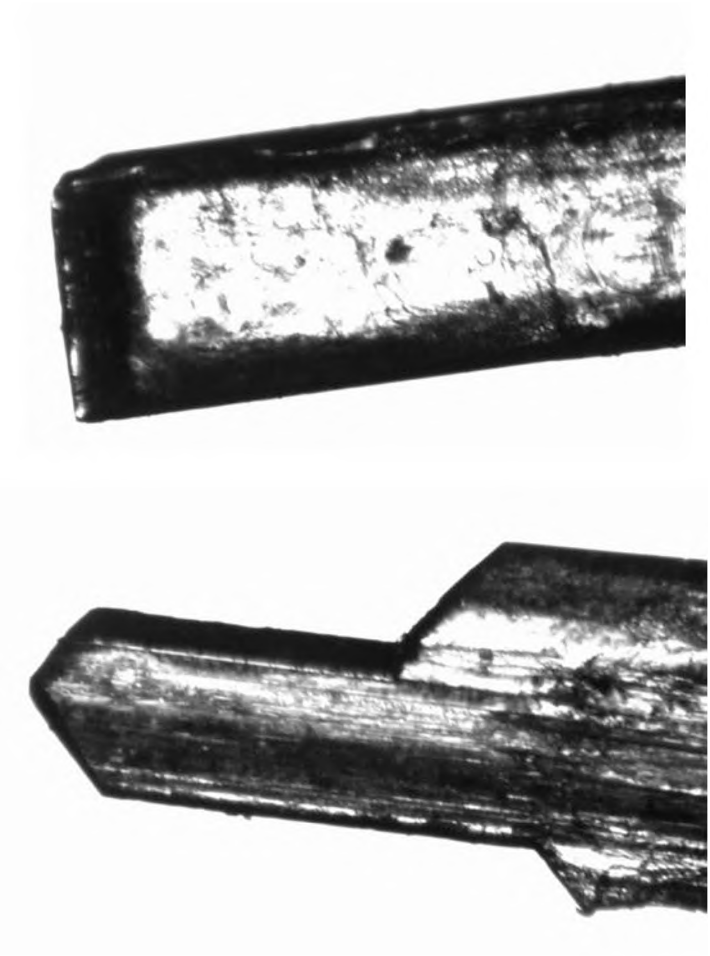

Figure 8.5: Experimental habit phase **II** grown from heptane solution. This habit could not be indexed on a goniometer, so no indices are given.

Table 8.3: F-faces and corresponding attachment energies of the three phases of Venlafaxine

Phase **I**		Phase **II**		Phase **III**	
(hkl)	E_{att} [kcal·mol^{-1}]	(hkl)	E_{att} [kcal·mol^{-1}]	(hkl)	E_{att} [kcal·mol^{-1}]
$\{002\}$	-23.25	$\{00\bar{2}\}$	-24.41	$\{00\bar{2}\}$	-26.14
$\{\bar{1}01\}$	-36.21	$\{0\bar{1}\bar{1}\}$	-79.73	$\{\bar{1}0\bar{1}\}$	-45.25
$\{01\bar{1}\}$	-46.50	$\{012\}$	-86.38	$\{01\bar{1}\}$	-45.83
$\{01\bar{2}\}$	-46.83	$\{10\bar{4}\}$	-92.11	$\{01\bar{2}\}$	-48.13
$\{\bar{1}0\bar{1}\}$	-48.88	$\{013\}$	-93.03	$\{\bar{1}0\bar{2}\}$	-51.33
$\{110\}$	-59.15	$\{10\bar{2}\}$	-93.19	$\{\bar{1}\bar{1}0\}$	-62.12
$\{\bar{1}1\bar{1}\}$	-61.15	$\{\bar{1}00\}$	-94.33	$\{111\}$	-64.81
$\{11\bar{1}\}$	-62.81	$\{\bar{1}0\bar{2}\}$	-95.47	$\{1\bar{1}2\}$	-68.65
$\{1\bar{1}2\}$	-63.46	$\{104\}$	-100.47	$\{\bar{1}1\bar{3}\}$	-73.20
$\{\bar{1}0\bar{3}\}$	-65.46	$\{0\bar{1}\bar{4}\}$	-102.04		
$\{11\bar{2}\}$	-67.45	$\{111\}$	-122.02		
$\{1\bar{1}3\}$	-71.27	$\{\bar{1}\bar{1}0\}$	-123.08		
$\{\bar{1}1\bar{4}\}$	-79.08	$\{\bar{1}\bar{1}1\}$	-125.74		
		$\{\bar{1}\bar{1}\bar{2}\}$	-126.02		
		$\{\bar{1}\bar{1}2\}$	-128.49		
		$\{\bar{1}\bar{1}\bar{3}\}$	-130.02		
		$\{1\bar{1}\bar{3}\}$	-131.23		
		$\{1\bar{1}\bar{4}\}$	-134.41		
		$\{\bar{1}\bar{1}\bar{4}\}$	-135.09		
		$\{\bar{1}15\}$	-138.40		
		$\{\bar{1}\bar{1}\bar{5}\}$	-140.16		
		$\{1\bar{1}\bar{6}\}$	-142.40		
		$\{\bar{1}\bar{1}\bar{6}\}$	-147.76		
		$\{1\bar{1}\bar{7}\}$	-150.50		
		$\{117\}$	-155.37		

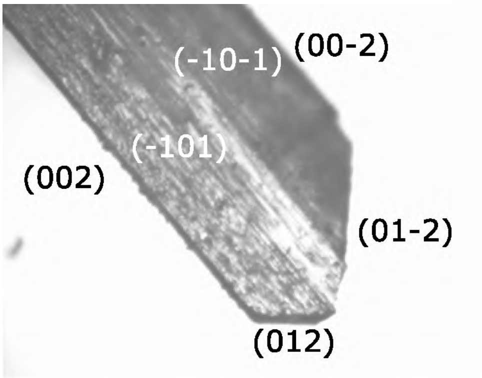

Figure 8.6: Experimental habit phase **III** grown from heptane solution.

Monte Carlo growth simulations

The growth rates of all connected net orientations of phase **I** as a function of the relative driving force $\Delta\mu/kT$ are displayed in Figure 8.9. As can be seen from the figure the three experimentally observed orientations have the lowest growth rate in the right order $R_{\{002\}} < R_{\{10\bar{1}\}} < R_{\{012\}}$. The habit at a relative driving force of $\Delta\mu/kT$=2.4, the lowest value simulated where the {002} form shows growth, is displayed in Figure 8.10.

The existence of two distinct habits in one single crystallization batch (see Figure 8.3) can be explained by the fact that the {002} orientation grows either via a spiral growth mechanism or via a 2D nucleation mechanism. To test this hypothesis, simulations of the {002} orientation with a spiral growth mechanism were also performed. This is accomplished by using a dislocation line bounded by two dislocations with opposite Burger's vectors (see also Figure 8.11). The height of the Burger's vector is equal to the length of the **c**-axis.

The resulting growth morphology of phase **I**, also at a relative driving force of 2.4, with the {002} form having a spiral growth mechanism, is displayed in Figure 8.12. The morphological importance of the {002} face is much lower than without a spiral growth mechanism (see Figure 8.10) and the $\{10\bar{1}\}$ face becomes dominant, as was also seen experimentally.

For phase **II**, the simulated growth rate as a function of $\Delta\mu/kT$ is displayed in Figure 8.13. At $\Delta\mu/kT >$ 7.0, the {002} orientation starts to grow. The morphology at that value for $\Delta\mu/kT$ is displayed in Figure 8.14. As can be seen from this Figure, when comparing it to the experimental morphology, the predicted morphology is not correct. An octagonal flat crystal is predicted, with the large face being {002}, and the side faces $\{10\bar{4}\}$, {110} and {011}. Either $R_{10\bar{4}}$ or R_{011} is too large, resulting not in a plank-like morphology, but in this octagonal shape.

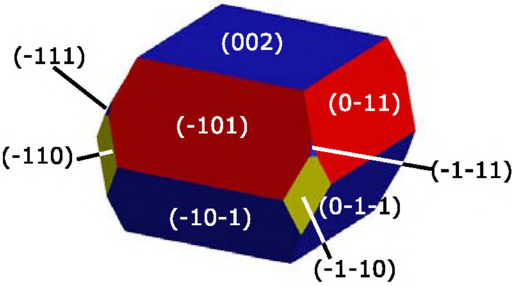

(a) BFDH morphology of phase **I**.

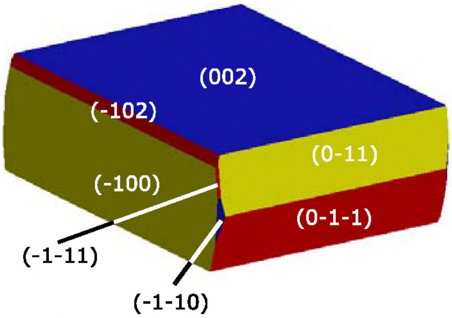

(b) BFDH morphology of phase **II**.

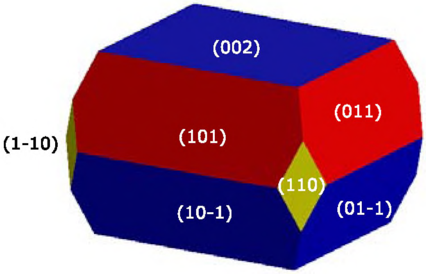

(c) BFDH morphology of phase **III**.

Figure 8.7: The BFDH morphologies of the three phases of Venlafaxine

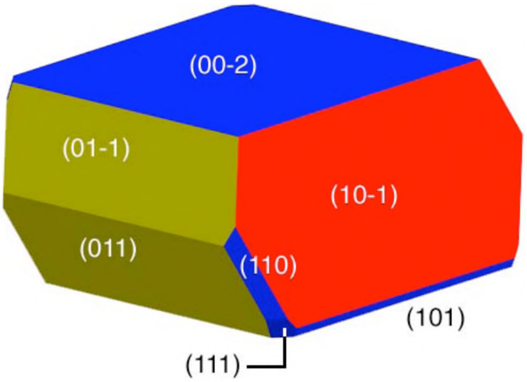

(a) Attachment energy morphology of phase **I**

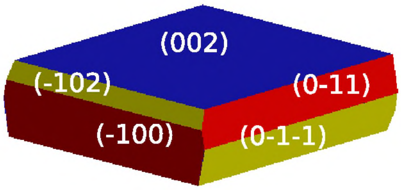

(b) Attachment energy morphology of phase **II**

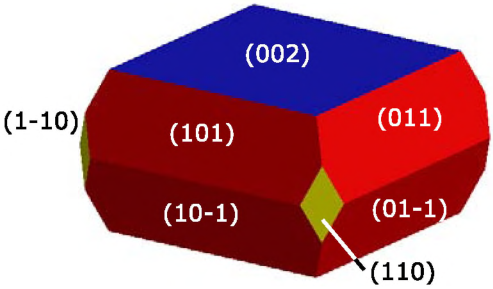

(c) Attachment energy morphology of phase **III**

Figure 8.8: The attachment energy morphologies of the three phases of Venlafaxine.

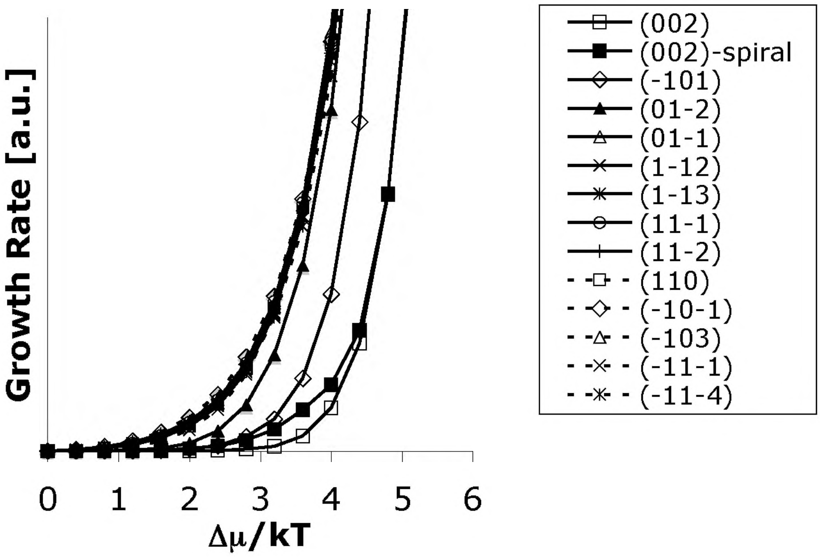

Figure 8.9: Monte Carlo growth rate simulations for phase **I**.

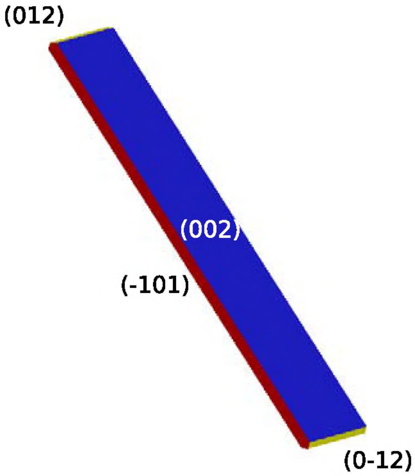

Figure 8.10: Predicted morphology for phase **I** at $\Delta\mu/kT$=2.4.

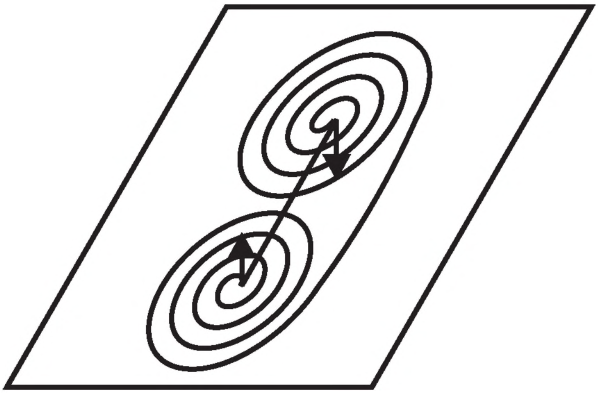

Figure 8.11: Spiral growth scheme used in MONTY. Two dislocations with opposite Burger's vector (indicated with arrows) create a dislocation line from which two opposite spirals can grow.

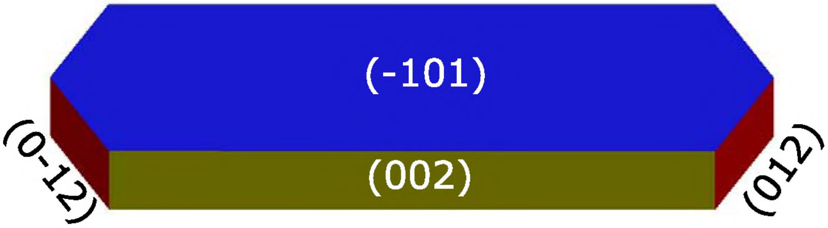

Figure 8.12: Predicted morphology at $\Delta\mu/kT$=2.4 for phase **I** with the {002} orientation having a spiral growth mechanism.

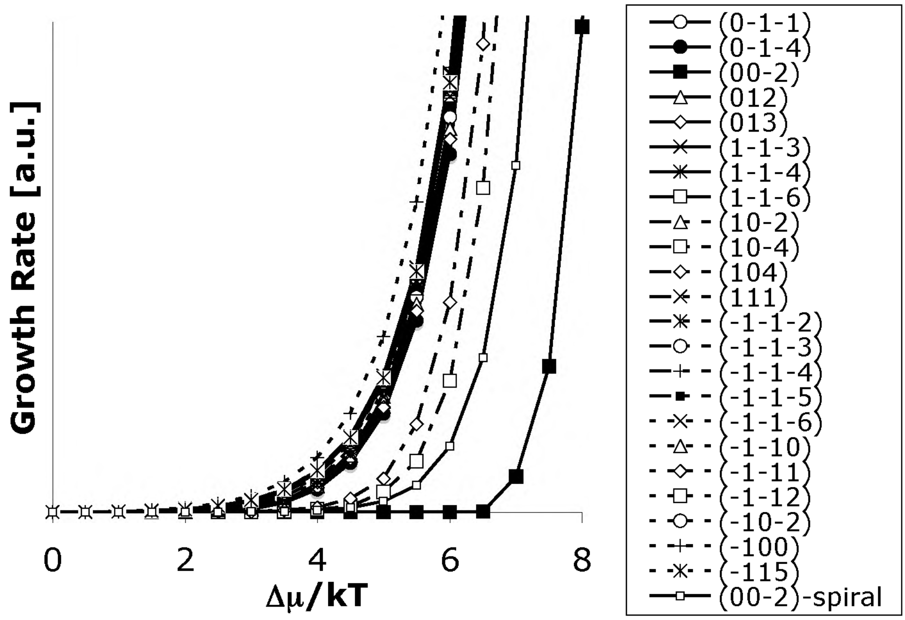

Figure 8.13: Monte Carlo growth rate simulations for phase **II**.

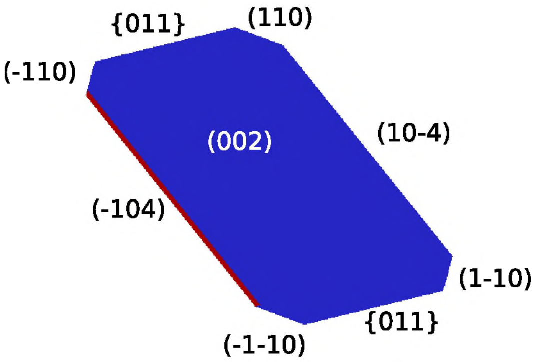

Figure 8.14: Predicted morphology for phase **II** at $\Delta\mu/kT$=7.0.

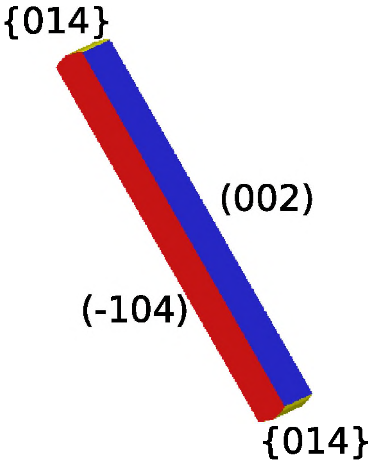

Figure 8.15: Predicted morphology at $\Delta\mu/kT$=4.0 for phase **II** with the {002} orientation having a spiral growth mechanism. The side faces are {104} and the top faces are {014}.

The high driving force at which phase **II** is predicted to start growing, i.e. $\Delta\mu/kT>$ 7.0, hints at the fact that another growth mechanism may be dominant on the {002} orientation. To see the effect of spiral growth, simulations were run using a a spiral growth mechanism. Using the spiral growth mechanism for phase **II** a more plank-like morphology is predicted at lower driving force value, $\Delta\mu/kT$=4.0 (see Figure 8.15). This shape corresponds better to the experimentally observed morphology. Comparing, however, the orientation of the top faces with the experimentally observed ones (see Figure 8.5), the prediction seems to be incorrect. As discussed before, the presence of domains in this phase leading to striations on the top and side faces probably gives rise to ill-defined orientations, which could not be indexed. The growth of these faces is then deterimned mainly by the domain boundaries acting as step sources, rather than by a 2D nucleation mechanism. Such an effect of domain walls has been observed for, e.g., gibbsite crystals.[121]

The simulated growth rates of phase **III** are displayed in Figure 8.16 and the predicted morphology at $\Delta\mu/kT$=4.0 is displayed in Figure 8.17. Although the predicted morphology is quite close to the experimentally observed habit, the predicted indices of the side faces are not correct. The short edges of the rectangle are predicted to be {101}, but actually they are {012}, and vice versa. As phase **III** grows as a conglomerate of stacked domains of both enantiomorphs[120] the relative morphological importance of these two faces might be influenced by that. Face indexation on a goniometer shows that both the conglomerate and the enantiopure crystals have the same indices and morphological importance, in contrast to phase **II**. This is explained by the difference in space group symmetry for th phases: phase **II** has a monoclinic space group (P 1 2_1/c 1) with its

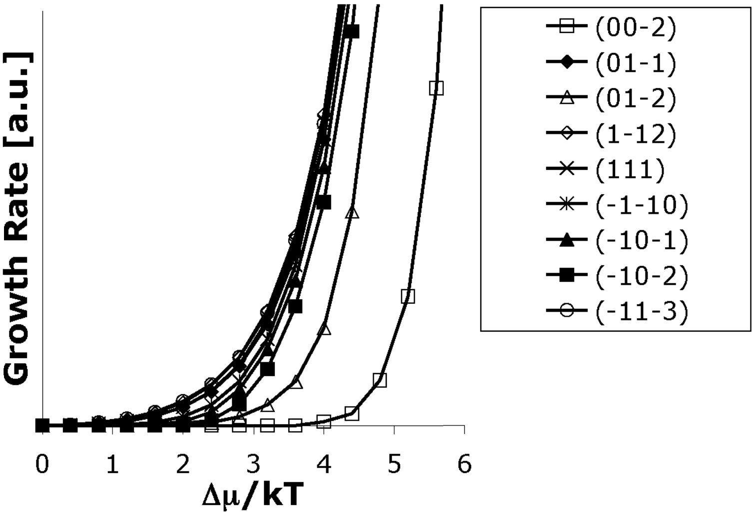

Figure 8.16: Monte Carlo growth rate simulations for phase **III**.

unique axis parallel to the long axis of the crystal. This gives rise to mutually inclined microfacets on the top faces for the twin domains. This, together with the domain boundarys acting as step sources explains the inability to index the crsytals of phase **II**. Phase **III**, on the other hand, has an orthorhombic space group ($P2_12_12_1$) leading to no inclination between the microfacets on the top faces. The presence of the domains, however, can still lead to different growth rates for the topfaces, as well as the side faces, compared to the predictions.

8.4 Conclusions

From the free base form of the anti-depressive drug Venlafaxine, the dominant morphologies of three polymorphs were studied experimentally. Using theories with different levels of complexity, the observed growth morphologies were correlated with the predicted morphologies. For all polymorphs the predicted morphology according to the BFDH theory does not give good results. The Hartman-Perdok theory does better, but fails to predict some indices and - more importantly - fails to predict the rectangular plank-like habits of the polymorphs and instead predicts square plank or cube-like morphology.

The results of the Monte Carlo growth simulations, which account for both the driving force and the growth mechanism, are very promising. For phase **I** the predictions reproduce the experimentally observed morphology using a 2D nucleation mechanism. A second habit, also observed experimentally, in which

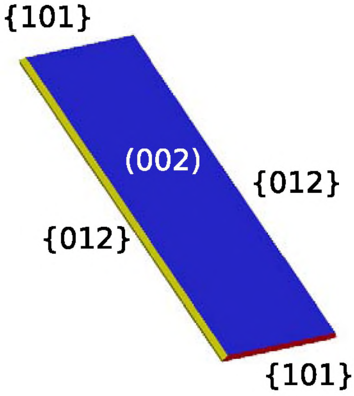

Figure 8.17: Predicted morphology for phase **III** at $\Delta\mu/kT$=4.0

$\{\bar{1}01\}$ is the dominant face, is found for phase **I** when a spiral growth mechanism is used for the $\{002\}$ orientation.

The simulated growth rate of the $\{002\}$ orientations of phase **II** was very low until high driving forces. Consequently, the predicted morphology did not agree very well with the experimentally observed morphology. When a spiral growth mechanism was used here, the morphology could be predicted at lower $\Delta\mu/kT$ values. This reproduced the experimentally observed morphology more accurately. The observed domains in the crystal structure of phase **II**, interpreted as twin domains, may explain the differences between the morphologies obtained using simulations of 2D nucleation and the observerd morphology. The twin domains may act as step sources, facilitating growth at lower driving force.

The simulations of phase **III** also show a rectangular plate-like habit, in close correlation with the observed habit. The relative morphological importance of the $\{101\}$ and $\{012\}$ faces is not reproduced however; the $\{101\}$ faces are predicted to be at the short end of the rectangle, whereas the $\{012\}$ faces are experimentally observed to be the short side of the rectangle, and vice versa.

It can thus be concluded that the MONTY simulations are a promising tool for studying crystal growth. Although not all indices of phase **III** could be predicted correctly, all phases did give a semi-quantitative agreement between the experimentally observed habit and the predicted morphology, as far as the overall shape is concerned. The inability of the BFDH method and attachment energy method to predict the morphology correctly for any of the phases shows that the Monte Carlo simulations are a welcome addition to the set of tools for morphology prediction. It is not surprising that when crystals show a more complicated growth behavior than that captured by the mechanisms used by MONTY, e.g. when twinning causes striations and macrosteps, which in turn act as step sources, the simulations no longer show a good agreement with the observed growth behaviour.

Chapter 9

Polymorphism or structural disorder in Ondansetron

9.1 Introduction

Active pharmaceutical ingredients, which are commonly organic molecules with a molecular weight below about 500, have the tendency to crystallize in different crystalline structures. This phenomenon is called polymorphism[122] and which polymorph is formed depends on the conditions during crystallization, for instance the solvent used, the supersaturation, the temperature and the pressure employed during crystallization. Also the crystallization method has an influence on polymorph formation, e.g. cooling crystallization, evaporative crystallization, anti-solvent addition, vapor growth, grinding, etc.

Polymorphs are relevant to the scientific community as well as to the industry. From a scientific point of view, the occurrence of different polymorphs is interesting as it is an expression of the subtle interplay of various supramolecular interactions and preparation conditions. As such, it gives the opportunity to prepare tailored materials, for instance with respect to crystal morphology, particle size distribution, thus enhancing processing properties. Industry, and in particular the pharmaceutical industry, are interested in polymorphism as different polymorphs can give rise to different bio-availabilities of a drug substance. Generally, the most stable polymorph is used in a formulation of a drug product, to prevent transformation of a crystalline form in a marketed product, adversely affecting the bio-availability. A famous example of this is found in Abbott's formulation of ritonavir, for which a more stable polymorph appeared when the product was already on the market.[123] The more stable polymorph had much lower solubility and was consequently not compatible with the semi-solid formulation of the initially formed, metastable polymorph.

As creating a new polymorph is regarded as a novel 'invention', polymorphs can be patented. It is therefore of crucial importance to understand what constitutes a polymorph, a question that has for instance been addressed in a number of papers of Zaworotko *et al.* and Desiraju *et al.* on the structure of poly-

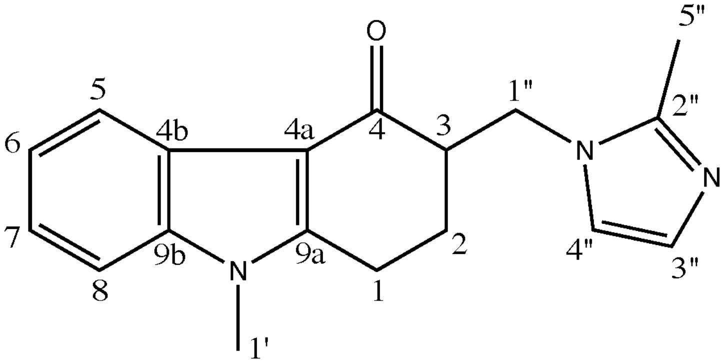

Figure 9.1: Molecular structure of Ondansetron

morphs of acetylsalicylic acid (Aspirin).[124, 125, 126]. There it was argued by the former authors that a second form of aspirin was found, whereas the latter authors argue that in fact aspirin consists of two different, intergrown crystal forms. Other forms of polymorphism, like tautomeric or conformational polymorphism, can have definition issues. For tautomeric polymorphism, the question is whether we deal with the same molecule between polymorphs, and for conformational polymorphism the question is how small the differences in conformations can be to still be able to speak of distinct polymorphs.

The molecule studied in this chapter, Ondansetron, is a serotonin 5-HT$_3$ receptor antagonist, used mainly to treat nausea and vomiting following chemotherapy. The molecular structure is shown in Figure 9.1. The crystal structure of Ondansetron is not known, although in various patent applications different polymorphs are claimed, judged from their different powder x-ray diffraction patters and melting points.[127, 128] From the results shown in this chapter, it is hypothesized that the structure of Ondansetron is in fact a solid solution of enantiomers and that the differences in XRPD patterns can be explained by small differences in mesoscopic structure, like local order, domain size and mosaicity, and, possibly, a small difference in water content. Thus, in addition to the aforementioned intergrowth of two crystal structures, tautomeric polymorphism and conformational polymorphism, another area where the definition of polymorphism is put to the test is addressed.

9.2 Methods

9.2.1 Sample preparation

Solution growth

Two samples of solid Ondansetron were prepared in solution, ODS-1 and ODS-2. ODS-1 was prepared using 0.5 g of Ondansetron dissolved in a mixture of 25 mL of ethanol and 10 mL of water while heating. The clear solution was cooled to room temperature and left at that temperature for a few days. The crystals formed were filtered off and dried in air for 2 days. NMR analysis showed that no ethanol was present in the sample, and the TGA mass-loss observed was 1.8%. ODS-2 was prepared using 0.3 g of Ondansetron dissolved in 50 mL of methanol while heating. The clear solution was cooled to room temperature and left at that temperature for a few days. The crystals formed were filtered off and dried in air for 2 days. Again, NMR showed no methanol in the sample, and the TGA mass-loss was 1.6%.

Vapor phase growth

In order to obtain suitable crystals for single crystal XRD, vapor growth was performed in a glass tube at 433 K under a reduced pressure of $1.9{\cdot}10^{-4}$ bar. The starting material was placed at the lower end of the tube, which was positioned in the hot part of the furnace. Crystals were deposited at the colder higher end of the tube, giving sample ODS-3.

9.2.2 X-ray powder diffraction

X-ray powder diffraction was performed on the investigated samples using a Bruker D8 AXS Advance X-ray Diffractometer with a hot-humidity stage and VÅNTEC-1 detector. The D8 was equipped with a Johansson type monochromator. The detector had an effective angular region of 2°. The data were collected in reflection geometry using monochromatic Cu $K\alpha_1$ radiation. The climate chamber experiments were performed using a heating rate of 1°C/min, while keeping the temperature constant during 10 minutes after each heating step of 10°C. Upon heating, the sample was flushed with dry nitrogen; upon cooling with ambient air.

9.2.3 Single crystal X-ray diffraction

A single crystal was mounted in air on a glass fiber. Intensity data were collected at -65°C. A Nonius KappaCCD single-crystal diffractometer was used (phi and omega scan mode) using graphite monochromated Mo-$K\alpha$ radiation. Unit cell dimensions were determined from the angular setting of 17 reflections. Intensity data were corrected for Lorentz and polarization effects. SADABS multi-scan correction[129] was applied. The structure was solved by the program CRUNCH[130] and was refined with standard methods using SHELXL97[131] with anisotropic parameters for the non-hydrogen atoms. All hydrogens were placed at calculated positions and were freely refined riding on the parent atoms. Initial refinement showed exceptional large and anisotropic thermal ellipsoids for atoms 2 and 3 (in both molecules in the asymmetric unit) together with a bad geometry for these atoms. This indicated that these atoms are disordered over two positions which corresponds to two possible conformations of the Ondansetron molecules. A suitable model describing this static disorder could be defined and refinement led to acceptable geometries for the resulting positions of atoms 2 and 3. Refinement of the occupancy factors for the possible conformers of the Ondansetron molecules showed that for both symmetry independent molecules the two conformations are almost equally present. From a difference Fourier map a water molecule could be located that has an occupancy factor around 50 percent. The (2-methyl-1H-imidazol-1-yl)methyl sidegroup of one of the Ondansetron molecules is badly defined by the data and could only be refined by restraining its geometry to the one of the other molecule. Apparently the disorder in the conformation in the six-membered ring formed by atoms 1, 2, 3, 4, 4a and 9a also influences the orientation of this sidegroup. A structure determination summary, a list of atom coordinates, a list of bond lengths and angles, a list of anisotropic displacement parameters and a list of hydrogen coordinates are given in Table 9.3, 9.4, 9.5, 9.6 and 9.7 respectively (see Appendix).

9.2.4 Karl-Fischer titrations

To determine the water content of the samples, Karl-Fisher titrations were performed. These titrations generally have the following reaction scheme[132]:

$$\underset{\text{[alcohol]}}{\mathrm{ROH}} + \mathrm{SO_2} + \underset{\text{[base]}}{\mathrm{R'N}} \longrightarrow \underset{\text{[alkylsulfite salt]}}{\mathrm{[R'NH]SO_3R}} + \underset{\text{[water]}}{\mathrm{H_2O}} + \underset{\text{[iodine]}}{\mathrm{I_2}} + 2\,\mathrm{R'N} \longrightarrow$$

$$\underset{\text{[hydroiodic acid salt]}}{2\,\mathrm{[R'NH]I}} + \underset{\text{[alkylsulfate salt]}}{\mathrm{[R'NH]SO_4R}}$$

The solvent is a primary alcohol, which reacts with sulfur dioxide (SO_2) and base to form an intermediate alkylsulfite salt. When this salt is oxidized with iodine (I_2) to form an alkylsulfate salt, this reaction consumes water. When all the water has reacted, the excess iodine is detected voltammetrically.

9.2.5 Molecular modeling

Molecular mechanics modeling was performed using the Dreiding v2.21 force field[88], as implemented in Cerius^2.[89] Atomic partial charges were generated using the Gasteiger charge equilibration method.[133] The geometry of crystal structures was optimized using Ewald summation for the van der Waals and electrostatic interactions. A constant value of ϵ_r was used in the electrostatic calculations. Energies of individual molecules were calculated without a cutoff distance for van der Waals and electrostatic interactions. Lattice energies were calculated by subtracting the total energy of the individual molecules from the total energy of the crystal structure.

9.2.6 Differential Scanning Calorimetry

To study the thermal behavior, DSC was employed using a Mettler Toledo DSC822e machine. Three heating rates were used, 10, 1 and 0.1°C/min, as different heating rates can give very different melting points and transitions.

9.2.7 Solid state NMR

Spectra were recorded on a Chemagnetics/Varian CMX-Infinity three channel 400 MHz machine, using variable cross polarization and interrupted decoupling while using magic angle spinning at 6.4 kHz. Using different contact times (0.05 and 2.5 ms) the peak assignments of the carbon atoms were made. ^{13}C chemical shift prediction was done using Chemdraw Ultra, version 10.0.

9.3 Results and discussion

9.3.1 Sample preparation

Solution growth

Samples obtained from ethanol/water (ODS-1) and methanol (ODS-2) were inspected using optical microscopy with oil immersion. The morphology of the crystallites was found the be needle-like for both samples. Pictures of both samples are shown in Figure 9.2.

Vapor phase growth

Growth of crystals from vapor resulted in small (0.19 x 0.05 x 0.03 mm) crystals, which were used for single crystal X-ray diffraction.

9.3.2 Crystal structure determination

Single Crystal X-ray Diffraction

Both molecules in the asymmetric unit show conformational disorder which has a specific consequence for the chirality of the Ondansetron molecules. Switching between the two possible positions of atoms 2 and 3 also means a switching between the R and S enantiomer. This means that four combinations in the

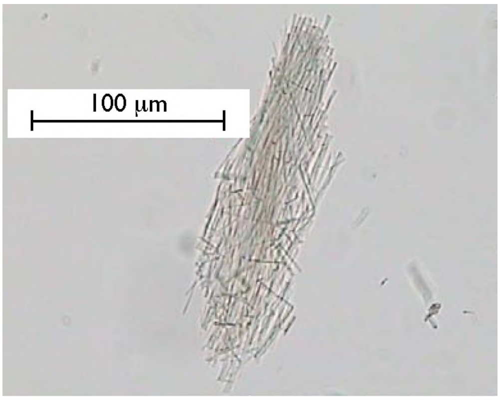

(a) ODS-1

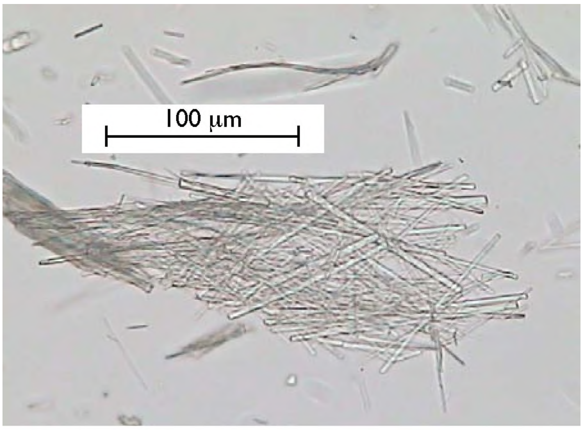

(b) ODS-2

Figure 9.2: Microscopy images of ODS-1 and ODS-2 obtained with oil immersion.

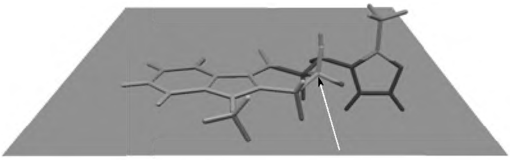

(a) (R)-Ondansetron

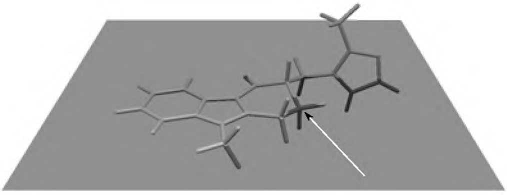

(b) (S)-Ondansetron

Figure 9.3: The two molecules from the asymmetric unit resulting from the single crystal X-ray diffraction structure refinement. The R-enantiomer is shown in (a), the S-enantiomer in (b). A grey plane has been drawn through the indole fragment of the molecules. In both cases an arrow has been drawn to indicate the position of carbon 2 being either above the grey plane in (a) or below the grey plane in (b).

asymmetric unit cell are possible for $Z' = 2$: R-up+R-up, R-up+S-down, S-down+R-up and S-down+S-down (see Figure 9.3 and Section 9.3.2).

From the single crystal X-ray structure a residual water molecule was found to bridge the imidazole side groups of the Ondansetron molecules in the solid state. As the sample was obtained using growth from the vapor phase, at low pressure and elevated temperature, it is very unlikely that this water was present during the crystal formation. The presence of the water in the structure was confirmed using Karl-Fisher titrations, and determined to be approximately one molecule of water per unit cell, i.e. 1 water molecule per 4 Ondansetron molecules.

X-ray Powder Diffraction

The powders of ODS-1 and ODS-2 gave similar XRPD spectra, as can be seen from Figure 9.4. In the difference plot, it can be seen that some peaks appear at slightly different 2θ-values, which may indicate polymorphism, for instance due to small differences in conformation of the molecules, giving rise to small expansions or contractions of the unit cell.

Differential Scanning Calorimetry

The DSC thermograms of ODS-1 and ODS-2 are shown in Figure 9.5. The melting peaks observed are 246, 235 and 217°C for ODS-1 and 245, 235 and

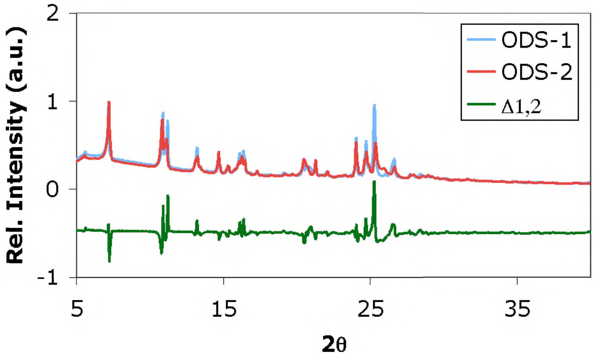

Figure 9.4: XRPD patterns of as-prepared ODS-1 and ODS-2, including a difference plot. The difference plot is shifted downwards for clarity to prevent overlap of difference and XRPD spectra.

215°C for ODS-2, for the heating rates of 10, 1 and 0.1 °C/min respectively. Looking at the magnified portions of the DSC thermograms, it can be seen that a small, broad event occurs between 50 and 150°C. This is attributed to the loss of water.

Dehydration studied by XRPD

In a second experiment, the samples were measured in a climate chamber, where temperature and humidity were controlled separately. Upon heating of the samples to 155 °C, water is liberated from the crystal structure, giving an anhydrate. Interestingly, the ODS-1 and ODS-2 samples give slightly different anhydrate powder patterns at elevated temperature, as is shown in Figure 9.6. Especially the location of the second large peak (around 10° 2θ) in both powder patterns, associated to the overlapping reflections of $(01\bar{1})$, (012) and (002), is shifted with a difference of approximately 0.13° 2θ. Upon cooling under ambient conditions the structures reverted back to their original hydrated patterns. The differences in peak intensity might be an indication of preferred orientation in one of the anhydrate structures. The morphology of both forms, however, is a fine needle oriented along [100], making this interpretation unlikely.

Solid-state NMR

To get more detailed information about possible disorder in the solid state for both ODS-1 and ODS-2, solid-state NMR was used. The ^{13}C spectra for powder samples of ODS-1 and ODS-2 are shown in Figure 9.7 and the peak assignments are listed in Table 9.1. As can be seen from the table, there are no large differences in peak positions and the peaks appear approximately at the predicted chemical shift values. For both ODS-1 and ODS-2, the peak that belongs to

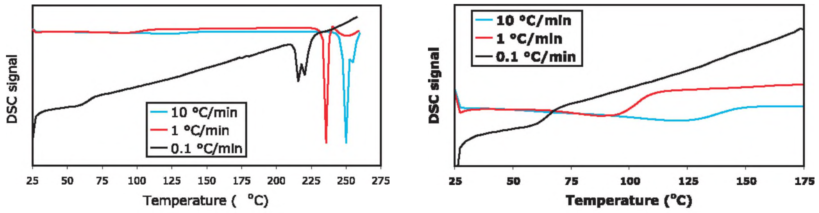

(a) ODS-1 (b) ODS-1

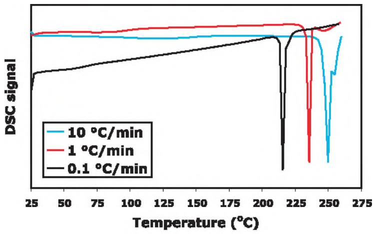

(c) ODS-2 (d) ODS-2

Figure 9.5: DSC thermograms of ODS-1 and ODS-2 with three different heating rates. Figures (b) and (d) show magnified sections, to more clearly show the loss of water at lower temperatures.

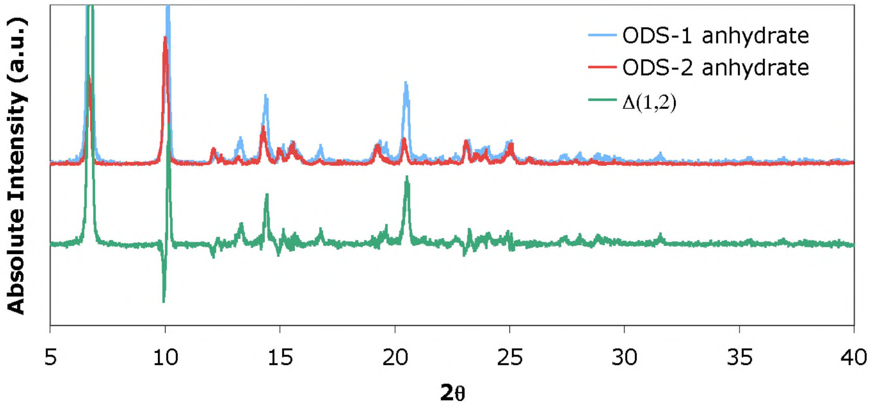

Figure 9.6: XRPD spectra of the anhydrates of ODS-1 and ODS-2, including a difference plot. The difference plot is shifted downwards for clarity to prevent overlap of difference and XRPD spectra.

Table 9.1: Solid state NMR peak assignments for ODS-1 and ODS-2.

Carbon	ODS-1 [ppm]	ODS-2 [ppm]	Predicted [ppm]
5”	13.25	12.72	13.9
5”	14.03	14.00	
5”	15.39	15.33	
1	20.76	20.81	20.2
1	21.60	21.58	
2	24.57	24.57	24.5
2	25.48	25.05	
1’	28.52	28.48	29.5
1”	43.28	43.32	45.5
1”	45.37	45.40	
1”	48.51	48.48	
3	46.63	46.55	49.3

carbon 5”, at approximately 13 ppm, are split in three separate peaks. The orientation of the (2-methyl-1H-imidazol-1-yl)methyl sidegroup involving carbon 5”can be with the methyl group above or below the conjugated indole ring system. Other peaks (carbon 1 at around 21 ppm, carbon 2 at around 25 ppm and carbon 1” at around 45 ppm) also show splitting in two or three peaks. The peak-splitting of these carbons can be rationalized by the fact that these carbon atoms are affected by the two possible conformers (see Figure 9.8), that give rise to different surroundings of these atoms in the solid state. As more peaks are observed than are expected based on the number of molecules in the asymmetric unit, this is an indication towards disorder in the solid state.

Modeling of conformers

To get insight into the possible conformations of the Ondansetron molecules in the solid state, molecular modeling was performed. In particular, the influence of the starting conformation on the minimized geometry of the crystal structure was studied. As a starting point the (badly resolved) single crystal X-ray structure from the vapor-grown crystal was taken. This structure has space group $P\bar{1}$, i.e. has an inversion center. This implies that the two molecules in the asymmetric unit can be either both R or both S, or one R and the other S. In all cases, the inversion center will give the other enantiomer, leading to the racemic compound. From the single crystal structure, the chirality of the Ondansetron molecules could not be established, and that leads, in combination with two molecules in the asymmetric unit, and two different ring conformations (see Figure 9.8), to a total of 16 different unit cell structures.

Four starting conformations were selected from a conformer search in which the two dihedral angles of the bonds between carbons 3 and 1änd 1änd the

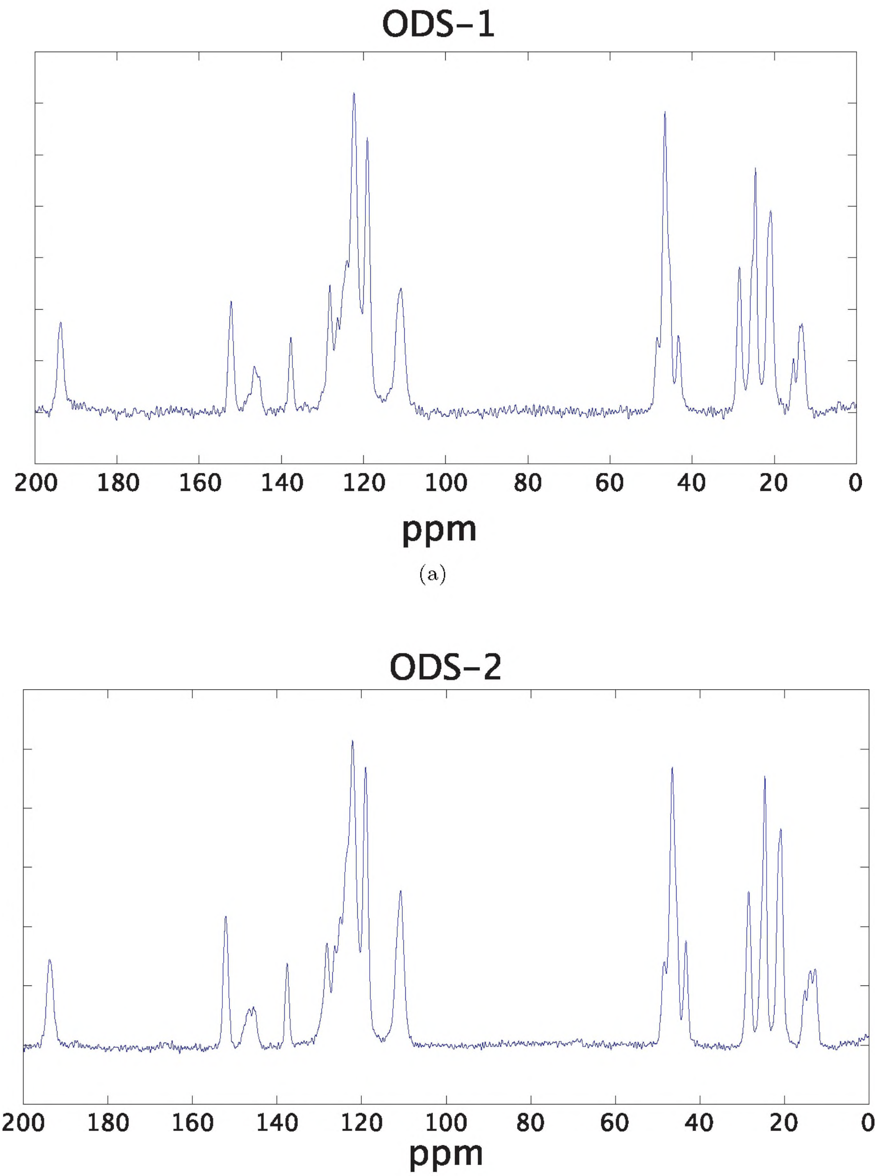

(a)

(b)

Figure 9.7: Solid state ^{13}C-NMR spectra of ODS-1 (a) and ODS-2 (b).

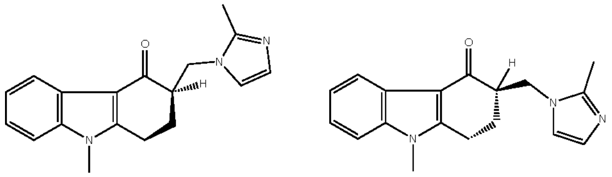

(a) R-Ondansetron ‘up’ (b) R-Ondansetron ‘down’

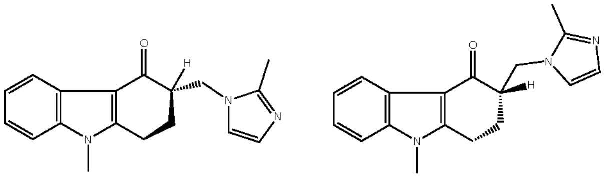

(c) S-Ondansetron ‘up’ (d) S-Ondansetron

Figure 9.8: Two conformers for each enantiomer of Ondansetron, depending on the orientation of the puckered six-membered ring.

Table 9.2: The 4 possible solid state structures for Ondansetron.

Molecule 1				Molecule 2				Lattice Energy
Before opt.		After opt.		Before opt.		After opt.		[kcal·mol^{-1}]
R/S	Ring	R/S	Ring	R/S	Ring	R/S	Ring	
R	Up	R	Up	R	Up	R	Up	-33.128
R	Up	R	Up	S	Down	S	Down	-33.571
S	Down	S	Down	R	Up	R	Up	-33.014
S	Down	S	Down	S	Down	S	Down	-33.685

imidazole nitrogen were varied systematically. The four starting conformations were either 'R-up', 'R-down', 'S-up' or 'S-down' (see Figure 9.8). Each generated conformer was minimized, thus finding the combination of the two dihedral angles having the lowest energy. These four starting conformers were used two at a time to generate the asymmetric unit of the crystal structure, by aligning the well-resolved conjugated indole ring system from the single crystal X-ray structure with the molecules generated from the conformer search. Rebuilding the crystals followed by subsequent minimization of the crystal structure gave the lattice energies (see Table 9.2). This last minimization was performed in a two-step procedure: first the newly placed molecules were allowed to find their minimum energy geometry in the crystal structure without changing the cell parameters and in a second minimization run, the cell parameters were allowed to relax too. This was done to prevent large changes in the cell parameters upon minimization of the newly placed molecules in the crystal, which might have unfavorable intermolecular interactions due to their initial conformations. From the building of the crystals and subsequent minimization, it was found that only combinations of the R-enantiomer having the 'up' ring-puckering and the S-enantiomer having the 'down' puckering led to crystal structures in which 1) crystal structures could be obtained without molecules overlapping, 2) the ring puckering was left unchanged upon minimization and 3) the lattice parameters did not change much compared to the known lattice parameters. This corresponds to the findings of the single crystal X-ray diffraction (see Section 9.3.2). As can be seen from Table 9.2, four possible crystal structures are found when the R-up molecules and S-down molecules are positioned in any combination, without significant differences in lattice energy: the four lattice energies are within 1 kcal·mol^{-1}, which is within the error associated with the forcefield used. In Figure 9.9 space-filling models of both the R-up and S-down configuration are shown; it can be seen that the side group occupies more or less the same space in both cases.

9.3.3 Further discussion

Considering the results of all techniques employed, detailed discussion of the structure of Ondansetron, obtained as samples from ethanol/water and methanol and from vapor growth experiments becomes possible. From the single crystal X-ray it was found that molecular disorder is present in the structure: at each site in the solid either an R-up or and S-down molecule can be found. The XRPD patterns show that there is very little difference in the structure of ODS-1 and ODS-2, and an explanation for this may be found in differences in mesoscopic structure, like local order, domain size and mosaicity, and, possibly, a small difference in water content. Upon heating the two samples under dry conditions, water is liberated from the solid materials and two slightly different anhydrate powder patterns are found, which revert back to their original hydrate patterns upon cooling under ambient conditions. In light of the disorder

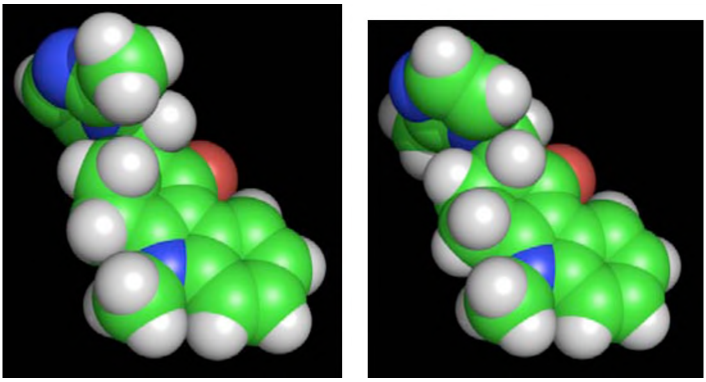

(a) (b)

Figure 9.9: Two conformers of Ondansetron; (a) shows the S-down conformer, (b) shows the R-up conformer.

hypothesis, the differences in the two anhydrate patterns may be explained by differences in local structure and crystallinity. As water is evaporated from the samples before the melting occurs, as was found in the DSC and TGA analyses, this means that the two anhydrates, which gave slightly different powder patterns, do have the same melting points.

Solid-state NMR confirms the disorder: the 5" carbon in the sidegroup shows 3 different peaks, which can be associated with three different surroundings in the solid state, originating from the four combinations. This gives rise to three different types of neighbors: R-up next to R-up, R-up next to S-down and S-down next to S-down. The different ring puckering values are also reflected in two different peaks for carbon atoms 1 and 2. Lastly, the results of molecular modeling again confirm the disorder hypothesis. Four different combinations can be formed of the 'R-up' and 'S-down' molecules in the asymmetric unit with Z'=2. These four combinations all give lattice energies that lie within 1 $\text{kcal}\cdot\text{mol}^{-1}$, which indicates that there is no energetically favorable combination: each molecule, either in the 'R-up' or 'S-down' conformation, can be built into the crystalline lattice without a significant energy difference. This then leads to the conclusion that the structure of Ondansetron is in fact a solid solution.

The morphology of the samples grown from methanol and ethanol/water solutions also sheds light on the disorder hypothesis. The crystals obtained are all needle-like. For needle-like crystals it has been found that the growth is fast in the needle direction because of very low or absent barriers for incorporation of molecules, even at very low supersaturation.[30, 31, 49] When molecules are incorporated that fast into the solid, the likelihood for the occurrence of defects is larger. In this case, the 'defect' is found in the fact that the crystalline lattice does not discriminate between the different enantiomers when they are being built in, only their conformation: R-up and S-down are built in, not R-down nor S-up. As changing the conformation of the molecules between the 'up' and 'down' ring-puckering is thought to be relatively easy, the molecule adapts its conformation as needed upon crystallizing.

To come back to the question whether the structures found should be regarded as polymorphs or not, we can say that the two hydrates, ODS-1 and ODS-2 may be slightly different in terms of their powder patters, but that due to the solid state disorder found from NMR and molecular modeling these two structures are not polymorphs. Rather, they are two different manifestations of a solid solution. The two anhydrates, found upon heating the two samples under dry nitrogen, can also not be regarded as different polymorphs, as they have the same melting point, as found from DSC. The small differences in the powder patterns, both for the hydrated and dehydrated samples, may be explained by differences in crystallinity and local order. The observation that upon hydrating the anhydrates, the XRPD patterns revert to their original patterns is an indication that the local disorder can be considered as a "frozen-in" structure, that is determined by the presence of water in its growth history.

9.4 Conclusions

The crystal structure of Ondansetron was studied using a variety of methods, including single crystal X-ray diffraction, powder X-ray diffraction, solid-state NMR and molecular modeling. For two samples, obtained from methanol and ethanol/water, it was found that their crystal structure is in fact a solid solution of enantiomers: at each lattice site either an R- or an S-enantiomer can be present, each in a different conformation. These combinations of enantiomer and conformation give rise to two molecular configurations that do not differ to a great extent.

These results show that powder patterns that differ only slightly are not enough to fully characterize the existence of two different polymorphs. In the case of Ondansetron, additional techniques were required to get proper insight in the reasons for the small differences of the hydrated and dehydrated samples. This leads to the conclusion that even in the case of small but clear differences between powder patters, answering the question whether to speak of two different polymorphs based on their powder patterns alone does not suffice. Further characterization, for instance using DSC, solid-state NMR and molecular modeling, is necessary for a complete picture.

9.5 Appendix

Identification code	ZJAK22
Crystal colour	translucent colourless
Crystal shape	rough rod
Crystal size	0.19 x 0.05 x 0.03 mm
Empirical formula	C18 H19 N3 O1.25
Formula weight	297.36
Temperature	208(2) K
Radiation / Wavelength	MoKα (graphite mon.) / 0.71073 Å
Crystal system, space group	Triclinic, P-1
Unit cell dimensions	a, α= 7.3325(15) Å, 68.76(11) °
17 reflections	b, β= 13.06(2) Å, 89.46(4) °
2.460 ¡ theta ¡ 22.000)	c, γ= 16.871(13) Å, 86.47(6) °
Volume	1502(3) Å^3
Z, Calculated density	4, 1.315 Mg/m^3
Absorption coefficient	0.085 mm^{-1}
Diffractometer / scan	Nonius KappaCCD with area detector phi and omega scan
F(000)	632
Theta range for data collection	2.46 to 22.00 °
Index ranges	$-7 \leq h \leq 7$, $-13 \leq k \leq 13$, $-17 \leq l \leq 17$
Reflections collected / unique	24309 / 3683 [R(int) = 0.2532]
Reflections observed	1738 ([Io¿2σ(Io)])
Completeness to $2\theta = 22.00$	99.9%
Absorption correction	SADABS multiscan correction (Sheldrick, 1996)
Refinement method	Full-matrix least-squares on F^2
Computing	SHELXL-97 (Sheldrick, 1997)
Data / restraints / parameters	3683 / 772 / 410
Goodness-of-fit on F^2	1.077
SHELXL-97 weight parameters	0.105200 28.183601
Final R indices [I¿2sigma(I)]	R1 = 0.1925, wR2 = 0.3932
R indices (all data)	R1 = 0.3082, wR2 = 0.4526
Extinction coefficient	0.007(3)
Largest diff. peak and hole	0.528 and -0.512 e.Å^{-3}

Table 9.3: Crystal data and structure refinement for ZJAK22.

	x	y	z	U(eq)
C(1A1)	4590(5)	6948(19)	2673(14)	39(8)
C(1A2)	5470(5)	6800(2)	2700(15)	40(7)
C(2A1)	5430(5)	6231(19)	3549(14)	32(9)
C(2A2)	4370(5)	6359(18)	3477(14)	34(7)
C(3A)	4524(19)	5142(10)	3920(7)	40(3)
C(4A)	4464(18)	4633(10)	3273(7)	36(3)
N(5A)	4128(16)	3550(8)	3441(6)	44(3)
C(6A)	4119(18)	3369(10)	2697(7)	37(3)
C(7A)	3800(2)	2391(11)	2570(9)	50(4)
C(8A)	3850(2)	2456(12)	1735(9)	58(4)
C(9A)	4220(2)	3427(12)	1070(9)	51(4)
C(10A)	4540(2)	4400(11)	1179(8)	46(4)
C(11A)	4456(19)	4351(10)	2025(7)	39(3)
C(12A)	4675(18)	5168(10)	2425(7)	37(3)
C(13A)	5053(19)	6281(10)	2076(7)	40(3)
C(14A)	3750(2)	2737(12)	4249(8)	56(4)
O(15A)	5209(12)	6814(7)	1294(5)	41(3)
C(16A)	5440(2)	8051(10)	2287(8)	56(4)
N(17A)	5640(2)	8640(12)	2850(9)	85(4)
C(18A)	4790(3)	9134(16)	3236(12)	88(5)
N(19A)	5280(2)	9540(12)	3721(9)	91(5)
C(20A)	7240(3)	9206(19)	3676(14)	114(6)
C(21A)	7550(3)	8649(17)	3228(12)	95(5)
C(22A)	2840(2)	9326(15)	2982(13)	129(8)
C(1B1)	10590(4)	6634(15)	1272(11)	29(6)
C(1B2)	9770(7)	6730(2)	1300(17)	43(10)
C(2B1)	9280(4)	6194(15)	776(12)	38(7)
C(2B2)	10450(7)	6020(3)	830(2)	52(11)
C(3B)	9550(2)	4951(10)	1052(7)	45(4)
C(4B)	9469(17)	4478(10)	1995(7)	34(3)
N(5B)	9074(17)	3408(9)	2448(7)	53(3)
C(6B)	9000(19)	3255(11)	3293(8)	47(3)
C(7B)	8690(2)	2288(12)	4004(9)	62(4)
C(8B)	8670(2)	2419(13)	4776(9)	65(4)
C(9B)	9030(2)	3398(13)	4868(9)	67(5)
C(10B)	9450(19)	4336(12)	4196(8)	52(4)
C(11B)	9419(18)	4232(11)	3397(7)	40(3)
C(12B)	9657(19)	5028(10)	2531(7)	40(3)
C(13B)	10020(19)	6141(10)	2234(7)	41(3)
C(14B)	8840(2)	2567(11)	2110(10)	57(4)
O(15B)	10161(14)	6708(8)	2689(6)	50(3)
C(16B)	10440(2)	7881(10)	1002(7)	55(4)
N(17B)	10591(17)	8470(9)	88(6)	52(3)
C(18B)	9590(2)	9072(12)	-526(8)	54(4)
N(19B)	10108(19)	9497(10)	-1255(7)	59(3)
C(20B)	12020(2)	9141(13)	-1093(9)	73(5)
C(21B)	12380(2)	8508(13)	-326(9)	63(4)
C(22B)	7640(2)	9202(13)	-354(10)	64(4)
O(1)	3370(4)	-60(2)	5017(16)	121(15)

Table 9.4: Atomic coordinates (x 10^4) and equivalent isotropic displacement parameters (Å^2 x 10^3) for ZJAK22. U(eq) is defined as one third of the trace of the orthogonalized U$_{ij}$ tensor.

Bond	Bond length	Angle	deg	Angle	deg
C(1A1)-C(16A)	1.52(2)	C(16A)-C(1A1)-C(2A1)	113(2)	C(1B2)-C(2B2)-C(3B)	115(3)
C(1A1)-C(2A1)	1.54(4)	C(16A)-C(1A1)-C(13A)	107.4(17)	C(4B)-C(3B)-C(2B2)	106.2(15)
C(1A1)-C(13A)	1.57(2)	C(2A1)-C(1A1)-C(13A)	105(2)	C(4B)-C(3B)-C(2B1)	107.9(12)
C(1A2)-C(2A2)	1.48(4)	C(2A2)-C(1A2)-C(13A)	111(2)	C(2B2)-C(3B)-C(2B1)	33.4(17)
C(1A2)-C(13A)	1.48(2)	C(2A2)-C(1A2)-C(16A)	116(2)	C(12B)-C(4B)-N(5B)	110.0(10)
C(1A2)-C(16A)	1.53(3)	C(13A)-C(1A2)-C(16A)	111.8(17)	C(12B)-C(4B)-C(3B)	126.3(11)
C(2A1)-C(3A)	1.52(2)	C(3A)-C(2A1)-C(1A1)	111(2)	N(5B)-C(4B)-C(3B)	123.6(10)
C(2A2)-C(3A)	1.49(2)	C(1A2)-C(2A2)-C(3A)	116(2)	C(6B)-N(5B)-C(4B)	108.9(10)
C(3A)-C(4A)	1.472(14)	C(4A)-C(3A)-C(2A2)	108.2(12)	C(6B)-N(5B)-C(14B)	124.5(12)
C(4A)-C(12A)	1.358(14)	C(4A)-C(3A)-C(2A1)	109.3(13)	C(4B)-N(5B)-C(14B)	126.5(11)
C(4A)-N(5A)	1.376(14)	C(2A2)-C(3A)-C(2A1)	30.3(12)	N(5B)-C(6B)-C(11B)	109.0(10)
N(5A)-C(6A)	1.358(13)	C(12A)-C(4A)-N(5A)	110.2(10)	N(5B)-C(6B)-C(7B)	129.7(12)
N(5A)-C(14A)	1.430(14)	C(12A)-C(4A)-C(3A)	125.1(11)	C(11B)-C(6B)-C(7B)	121.2(12)
C(6A)-C(7A)	1.403(15)	N(5A)-C(4A)-C(3A)	124.6(10)	C(8B)-C(7B)-C(6B)	115.0(14)
C(6A)-C(11A)	1.404(15)	C(6A)-N(5A)-C(4A)	108.9(10)	C(7B)-C(8B)-C(9B)	123.0(14)
C(7A)-C(8A)	1.381(16)	C(6A)-N(5A)-C(14A)	123.9(11)	C(10B)-C(9B)-C(8B)	123.5(13)
C(8A)-C(9A)	1.395(17)	C(4A)-N(5A)-C(14A)	127.1(11)	C(9B)-C(10B)-C(11B)	114.5(13)
C(9A)-C(10A)	1.381(16)	N(5A)-C(6A)-C(7A)	128.2(11)	C(6B)-C(11B)-C(10B)	122.5(12)
C(10A)-C(11A)	1.408(15)	N(5A)-C(6A)-C(11A)	109.1(10)	C(6B)-C(11B)-C(12B)	105.2(10)
C(11A)-C(12A)	1.469(15)	C(7A)-C(6A)-C(11A)	122.7(11)	C(10B)-C(11B)-C(12B)	132.1(12)
C(12A)-C(13A)	1.401(15)	C(8A)-C(7A)-C(6A)	115.4(13)	C(4B)-C(12B)-C(13B)	121.9(11)
C(13A)-O(15A)	1.257(12)	C(7A)-C(8A)-C(9A)	121.8(13)	C(4B)-C(12B)-C(11B)	106.7(10)
C(16A)-N(17A)	1.435(15)	C(10A)-C(9A)-C(8A)	124.0(13)	C(13B)-C(12B)-C(11B)	131.4(11)
N(17A)-C(18A)	1.218(17)	C(9A)-C(10A)-C(11A)	114.8(12)	O(15B)-C(13B)-C(12B)	125.3(11)
N(17A)-C(21A)	1.545(19)	C(6A)-C(11A)-C(10A)	121.3(11)	O(15B)-C(13B)-C(1B2)	118.2(15)
C(18A)-N(19A)	1.196(17)	C(6A)-C(11A)-C(12A)	105.4(10)	C(12B)-C(13B)-C(1B2)	114.9(14)
C(18A)-C(22A)	1.476(19)	C(10A)-C(11A)-C(12A)	133.3(12)	O(15B)-C(13B)-C(1B1)	119.0(12)
C(18A)-C(20A)	1.98(2)	C(4A)-C(12A)-C(13A)	122.3(11)	C(12B)-C(13B)-C(1B1)	115.0(11)
N(19A)-C(20A)	1.49(2)	C(4A)-C(12A)-C(11A)	106.3(10)	C(1B2)-C(13B)-C(1B1)	22.9(17)
C(20A)-C(21A)	1.235(19)	C(13A)-C(12A)-C(11A)	131.3(11)	N(17B)-C(16B)-C(1B2)	117.8(14)
C(1B1)-C(16B)	1.52(2)	O(15A)-C(13A)-C(12A)	124.4(11)	N(17B)-C(16B)-C(1B1)	114.3(12)
C(1B1)-C(2B1)	1.54(3)	O(15A)-C(13A)-C(1A2)	119.8(13)	C(1B2)-C(16B)-C(1B1)	23.3(16)
C(1B1)-C(13B)	1.58(2)	C(12A)-C(13A)-C(1A2)	115.5(13)	C(18B)-N(17B)-C(16B)	138.4(14)
C(1B2)-C(2B2)	1.48(4)	O(15A)-C(13A)-C(1A1)	117.9(13)	C(18B)-N(17B)-C(21B)	101.2(11)
C(1B2)-C(13B)	1.49(3)	C(12A)-C(13A)-C(1A1)	114.5(12)	C(16B)-N(17B)-C(21B)	120.3(11)
C(1B2)-C(16B)	1.52(3)	C(1A2)-C(13A)-C(1A1)	24.8(13)	N(19B)-C(18B)-N(17B)	124.9(15)
C(2B1)-C(3B)	1.52(2)	N(17A)-C(16A)-C(1A1)	115.5(13)	N(19B)-C(18B)-C(22B)	118.2(13)
C(2B2)-C(3B)	1.50(3)	N(17A)-C(16A)-C(1A2)	116.4(13)	N(17B)-C(18B)-C(22B)	116.8(13)
C(3B)-C(4B)	1.486(14)	C(1A1)-C(16A)-C(1A2)	25.1(13)	N(19B)-C(18B)-C(20B)	45.8(8)
C(4B)-C(12B)	1.355(14)	C(18A)-N(17A)-C(16A)	143.1(17)	N(17B)-C(18B)-C(20B)	79.2(10)
C(4B)-N(5B)	1.376(14)	C(18A)-N(17A)-C(21A)	97.4(13)	C(22B)-C(18B)-C(20B)	163.9(11)
N(5B)-C(6B)	1.367(14)	C(16A)-N(17A)-C(21A)	119.2(14)	C(18B)-N(19B)-C(20B)	97.0(12)
N(5B)-C(14B)	1.428(14)	N(19A)-C(18A)-N(17A)	130.9(18)	C(21B)-C(20B)-N(19B)	114.0(14)
C(6B)-C(11B)	1.402(15)	N(19A)-C(18A)-C(22A)	117.1(18)	C(21B)-C(20B)-C(18B)	76.8(11)
C(6B)-C(7B)	1.422(16)	N(17A)-C(18A)-C(22A)	111.8(17)	N(19B)-C(20B)-C(18B)	37.2(6)
C(7B)-C(8B)	1.373(17)	N(19A)-C(18A)-C(20A)	48.5(10)	C(20B)-C(21B)-N(17B)	102.8(14)
C(8B)-C(9B)	1.384(18)	N(17A)-C(18A)-C(20A)	82.4(12)		
C(9B)-C(10B)	1.382(17)	C(22A)-C(18A)-C(20A)	164.9(16)		
C(10B)-C(11B)	1.403(15)	C(18A)-N(19A)-C(20A)	94.4(14)		
C(11B)-C(12B)	1.472(15)	C(21A)-C(20A)-N(19A)	114.3(17)		
C(12B)-C(13B)	1.397(15)	C(21A)-C(20A)-C(18A)	77.3(13)		
C(13B)-O(15B)	1.254(13)	N(19A)-C(20A)-C(18A)	37.1(7)		
C(16B)-N(17B)	1.460(14)	C(20A)-C(21A)-N(17A)	102.7(16)		
N(17B)-C(18B)	1.256(15)	C(16B)-C(1B1)-C(2B1)	113.3(18)		
N(17B)-C(21B)	1.474(17)	C(16B)-C(1B1)-C(13B)	107.3(14)		
C(18B)-N(19B)	1.219(15)	C(2B1)-C(1B1)-C(13B)	106.4(17)		
C(18B)-C(22B)	1.473(18)	C(2B2)-C(1B2)-C(13B)	111(3)		
C(18B)-C(20B)	2.00(2)	C(2B2)-C(1B2)-C(16B)	116(3)		
N(19B)-C(20B)	1.443(18)	C(13B)-C(1B2)-C(16B)	112(2)		
C(20B)-C(21B)	1.277(17)	C(3B)-C(2B1)-C(1B1)	110.8(18)		

Table 9.5: Bond lengths [Å] and angles [°] for ZJAK22.

	x	y	z	U(eq)
H(1A1)	3252	7060	2716	46
H(1A2)	6756	6550	2884	48
H(2A1)	6742	6087	3488	38
H(2A2)	5282	6631	3940	38
H(2A3)	3083	6589	3323	41
H(2A4)	4730	6699	3878	41
H(3A1)	5216	4649	4420	48
H(3A2)	3281	5270	4097	48
H(7A)	3568	1737	3022	61
H(8A)	3618	1830	1610	69
H(9A)	4259	3418	516	61
H(10A)	4797	5044	722	56
H(14A)	3018	2187	4167	84
H(14B)	3075	3085	4592	84
H(14C)	4884	2387	4537	84
H(16A)	6655	7926	2075	67
H(16B)	4694	8518	1797	67
H(20A)	8174	9402	3964	137
H(21A)	8667	8314	3139	114
H(22A)	2730	9564	2368	193
H(22B)	2276	9892	3168	193
H(22C)	2221	8649	3242	193
H(1B1)	11868	6381	1211	35
H(1B2)	8429	6824	1200	52
H(2B1)	8017	6398	875	46
H(2B2)	9514	6532	165	46
H(2B3)	11765	5855	945	62
H(2B4)	10281	6433	222	62
H(3B1)	8586	4669	802	53
H(3B2)	10734	4746	860	53
H(7B)	8502	1610	3951	74
H(8B)	8399	1817	5264	78
H(9B)	8997	3427	5417	80
H(10B)	9729	4990	4269	62
H(14D)	9785	2588	1700	86
H(14E)	7648	2689	1831	86
H(14F)	8914	1854	2568	86
H(16C)	9255	8101	1187	65
H(16D)	11395	8104	1296	65
H(20B)	12912	9356	-1513	88
H(21B)	13503	8155	-86	75
H(22D)	7497	9483	104	96
H(22E)	7105	8493	-190	96
H(22F)	7022	9714	-862	96

Table 9.6: Hydrogen coordinates (x 10^4) and isotropic displacement parameters (Å^2 x 10^3) for ZJAK22.

	U11	U22	U33	U23	U13	U12
C(3A)	47(9)	36(8)	34(7)	-11(6)	16(7)	7(7)
C(4A)	31(8)	43(6)	31(6)	-9(4)	0(6)	1(7)
N(5A)	60(8)	41(6)	27(5)	-10(4)	1(6)	4(6)
C(6A)	41(8)	32(6)	33(5)	-11(5)	-11(6)	16(6)
C(7A)	45(9)	52(7)	59(7)	-24(6)	-1(8)	-21(8)
C(8A)	61(10)	58(8)	70(8)	-41(7)	14(9)	-12(8)
C(9A)	47(9)	60(9)	57(8)	-34(6)	3(8)	-17(8)
C(10A)	54(10)	53(8)	36(6)	-20(6)	3(7)	-1(8)
C(11A)	39(8)	43(6)	38(5)	-19(5)	5(7)	4(7)
C(12A)	37(8)	45(6)	30(5)	-14(4)	1(6)	-4(7)
C(13A)	44(9)	49(6)	25(6)	-10(5)	-2(7)	-8(7)
C(14A)	63(11)	53(9)	33(7)	7(6)	-8(8)	-4(8)
O(15A)	48(6)	41(6)	33(5)	-14(4)	0(5)	8(5)
C(16A)	84(11)	39(8)	32(8)	0(6)	5(7)	5(8)
N(17A)	137(10)	65(10)	57(9)	-24(6)	20(8)	-20(9)
C(18A)	131(9)	65(13)	65(13)	-22(8)	2(10)	2(10)
N(19A)	164(12)	55(10)	56(10)	-21(7)	36(9)	-33(9)
C(20A)	148(11)	108(16)	94(15)	-42(10)	-7(12)	-25(13)
C(21A)	121(10)	103(15)	63(12)	-29(9)	10(10)	-18(11)
C(22A)	99(10)	64(13)	128(17)	80(11)	-2(10)	-10(10)
C(3B)	40(9)	58(9)	39(6)	-19(6)	-10(7)	-15(7)
C(4B)	17(7)	55(7)	35(5)	-21(5)	-11(6)	-7(6)
N(5B)	66(9)	54(6)	48(6)	-26(5)	-2(7)	-16(7)
C(6B)	40(9)	49(7)	48(6)	-12(5)	8(7)	-11(7)
C(7B)	56(10)	65(8)	55(7)	-10(6)	1(9)	-9(8)
C(8B)	61(11)	70(9)	39(7)	6(7)	2(8)	15(9)
C(9B)	70(12)	91(11)	34(7)	-20(7)	9(8)	19(10)
C(10B)	33(9)	79(9)	48(7)	-29(6)	10(7)	5(8)
C(11B)	26(8)	61(7)	37(5)	-19(5)	-12(6)	-4(7)
C(12B)	40(8)	41(6)	41(6)	-18(5)	-13(7)	6(7)
C(13B)	46(9)	51(6)	29(7)	-19(5)	1(7)	-4(7)
C(14B)	56(11)	45(8)	75(11)	-28(8)	-17(9)	8(8)
O(15B)	73(8)	43(6)	38(6)	-19(5)	-3(5)	2(5)
C(16B)	82(11)	50(8)	25(6)	-9(5)	-10(6)	17(8)
N(17B)	88(8)	46(8)	21(5)	-10(5)	-16(5)	-6(6)
C(18B)	93(7)	36(9)	27(6)	-6(6)	-15(6)	14(8)
N(19B)	102(8)	43(8)	27(5)	-3(5)	-17(6)	-11(7)
C(20B)	101(8)	53(11)	45(8)	7(8)	5(7)	-12(9)
C(21B)	79(8)	55(10)	44(8)	-4(7)	-9(6)	-15(8)
C(22B)	88(8)	44(10)	62(11)	-23(9)	-15(7)	-2(9)
O(1)	180(3)	100(2)	90(2)	-56(17)	13(18)	-2(19)

Table 9.7: Anisotropic displacement parameters (Å^2 x 10^3) for ZJAK22. The anisotropic displacement factor exponent takes the form: $-2\pi^2$ [h^2 a^{*2} U11 + ... + 2 h k a* b* U12]

Chapter 10

The needle-like morphology of Ondansetron explained by Monte Carlo simulations and step energy calculations

10.1 Introduction

In the previous chapter, the crystal structure of Ondansetron, whose structure is shown in Figure 10.1, was studied using single crystal and powder X-ray diffraction, DSC, solid-state NMR and molecular modeling. Two samples were studied, one obtained from an ethanol/water mixture, the other from methanol. It was found that the crystal structure of Ondansetron is in fact a solid solution of enantiomers: at each site in the lattice either an R- or an S-enantiomer can be present, each having a specific conformation of the six-membered ring consisting of carbon-atoms 1, 2, 3, 4, 4a and 9a (see Figure 10.1). In this chapter the experimental needle-like morphology is studied using three modeling techniques: the attachment energy method, Monte Carlo simulations and step energy calculations. The results of these methods are compared, and it will be shown that the latter two methods give a good agreement with the morphology observed experimentally. The needle-like morphology of Ondansetron can thus be understood in terms of different 2D-nucleation barriers, as it is found from the Monte Carlo simulations and step energy calculations that the nucleation barrier of the $\{0kl\}$ zone is considerably higher than of crystalline orientations with indices $\{hkl\}$ with $h \neq 0$.

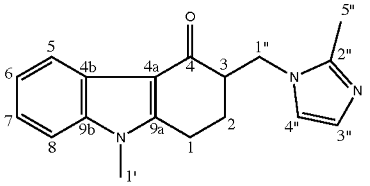

Figure 10.1: A molecule of Ondansetron, with the numbering scheme used in this chapter.

10.2 Methods

Growth of crystals from solution

Two samples of solid Ondansetron were prepared, ODS-1 and ODS-2. ODS-1 was prepared using 0.5 g of Ondansetron dissolved in a mixture of 25 mL of ethanol and 10 mL of water while heating. The clear solution was cooled to room temperature and left at that temperature for a few days. The crystals formed were filtered off and dried in air for 2 days. NMR analysis showed that no ethanol was present in the sample, and the mass-loss, determined by thermogravimetric analysis (TGA), was 1.8%. ODS-2 was prepared using 0.3 g of Ondansetron dissolved in 50 mL of methanol while heating. The clear solution was cooled to room temperature and left at that temperature for a few days. The crystals formed were filtered off and dried in air for 2 days. Again, NMR showed no methanol in the sample, and the TGA mass-loss was found to be 1.6%.

10.2.1 Molecular modeling

Molecular modeling was performed using the Cerius^2 modeling software.[89] The Dreiding forcefield (v2.21) was used with a constant value for $\epsilon = 1$. [89] Atomic partial charges were generated using the Gasteiger charge equilibration method.[133] Crystal structures were minimized using Ewald summation for the electrostatic and van der Waals interactions. Crystal graphs were calculated using the Hartman-Perdok module of the Cerius^2 software, calculating the electrostatic and van der Waals interactions directly, without a cutoff distance. All bonds with a bond strength above kT were used in the crystal graph.

10.2.2 Connected nets and attachment energies

The Facelift program was used to calculate connected nets[19] and attachment energies, using the crystal graphs as input.[65] The algorithm finds all periodic bond chains (PBCs) as direct chains from the crystal graph and by systematically combining these PBCs finds the connected net orientations.

10.2.3 Monte Carlo simulations

Monte Carlo crystal growth simulations were performed using the MONTY simulation package.[9] A simulation grid of 40×40 unit cells was used and the simulations were run for 500 cycles at values of $\Delta\mu/kT$ between 0 and 25. Each cycle consisted of 10000 MC events, and each simulation was preceded by 100000 relaxation events. The simulations were run starting at the highest values for $\Delta\mu/kT$ and the results of the higher values of $\Delta\mu/kT$ were used at input for simulations at lower $\Delta\mu/kT$. Thus the resulting surface structure after a simulation at $\Delta\mu/kT$=25 is used as input for the following simulation at $\Delta\mu/kT$=24, in order to prevent artifacts arising from too short relaxation times at lower $\Delta\mu/kT$-values.

10.2.4 Step energy calcuations

Step energies were calculated using the STEPLIFT calculation package for all connected net orientations obtained.[49] From the step energies obtained the equilibrium shape of the 2D island was calculated and used to calculate relative growth rates for each orientation as a function of the driving force $\Delta\mu/kT$. It was assumed that all faces grow by a birth and spread mechanism.

10.3 Experimental morphology

The experimental morphology for both samples was found to be needle-like. Micrographs, obtained using oil immersion, are shown in Figure 10.2.

10.4 Crystal graph calculation

From studies using X-ray single crystal and powder diffraction, solid-state NMR and molecular modeling it was found that the crystal structure of Ondansetron is in fact a solid solution of enantiomers (see Chapter 9). At each site in the crystal lattice, an R- or an S-enantiomer can be built in, each in a specific conformation. The conformation is dependent on the puckering of the six-membered ring made up of carbon atoms 1, 2, 3, 4, 4a and 9a (for atom numbering see Figure 10.1). When an R-enantiomer is built in, the conformation will be with the carbon atom 2 above the plane of the indole conjugated ring system, when an S-enantiomer is built in the carbon atom 2 will be below this plane. These conformations are further referred to as 'R-up' or 'Ru' and 'S-down' or 'Sd'. The spacegroup of the crystal structure was determined from single crystal X-ray diffraction to be $P\bar{1}$, with $Z' = 2$, which means that four different crystal structures can be made to represent the disordered solid, i.e. solid solution. These four crystal structures were found to have more or less the same lattice energy and lattice parameters, which are listed in Table 10.1.

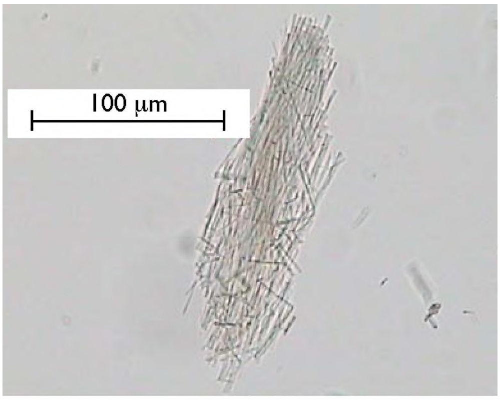

(a) ODS-1

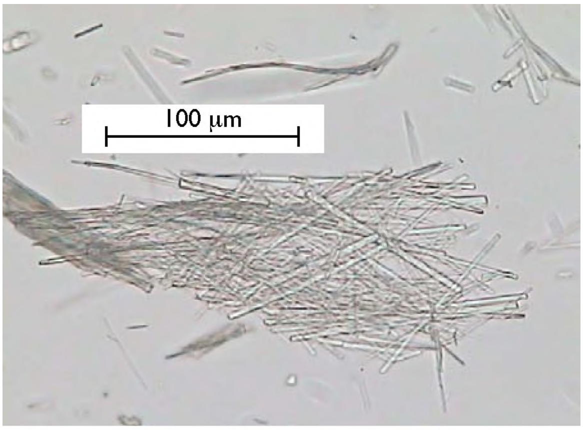

(b) ODS-2

Figure 10.2: Micrographs of ODS-1 and ODS-2 obtained using oil immersion.

Structure	a	b	c	α	β	γ	Lattice energy
	[Å]	[Å]	[Å]	[^{o}]	[^{o}]	[^{o}]	[kcal·mol^{-1}]
Ru+Ru	7.63	13.07	17.33	68.06	90.18	86.32	−33.13
Ru+Sd	7.44	13.05	17.90	67.53	87.13	84.14	−33.57
Sd+Ru	7.45	13.42	17.90	65.65	86.84	84.52	−33.01
Sd+Sd	7.47	13.00	17.83	67.84	88.98	89.43	−33.69

Table 10.1: Lattice parameters and lattice energies of the four unit cell configurations of Ondansetron after minimization. The entries in the structure column refer to the first and second molecule in the asymmetric unit being either the R-enantiomer in the 'up' conformation (Ru) or the S-enantiomer in the 'down' conformation (Sd).

Table 10.2: Crystal graph data for 'R-up + R-up' and 'R-up + S-down'.

R-up + R-up		R-up + S-down	
Bond	Bond strength [kcal · mol^{-1}]	Bond	Bond strength [kcal · mol^{-1}]
$1-2[000]$	-15.84	$1-2[000]$	-15.47
$1-2[\bar{1}00]$	-14.41	$1-2[\bar{1}00]$	-14.93
$1-3[000]$	-5.66	$1-3[000]$	-5.96
$1-4[000]$	-2.56	$1-4[11\bar{1}]$	-2.53
$1-4[10\bar{1}]$	-2.50	$1-4[000]$	-2.53
$1-1[0\bar{1}0]$	-2.40	$1-1[0\bar{1}0]$	-2.36
$1-4[11\bar{1}]$	-2.29	$1-4[01\bar{1}]$	-2.21
$1-4[100]$	-1.99	$1-4[00\bar{1}]$	-2.13
$1-3[00\bar{1}]$	-1.94	$1-4[10\bar{1}]$	-1.93
$1-4[01\bar{1}]$	-1.93	$1-1[\bar{1}00]$	-1.72
$1-4[00\bar{1}]$	-1.77	$1-4[100]$	-1.61
$1-1[\bar{1}00]$	-1.50	$1-3[00\bar{1}]$	-1.28
$1-2[010]$	-1.25	$1-2[010]$	-1.24
$1-2[\bar{1}10]$	-1.07	$1-2[\bar{1}10]$	-1.17
$2-4[10\bar{1}]$	-5.91	$2-4[10\bar{1}]$	-5.88
$2-4[11\bar{1}]$	-4.89	$2-4[11\bar{1}]$	-4.95
$2-4[100]$	-2.00	$2-2[\bar{1}00]$	-1.60
$2-2[\bar{1}00]$	-1.44	$2-4[100]$	-1.52
		$2-4[01\bar{1}]$	-0.74

Although the real crystals ODS-1 and ODS-2 are solid solutions of the 'Ru' and the 'Sd' molecules, the four crystal structures of Table 10.1 can be considered as limiting cases of the real structure. As crystal graphs can not be calculated for solid solutions, crystal graphs were calculated for all four structures, using the minimized crystal structures. The crystal graphs are listed in Table 10.2 and 10.3.

10.5 Connected nets and attachment energies

For the combination of 'R-up + R-up' molecules in the asymmetric unit connected nets were found using the crystal graph listed in Table 10.2. For this graph 630 PBCs were found, which, when combined, gave a total of 656 connected nets in 76 crystallographic orientations. The graph with the 'R-up + S-down' combination (see Table 10.2) gave 716 PBCs which gave a total of 910 connected nets in 93 crystallographic orientations. The combination of 'S-down + R-up' (see Table 10.3) gave 804 PBCs and 980 connected nets in 100 orientations and the 'S-down + S-down' (see Table 10.3) combination gave 730 PBCs and 707 connected nets in 80 crystallographic orientations.

Table 10.3: Crystal graph data for ‘S-down + R-up’ and ‘S-down + S-down’.

S-down + R-up		S-down + S-down	
Bond	Bond strength $[\mathrm{kcal}\cdot\mathrm{mol}^{-1}]$	Bond	Bond strength $[\mathrm{kcal}\cdot\mathrm{mol}^{-1}]$
$1-2[000]$	-16.00	$1-2[100]$	-15.49
$1-2[\bar{1}00]$	-14.87	$1-2[000]$	-15.05
$1-3[000]$	-6.21	$1-3[10\bar{1}]$	-5.84
$1-4[000]$	-2.41	$1-3[11\bar{1}]$	-4.83
$1-4[01\bar{1}]$	-2.32	$1-4[100]$	-2.42
$1-4[10\bar{1}]$	-2.19	$1-4[11\bar{1}]$	-2.38
$1-4[11\bar{1}]$	-1.91	$1-4[00\bar{1}]$	-2.09
$1-1[0\bar{1}0]$	-1.89	$1-4[000]$	-2.05
$1-1[\bar{1}00]$	-1.71	$1-4[01\bar{1}]$	-1.77
$1-3[00\bar{1}]$	-1.62	$1-4[10\bar{1}]$	-1.75
$1-4[00\bar{1}]$	-1.49	$1-3[100]$	-1.71
$1-4[100]$	-1.46	$1-1[\bar{1}00]$	-1.55
$1-2[\bar{1}10]$	-1.34	$1-2[0\bar{1}0]$	-1.32
$1-2[010]$	-1.03	$1-2[1\bar{1}0]$	-1.14
$2-4[10\bar{1}]$	-6.10	$2-4[000]$	-5.86
$2-4[11\bar{1}]$	-4.68	$2-2[0\bar{1}0]$	-2.33
$2-2[\bar{1}00]$	-1.61	$2-2[\bar{1}00]$	-1.28
$2-4[01\bar{1}]$	-0.89	$2-4[00\bar{1}]$	-1.22
$2-4[100]$	-0.87	$2-4[010]$	-0.86
$2-4[1\bar{1}0]$	-0.86		

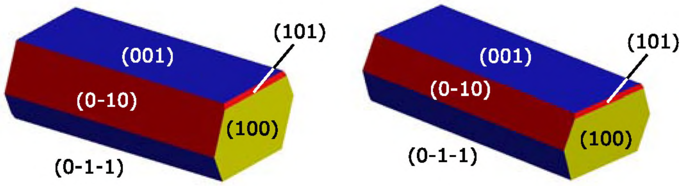

(a) R-up + R-up (b) R-up + S-down

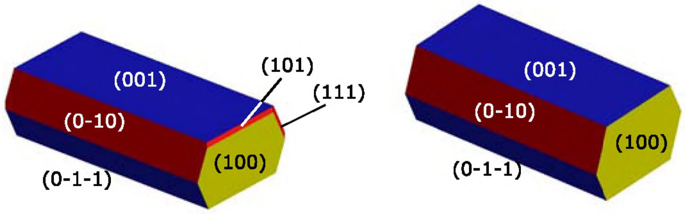

(c) S-down + R-up (d) S-down + S-down

Figure 10.3: Predicted morphologies based on the attachment energy.

For all four structures the predicted morphology based on the attachment energies, calculated from the crystal graph, are displayed in Figure 10.3. The shapes are very similar: only the appearance of {101} on all alternatives except 'S-down + S-down' and {111} on 'S-down + R-up' differentiate the four combinations. These differences are small, as the main contribution to the morphology is made by the {100}, {001}, {010} and {011} orientations. Comparing these morphologies to the ones found experimentally, it is clear that the attachment energy method fails in predicting the needle-like morphology of Ondansetron. The failure of the attachment energy method to predict the correct aspect ratio for needle-like morphologies is well-known.[9, 30, 31, 50, 49] The fact that all four alternatives give quite similar morphologies, shows that the differences between the four alternatives with respect to packing of the molecules in the crystal do not influence the predicted morphology to a significant degree. On the one hand, this confirms the supposition that the crystal structure is a solid solution, with the four alternatives as limiting cases. On the other hand, making the distinction between any of the four alternatives seems to be somewhat irrelevant.

10.6 Step energy calculations

To study the crystal structure and morphology of Ondansetron, represented by the four alternatives of local structure in the solid solution of the crystal, in more detail, the STEPLIFT[49] program was used to calculate growth rates as a function of driving force $\Delta\mu/kT$ using the four crystal graphs listed in Tables 10.2 and 10.3. The initial step of calculation of the connected net orientations gave a number of connected nets that are not stoichiometric, with respect to the unit cell content. As the symmetry of the crystal (spacegroup $P\bar{1}$) does not allow for non-stoichiometric connected nets (e.g. (022)), these connected nets were removed before starting the STEPLIFT procedure. Due to the large number of bonds in the crystal graph, calculations of the shape and energy of the 2D-nuclei on all remaining connected net orientations took 15-30 minutes on a modern workstation. Once all energies were known, all energies that were larger than zero (i.e. having a 2D nucleation barrier) were used to calculate relative growth rates of all connected net orientations as a function of the driving force. The results are shown in Figure 10.4.

As can be seen in the Figure, the orientations in the $\{0kl\}$ zone have the highest 2D-nucleus energy, and, consequently, the highest 2D nucleation barrier. All other orientations that have a positive 2D nucleus energy, have much smaller 2D nucleation barriers, resulting in a higher growth rate at lower $\Delta\mu/kT$-values. The resulting morphologies are shown in Figure 10.5 and it can be seen that a flat needle-like morphology is predicted in all four cases.

10.7 Monte Carlo simulations

For all combinations a selection of connected net orientations was made for the Monte Carlo simulations, because the number of connected nets found – between 76 and 100 connected net orientations – is too high to simulate: the simulations would take too long for all of them to complete, and only a few orientations would end up on the final morphology. To come to a selection of connected net orientations that are of interest, the crystal graphs' complexity was reduced to only include bonds with a bond strength below -2.0 kcal·mol^{-1}. This reduced the maximum connectivity by approximately half the number of bonds, while only retaining the stronger bonds. The remaining connected net orientations were used for the Monte Carlo simulations, using the crystal graphs with a cutoff-value of kT. The crystal graphs with reduced complexity were thus only used to come to a usable set of connected net orientations. The simulated growth rates as a function of $\Delta\mu/kT$ are displayed in Figure 10.6.

As can be seen from Figure 10.6, there is a clear trend: orientations that are in the $\{0kl\}$ zone have a higher 2D nucleation barrier compared to orientations that are not in this zone. Consequently, these orientations $\{0kl\}$ start to grow only at higher $\Delta\mu/kT$-values, at which the other orientations already show relatively fast growth. This means, in the end, that a needle morphology is predicted for all four alternatives, with the needle's long axis along the **a**-axis. The resulting morphologies, predicted at $\Delta\mu/kT$=22.0, are shown in Figure 10.7.

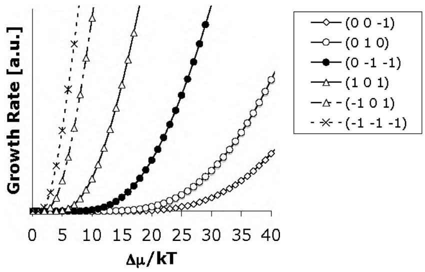

(a) R-up + R-up

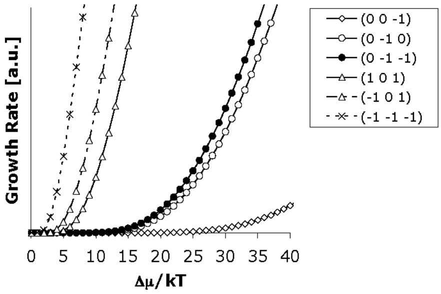

(b) R-up + S-down

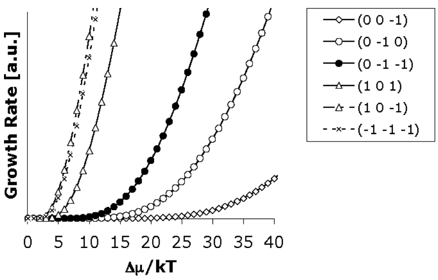

(c) S-down + R-up

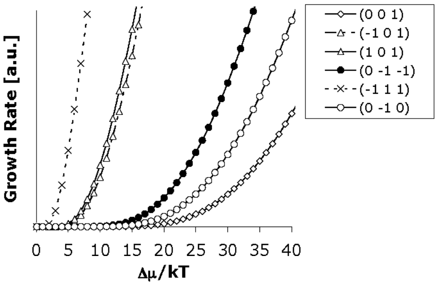

(d) S-down + S-down

Figure 10.4: Calculated growth rates as a function of the driving force $\Delta\mu/kT$. These growth rates were calculated using the STEPLIFT program. For clarity only the six slowest growing faces are shown in each figure.

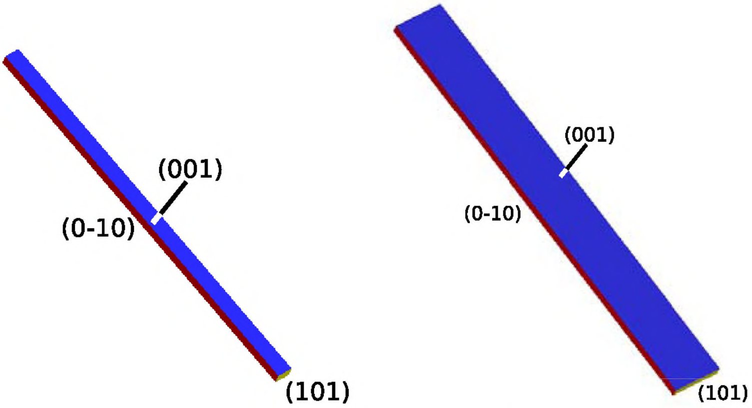

(a) Ru+Ru at $\Delta\mu/kT$=28.0 (b) Ru+Sd at $\Delta\mu/kT$=35.0

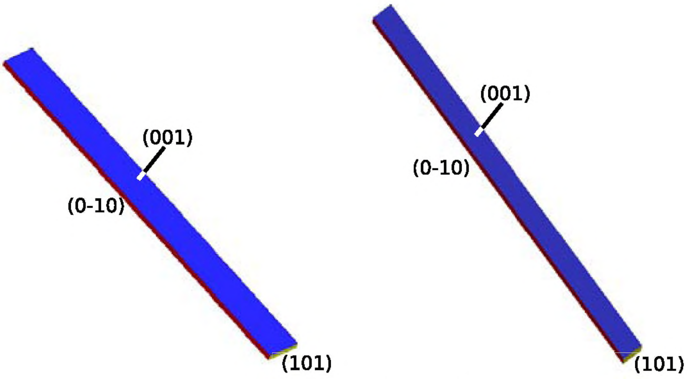

(c) Sd+Ru at $\Delta\mu/kT$=31.0 (d) Sd+Sd at $\Delta\mu/kT$=24.0

Figure 10.5: Predicted morphologies using growthrates from Figure 10.4.

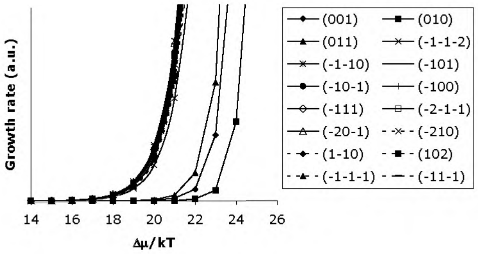

(a) R-up + R-up

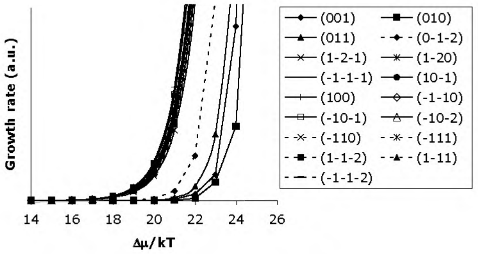

(b) R-up + S-down

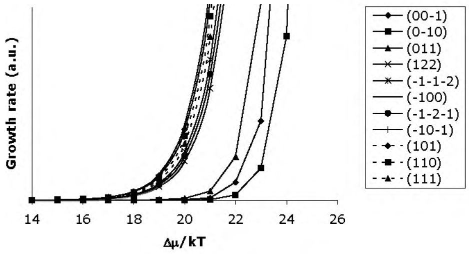

(c) S-down + R-up

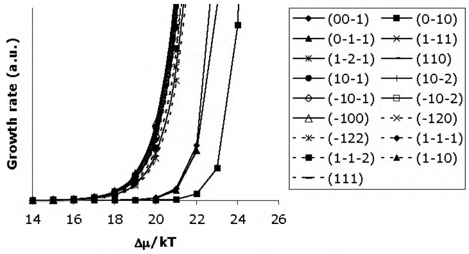

(d) S-down + S-down

Figure 10.6: Simulated growth rates as a function of the driving force $\Delta\mu/kT$. These growth rates were obtained from the MONTY crystal growth simulation program.

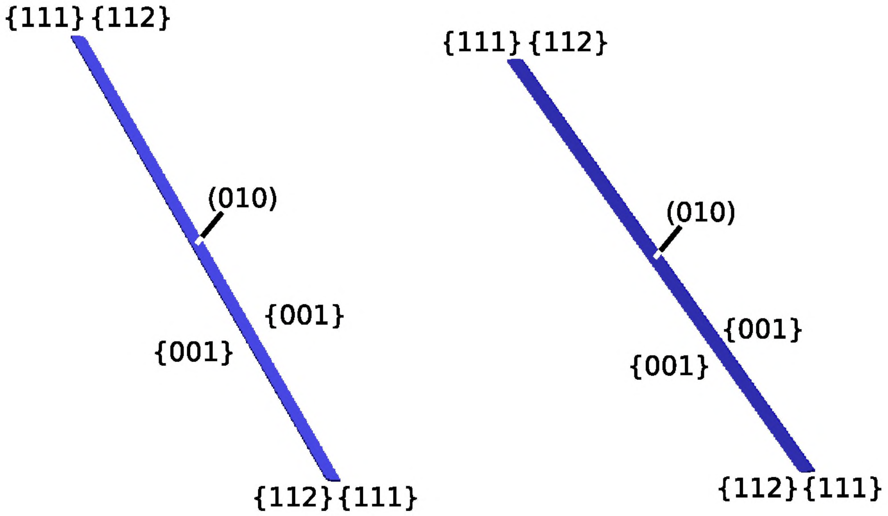

(a) R-up + R-up

(b) R-up + S-down

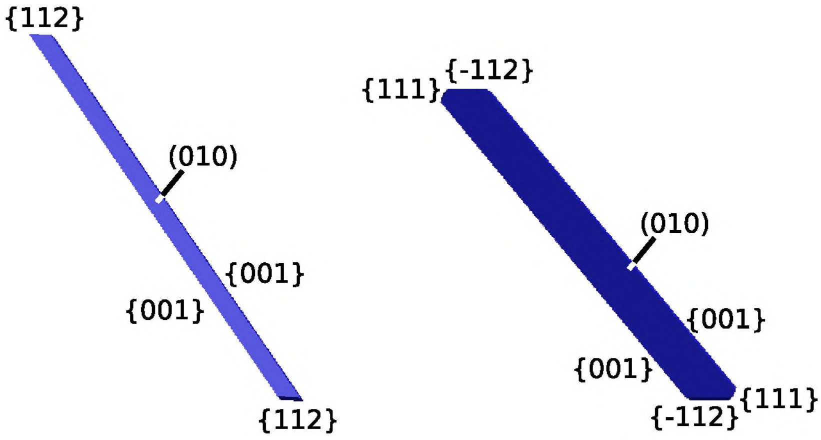

(c) S-down + R-up

(d) S-down + S-down

Figure 10.7: Predicted morphologies at $\Delta\mu/kT$=22.0 using growthrates from Figure 10.6.

Interestingly, the slowest growing orientation is in all cases the $\{010\}$ orientation for the MONTY results, whereas in the STEPLIFT results it is always the $\{001\}$ orientation and vice versa.

10.8 Conclusions

For all four alternative combinations of R-enantiomers in the up-conformation and S-enantiomers in the down-configuration, very similar crystal structures were found. When these four alternatives are used as input in various morphology prediction methods, the predictions are also quite similar, within each method. The predictions of the morphology based on the attachment energy, all show a slightly elongated block-like morphology, which does not correspond to the experimentally observed morphologies. The experimental needle-like morphologies are predicted more accurately by both the step energy calculations and the Monte Carlo simulations, clearly showing their superior prediction power for complex organic materials. These two methods show a clear trend for all combinations: the $\{0kl\}$ zone has higher 2D-nucleation barriers compared to the $\{hkl\}$ with $h \neq 0$ zone, thus explaining the needle-like morphology, oriented along the direction of the $\mathbf{a}$-axis.

The fact that the prediction results are very similar for each method used, is another strong indication that the four alternative crystal structures are a good representation the actual crystal structure: each alternative represents one possibility of local structure in the solid solution, and the fact that the predictions do not differentiate between the alternatives to an appreciable extent, reinforces the hypothesis that the crystal structure is indeed a solid solution.

It is therefore shown that the prediction of morphology can be extended to solid solutions, by studying the various possible local structures and using these as local snapshots of the solid solution, which can be thought of a representation of these local structures. The fact that there are no large energetic or morphological differences between the different local structures indicates the reason for the formation of a solid solution: there is not one structure that would crystallize favorably over the others.

Bibliografie

[1] S. R. Vippagunta, H. G. Brittain, and D. J. W. Grant. Crystalline solids. *Adv. Drug Delivery Rev.*, (2001), **48**, 3–26.

[2] P. York. Solid-state properties of powders in the formulation and processing of solid dosage forms. *Int. J. Pharm.*, (1983), **14**, 1–28.

[3] J. D. H Donnay and G. Harker. A new law of crystal morphology extending the law of Bravais. *Am. Mineral.*, (1937), **22**, 446–467.

[4] J. D. H Donnay and G. Harker. Assemblage liaisons et structure cristalline. *C. R. Acad. Sci. Paris*, (1961), **252**, 908–909.

[5] P. Hartman and W. Perdok. On the relations between structure and morphology of crystals. I. *Acta Cryst.*, (1955), **8**, 49–52.

[6] P. Hartman and W. Perdok. On the relations between structure and morphology of crystals. II. *Acta Cryst.*, (1955), **8**, 521–524.

[7] P. Hartman and W. Perdok. On the relations between structure and morphology of crystals. III. *Acta Cryst.*, (1955), **8**, 525–529.

[8] P. Hartman and P. Bennema. The attachment energy as a habit-controlling factor I. Theoretical considerations. *J. Cryst. Growth*, (1980), **49**, 145–156.

[9] S. X. M. Boerrigter, G. P. H. Josten, J. van de Streek, F. F. A. Hollander, J. Los, H. M. Cuppen, P. Bennema, and H. Meekes. MONTY: Monte carlo crystal growth on any crystal structure in any crystallographic orientation: Application to fats. *J. Phys. Chem. A*, (2004), **108**, 5894–5902.

[10] G. Wulff. Zur Frage der Geschwindigkeit des Wachstums und der Auflösing der Kristallflächen. *Z. Krist.*, (1901), **34**, 449–530.

[11] P. Bennema, E. A. Giess, and J. E. Weidenborner. Morphology of garnets and structure of F slices determined from a PBC analysis. *J. Cryst. Growth*, (1983), **62**, 41–60.

[12] R. Docherty, G. Clydesdale, K. J. Roberts, and P. Bennema. Application of BFDH, attachment energy and Ising models to predicting and understanding the morphology of molecular crystals. *J. Phys. D*, (1991), **24**, 89–99.

[13] R. F. P. Grimbergen, M. Reedijk, H. Meekes, and P. Bennema. Growth behavior of crystal faces containing symmetry-related connected nets: A case study of naphthalene and anthracene. *J. Phys. Chem. B*, (1998), **102**, 2646–2653.

[14] D. Winn and M. F. Doherty. Modeling crystal shapes of organic materials grown from solution. *AIChE J.*, (2000), **46**, 1348–1367.

[15] T. Beyer, G. M. Day, and S. L. Price. The prediction, morphology, and mechanical properties of the polymorphs of paracetamol. *J. Am. Chem. Soc.*, (2001), **123**, 5086–5094.

[16] P. Mougin, G. Clydesdale, R. B. Hammond, and K. J. Roberts. Molecular and solid-state modeling of the crystal purity and morphology of ϵ-caprolactam in the presence of synthesis impurities and the imino-tautomeric species caprolactim. *J. Phys. Chem. B*, (2003).

[17] S. G. Gadewar, H. M. Hofmann, and M. F. Doherty. Evolution of crystal shape. *Crystal Growth & Design*, (2004), **4**, 109–112.

[18] M. Brunsteiner, A. G. Jones, F. Pratola, S. L. Price, and S. J. R. Simons. Toward a molecular understanding of crystal agglomeration. *Crystal Growth & Design*, (2005), **5**, 3–16.

[19] R. F. P. Grimbergen, H. Meekes, P. Bennema, C. S. Strom, and L. J. P. Vogels. On the prediction of crystal morphology I: the Hartman-Perdok theory revisited. *Acta Cryst. A*, (1998), **54**, 491–500.

[20] J. P. van der Eerden. *Handbook of Crystal Growth*, chapter 6. Crystal growth mechanisms, page 307. North-Holland Elsevier, Amsterdam, (1993).

[21] H. M. Cuppen, H. Meekes, W. J. P van Enckevort, P. Bennema, and E. Vlieg. The effects of kink correlation and the Monte Carlo probability scheme on the step structure and velocity. *Surface Science*, (2003), **525(1)**, 1–12.

[22] M. Kotrla and A. C. Levi. Kinetics of crystal growth near the roughening transition: a Monte Carlo study. *Surf. Sci.*, (1994), **317**, 183–193.

[23] G. Mazzeo, G. Jug, A. C. Levi, and E. Tosatti. Roughening and preroughening in nonreconstructed fcc(110) surfaces: A monte carlo study. *Phys. Rev. B*, (1994), **49**, 7625.

[24] H. M. Cuppen, H. Meekes, E. van Veenendaal, W. J. P. van Enckevort, P. Bennema, M. Reedijk, J. Arsic, and E. Vlieg. Kink density and propagation velocity fo the [0 1 0] step on the Kossel (1 0 0) surface. *Surf. Sci.*, (2002), **506**, 183–195.

[25] H. M. Cuppen, H. Meekes, W. J. P van Enckevort, G. W. M. Vissers, and E. Vlieg. Kinetic roughening of Kossel and non-Kossel steps. *Surf. Sci.*, (2004), **569**, 33–46.

[26] H. M. Cuppen, H. Meekes, W. J. P. van Enckevort, and E. Vlieg. Kink incorporation and step propagation in a non-Kossel model. *Surf. Sci.*, (2004), **571**, 41–62.

[27] H. M. Cuppen, H. Meekes, W. J. P. van Enckevort, E. Vlieg, and H. J. F. Knops. Nonequilibrium free energy and kinetic roughening of steps on the Kossel (0 0 1) surface. *Phys. Rev. B*, (2004), **69**, 245404.

[28] S. Piana and J. D. Gale. Understanding the barries to crystal growth: dynamical simulation of the dissolution and growth of urea from aqueous solution. *J. Am. Chem. Soc.*, (2005), **127**, 1975–1982.

[29] S. Piana, M. Reyhani, and J. D. Gale. Simulating micrometre-scale crystal growth from solution. *Nature*, (2005), **483**, 70–73.

[30] H. M. Cuppen, A. R. T. van Eerd, and H. Meekes. Needlelike morphology of aspartame. *Crystal Growth & Design*, (2004), **4(5)**, 989–997.

[31] H. M. Cuppen, G. Beurskens, S. Kozuka, K. Tsukamoto, J. M. M. Smits, R. de Gelder, R.F.P. Grimbergen, and H. Meekes. Crystal structure and growth behavior of aspartame form I-A. *Crystal Growth & Design*, (2005), **5**, 917–923.

[32] H. M. Cuppen, W. S. Graswinckel, and H. Meekes. Screw dislocations on polycenes: a requirement for crystallisation. *Crystal Growth & Design*, (2004), **4**, 1351–1357.

[33] P. Bennema. *Handbook of Crystal Growth*, chapter 7. Growth and morphology of crystals: integration of theories of roughening and Hartman-Perdok theory, page 477. North-Holland Elsevier, Amsterdam, (1993).

[34] J. J. M. Rijpkema, H. J. F. Knops, P. Bennema, and J. P. van der Eerden. Determination of the Ising critical temperature of F slices with an application to garnet. *J. Cryst. Growth*, (1982), **61**, 295–306.

[35] F. F. A. Hollander, S. X. M. Boerrigter, J. van de Streek, R. F. P. Grimbergen, H. Meekes, and P. Bennema. The implication of the connected net topology on the morphology of β-monoacid triacylglycerol crystals. *J. Phys. Chem. B*, (1999), **103**, 8301–8309.

[36] D. Braga. Crystal engineering, where from? Where to? *Chem. Comm.*, (2003), 2751–2754.

[37] K. Biradha. Crystal engineering: from weak hydrogen bonds to coordination bonds. *CrystEngComm*, (2003), **5**, 374–384.

[38] G. R. Desiraju. *Crystal engineering. The design of organic solids.* Materials Science Monographs. Elsevier, Amsterdam, (1989).

[39] J. M. Lehn. *Supramolecular Chemistry. Concepts and perspectives.* VCH, Weinheim, (1995).

[40] B. Moulton and M. J. Zaworotko. From molecules to crystal engineering: Supramolecular isomerism and polymorphism in network solids. *Chem. Rev.*, (2001), **101**, 1629–1658.

[41] S. L. James. Metal-organic frameworks. *Chem. Soc. Rev.*, (2003), **32**, 276–288.

[42] J. D. Dunitz. Phase transitions in molecular crystals from a chemical viewpoint. *Pure & Appl. Chem.*, (1991), **63**, 177–185.

[43] X. Y. Liu, E. S. Boek, W. J. Briels, and P. Bennema. Prediction of crystal growth morphology based on structural analysis of the solid fluid interface. *Nature*, (1995), **374**, 342.

[44] J. H. ter Horst, R. M. Geertman, and G. M. van Rosmalen. The effect of solvent on crystal morphology. *J. Cryst. Growth*, (2001), **230**, 277–284.

[45] J. H. ter Horst. Molecular modelling of the crystallization of polymorphs. part I: The morphology of HMX polymorphs. *J. Cryst. Growth*, (2002), **237-239**, 2215–2220.

[46] A. L. Rohl. Computer prediction of crystal morphology. *Current Opinion in Solid State and Materials Science*, (2003), **7**, 21–26.

[47] C. Stoica, P. Verwer, H. Meekes, P.C.J.M. van Hoof, F. M. Kaspersen, and E. Vlieg. Understanding the effect of a solvent on the crystal habit. *Crystal Growth & Design*, (2004), **4**, 765–768.

[48] H. Meekes, R. F. P. Grimbergen, and P. Bennema. On the prediction of crystal morphology II: Symmetry roughening of pairs of connected nets. *Acta Cryst. A*, (1998), **54**, 501–510.

[49] M. A. Deij, H. Meekes, and E. Vlieg. The step energy as a habit controlling factor. Application to the morphology prediction of aspartame, venlafaxine and a yellow isoxazolone dye. *Crystal Growth & Design*, (2007), Accepted for publication.

[50] M. A. Deij, E. Aret, S. X. M. Boerrigter, L. van Meervelt, G. Deroover, H. Meekes, and E. Vlieg. Experimental and computational growth morphology of two polymorphs of a yellow isoxazolone dye. *Langmuir*, (2005), **21**, 3831–3837.

[51] A.A. Chernov, L. N. Rashkovich, I. V. Yaminski, and N. V. Gvozdev. Kink kinetics, exchange fluxes, 1D 'nucleation' and adsorption on the (010) face of orthorhombic lysozyme crystals. *J. Phys. Condens. Matter*, (1999), **11**, 9969–9984.

[52] S. X. M. Boerrigter, H. M. Cuppen, R. I. Ristic, J. N. Sherwood, P. Bennema, and H. Meekes. Explanation for the supersaturation-dependent morphology of monoclinic paracetamol. *Crystal Growth & Design*, (2002), **2(5)**, 357–361.

[53] L. A. Zepeda-Ruiz, A. Maiti, R. Gee, G. H. Gilmer, and B. L. Weeks. Size and habit evolution of PETN crystals - a lattice Monte Carlo study. *J. Cryst. Growth*, (2006), **291**, 461–467.

[54] M. A. Deij, J. H. Los, H. Meekes, and E. Vlieg. On the determination of step energies. Theoretical considerations and application to an anisotropic Kossel model. *J. Appl. Cryst.*, (2006), **39**, 563–570.

[55] J. Andzelm, C. Kölmel, and A. Klamt. Incorporation of solvent effects into density functional calculations of molecular energies and geometries. *J. Chem. Phys.*, (1995), **103**, 9312–9320.

[56] H. van Beijeren and I. Nolden. *Structure and Dynamics of Surfaces II*, chapter 7. The Roughening Transition, pages 259–300. Springer-Verlag, New York, (1987).

[57] W. K. Burton, N. Cabrera, and F. C. Frank. The growth of crystals and the equilibrium structure of their surfaces. *Philos. Trans. R. Soc. London*, (1951), **243**, 299.

[58] W. Kossel. Zur Theorie des Kristallwachstums. *Nachr. Ges. Wiss. Göttingen, Math.-Phys. Kl.*, (1927), **2**, 135.

[59] M. den Nijs and K. Rommelse. Preroughening transitions in crystal surfaces and valence-bond phases in quantum spin chain. *Phys. Rev. B*, (1989), **40**, 4709–4734.

[60] G. Mazzeo, E. Carlon, and H. van Beijeren. Phase diagram of the two component body-centered solid-on-solid model. *Phys. Rev. Lett.*, (1995), **74**, 1391–1394.

[61] R. F. P. Grimbergen, P. Bennema, and H. Meekes. On the prediction of crystal morphology III: Equilibrium and growth behaviour of crystal faces containing multiple connected nets. *Acta Cryst. A*, (1999), **55**, 84–94.

[62] N. Akutsu and Y. Akutsu. Ambiguity of anisotropic interface tension for complex crystals. *J. Phys. Soc. Japan*, (1995), **64**, 736–756.

[63] M. Plomp, W. J. P. van Enckevort, and E. Vlieg. Etching and surface termination of $K_2Cr_2O_7$ {0 0 1} faces observed using in situ atomic force microscopy. *J. Cryst. Growth*, (2000), **216**, 413–427.

[64] W. J. P van Enckevort and P. Bennema. Interlacing of growth steps on crystal surfaces as a consequence of crystallographic symmetry. *Acta Cryst. A*, (2004), **60**, 532–541.

[65] R.F.P. Grimbergen, P.J.C.M. van Hoof, H. Meekes, and P. Bennema. *C-program* FACELIFT *for connected net analysis, Dept. of Solid State Chemistry, University of Nijmegen, hugo.meekes@science.ru.nl.*

[66] S. B. van Albada, M. J. Rost, and J. W. M. Frenken. Asymmetric and symmetric Wulff constructions of island shapes on a missing-row reconstructed surface. *Phys. Rev. B*, (2002), **65**, 205421.

[67] S. Kodambaka, S. V. Khare, I. Petrov, and J. E. Greene. Two-dimensional island dynamics: role of step energy anisotropy. *Surface Science Reports*, (2006), **60**, 55–77.

[68] F. F. A. Hollander, M. Plomp, J. van de Streek, and W. J. P. van Enckevort. A two-dimensional Hartman-Perdok analysis of polymorphic fat surfaces observed with atomic force microscopy. *Surface Science*, (2000), **471**, 101–113.

[69] G. E. W. Husbands, J. P. Yardley, and E. A. Muth. Phenylethylamine derivatives and intermediates therefor. Patent No. EP0112669B1, (1987).

[70] M. A. Deij, J. van Eupen, H. Meekes, P. Bennema, and E. Vlieg. Experimental and computational morphology of three polymorphs of the free base form of venlafaxine. *Submitted for publication in Int. J. Pharm.*.

[71] M. Hatada, J. Jancarik, Graves. B., and S-H. Kim. Crystal structure of aspartame, a peptide sweetener. *J. Am. Chem. Soc.*, (1985), **107**, 4279–4282.

[72] E. Aret, H. Meekes, E. Vlieg, and G. Deroover. Polymorphic behavior of a yellow isoxazolone dye. *Dyes and Pigments*, (2007), **72**, 339–344.

[73] E. van Veenendaal, P.C.J.M. van Hoof, J. van Suchtelen, W.J.P. van Enckevort, and P. Bennema. Kinetic roughening of the Kossel (1 0 0) surface: confrontation of classical criteria with Monte Carlo results. *Surf. Sci.*, (1998), **417**, 121.

[74] D. S. Coombes, C. R. A. Catlow, J. D. Gale, A. L. Rohl, and S. L. Price. Calculation of attachment energies and relative volume growth rates as an aid to polymorph prediction. *Crystal Growth & Design*, (2005), **5**, 879–885.

[75] J. H. ter Horst and D. H. Kashchiev. Determination of the nucleus size from the growth probability of clusters. *J. Chem. Phys*, (2003), **119**, 2241–2246.

[76] J. H. ter Horst and P. J. Jansens. Nucleus size and Zeldovich factor in two-dimensional nucleation at the Kossel crystal (0 0 1) surface. *Surface Science*, (2005), **574**, 77–88.

[77] J. H. ter Horst, H. J. M. Kramer, and P. J. Jansens. Towards an a priori product quality prediction method by combining process modeling and molecular simulations. *Chem. Eng. Technol.*, (2006), **29**, 175–182.

[78] D. Kashchiev. *Nucleation, basic theory with applications.* Butterworth Heinemann, Oxford, (2000).

[79] J. H. ter Horst, H. J. M. Kramer, and P. J. Jansens. A new molecular modeling approach to predict concomitant nucleation of polymorphs. *Crystal Growth & Design*, (2002), **2**, 351–356.

[80] N. Metropolis, A. W. Rosenbluth, M. N. Rosenbluth, A. H. Teller, and E. Teller. Equation of state calculations by fast computing machines. *J. Chem. Phys.*, (1953), **21**, 1087–1092.

[81] N. Metropolis and S. Ulam. The Monte Carlo method. *J. Am. Stat. Assoc.*, (1949), **44**, 335–341.

[82] A. B. Bortz, M. H. Kaloz, and J. L. Lebowitz. A new algorithm for Monte Carlo simulation of Ising spin systems. *J. Comp. Phys.*, (1975), **17**, 10–18.

[83] W. Ostwald. Über die Bildung und Umwandlung fester Körper. *Z. Physik. Chem.*, (1897), **22**, 289–330.

[84] J. Bernstein, R. J. Davey, and J-O. Henck. Concomitant polymorphs. *Angew. Chem. Int. Ed*, (1999), **38**, 3440.

[85] J. S. van Duijneveldt and D. Frenkel. Computer simulation study of free energy barriers in crystal nucleation. *J. Chem. Phys.*, (1992), **96**, 4655–4668.

[86] J-M. Leyssale, J. Delhomme, and C. Millot. Molecular simulation of the homogeneous crystal nucleation of carbon dioxide. *J. Chem. Phys.*, (2005), **122**, 184518.

[87] J-M. Leyssale, J. Delhomme, and C. Millot. Atomistic simulation of the homogeneous nucleation and the growth of N_2 crystallites. *J. Chem. Phys.*, (2005), **122**, 104510.

[88] S. L. Mayo, B. D. Olafson, and W. A. Goddard III. Dreiding: A generic force field for molecular simulations. *J. Phys. Chem.*, (1990), **94**, 8897–8909.

[89] *Cerius^2 User Guide.* Accelrys Inc., 9685 Scranton Road, San Diego, CA, USA, (1997).

[90] Wendy D. Cornell, Piotr Cieplak, Christopher I. Bayly, and Peter A. Kollman. Application of RESP charges to calculate conformational energies, hydrogen bond energies and free energies of solvation. *J. Am. Chem. Soc.*, (1993), **115**, 9620–9631.

[91] G. Nichols and C. S. Frampton. Physicochemical characterization of the orthorhombic polymorph of paracetamol crystallized from solution. *J. Pharm. Sci.*, (1998), **87**, 684–693.

[92] M. Haisa, S. Kashino, and H. Maeda. The orthorhombic form of p-hydroxyacetanilide. *Acta Cryst. B*, (1974), **30**, 2510.

[93] M. A. Mikhailenko. Growth of large single crystals of the orthorhombic paracetamol. *J. Cryst. Growth*, (2004), **265**, 616–618.

[94] M. L. Peterson, S. L. Morissette, C. McNulty, A. Goldswweig, P. Shaw, M. LeQuesne, J. Monagle, N. Encina, J. Marchionna, A. Johnson, J. Gonzalez-Zugasti, A. V. Lemmo, S. J. Ellis, M. J. Cima, and O. Almarsson. Iterative high-throughput polymorphism studies on acetaminophen and an experimentally derived structure for form III. *J. Am. Chem. Soc.*, (2002), **124**, 10958–10959.

[95] P. Espeau, R. Ceolin, J-L. Tamarit, M-A. Perrin, J-P. Gauchi, and F. Leveiller. Polymorphism of paracetamol: Relative stabilities of the monoclinic and orthorhombic phases inferred from topological pressure-temperature and temperature-volume phase diagrams. *J. Pharm. Sci.*, (2005), **94**, 524–539.

[96] C. P. M. Roelands, J. H. ter Horst, H. J. M. Kramer, and P. J. Jansens. The unexpected formation of the stable beta phase of L-glutamic acid during pH shift precipitation. *J. Cryst. Growth*, (2005), **275**, e1389–e1395.

[97] M. Kitamura. Polymorphism in the crystallization of L-glutamic acid. *J. Cryst. Growth*, (1989), **96**, 541–546.

[98] E. S. Ferrari and R. J. Davey. Solution-mediated transformation of α to β L-glutamic acid: rate enhancement due to secondary nucleation. *Crystal Growth & Design*, (2004), **4**, 1061–1068.

[99] T. Ono, H. J. M. Kramer, J. H. ter Horst, and P. J. Jansens. Process modeling of the polymorphic transformation of L-glutamic acid. *Crystal Growth & Design*, (2004), **4**, 1161–1167.

[100] R. B. Hammond, K. Pencheva, and K. J. Roberts. Simulation of energetic stability of facetted L-glutamic acid nanocrystalline clusters in relation to their polymorphic phase stability as a function of crystal size. *J. Phys. Chem. B*, (2005), **109**, 19552.

[101] P. Bennema and J. P. van der Eerden. *Crystal graphs, connected nets, roughening transition and the morphology of crystals*, chapter 1, pages 1–75. Terrapub, Tokyo, (1987).

[102] J. Prywer. Kinetic and geometric determination of the growth morphology of bulk crystals: recent developments. *Progr. Cryst. Growth. Char. Mater.*, (2005), **50**, 1–38.

[103] Z. Berkovitch-Yellin, J. van Mil, L. Addadi, M. Idelson, M. Lahav, and L. Leiserowitz. Crystal morphology engineering by “tailor-made” inhibitors: a new probe to fine intermolecular interactions. *J. Am. Chem. Soc.*, (1985), **107**, 3111–3122.

[104] J. Nyvlt and J. Ulrich. *Admixtures in crystallization.* VCH, Weinheim, (1995).

[105] R. Davey, W. Fila, and J. Garside. The influence of biuret on the growth kinetics of urea crystals from aqueous solutions. *J. Cryst. Growth*, (1986), **79**, 607–613.

[106] I. Weissbuch, R. Popovitz-Biro, M. Lahav, and L. Leiserowitz. Understanding and control of nucleation, growth, habit, dissolution and structure of two- and three-dimensional crystals using tailor-made additives. *Acta Cryst. B*, (1995), **B51**, 115–148.

[107] M. Lahav and L. Leiserowitz. Tailor-made auxiliaries for the control of nucleation, growth and dissolution of two- and three-dimensional crystals. *J. Phys. D*, (1993), **26**, B22–B31.

[108] A.A. Chernov. Crystal growth between the centuries. *J. Mat. Sci.*, (2001), **12**, 437–449.

[109] C. Guguta, H. Meekes, and R. de Gelder. Crystal structure of aspartame anhydrate from powder diffraction data. Structural aspects of the dehydration process of aspartame. *Crystal Growth & Design*, (2006), **6**, 2686–2892.

[110] Barbara Rodríguez-Spong, Christopher P. Price, Adivaraha Jayasankar, Adam J. Matzger, and Naír Rodríguez-Hornedo. General principles of

pharmaceutical solid polymorphism: a supramolecular perspective. *Adv. Drug Delivery Rev.*, (2004), **56**, 241–274.

[111] S. D. Finnie, R. I. Ristic, J. N. Sherwood, and A. M. Zikic. Morphological and growth rate distributions of small self-nucleated paracetamol crystals grown from pure aqueous solutions. *J. Cryst. Growth*, (2001), **207**, 308–318.

[112] S. Garnier, S. Petit, and G. Coquerel. Influence of supersaturation and structurally related additives on the crystal growth of α-lactose monohydrate. *J. Cryst. Growth*, (2002), **234**, 207–219.

[113] Holmbäck, X. and Rasmuson, Å. C. Size and morphology of benzoic acid crystals produced by drowning-out crystallization. *J. Cryst. Growth*, (1999), **198-199**, 780–788.

[114] D. H. Gay and A. L. Rohl. MARVIN - a new computer code for studying surface and interfaces and its application to calculating the crystal morphologies of corundum and zircon. *J. Chem. Soc., Faraday Trans.*, (1995), **91**, 925–936.

[115] G. Clydesdale, K. J. Roberts, and R. Docherty. HABIT95 - a program for predicting the morphology of molecular crystals as a function of the growth environment. *J. Cryst. Growth*, (1996), **166**, 78–83.

[116] M. J. Frisch and G. W. et. al Trucks. Gaussian 94 (Revision D.4). *Gaussian, Inc., Pittsburgh PA*, (1995).

[117] M. J. Frisch, G. W. Trucks, and et al. Gaussian 98 (Revision A.5). *Gaussian Inc., Pittsburgh PA.*, (1998).

[118] A. Pigache, P. Cieplak, and F.-Y. Dupradeau. Automatic and highly reproducible RESP and ESP charge drivation: Application to the development of programs RED and X RED. *227th ACS National Meeting, Anaheim, CA, March 28 - April 1, 2004*, (2004).

[119] Frantisek Picha, Joan Cucala Escoi, and Rolf Keltjens. Venlafaxine Base. WO03/082806 and US2003191347, (2003).

[120] J. Th. H. van Eupen, W.W.J Elffrink, R. Keltjens, P. Bennema, R. de Gelder, J. M. M. Smits, E. R. H. van Eck, A. P. M. Kentgens, M. A. Deij, H. Meekes, and E. Vlieg. Experimental phase diagram of three polymorphs of venlafaxine base. (to be published).

[121] C. Sweegers, H. Meekes, W. J. P van Enckevort, I. D. K. Hiralal, and A. Rijkeboer. Growth rate analysis of gibbsite single crystals growing from aqueous sodium aluminate solutions. *Crystal Growth & Design*, (2004), **4**, 185–198.

[122] J. Bernstein. *Polymorphism in molecular crystals.* Clarendon Press, (2002).

[123] J. Bauer, S. Spanton, R. Henry, J. Quick, W. Dziki, W. Porter, and J. Morris. Ritonavir: an extraordinary example of conformational polymorphism. *Pharm. Res.*, (2001), **18**, 859–866.

[124] P. Vishweshwar, J. A. McMahon, M. Oliveira, M. L. Peterson, and M. J. Zaworotko. The predictably elusive form II of aspirin. *J. Am. Chem. Soc.*, (2005), **127**, 16802–16803.

[125] A. D. Bond, R. Boese, and G. R. Desiraju. On the polymorphism of aspirin. *Angew. Chem. Int. Ed*, (2006), **46**, 615–617.

[126] A. D. Bond, R. Boese, and G. R. Desiraju. On the polymorphism of aspirin: crystalline aspirin as intergrowths of two polymorphic domains. *Angew. Chem. Int. Ed*, (2006), **46**, 618–622.

[127] R. J. H. Westheim and F. van Dalen. Ondansetron forms and processes of making the same. US2004/0198794, (2004).

[128] P. Dalmases Barjoan, L. Solà Candarell, F. Alcobe Olle, and M. C. Puijaner Vallet. New polymorphic forms of Ondansetron, Processes for preparing them, pharmaceutical compositions containing them and their use as antiemetics. WO2005/080381, (2005).

[129] G. M. Sheldrick. SADABS. Program for Empirical Absorption Correction.

[130] R. de Gelder, R. A. G. de Graaff, and H. Schenk. *Acta Cryst.*, (1993), **A49**, 287–293.

[131] G. M. Sheldrick. SHELX-97. Program for the refinement of crystal structures. *University of Göttingen*, (1997).

[132] K. Fischer. Neues Verfahren zur maßanalytischen Bestimmung der Wassergehaltes von Flüssigkeiten und festen Körpern. *Angew. Chem.*, (1935), **48**, 394–396.

[133] J. Gasteiger and M. Marsili. Iterative partial equilization of orbital electronegativity - a rapid access to atomic charges. *Tetrahedron*, (1980), **36**, 3219–3228.

Summary

This thesis is the result of four years of research into modeling of crystal growth of organic materials. New methods were developed to study crystal growth, because older methods, which are widely used, do not give satisfactory results for complex systems. The methods were developed with general applicability, speed and relevance to industry in mind. They therefore do not focus on a single problem, or a small subset of problems, but try to be as general as possible, while still offering new and fundamental insights in the problems of interest.

In this thesis the focus is on modeling of three important aspects: nucleation, the role of steps during growth, and the final morphology of crystals. The first subject, nucleation, is very important in polymorphism. As different polymorphs may form during crystallization, and usually only one is desired, the nucleation phase is critical for the formation of the desired polymorph. The research on nucleation, reported on in this thesis in Chapters 4 and 5, consists of the development of a new method where the probability that a small cluster of molecules grows out to a macroscopic crystal is simulated using Monte Carlo crystal growth simulations. These simulations, based on a random Monte Carlo process, allow for the determination of the cluster growth probability, both as a function of initial cluster size and as a function of driving force. Using such simulations, nucleation rates for different polymorphs can be calculated, thus giving insight in the nucleation behavior of all polymorphs simulated. Ultimately this will lead to an *a priori* product quality prediction, when the results of the simulations are combined with process simulations to obtain particle size distributions and product polymorphic fractions.

When a crystal is growing, the relative growth rate as a function of crystal orientation determines the final shape. The growth rates can be obtained from Monte Carlo crystal growth simulations, where crystal growth is simulated both as a function of crystal orientation and as a function of driving force for crystallization. These simulations then allow for a prediction of the final crystal shape, or morphology, as a function of driving force. These simulations, however, can take quite a long time and, more importantly, do not offer a fundamental understanding of the crystal growth processes taking place. A fundamental understanding of crystal growth, based in the first instance on 2D nucleation, is offered by the newly developed automated routine called STEPLIFT, which calculates the lowest energy 2D nucleus for all connected net orientations from

the crystal graph. During the development of this automated routine, the need to clearly define the way that step energies should be calculated in a general case led to the development of a new method for the calculation of step energies. The results of this new method, and the application of the STEPLIFT routine to a number of organic materials are described in Chapters 2 and 3. The role of steps during crystal growth, as is fleshed out further in Chapter 1, further adds to the importance of looking in detail at step structures during crystal growth.

From the STEPLIFT routine crystal growth rates can be computed, as a function of crystal orientation as well as driving force, leading to the prediction of crystal morphology, which is the third subject of this thesis. Using the newly developed STEPLIFT routine as well as the already existing Monte Carlo growth simulation methods, the prediction of crystal morphology is studied for a number of different 'real-world' systems in Chapters 7, 8, and 10.

Thus, in Chapter 7, the two very different crystal habits of a yellow dye used in the photographic industry is studied using Monte Carlo simulations. The next chapter deals with Venlafaxine, an anti-depressant pharmaceutical, which has three different polymorphs. In a comparison of established and new morphology prediction methods, it is found that the BFDH and attachment energy model do not suffice for the correct prediction of the crystal morphology. Monte Carlo simulations are used, with either 2D-nucleation or spiral growth mechanism, to correctly model the morphologies observed experimentally. The last two chapters, 9 and 10 deal with another pharmaceutical, Ondansetron. The crystal structure of this molecule was unknown, and in Chapter 9, using different experimental methods, it was found that the crystal structure is a solid solution of enantiomers. The extreme needle-like morphology of Ondansetron is modeled using step energy calculations and Monte Carlo simulations, which clearly show that the needle-like morphology can be explained from the fact that a family of faces in the same crystallographic zone has a substantially higher 2D-nucleation barrier, compared to faces outside of that zone. This, in turn, explains the experimentally observed needle-like morphology from the large difference in growth rates for the faces in the zone, and those outside the zone.

The remaining chapter, Chapter 6, puts forward a new theoretical approach to the rational design of habit modifiers. This approach is again based on the Monte Carlo crystal growth simulations, now expanded with routines to monitor the creation and annihilation of growth sites on the growing crystal surface. Using the statistics thus obtained from the growth process, a method is proposed to quantify the importance of growth site configurations to the growth process. These contribution values of all possible growth site configurations, which are different for each orientation simulated, allow for the identification of a subset of configurations that have both a high and a selective contribution to the growth of a single face. When these configurations can be identified, they can be used as the starting point of a process of rational design of tailor-made additives, able to modify the crystal morphology in the desired way.

Samenvatting

Dit proefschrift is het resultaat van vier jaar modelleren van kristalgroei van organische materialen. Aangezien veelgebruikte methoden om kristalgroei te modelleren in complexe gevallen geen bevredigende resultaten geven, zijn nieuwe methoden ontwikkeld voor het modelleren van kristalgroei. De nieuwe methoden zijn ontwikkeld zodat ze algemeen toepasbaar zijn en een industriële relevantie hebben. De methoden proberen daarom zo algemeen mogelijk te zijn, in plaats van zich toe te spitsen op een kleine subset van toepassingen, maar geven tegelijkertijd ook nieuwe en fundamentele inzichten in de bestudeerde materie.

In dit proefschrift wordt het modelleren van drie belangrijke aspecten behandeld: nucleatie, de rol van stappen tijdens kristalgroei en de uiteindelijke morfologie van kristallen. Het eerste onderwerp, nucleatie, is belangrijk voor polymorfie. Tijdens kristallisatie kunnen zich verschillende polymorfen vormen – in het algemeen is slechts één polymorfe vorm gewenst – en de nucleatie stap is dus cruciaal voor de vorming van de juiste polymorf. Het onderzoek naar nucleatiegedrag is terug te vinden in de hoofdstukken 4 en 5 en bestaat uit de ontwikkeling van een nieuwe methode waarmee de waarschijnlijkheid van het uitgroeien van een klein cluster van moleculen tot een macroscopisch kristal wordt gesimuleerd met behulp van Monte Carlo groei simulaties. Deze simulaties geven inzicht in de groeiwaarschijnlijkheid als functie van de initiële grootte van het cluster en als functie van de drijvende kracht voor kristal groei. Met behulp van dergelijke simulaties kunnen de nucleatie snelheden worden bepaald, wat uiteindelijk zal leiden tot een *a priori* voorspelling van product kwaliteit, wanneer de resultaten worden gecombineerd met proces simulaties om zo de deeltjesgrootteverdeling en polymorfe fracties te bepalen.

De relatieve groeisnelheid van de facetten van een kristal bepalen de uiteindelijke vorm van een kristal. Deze groeisnelheden kunnen gemodelleerd worden met behulp van Monte Carlo groei simulaties, waarbij kristalgroei wordt gesimuleerd als functie van de oriëntatie en als functie van de drijvende kracht. Deze simulaties voorspellen op deze wijze de uiteindelijke vorm van de kristallen, ofwel de morfologie, als functie van de drijvende kracht. Deze simulaties zijn echter vrij rekenintensief en wat wellicht nog belangrijker is, ze geven geen fundamenteel inzicht in de processen die ten grondslag liggen aan de kristalgroei. Dit fundamentele begrip wordt wel verkregen door te kijken naar de invloed van de staprandenergieën van 2D nuclei op groeiende oppervlakken. STEPLIFT is ontwikkeld om deze stapranden op willekeurige oriëntaties van willekeurige kristallen te berekenen op basis van de kristalgraaf. Tijdens het ontwikkelen van deze routine bleek dat er eerst een algemene methode voor het bepalen van staprandenergieën ontwikkeld moest worden. De resultaten van deze nieuwe methode, en de toepassing van de STEPLIFT routine op een aantal organische materialen is terug te vinden in de hoofdstukken 2 en 3. De belangrijke rol van stappen tijdens kristalgroei, die ook in hoofdstuk 1 naar voren wordt gebracht, is de motivatie om in detail naar de stap structuren tijdens groei te kijken.

De STEPLIFT routine kan de groeisnelheden als functie van oriëntatie en drijvende kracht te berekenen, wat leidt tot een voorspelling van de morfologie, het derde onderwerp van dit proefschrift. Gebruikmakend van bestaande Monte Carlo simulaties en van de STEPLIFT berekeningen wordt de morfologie van een aantal 'echte' kristallen bestudeerd in de hoofdstukken 7, 8 en 10.

In hoofstuk 7 worden de zeer verschillende morfologieën van twee polymorfen van een gele kleurstof uit de fotografische industrie bestudeerd met behulp van Monte Carlo simulaties. Het daaropvolgende hoofdstuk behandelt Venlafaxine, een anti-depressivum, met drie verschillende polymorfen. In een vergelijking van morfologievoorspellingsmethoden wordt aangetoond dat de bestaande BFDH en 'attachment energy' modellen niet meer voldoen voor de voorspelling van de morfologie van deze kristallen. Met behulp van Monte Carlo simulaties, gebaseerd op 2D nucleatie en spiraalgroei, wordt de correcte morfologie van deze polymorfen gereproduceerd. De laatste twee hoofdstukken, 9 en 10, behandelen een andere farmaceutisch actieve stof, Ondansetron. De kristalstructuur van deze stof was onbekend, en in hoofdstuk 9 wordt met behulp van verschillende technieken aannemelijk gemaakd dat de kristalstructuur bestaat uit een wanordelijke rangschikking van enantiomeren. De morfologie van de extreem naaldvormige Ondansetron kristallen wordt gemodelleerd met behulp van staprandenergie berekeningen en Monte Carlo simulaties, welke beide aantonen dat de naaldvormige kristallen ontstaan doordat een zone van kristallografische oriëntaties een substantieel hogere 2D nucleatiebarrière heeft, vergeleken met de andere oriëntaties.

In hoofdstuk 6 wordt tenslotte een nieuwe theoretische aanpak van het rationele ontwerp van zgn. 'habit modifiers' geïntroduceerd. Deze aanpak is wederom gebaseerd op Monte Carlo simulaties van kristalgroei, nu met extra routines om de creatie en annihilatie van groei configuraties op het groeiend kristal oppervlak bij te houden. Met behulp van de zo verkregen statistieken kan de relatieve importantie van alle groei configuraties worden bepaald. Wanneer deze relatieve importanties bekend zijn als functie van de oriëntatie en de drijvende kracht, kan een verzameling van groei configuraties waarvan de importantie en ook de selectiviteit in het groeiproces hoog is worden geïdentificeerd. Deze subset van groei configuraties kan dan het aanknopingspunt van een rationeel ontwerp van 'habit modifiers' zijn, om zo de kristal morfologie op de gewenste manier te beïnvloeden.

List of Publications

"Polymorph nucleation studied by 3D nucleation simulations. Application to a yellow isoxazolone dye, paracetamol and L-glutamic acid" M. A. Deij, J. H. ter Horst, H. Meekes, P. Jansens and E. Vlieg, J. Phys. Chem. B., 2006, **111**(7), 1523-1530.

"Towards rational design of tailor-made additives using growth site statistics" M. A. Deij, T. Vissers, H. Meekes and E. Vlieg, Crystal Growth & Design, 2007, **7**(4), 778-786.

"Crystal structure, experimental and computational morphology of three polymorphs of the free base form of Venlafaxine" M. A. Deij, J. van Eupen, H. Meekes, P. Verwer, P. Bennema and E. Vlieg, *Submitted to Int. J. Pharm.*

"Steps on surfaces in modeling crystal growth" M. A. Deij, H. M. Cuppen, H. Meekes and E. Vlieg, *Accepted for publication in Crystal Growth & Design.*

"The step energy as a habit controlling factor. Application to the morphology prediction of aspartame, Venlafaxine and a yellow isoxazolone dye" M. A. Deij, H. Meekes and E. Vlieg, *Accepted for publication in Crystal Growth & Design.*

"On the determination of step energies. Theoretical considerations and application to an anisotropic Kossel model", M. A. Deij, J. H. Los, H. Meekes and E. Vlieg, J. Appl. Cryst., 2006, **39**, 563-570.

"Liquid ordering at the KDP {100}-solution interface", D. Kaminski, N. Radenovic, M. A. Deij, W. J. P. van Enckevort, and E. Vlieg, Crystal Growth & Design, 2006, **6**(2), 588-591.

"Experimental and computational growth morphology of two polymorphs of a yellow isoxazolone dye", M.A. Deij, E. Aret, S.X.M. Boerrigter, L. van Meervelt, G. Deroover, H. Meekes, E. Vlieg, Langmuir 2005, **21**, 3831-3837.

"pH-dependent liquid order at the solid-solution interface of KH_2PO_4 crystals", D. Kaminski, N. Radenović, M. A. Deij, W. J. P. van Enckevort and E. Vlieg, Phys. Rev. B, 2005, **72**, 245404.

"Crystal growth and morphology: new developments in an integrated Hartman-Perdok - connected net - roughening transition theory, supported by computer simulations", P. Bennema, H. Meekes, S.X.M. Boerrigter, H.M. Cuppen, M.A. Deij, J. van Eupen, P. Verwer, and E. Vlieg, Crystal Growth & Design, 2004, **4**, 905-913

"Attachment of molecules at a molecular printboard by multiple host-guest interactions", J. Huskens, M. A. Deij and D. N. Reinhoudt, Angewandte Chemie Int. Ed., 2002, **41**, 4467-4471

"Monolayer of a Na^+-Selective Fluoroionophore on Glass: Connecting the Fields of Monolayers and Optical Detection of Metal Ions", N.J. van der Veen, S. Flink, M.A. Deij, R.J.M. Egberink, F.C.J.M. van Veggel en D.N. Reinhoudt, J. Am. Chem. Soc., 2000, **112**(25), 6112-6113

"A Computer Program for Visualisation of and Practice with Molecular Models Accessible on the Internet", F. Coenders, M.A. Deij, H. Kramers-Pals, Paper presented on the 4th Computer Based Learning in Science (CBLIS) Conference, held in 1999 at University of Twente

Curriculum Vitae

Education

2002 - 2006		**PhD student, IMM Department for Solid State Chemistry, Radboud University Nijmegen** *Modeling crystal growth of organic materials: nucleation, steps and morphology*
1999 - 2001		**PhD student, Supramolecular Chemistry and Technology, University of Twente** *Cooperativity in supramolecular interactions studied at cyclodextrin monolayer interfaces*
1994 - 1999		**Chemistry and Technology, University of Twente** M.Sc. in Supramolecular Chemistry and Technology M.Sc. Thesis Subject: *"Monolayers of calix[4]arene chromoionophores for the optical detection of heavy metal ions"* (9)
1988 - 1994		**Secondary School**
	1988 - 1990	Chr. Gymnasium, Utrecht
	1990 - 1994	Herman Jordan Lyceum, Zeist Subjects taken: Dutch (7), English (8), History (7), Mathematics A (8), Mathematics B (7), Chemistry (7) and Physics (8)

(also see next page)

Work Experience

From November 2006	Scientist Predictive Technologies / Project Leader Solid State Research at Avantium Technologies B.V. Amsterdam
October 2002 - October 2006	PhD research at IMM Department for Solid State Chemistry with Prof. Elias Vlieg, Radboud University Nijmegen *Research into crystal growth and polymorphism of organic materials using molecular modelling techniques, Monte Carlo simulations and new methods to determine step energies.*
– September - October 2005	Extended visit at the Nanochemistry Research Institute in the group of Prof. Julian Gale, Curtin University, Perth, Australia *Integration of a Monte Carlo simulation program with a molecular modelling visualization package.*
November 2001 - October 2002	Chemist at Glaucus Proteomics, Odijk *Responsible for the development of new biocompatible surfaces for proteomics microarray applications.*
August 1999 - November 2001	PhD research at Department of Supramolecular Chemistry and Technology with Prof. David Reinhoudt, University of Twente *Study of cooperativity in supramolecular interactions between monolayers of receptors and molecules in solution.*
May 1998 - July 1998	Internship in the group of Prof. Manfred Reetz at the Max Planck Institute für Kohlenforschung Mülheim a.d. Ruhr, Germany *Development of new ligands for catalysts in chiral reactions.*

Synthon

Synthon is a Dutch pharmaceutical company which develops and manufactures generic medicines. Employing 650 staff worldwide Synthon has affiliate companies in the Netherlands and abroad.

R&D is a vital component of the overall production chain and so also forms the heart of our organisation. Synthon structurally invests in talented researchers and in advanced outfitting of all laboratories. Currently we are working hard on developing a range of new and promising products, which are expected to be ready for the market in the coming years. In addition to chemical and pharmaceutical research, we also carry out analytical and clinical research at our locations in The Netherlands, Czech Republic, Spain and the United States.

Synthon prefers to concentrate on medicines with complex chemical structures and welcomes the challenge of developments in fields such as biotechnology, which will result in a whole new generation of medicines.

More than in any other sector, intellectual property plays a crucial role in the pharmaceutical industry. Before product development is started, extensive intellectual property research is carried out. To avoid violating an existing patent. But also to identify potential opportunities for us to patent the active substance, the method of synthesis or the formulation. This is a complex matter that makes high demands on our patent attorneys. They combine specialist knowledge on international patent law with insight into the technical aspects of our business.

Synthon deliberately chose to be a vertically integrated company. Which means that our work does not stop at the laboratory, but continues through to production. In this way, the active substances are produced in the Czech Republic and Argentina, while the tablets, capsules, powders, drops and other dosage forms are formulated in Spain. The medicines are subsequently packed in Spain or in the United States. Synthon products are made available worldwide through marketing partners in many countries.